523189

Sandia National Laboratories
Technical Baseline Reports

WBS 1.3.5.3
Compliance Monitoring
WBS 1.3.5.4
Repository Investigations
Milestone RI130

July 31, 2002

Prepared for the United States Department of Energy
Carlsbad Field Office

Sandia National Laboratories

Sandia National Laboratories
Technical Baseline Reports

WBS 1.3.5.3
Compliance Monitoring
WBS 1.3.5.4
Repository Investigations
Milestone RI130

July 31, 2002

Prepared for the United States Department of Energy
Carlsbad Field Office

Sandia National Laboratories

Sandia National Laboratories
Technical Baseline Reports

WBS 1.3.5.3
Compliance Monitoring
WBS 1.3.5.4
Repository Investigations

for Paul E. Shoemaker 08/01/02

F.D. Hansen, Acting Manager 6822 Date

The contents of this report follow the WBS structure for Sandia's FY2002 program. Subject matter includes compliance monitoring and repository investigations and follows the WBS numerically. The intent of this organization is to facilitate direct comparison between the BOE's and progress, thereby providing the CBFO with current technical status and program tracking information.

Table of Contents

TABLE OF CONTENTS

July 31, 2002

1 Executive Summary

EXECUTIVE SUMMARY

1.1 Introduction

This report fulfills the requirements of Milestone RI130. It is the fourth report in a series that also includes Sandia National Laboratories (SNL) (2001a, 2001b, and 2002). This report comprises sections on Compliance Monitoring (Section 2), Geochemistry (Section 3), Engineered Barriers (Section 4) and Rock Mechanics (Section 5).

1.2 Compliance Monitoring

Sandia National Laboratories – Carlsbad Programs Group (SNL), the Scientific Advisor to the US Department of Energy (DOE) Carlsbad Field Office for the Waste Isolation Pilot Plant (WIPP), is responsible for the evaluation of data acquired from WIPP monitoring programs implemented to meet the compliance requirements of the US Environmental Protection Agency (EPA). Annually, SNL evaluates ten compliance-monitoring parameters (COMPs) comparing current derived values for each parameter against both expected repository performance (defined in terms of Trigger Values) and assumptions used for the performance assessment (PA) in DOE's 1996 Compliance Certification Application (CCA). COMPs formally evaluated in this process focus on hydrology, geomechanics, surface subsidence, human intrusion, and waste activity. On a continual basis, SNL also assesses monitoring data acquired by the WIPP Management and Operating (M&O) Contractor to track trends, identify anomalies in data if present, and determine overall effectiveness of the monitoring programs relative to compliance needs.

During the annual 2000 COMPs evaluation, SNL identified a trend in one hydrologic COMP, i.e., changes in Culebra groundwater levels. In particular, groundwater levels in the Culebra Member of the Rustler Formation were rising faster than predicted in the CCA PA, contrary to the assumption that Culebra water levels were at steady state and would rise only in response to a long-term climate change. In the subsequent annual COMPs evaluation, the water-level-rise trend continued. An extensive investigation into the cause(s) of the water-level rise, as well as an assessment of the potential impacts such rises might have on CCA PA models and assumptions, has been initiated. Implementation of this investigation has occurred and is the responsibility of SNL. The status of the investigation, as well as other routine data assessment activities, is provided in three subsections of this report as described below. Results of the next comprehensive COMPs evaluation, which includes discussions of all ten monitored parameters, are not presented herein, but will be provided in the annual 2002 COMPs report to be submitted to DOE in October 2002.

Subsection 2.1, Magenta Hydrological Flow Model, describes activities conducted by SNL to develop a hydrologic flow model for the Magenta Member of the Rustler. The hydrology of the Magenta has never been well characterized because the

Culebra, located below the Magenta, is more transmissive than the Magenta and would, therefore, be the preferred transport pathway should radionuclides reach the Rustler. However, renewed interest in Magenta hydrology has arisen because several plausible scenarios explaining the rising water levels in the Culebra involve vertical flow through or leakage from the Magenta to the Culebra. Thus, a flow model of the Magenta is needed to characterize these scenarios. Discussions in Subsection 2.1 focus specifically on: recompletion of seven wells to the Magenta and the subsequent monitoring of water levels in these recompleted wells; water-quality testing and analysis in one recently recompleted Magenta well (H-9c); and results of a technical and quality surveillance of the Magenta hydrology scientific notebooks used to document Magenta activities.

Subsection 2.2, Culebra Water-Level Rise Investigations, provides background information that documents the relevant Culebra hydrology assumptions used in the CCA PA, the process used to identify current rises in Culebra groundwater levels, and various SNL test and analysis plans implemented to investigate the cause(s) of the Culebra water-level rises. In addition, on-going monitoring and technical activities are described and their status is discussed. Monitoring activities specifically addressed include: continuous water-level measurements in selected wells using electronic sensors (i.e., TROLLS); continuous meteorological monitoring near the H-7 and H-9 well pads; and injection-well monitoring near the H-9 well pad. Related technical activities addressed in this report include: development of well test data-interpretation software (i.e., nSIGHTS) to be used to quantify uncertainty in Culebra transmissivity (T) estimates made from well-test data acquired from previous studies; documentation of plausible scenarios explaining Culebra water-level rises; identification of factors causing Culebra water-level rises and the effects of water-level changes on calibration of Culebra T fields; and drafting of a test plan for Dewey Lake Formation geohydrological investigations to support testing of vertical leakage/infiltration scenarios that may explain Culebra water-level rises.

In contrast to Subsections 2.1 and 2.2, Subsection 2.3, WIPP Hydrologic Data Assessment, describes routine assessments of WIPP hydrological monitoring data rather than results of specific water-level rise investigations. The current groundwater-monitoring network is described and the status of activities at individual wells is summarized with particular emphasis on observed deviations from normal well behavior and well activities performed and monitored by the M&O and SNL, respectively. The subsection concludes with the description of a remote-monitoring-system pilot study conducted at C-2737 including preliminary results for water-level measurements made both in the Magenta and Culebra members of the well.

1.3 Geochemistry

Section 3, Geochemistry, describes ongoing laboratory studies of microbial gas generation at Brookhaven National Laboratory (BNL), a lab study of microbial gas generation to be initiated at SNL in Carlsbad, and four studies of actinide chemistry.

Los Alamos National Laboratory – Carlsbad Operations (LANL-CO) is now the lead organization for WIPP-related lab studies of actinide chemistry. Therefore, three of the four studies of actinide chemistry described in Section 3 pertain to lab studies carried out previously, and/or the use of results from previous lab studies in PA. The other involves the chemical behavior of a byproduct of brine radiolysis that could affect the mobility of Pu and other actinide elements in the repository.

Subsection 3.1, Re-Evaluation of Microbial Gas Generation under Expected Waste Isolation Pilot Plant Conditions, discusses ongoing lab studies of microbial gas generation at Brookhaven National Laboratory (BNL). This progress report, by Jeffrey B. (Jeff) Gillow and Dr. Arokiamsamy J. (A. J.) Francis of BNL emphasizes: (1) recent results from long-term experiments with cellulosics under humid conditions; (2) recent results of long-term experiments with irradiated and unirradiated plastics and rubbers under inundated conditions; (3) a description of recently initiated experiments using radiolabeled carbon (^{14}C) substrate at relative humidities (RHs) of 10, 40, 60, and 70%. CO_2 (carbon dioxide) production from amended, inoculated, and unamended, inoculated humid experiments with cellulosics (papers), initially aerobic and anaerobic, without bentonite, has leveled off, consistent with other analyses during the last two years. The initially aerobic, humid experiments have now lasted 3,334 days (9.1 years); the initially anaerobic, humid runs have lasted 2,945 days (8.1 years). Initially aerobic, unamended, inoculated humid experiments with cellulosics and bentonite appear to be producing additional CO_2, but this production may not be significant, given the uncertainty of the analyses. In any case, the runs with bentonite are no longer relevant to the WIPP. (When these tests were started eight or nine years ago, SNL included bentonite in many of its studies to evaluate the effects of this potential constituent of a crushed salt-bentonite backfill.) Recent analyses for CH_4 (methane) in inundated experiments with irradiated and unirradiated plastics and rubbers imply that significant quantities of this gas have not been produced since the last analysis. Therefore, there has not been significant gas generation from (or significant microbial degradation of) plastics and rubbers during the 2,920 or 3,070 days (8.0 or 8.4 years) since these experiments were started.

Subsection 3.2, Experimental Study of Microbial Gas Generation under WIPP-Relevant Humid Conditions, is a test plan for a lab study of microbial gas generation to be initiated at SNL in Carlsbad. Dr. Yifeng Wang of SNL's Carlsbad Programs Group prepared this test plan, which will be posted on SNL's Nuclear Waste Management Program (NWMP) On-Line Documents web site. The objective of these experiments is to simulate humid conditions more accurately than the ongoing experiments described in Subsection 3.1, which have been carried out with small but potentially significant quantities of water contained in the inocula. The new experiments will include two significant improvements: (1) removal of this H_2O by desiccation between the time of inoculation and the start of the experiments; (2) maintenance of constant values of relative humidity during the experiments by various saturated salt solutions present during the experiments, but not in contact with the microorganisms and the cellulosic materials (papers) used as the substrate. These experiments will yield more realistic gas generation rates for humid conditions, which will in turn result in more realistic

predictions of spallings releases and other pressure-induced direct releases of radionuclides following human intrusion of the repository.

Subsection 3.3, *Effects of Actinide Complexation by Organic Ligands on WIPP Performance Assessment*, describes the use of results from of previous lab studies of organoactinide complexation in PA. Dr. Donald E. (Don) Wall of SNL presented this material as a poster at the 223rd American Chemical Society National Meeting, April 7-11, in Orlando, FL. Wall's presentation included: (1) an overview of the design of the repository, (2) an overview of PA, especially the release scenarios and the types of releases expected following human intrusion; (3) the inventory of radionuclides and radionuclide release limits; (4) the inventory and expected concentrations of acetate, citrate, ethylenediaminetetraacetate (EDTA), and oxalate; (5) a summary of the stability constants for complexes between these organics and Nd(III), Th(IV), U(VI), Np(V), and Am(III) obtained by Dr. Gregory R. (Greg) Choppin and his students at Florida State University (FSU) for use in WIPP PA.

Subsection 3.4, Chemical Behavior of Hypochlorite in High Ionic Strength Solutions, is a revised test plan for an ongoing lab study of the chemical behavior of OCl^- (hypochlorite), a byproduct of α radiolysis of brine that could affect the mobility of Th, U, Np, and – especially Pu – in the repository. D. E. Wall prepared the original test plan and this revision, which will be posted on the *NWMP On-Line Documents* web site. This study has three objectives: (1) quantification of the decomposition rate of OCl^- under expected WIPP conditions, including the effects of brine type (5 m NaCl and modified Brine A, GWB, and ERDA-6), pH, and the presence of waste constituents such as metallic or oxidized iron); (2) identification of conditions that affect the complexation of metal ions by OCl^-; (3) determination of stability constants for important metal-OCl^- complexes. Wall will use the OCl^- decomposition rates obtained from this study – along with formation rates obtained from the literature and/or ongoing studies by LANL-CO personnel to estimate steady-state concentrations of OCl^- in the repository and the effects of OCl^- on the redox speciation of Pu. Initially, Wall will not use any radionuclides for this study, thus enabling him to carry his experiments in the SNL chemistry laboratory in Carlsbad. In particular, Wall will use stable Nd(III) – an excellent analog of Am(III) – to estimate stability constants for Am(III)-OCl^- and Pu(III)-OCl^- complexes. However, he could extend this work to experiments with radionuclides such as Th(IV) and Am(III) – or even Pu(III) and Pu(IV) – in the Carlsbad Environmental Monitoring and Research Center.

Subsection 3.5, Complexation of Americium by Humic, Fulvic and Citric Acids at High Ionic Strength, is a manuscript based on a presentation by Dr. Nathalie A. Wall, SNL, and three coauthors at Migration '01, September 16-21, 2001, in Bregenz, Austria. This manuscript will appear in *Radiochimica Acta* as part of the proceedings of this conference. Wall carried out this work while a postdoctoral student of G. R. Choppin at FSU. Her results for the Am(III)-citrate complex will – along with the results obtained for other complexes between acetate, citrate, EDTA, and oxalate, and Nd(III), Th(IV), U(VI), Np(V), and Am(III) obtained at FSU – provide the basis for including these

organics in the actinide solubility calculations for the Compliance Recertification Application.

Subsection 3.6, Use of Oxidation-State Analogs for WIPP Actinide Chemistry, discusses the use of the oxidation-state analogy to establish the solubilities of U(IV), NpIV), and – especially – Pu(III) and Pu(IV) used in the WIPP CCA PA. N.-A. Wall and three coauthors presented this material as a poster at the recent American Chemical Society National Meeting in Orlando. For the CCA PA, the WIPP Actinide Source Term Program used experimental data for Nd(III), Am(III), and Cm(III) and the oxidation-state analogy to establish the solubility of Pu(III) and Am(III), and experimental data for Th(IV) and the oxidation-state analogy to establish the solubility of U(IV), Np(IV), and Pu(IV). In response to criticism from WIPP review panels such as the New Mexico Environmental Evaluation Group, Wall discusses the strengths and weaknesses of the oxidation-state analogy, such as elimination of the difficulties involved in oxidation-state control required for redox-labile elements such as Pu, versus small but quantifiable deviations in chemical behavior.

1.4 Engineered Barriers

Subsection 4.1, Carbonation of Magnesium Oxide, describes part of an ongoing lab and modeling study of MgO at SNL in Carlsbad. This study comprises: (1) continuing characterization of Premier Chemicals MgO, the MgO currently being emplaced in the WIPP; (2) quantification of MgO hydration rates under humid and inundated conditions, and identification of hydration products and reaction path(s); (3) quantification of MgO carbonation rates and identification of the metastable Mg-carbonates and reaction path(s); (4) quantification of the effects of (possible) lithification on hydration and carbonation rates and reaction paths. This progress report, by Anna C. Snider and Dr. Yongliong Xiong of SNL, emphasizes recent results of carbonation experiments. In their report, Snider and Xiong report the first observation of nesquehonite ($MgCO_3 \cdot 3H_2O$) in MgO carbonation experiments in Carlsbad – in runs carried out under a controlled atmosphere with 5% CO_2. However, nesquehonite disappeared quickly from most of these experiments as hydromagnesite (apparently $Mg_5(CO_3)_4(OH)_2 \cdot 4H_2O$) formed. These observations, along with previous observations of persistent nesquehonite in early experiments with 100% CO_2 at SNL in Albuquerque and the absence of nesquehonite in ongoing experiments with 0.035% CO_2 (ambient, atmospheric P_{CO_2}) in Carlsbad, suggest that the overall (hydration and carbonation) reaction path periclase (MgO) → brucite ($Mg(OH)_2$) (or magnesium chloride hydroxide hydrate) → hydromagnesite is more likely in the WIPP than periclase → brucite (or magnesium chloride hydroxide hydrate) → nesquehonite → hydromagnesite, because carbonation of MgO will readily keep pace with slow microbial production of CO_2 and maintain P_{CO_2} at relatively low values.

Subsection 4.2, Experimental Work to Develop a Model for Cement-Brine Interactions, discusses a lab study by Dr. Charles R. Bryan at SNL. This progress report

includes results from experiments to quantify the effects of: (1) reactions between brine and powdered cement on brine chemistry; (2) the brine:cement ratio on alteration reaction and alteration products; (3) non-equilibrium processes, such as selective dissolution of cementitious phases, precipitation of mineral coatings or pore-filling phases, or fracturing caused by formation of expansive alteration products, on the cement degradation rate or reaction path(s). The results of these experiments, along with results from column-transport experiments and solubility experiments to determine Pitzer parameters for Al (aluminum) and Si (silicon), will provide the basis for a thermodynamic model for brine-cement interactions, and a kinetic model for the degradation of borehole plugs.

1.5 Rock Mechanics

Section 5 summarizes rock mechanics activities, which include investigations of the disturbed rock zone (DRZ) and geomechanical studies. These investigations are closely associated with international collaborations. Therefore, this progress report incorporates two international research focus areas as they relate to rock mechanics studies. Subsection 5.1, Fracture Analysis, concerns fracture analyses that examine damaged cores from the Asse Mine in Germany and similar cores from WIPP. We leverage our interest in the DRZ with an equally strong interest in the European repository community, to advance our collective understanding of the DRZ. As these studies mature, we will have developed a database of fracture over time and space in several applications. The collaboration will likely culminate with "bench-mark" calculations by both teams. An acceptable model of DRZ development and properties pertaining thereto would provide a strong basis for brine limitation in PA considerations.

Subsection 5.2, Crushed Salt Studies, describes crushed salt and its characteristics. International collaborations with the European Union BAMBUS II initiative have concentrated on crushed salt as a back-fill material. Both past and recent WIPP research and design have involved crushed and re-consolidating salt. In fact, the panel closure re-design includes a crushed salt component. Crushed salt studies are fundamental to WIPP applications in sealing systems and rock mechanics and crushed salt properties are of great interest to international collaborators. An understanding of the compaction behavior of crushed salt is necessary to perform engineering calculations, to model convergence effects, to quantify backfill consolidation, and currently to assess a panel closure system redesign for WIPP. These investigations examine crushed salt cores and similar materials using scanning electron microscopy to characterize porosity, mineralogy and structural features. The permeability of each salt sample was measured in the laboratory prior to impregnation. Compositional, structural, textural, diagenetic (compactional) and hydrologic features are documented. Characteristics of crushed salt and similar materials from the USA, Germany and Canada are compared.

Rock mechanics investigations conducted this year emphasize DRZ studies in the WIPP underground. Technical papers for the North American Rock Mechanics Symposium were prepared, reviewed, and submitted. These finished documents are included in Subsections 5.3 and 5.4 of this progress report. The presenters were unable to

attend this DRZ workshop; however, these papers will be published in workshop proceedings.

References

Sandia National Laboratories. 2001a. "Sandia National Laboratories Technical Baseline Reports, January 31, 2001." Carlsbad, NM: Sandia National Laboratories.

Sandia National Laboratories. 2001b. "Sandia National Laboratories Technical Baseline Reports, July 31, 2001." Carlsbad, NM: Sandia National Laboratories.

Sandia National Laboratories. 2002. "Sandia National Laboratories Technical Baseline Reports, January 31, 2002." Carlsbad, NM: Sandia National Laboratories.

2 COMPLIANCE MONITORING

2.1 Magenta Hydrological Flow Model[1]

T. W. Pfeifle, D. A. Chace, T. L. MacDonald and C. R. Bryan
Sandia National Laboratories, MS 1395
4100 National Parks Highway
Carlsbad, NM USA 88220

Abstract

The Magenta Dolomite Member of the Rustler Formation is a saturated, laterally extensive geohydrological unit located within a stratigraphic section of southeastern New Mexico that also contains the Waste Isolation Pilot Plant (WIPP). The WIPP, operated by the US Department of Energy (DOE) near Carlsbad, NM, is a geologic repository for disposal of transuranic and hazardous wastes. The disposal horizon is located at a depth of 2,150 feet and is sited in the massive salt beds of the Salado Formation that lies directly below the Rustler. At the location of the WIPP shafts, the Magenta is approximately 1,450 feet above the repository horizon or ~ 700 feet below ground surface. The Magenta could potentially provide a flow path for transport of radionuclides escaping the repository; however, a groundwater flow model of the Magenta has never been developed for use in transport modeling because previous studies have shown that the Culebra Member (located below the Magenta and also within the Rustler) is more transmissive than the Magenta and, thus, would be the preferred transport pathway should radionuclides reach the Rustler.

A flow model of the Culebra has been developed based on extensive geologic and hydrologic characterization of the WIPP site. One assumption in the Culebra flow model is that hydraulic heads in the Culebra are in static equilibrium and, therefore, are not expected to change with time unless some anthropogenic event occurs. Results of recent water-level measurements in wells completed to the Culebra have shown that these water levels are not static, but instead are rising. To explain these rising water levels, DOE has implemented an aggressive investigation of WIPP site hydrology including re-assessment of the Culebra flow model, development and testing of recharge/discharge scenarios, and additional field activities (well testing, geological/geophysical investigations, etc). One plausible scenario explaining the rising water levels in the Culebra is vertical leakage from the Magenta to the Culebra through existing or abandoned boreholes. Testing of this scenario requires the development of an accurate Magenta flow model.

Sandia National Laboratories (SNL), DOE's Science Advisor, has implemented a plan to recomplete and test up to 11 existing WIPP groundwater monitoring wells to acquire the data necessary to develop the required Magenta flow model. This report presents the status of these Magenta well-recompletion activities. The activities are subdivided into three general categories: (1) Magenta recompletion well monitoring; (2) recompletion and water quality testing in Magenta H-9c; and (3) technical and quality surveillance of Magenta hydrology notebooks.

[1] This work is covered by WBS #1.3.5.3.1.1 and 1.3.5.3.1.2

Background and Introduction

Previous hydrological and transport calculations for the WIPP Compliance Certification Application have shown that the consequences of a release of radionuclides to the Magenta are less significant than the consequences of a release to the Culebra. Therefore, most early studies concentrated on hydrological characterization and groundwater monitoring of the Culebra. Recently however, some of the focus has returned to the Magenta and activities are planned and currently under way to develop a groundwater flow model for the Magenta to evaluate scenarios explaining rising Culebra water levels and to understand better the hydrology in the region for evaluation of compliance monitoring hydrological data.

The development of the Magenta flow model requires a variety of spatial and temporal hydrological data for the Magenta including depth and thickness, transmissivity, storativity, hydraulic head, and fluid density. Depth and thickness have been well characterized through the drilling of approximately 100 wells and exploratory holes under previous studies; however, the other properties are not well established. Therefore, a plan for collecting additional hydrological data has been developed and implemented (Beauheim, 2000). The plan calls for the following activities:

- Recompletion of up to 11 wells to the Magenta
- Water quality/density measurements
- Selective slug tests and/or drill-stem tests
- Selective pumping tests
- Long-term water-level monitoring

In addition to these activities, water-level data from wells already completed to the Magenta are being assembled to supplement the data expected from the recompleted wells. To date, the Magenta well-recompletion activity has been initiated and historical water-level data from nine existing Magenta wells have been assembled.

The status of the Magenta flow model development is presented below under separate headings including: (1) Magenta recompletion well monitoring; (2) recompletion and water quality testing in Magenta H-9c; (3) surveillance of Magenta hydrology notebooks.

Magenta Recompletion Well Monitoring

The development of a Magenta flow model requires, among other activities, the recompletion of wells to the Magenta Member of the Rustler Formation so that water levels can be monitored and hydrological tests can be performed. Recompletion is being considered for 11 wells selected because they are in locations where Magenta data are currently lacking. For some of these wells, data on hydraulic head are particularly important (e.g., DOE-2, H-11b2, H-15, P-15), while in other wells (e.g., H-18 and WIPP-18), data on transmissivity are of primary importance. For completeness however, hydraulic-head, transmissivity, and fluid-density data will be collected from all locations.

Recompletion of the 11 wells was scheduled to occur in two phases. In the first phase, the six wells considered most important for the model development (i.e., DOE-2, H-18, H-15, H-11b2, P-15, and WIPP-18) were to be recompleted and instrumented to collect pertinent data. These data would then be evaluated to determine whether the database was adequate for construction of a reliable Magenta model, or whether additional data were needed from some or all of the remaining five wells (i.e., WIPP-13, H-14, DOE-1, ERDA-9, and H-17). If additional data were required, recompletion of the remaining five wells would occur during the second phase of the effort. The locations of all 11 wells are shown in Figure 1.

Early in 2001, six wells were recompleted to the Magenta during the first phase of this activity including DOE-2, H-11b2, H-14, H-15, H-18, and WIPP-18. Recompletion of P-15 rather than H-14 was scheduled for the first phase of the activity; however, while attempting to set the bridge plug in P-15, scale build-up in the casing was so extensive that the plug could not be positioned properly. The well casing was subsequently scraped to remove the scale, but the scraping revealed a hole in the casing near the ground surface. As a result, recompletion activities for P-15 were abandoned in favor of H-14.

Following the bailing of the recompleted wells under Phase I, water-level recovery in each of the six wells was characterized using both a sounder tape referenced to the top of casing and a submersible TROLL[2]. The water levels measured using the tape are plotted in Figure 2, which shows the recovery responses for all six wells. Sounder tape and TROLL data for individual wells are presented in Figures 3 through 8 and discussed below.

The water level in DOE-2 (Figure 3) continues to show a steady rise of about 1 foot/month and is currently at 3,065 feet above mean sea level (amsl). The Magenta wells nearest to DOE-2 are H-5c and H-6c (Figure 1). The current water levels in these wells are 3,157 feet (amsl) and 3,065 feet (amsl), respectively so, by simple interpolation, the steady-state water levels at DOE-2 are expected to be about 3,110 feet (amsl). Therefore, the water level in DOE-2 is not at its steady-state value and will likely continue to rise over time.

Following the bailing of WIPP-18, the water level in the well (Figure 4) recovered to a steady value of 3,140 feet (amsl). In July 2001, the water level began to drop at a steady rate of approximately 6 feet/month. The trend reversed in January 2002 and the water level in WIPP-18 is rising and is currently 3,133 feet (amsl). The drop in water levels was attributed to a leaky bridge plug placed between the Magenta and Culebra; however, the current trend is unexplained but could represent the arbitrary self-seating of the plug and subsequent recovery. Assuming the well condition is good and the current trend continues, the water level in the well will likely continue to rise consistent with other known hydrologic conditions in the area. However, because of the anomalous behavior of the water levels in this well, Sandia has recommended to Westinghouse TRU Solutions (WTS) that WIPP-18 be added to the well logging and integrity testing priority list. During logging, the bridge plug will be removed and eventually re-seated and well-casing integrity will be examined.

[2]A TROLL is an electronic transducer that is positioned below the water level in a well and measures the fluid pressure of the column of water standing above the transducer.

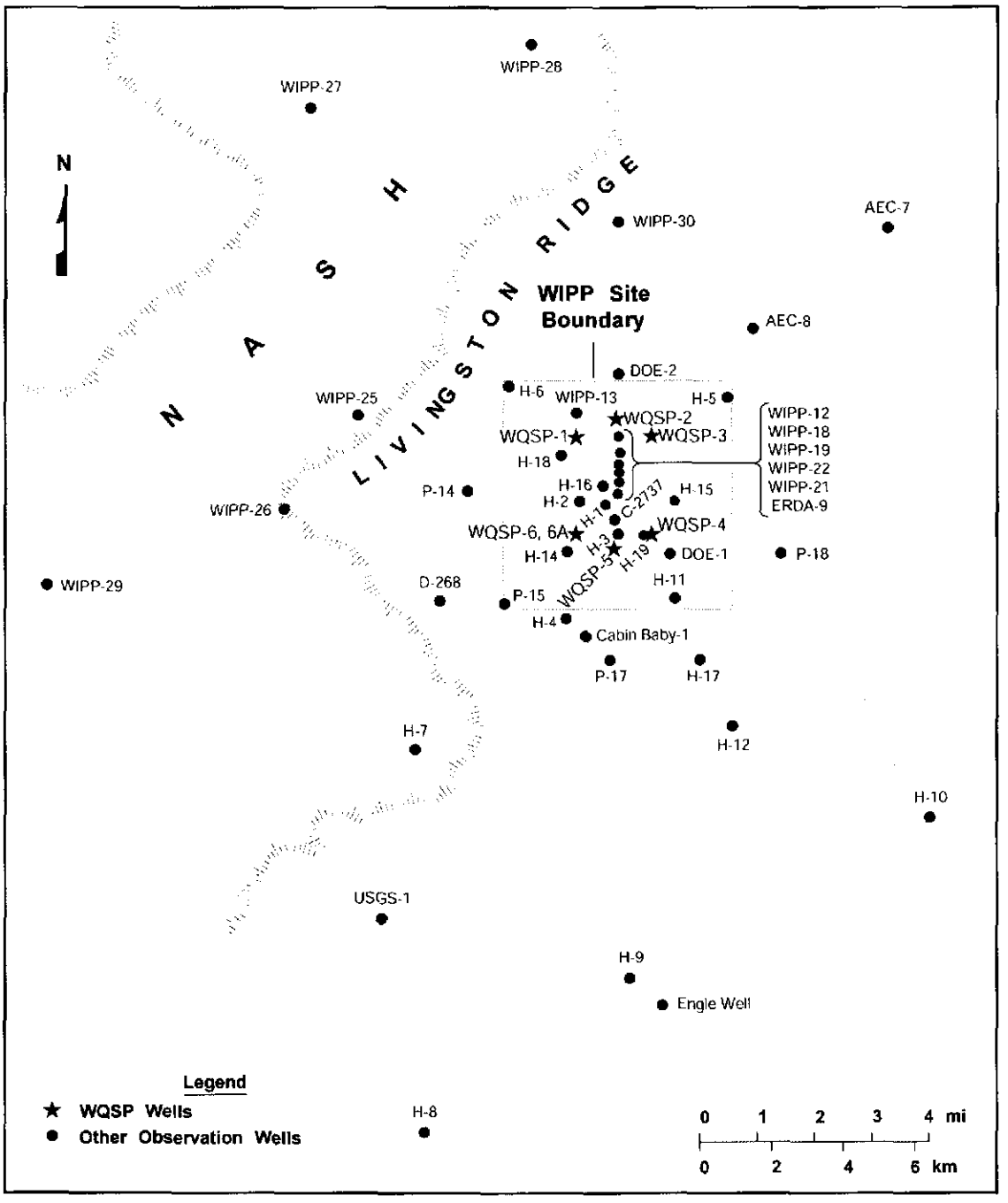

Figure 1. WIPP monitoring well location map.

The Magenta water level in H-18 (Figure 5) reached a peak shortly after the well was bailed, then monotonically decreased to a constant value of 3,078 feet (amsl). The current Magenta water level in H-18 is about 18 feet higher than the water level in the Culebra at this location. Northwest of H-18 at H-6, the Magenta water level is 13 feet higher than the Culebra water level, but to the south and east of H-18, the Magenta water level is approximately 100 feet higher than the Culebra water level. Because of this strong change in gradient from southeast to northwest, the difference in water levels between the Magenta and Culebra at H-18 is not well known. Pressure-density data from H-18 would be helpful in assessing the water levels at this location.

The Magenta water level in H-15 (Figure 6) has stabilized at approximately 3,113 feet (amsl). The current water level is consistent with the closest other wells completed to the Magenta (e.g., H-2, H-3, and H-5) and is approximately 100 feet higher than the water levels at adjacent Culebra wells consistent with previous knowledge about the hydraulic gradient between the Magenta and Culebra. As such, Sandia has recommended to WTS that the final development (pumping of several well bore volumes of water to remove stagnant well water and establish native water in the well bore) of H-15 be completed so that Sandia can initiate its well-testing activities including water-quality serial sampling and slug or pumping tests.

From April 2001 through October 2001, the Magenta water levels in H-14 rose steadily at a rate of approximately 15 feet/month (Figure 7). Since November 1, 2001, the water level rise has slowed considerably (1 foot/month) indicating well recovery is nearly complete. The current water level is 3,106 feet. The stabilized water level is expected to be between 3,100 and 3,120 feet (amsl), a range consistent with previous hydrological knowledge. Because data collected to date indicate the Magenta water levels in H-14 are representative of the site conditions, Sandia has recommended to WTS that the final development of the well be completed so that Sandia can initiate its well-testing activities.

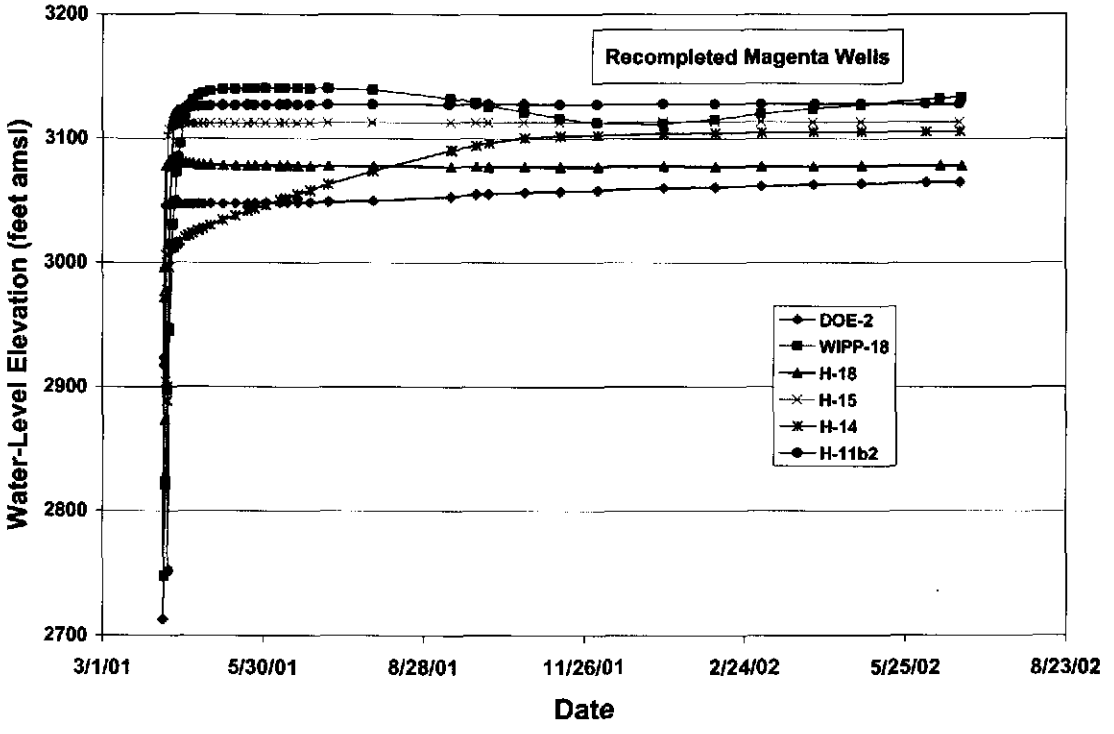

Figure 2. Water-level recovery for bailed wells re-completed to the Magenta.

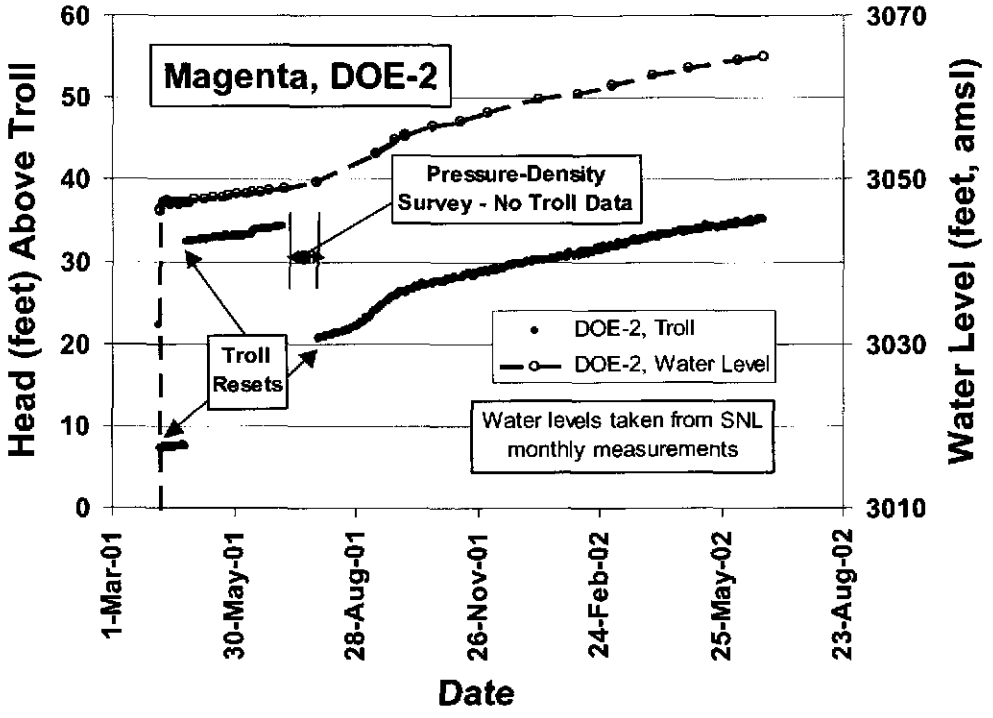

Figure 3. Magenta head levels measured at DOE-2.

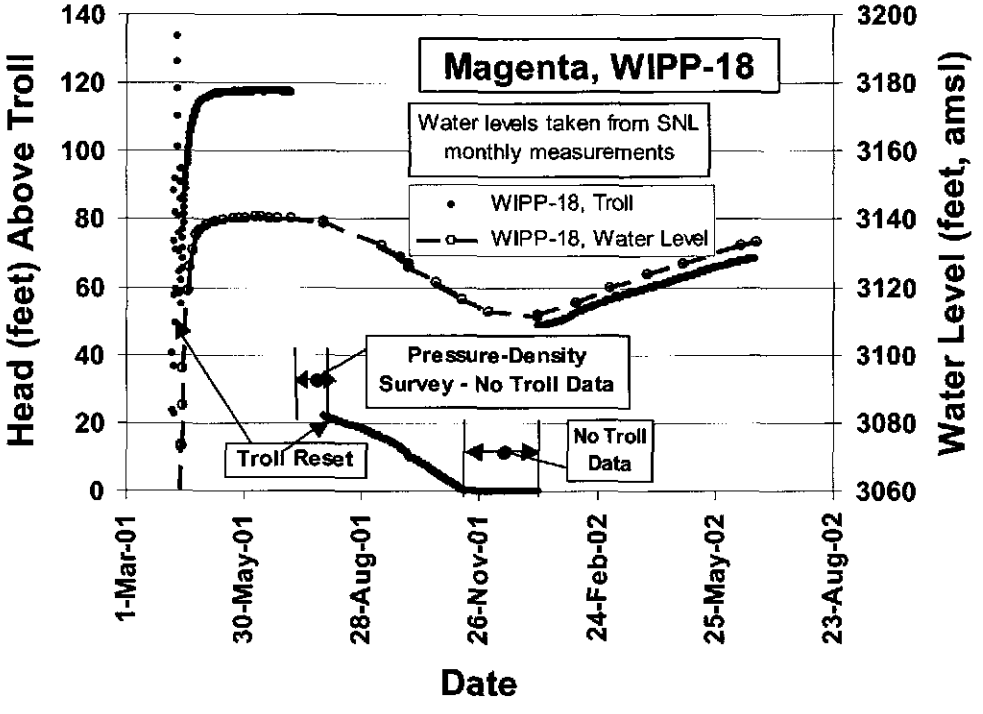

Figure 4. Magenta head levels measured at WIPP-18.

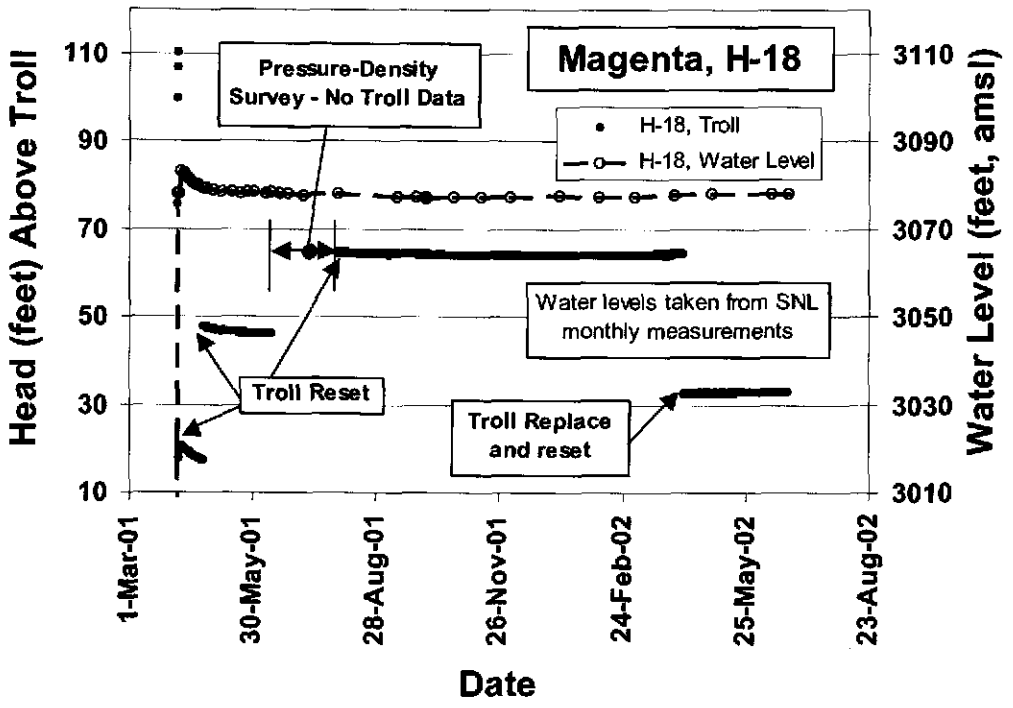

Figure 5. Magenta head levels measured at H-18.

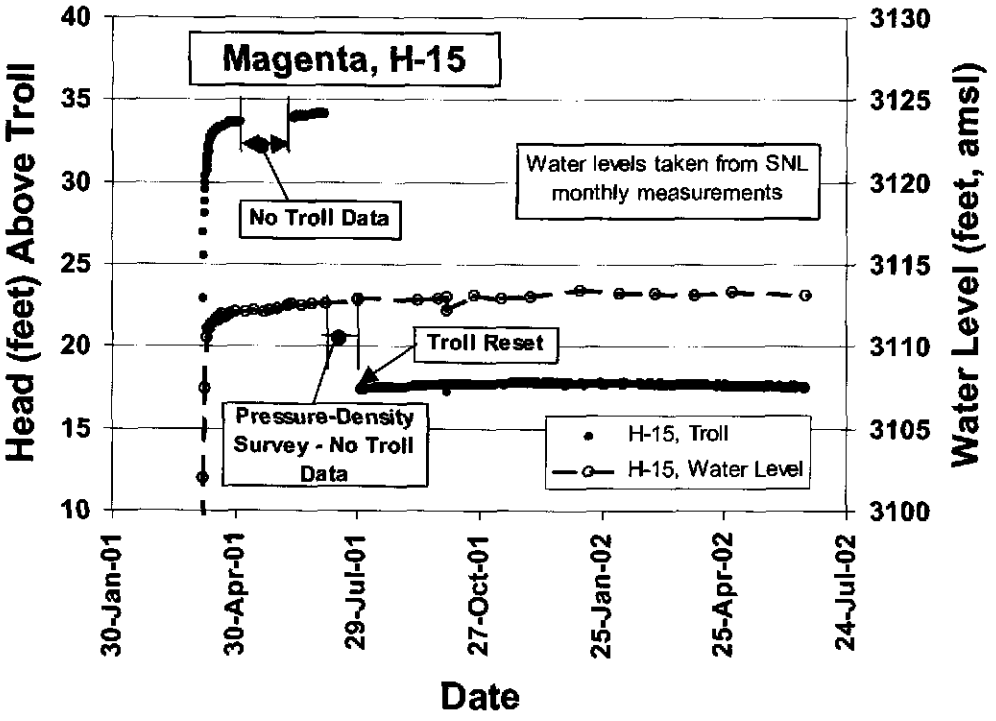

Figure 6. Magenta head levels measured at H-15.

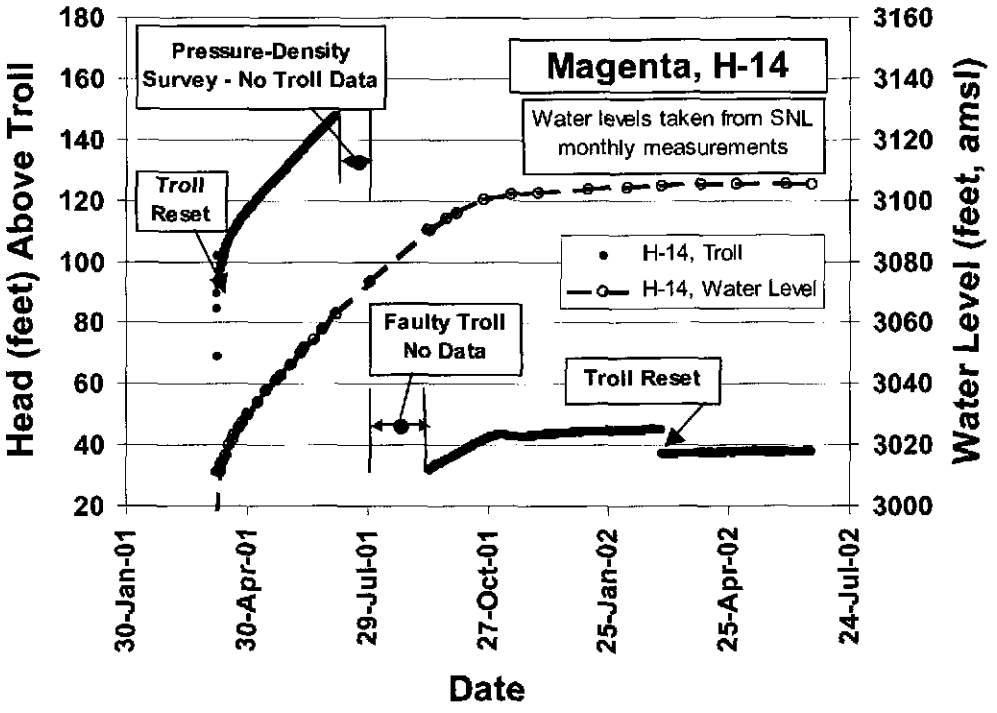

Figure 7. Magenta head levels measured at H-14.

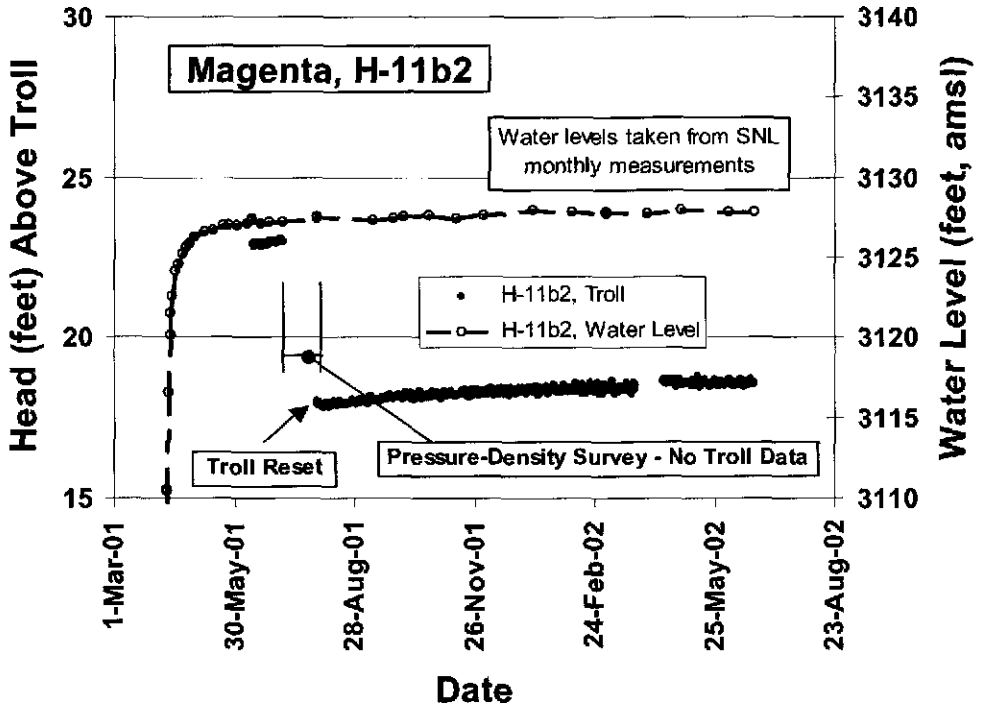

Figure 8. Magenta head levels measured at H-11b2.

The Magenta water level in H-11b2 (Figure 8) recovered quickly after the bailing activity and has essentially stabilized at 3,128 feet (amsl), a value consistent with previous hydrological knowledge at this location. Because data collected to date indicate the Magenta water levels in H-11b2 are representative of the site conditions, Sandia has recommended to WTS that the final development of the well be completed so that Sandia can initiate its well-testing activities.

Recompletion and Water Quality Testing in H-9c

RECOMPLETION

As part of the current and ongoing plugging and abandonment campaign being performed by WTS on the WIPP monitoring well network, H-9c was integrity logged and evaluated on November 19, 2001. The results of the H-9c integrity logging and evaluation were that this well would continue to provide reliable water levels. Figure 9 shows the location of H-9c.

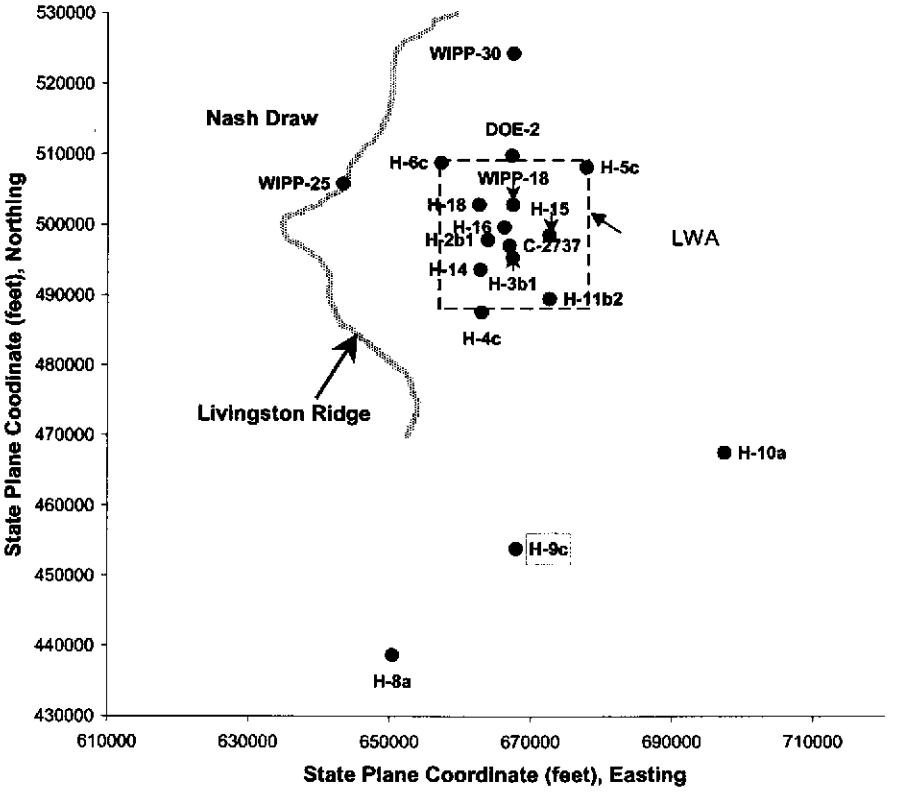

Figure 9. H-9c Magenta well location (along with other WIPP Magenta well locations).

In January of 2002, the Groundwater Task Force (GWTF), including members from DOE, WTS, and SNL, made the decision to recomplete H-9c as a Magenta monitoring well from a Culebra monitoring well. Table 1 provides information relevant to the H-9c recompletion to a Magenta monitoring well. Although H-9c was not originally included in Sandia's Magenta recompletion well network, its unplanned recompletion afforded an opportunity to add the well to the network. Thus, Beauheim (2000) governed these activities.

Figure 10 shows the H-9c configuration following the recompletion to a Magenta monitoring well.

WATER-QUALITY SAMPLING

All water-quality sampling activities associated with H-9c were performed under Beauheim (2000).

In preparation for the water-quality sampling activities, three wellbore volumes were pumped from H-9c to begin the process of purging the well of water not representative of actual Magenta water. Table 2 provides information regarding the activities performed in preparation for water-quality sampling.

Table 1. H-9c Recompletion Activities[(a)]

Operation	Date Completed	Time Completed (hh:mm)
Attach to inflatable bridge plug below Culebra interval.	January 10, 2002	09:50
Deflate inflatable (Culebra) bridge plug.	January 10, 2002	10:10
Remove inflatable (Culebra) bridge plug.	January 10, 2002	12:40
Install mechanical bridge plug below the Culebra interval (712' BTOC).	January 10, 2002	13:55
Install mechanical bridge plug below the Magenta interval (574' BTOC).	January 11, 2002	11:30
Add ~10 barrels (~210' of water) to H-9c in order to cushion the perf gun.	February, 19 2002	12:31
Perforated the Magenta interval (525' to 555' BTOC) with 122 shots total at 4 shots/foot.	February, 19 2002	14:01

(a) Information taken from Magenta hydrology Scientific Notebooks. Duplicate copies of notebooks are filed in the Sandia National Laboratories Records Center.

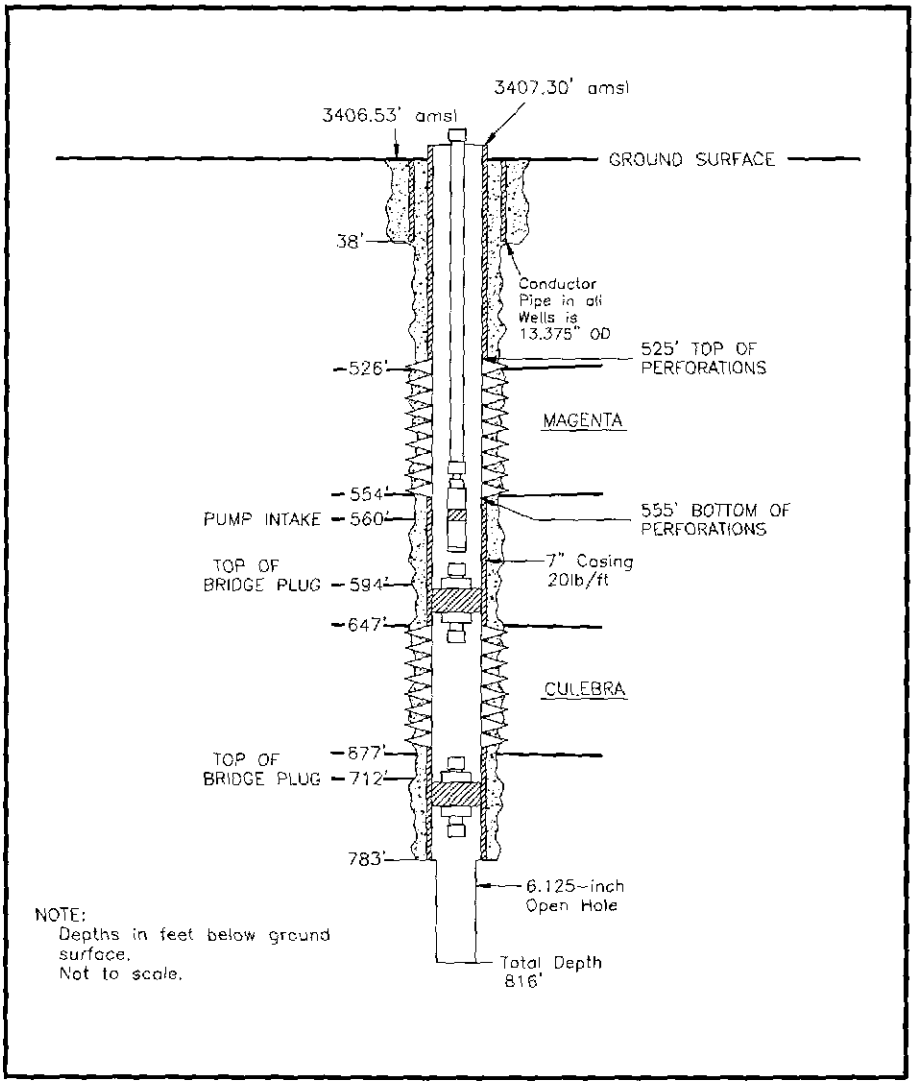

Figure 10. Current H-9c configuration.

Following the removal of approximately three wellbore volumes of water from H-9c, the system was allowed to recover fully to static water-level conditions prior to the initiation of water-quality sampling activities. Table 3 provides information regarding the activities performed during the water-quality sampling exercise.

A miniTROLL pressure/temperature gage was installed in H-9c during water-quality sampling to allow the pressure response to be measured and recorded electronically during sampling. This information, along with the associated flow-rate information, would enable a decision to be made regarding the feasibility of performing a constant-rate pumping test in H-9c for the purpose of hydraulic characterization.

Table 2. Pre-Water-Quality Sampling Activities[a]

Operation	Date Completed	Time Completed (hh:mm)
Installed 1.5-hp pump on 2-3/8" EUE tubing to a depth of 560'8" BGS.	April 9, 2002	14:35
Installed miniTROLL pressure/temperature gage (#4558) to a depth of 480' BTOC	April 9, 2002	16:38
Begin pumping to remove three wellbore volumes (WBV), which is ~1500 gallons, from H-9c with flow rate varying from 5.45 to 1.54 gpm.	April 10, 2002	09:44
Stop pumping due to water level approaching top of pump (~500 gallons removed).	April 10, 2002	11:20
Begin pumping in continuation of the removal of three WBVs of water from H-9c with flow rate varying from 5.40 to 3.50 gpm.	April 11, 2002	09:03
Stop pumping due to water level approaching top of pump (~450 gallons removed)	April 11, 2002	10:27
Began pumping in continuation of the removal of three WBVs of water from H-9c with flow rate varying from 5.71 to 2.95 gpm.	April 15, 2002	09:28
Stop pumping due to water level approaching top of pump (~500 gallons removed).	April 15, 2002	11:01

(a) Information taken from Magenta hydrology Scientific Notebooks. Duplicate copies of notebooks are filed in the Sandia National Laboratories Records Center.

Equipment

The equipment used during the water-quality sampling activities, along with calibration information, is given in Table 4.

Water-Quality Sampling Results

Two water samples were collected on May 22, 2002, from H-9c completed in the Magenta. Both were filtered, and one was acidified with HNO_3 to prevent precipitation of sulfates and carbonates. The samples were analyzed for major cations and anions in the geochemistry laboratory at Sandia National Laboratories/Carlsbad.

Each water sample was analyzed in duplicate. The cations Mg, Ca, K, and Na were analyzed by inductively-coupled-plasma optical emission spectroscopy (ICP-OES). Samples were diluted by a factor of 20, and analyzed with calibration standards made from certified single-element liquid standards and dried anhydrous salts (grade American Chemical Society certified). Sulfate was analyzed gravimetrically, by precipitation as $BaSO_4$.

Cl^- was measured using a solid-state chloride-specific electrode. Alkalinity was not measured, but should be insignificant relative to the concentrations of the other species present.

Table 3. Water-Quality Sampling Activities[a]

Operation	Date Completed	Time Completed (hh:mm)
Initiated a new test on the miniTROLL pressure gage.	May 22, 2002	09:16
Begin recording data from the Quantra flow cell and the Signet flow meter via the Geomation DAS.	May 22, 2002	09:47
Start pumping from H-9c associated with water-quality sampling.	May 22, 2002	10:08
Collect water sample from pump discharge to measure specific gravity and electrical conductivity as indicated in TP 00-03.	May 22, 2002	10:50
Take water quality measurement to assess stabilization of parameters.	May 22, 2002	11:27
Take water quality measurement to assess stabilization of parameters.	May 22, 2002	12:35
Both specific gravity and electrical conductivity are determined to be stable so the final water sample was taken for cation and anion analysis as per TP 00-03.	May 22, 2002	13:59
End pumping associated with water-quality sampling exercise (total volume pumped = 499.4 gallons < 1 wellbore volume of 529 gallons). The test was terminated because 1) the water-quality parameters were stable and 2) the water level was very close to the top of the perforations.	May 22, 2002	14:07

(a) Information taken from Magenta hydrology Scientific Notebooks. Duplicate copies of notebooks are filed in the Sandia National Laboratories Records Center.

Results are shown in Table 5. For the cations, there is little scatter in the data, with duplicates from both the acidified and unacidified samples yielding virtually identical values. The Cl^- results were somewhat more scattered — a more robust method is being investigated for future analyses. Three of the four results for SO_4 analysis are very consistent, but the fourth is low. It is possible this low value is due to loss of $BaSO_4$ during calcination, possibly by sample decrepitation.

The cation/anion charge balance for three of the samples is relatively good, within 2.5%. The fourth sample — for which the SO_4 value is suspect — has a considerably larger error in the charge balance, with a 12% difference. If the average of the SO_4 values for the other three analyses is used, this difference is reduced to less than 1%.

The two water-quality samples used in the analyses were collected at the end of a serial sampling phase designed to purge water from H-9c in sufficient quantities to ensure that natural formation water rather than stagnant (non-representative) water initially present in the well was being produced during purging. Parameters used to indicate that formation water was being produced during the serial sampling phase included specific conductivity and pH. Both

Table 4. Water-Quality Sampling Equipment[(a)]

Equipment	Serial #	Purpose	Calibration Date (mm/dd/yy)	Calibration Due (mm/dd/yy)
Geomation Data Acquisition System	08001406	Acquisition of electronic data from specified instruments (Quantra cell and Signet flow meter)	3/11/02	9/11/02
Carlon totalizing flow meter	2184427	Discrete and cumulative flow rate measurement (manual)	5/22/02	Prior to use
Quantra cell (Hydrolab Quantra water quality sensor package)	446915	Electronic temperature, pH, and fluid conductivity measurement	5/20/02	Prior to use
Cole-Parmer (Ertco) hydrometer	8292-16	Specific Gravity measurement	N/A	N/A
Mannix digital thermometer	N/A	Temperature measurement (manual)	N/A	N/A
Signet electronic flow sensor	60103028362	Electronic flow rate measurement	5/17/02	Prior to use
Grundfos 1.5-hp pump	N/A	Removal of fluid from borehole	N/A	N/A
YSI conductivity meter	99G1193	Fluid specific conductivity measurement (manual)	5/20/02	Prior to use
PH Testr 2	N/A	pH measurement (manual)	5/22/02	Prior to use
In-situ miniTROLL water monitoring probe	4558	Electronic pressure and temperature measurement	2/5/01	2/5/03

(a) Information taken from Magenta hydrology Scientific Notebooks. Duplicate copies of notebooks are filed in the Sandia National Laboratories Records Center.

Table 5. Analysis Results for Magenta Water Samples Collected on 5/22/02.

Sample	Mg^{2+} (mg/L)	Ca^{2+} (mg/L)	Na^{+} (mg/L)	K^{+} (mg/L)	Cl^{-} (mg/L)	SO_4^{2-} (mg/L)	cation/anion bal., % diff.
020522-H9C-1A	177	554	936	34.4	1023	2661	-0.49
020522-H9C-1B	178	558	930	34.8	1109	2616	-2.18
020522-H9C-2 (acidified) A	177	556	938	34.6	1051	*2181*	11.98
020522-H9C-2 (acidified) B	177	556	934	34.6	1090	2640	-2.19

parameters were measured continuously using electronic gages. Figures 11 and 12 show the temperature and the pH and fluid conductivity, respectively, as recorded by the data-acquisition

system and the associated electronic gages. Figure 12, in particular, shows that the fluid conductivity had reached stability prior to collecting the water samples to be analyzed for cations and anions. This was a requirement as indicated in Beauheim (2000).

Pressure Response Data and Interpretation

The water-level response and associated flow rates in H-9c during the well clean-out (the removal of three wellbore volumes of fluid in preparation for water-quality sampling) and water-quality sampling of the Magenta are shown in Figure 13.

The above-mentioned pre-water-quality sampling removal of three wellbore volumes of fluid from H-9c and the subsequent water-quality sampling were performed following Beauheim (2000). As indicated in Beauheim (2000), the Principal Investigator (PI) evaluated the pressure response and flow-rate data from the pumping activities in order to determine if H-9c could sustain a pumping rate of approximately 1 gallon per minute (gpm) for a 50-hour pumping test.

Scoping calculations were performed using data obtained from pumping during the water-quality sampling, along with the existing H-9c wellbore configuration and Magenta information at H-9c, as a means of evaluating the feasibility of performing a pumping test designed to characterize the hydraulic properties of the Magenta dolomite more formally at H-9c. The results of the scoping calculations indicate that a 50-hour pumping test could be performed at H-9c at a rate of 1 gpm. Further, the scoping calculations indicate that the system, as described, would reach the theoretical infinite-acting flow period within approximately 36 hours of pumping. Reaching this infinite-acting flow period serves to add confidence in the diagnosis of the conceptual model.

Technical and Quality Surveillance of Magenta Hydrology Notebook

The Magenta hydrology scientific notebooks are an integral tool used to document activities associated with Beauheim (2000). The compilation of these scientific notebooks is governed by the current version of SNL Nuclear Waste Management Program Procedure NP 20-2. The Magenta hydrology scientific notebooks require a technical and quality assurance (QA) review(s) every six months by an independent, technically-qualified individual to verify technical and QA adequacies of the scientific notebooks.

The second technical and QA review of the Magenta hydrology scientific-notebook was completed by Steve Wagner, SNL/6823, on April 2, 2002. The reviewer's comments, and the subsequent responses to the comments, were documented in the scientific notebook. David Chace, SNL/6821 completed a PI review of the scientific notebook on May 11, 2002 to verify analytical adequacies of the scientific notebook. Upon completion of the PI review, duplicate copies of the review were submitted to the SNL Carlsbad Program Group Record Center to protect the information contained in the notebook in the event the scientific notebook is lost or damaged.

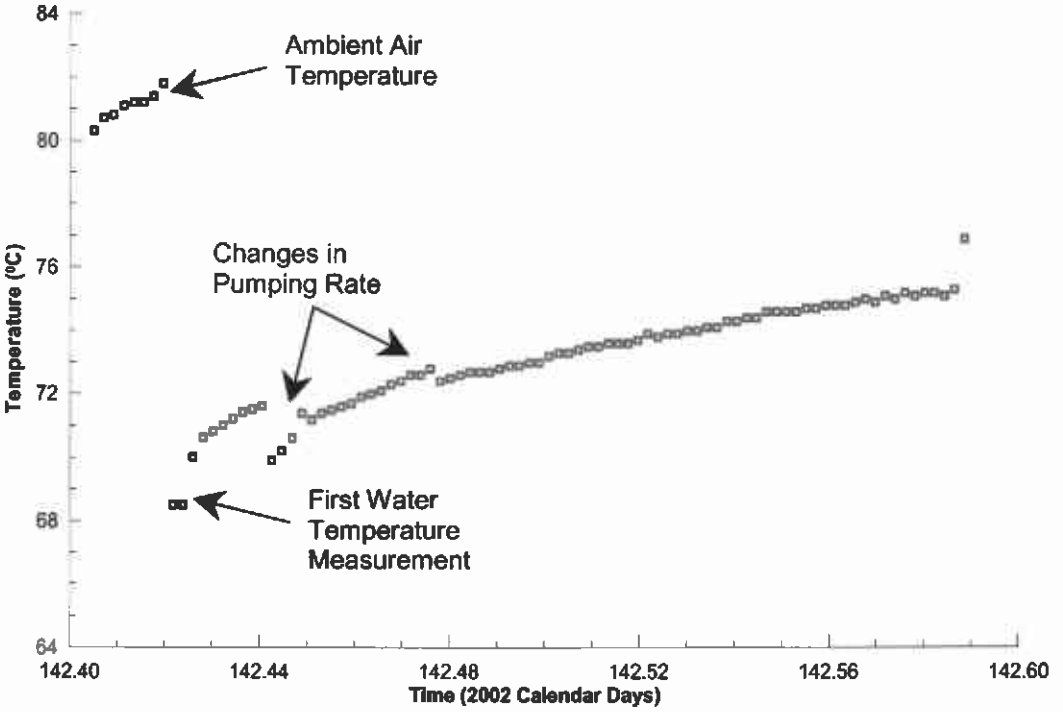

Figure 11. H-9c water temperature during water quality sampling.

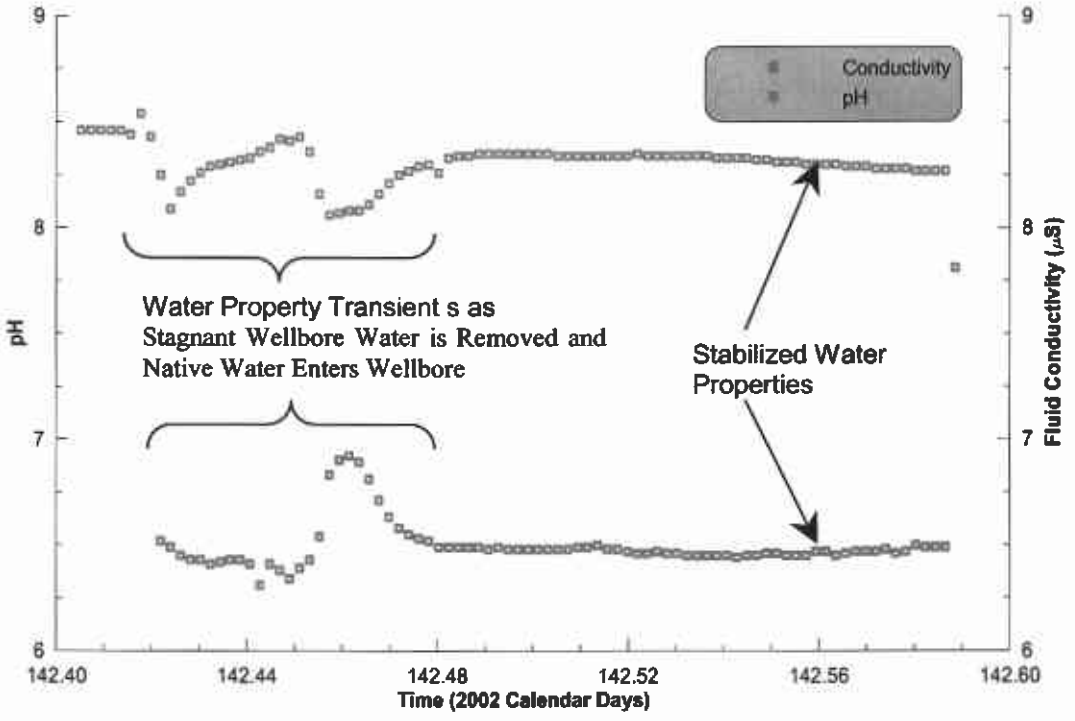

Figure 12. H-9c pH and conductivity during water quality sampling.

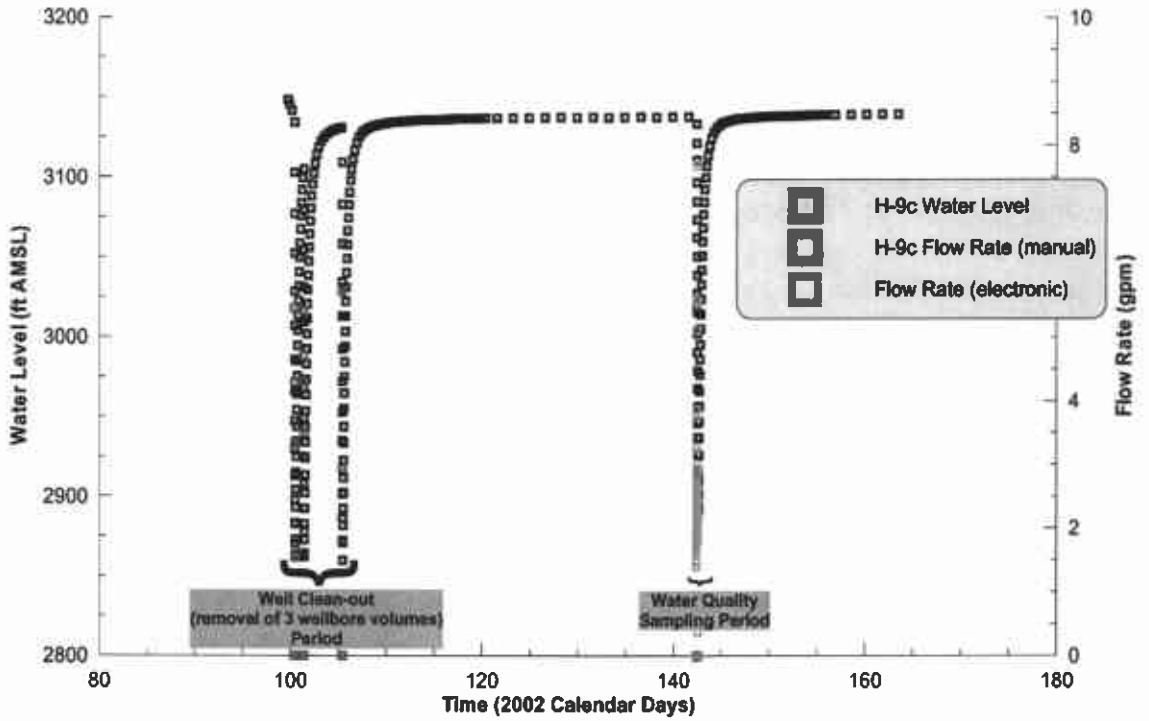

Figure 13. Water level and associated flow rates during Magenta pumping activities in H-9c .

The Magenta hydrology scientific notebooks will continue to undergo six-month reviews, or at an interval determined by the PI, until TP 00-03 activities are deemed completed. Other cognizant SNL personnel may perform technical, QA, and PI reviews of future scientific notebooks as required.

References

Beauheim, R.L. 2000. "Compliance Monitoring Program: Recompletion and Testing of Wells for Evaluation of Monitoring Data from the Magenta Member of the Rustler Formation on the WIPP Site." TP-00-03. Carlsbad, NM: Sandia National Laboratories.

Miller, J.G. 1999. "Scientific Notebooks." NP20-2, Rev. 1. Carlsbad, NM: Sandia National Laboratories.

2.2 Culebra Water-Level Rise Investigations[1]

R. L. Beauheim, T. W. Pfeifle, R. M. Roberts, and Mary-Alena Martell
Sandia National Laboratories, MS 1395
4100 National Parks Highway
Carlsbad, NM USA 88220

Abstract

Water-level rises in the Culebra Member of the Rustler Formation have resulted in the implementation of an extensive program to identify the cause(s) of the rises and the effects such rises might have on assumptions and conceptual models used by the US Department of Energy (DOE) to obtain certification of the Waste Isolation Pilot Plant (WIPP) as the nation's first nuclear waste repository. As part of this program, supplemental groundwater-monitoring activities have been initiated to obtain continuous water-level measurements in selected wells, continuous meteorological (rainfall) data at selected locations, and injection well metrics (e.g., pressure, injection volumes, etc) from industry (oil and gas) operators performing work near the WIPP site. Based on a review of historical WIPP hydrological data and related events that have or are occurring on and near the site, scenarios are being developed to explain the water-level rises and additional information is being gathered to test these hypotheses. In addition, the impact of current Culebra water-level rises on assumptions and conceptual models used by DOE is being analyzed. Other activities include the development of new well-test analysis software needed to quantify uncertainty in well-test analysis and the preparation of a draft test plan to characterize the geohydrology of the Dewey Lake Formation, a formation above the Rustler that may affect Culebra hydrology. The Culebra investigations make use of a phased approach so that work completed in one phase supports subsequent phases. The full Culebra water-level rise investigation is expected to be completed in three to five years with some phases completed within one year or less.

Background and Introduction

The WIPP Compliance Certification Application (CCA) calculations of flow and transport in the Culebra used transmissivity (T) fields for the Culebra that were calibrated to hydraulic heads measured at 32 wells located within or near the WIPP site. Calibrations were conducted iteratively by adjusting the T values until the simulated hydraulic heads predicted from the calibration model matched, within defined ranges of uncertainty, both the steady-state and transient (arising from hydraulic testing and shaft constructions and leakage) heads observed at the wells. In its certification of the WIPP, the US Environmental Protection Agency (EPA) required the DOE to monitor heads (groundwater levels) to provide assurance that assumptions used in the flow and transport modeling were valid. In response to this requirement, the DOE implemented a groundwater-monitoring program (GWMP) to measure water levels in approximately 70 WIPP wells. An additional subprogram of the DOE GWMP requires water-quality sampling and analyses from seven wells included in the monitoring network in response to both EPA and New Mexico Environment Department requirements.

[1] This work is covered by WBS #1.3.5.3.1.1 and #1.3.5.3.1.2

In recent years, water levels observed in many of the wells used in the T-field calibrations have exceeded (risen outside) the ranges of uncertainty established for the steady-state heads used in the CCA. Based on these observations, questions about the continued validity of the T-field calibrations and the flow and transport calculations based on those T fields have been raised by EPA and others. In addition, the assumption that the Culebra is at steady-state conditions has also received scrutiny. In response to the questions raised by the rising Culebra water levels, DOE has directed Sandia National Laboratories (SNL), its Science Advisor, to investigate the cause for the water-level rises, re-assess the assumptions and models used in the CCA flow and transport calculations, and, if required, revise the hydrologic conceptual model of the Culebra utilizing newly acquired data for use in future recertification performance assessment calculations.

As directed by DOE, SNL has developed and implemented an extensive investigation into the cause for the rising Culebra water levels. The major elements of the investigation (Powers, 2001) are as follows:

1. Documentation of hydrograph features and contributing events.
2. Development scenarios and hypotheses potentially explaining the Culebra water level rises.
3. Review of field and drillhole evidence for relevant events and processes.
4. Sensitivity analyses.
5. Scenario and hypothesis testing.

Documents controlling the Culebra investigations include:

SNL Test Plan TP 02-05	*Geohydrological Conceptual Model for the Dewey Lake Formation in the Vicinity of the Waste Isolation Pilot Plant (WIPP)* (Powers, 2002)
SNL Test Plan TP 01-01 –	*Examining Culebra Water Levels* (Powers, 2001)
SNL Test Plan TP 00-03 –	*Compliance Monitoring Program: Recompletion and Testing of Wells for Evaluation of Monitoring Data from the Magenta Member of the Rustler Formation on the WIPP Site* (Beauheim, 2000)
SNL Test Plan TP 99-10 –	*Groundwater Monitoring Activities: TROLL Measurements, Bell Canyon Injection Well Monitoring Near H-9, and Meteorological Monitoring at H-9* (Jepsen, 2000)

In addition to the elements described above, these documents describe the need to characterize the Magenta Member of the Rustler and the Dewey Lake Formation, collect water-level measurements and rainfall data more frequently than currently done in the GWMP, and investigate the influence of brine injection around the site. The information collected will be used directly in the development and testing of scenarios/hypotheses explaining the observed water-level rises. The Culebra investigations are expected to be completed within three to five years and will make use of a multi-phased approach.

The DOE has also directed SNL to evaluate the effects of the observed water-level changes on the calibration of Culebra T fields. The scope and technical approach for this evaluation are described in Beauheim (2002). This evaluation is expected to be completed in early FY03.

This report presents a status review of ongoing Culebra investigation activities during the period January 1, 2002 through June 30, 2002. Activities specifically addressed include:

- Ongoing monitoring of WIPP-site hydrological conditions:
  - Continuous water-level monitoring in selected wells
  - Meteorological monitoring at select well locations
  - Injection well monitoring near the H-9 well pad.
- Development of well-test data interpretation software (nSIGHTS).
- Development of water-level-rise scenarios.
- Evaluation of effects of head changes on calibration of T fields.
- Identification of causes of changing water levels.
- Development of a Dewey Lake geohydrological investigations test plan.

Each of these activities is discussed below under separate headings. Magenta hydrological activities are described in a separate section of this report (i.e., Section 2.1).

WIPP-Site Hydrological Monitoring

CONTINUOUS WATER-LEVEL MONITORING IN SELECTED WELLS

At present, Westinghouse TRU Solutions (WTS), the DOE Management and Operating Contactor, measures the water levels in the WIPP monitoring wells on a monthly basis using manually operated water-level sounder tapes. The locations of these monitoring wells are shown in Figure 1. Although this frequency is adequate for assessing the long-term regional changes in water levels, it does not necessarily give the resolution required to evaluate the effects of short-term transients (e.g., injection, precipitation, etc) on water levels in specific wells. Therefore, submersible TROLLs[2] have been placed in some monitoring wells to record, on a more or less continuous basis, the water levels in the Bell Canyon Formation and the Culebra (TROLLs are also being used to measure Magenta water levels – see Section 2.1 of this report).

[2] A TROLL is an electronic transducer that is positioned below the water level in a well and measures the fluid pressure of the column of water standing above the transducer.

In 1999, TROLLs were placed in six wells including four wells completed to the Culebra, i.e., H-9a, P-17, WIPP-13, and WIPP-30, and two wells completed to the Bell Canyon, i.e., AEC-8 and Cabin Baby-1. In March 2001, the TROLL used to monitor the Culebra water levels in WIPP-13 was moved to monitor Culebra water levels in H-7b1. In preparation for the plugging and abandonment of H-9a by WTS, the TROLL in the well was removed. Thus, TROLL measurements for only three Culebra and two Bell Canyon wells are currently being made. These TROLL data are shown in Figures 2 through 6.

The TROLL measurements are expressed as head above the current position of the TROLL. Head for each well is calculated from the measured TROLL pressure and a constant water density of 1.0 gram per cubic centimeter rather than the actual density of the water in each well. In future calculations, freshwater heads will be determined using well-specific water densities based on values determined from ongoing pressure-density (P-D) surveys being conducted by WTS. The gaps in time and the vertical offsets in heads shown in some of the TROLL data of Figures 2 through 6 indicate a TROLL was either removed (i.e., for calibration or some specific well activity) or re-positioned to ensure that a positive hydraulic pressure within the dynamic range of the instrument is maintained on the TROLL throughout the monitoring period, respectively.

In addition to the TROLL data described above, water level elevations (above mean sea level, amsl) determined by WTS from monthly surveys are also shown in Figures 2 through 6. The water levels shown for the Culebra wells have been adjusted to freshwater elevation heads by WTS using historical values for water density. In contrast, the water-level elevations shown for the Bell Canyon wells have not been corrected for water density because historical density data are not available for these wells.

The Culebra water levels measured in P-17 (Figure 2) show a 1.5-ft linear rise over the period May 1999 through July 2002. The TROLL measurements and the WTS manual measurements compared well during this monitoring period with two exceptions. During December 1999 to January 2000, the TROLL recorded a drop of 6 feet in the Culebra water level of P-17 in comparison to the constant water levels measured by WTS during this same time. The difference in measurements was attributed to a malfunction in the TROLL, which was subsequently replaced in March 2000. During October 2000 to January 2001, the WTS measurements showed a 2-foot perturbation, while the TROLL measurements indicated no such change. No explanation for this difference is currently available. The TROLL was replaced again in April 2001 as indicated by the small offset in the TROLL data on this date.

The TROLL measurements of Culebra water levels in WIPP-30 (Figure 3) were generally constant from May 1999 through January 2000. In early 2000, the TROLL was repositioned several times accounting for the offsets in the data. The TROLL was removed completely in July 2000 to allow for well work by WTS. Therefore, no TROLL data were acquired during July and August 2000. When the TROLL was returned to the well in September 2000, water levels rose rapidly in response to recovery from the well work and continue to rise at a rate of about 0.25 feet/month. The TROLL measurements and the WTS manual measurements compare well throughout the monitoring period. The WTS manual measurements indicate the Culebra water level in WIPP-30 is currently about 2 feet higher than the water levels measured immediately before the well work was initiated.

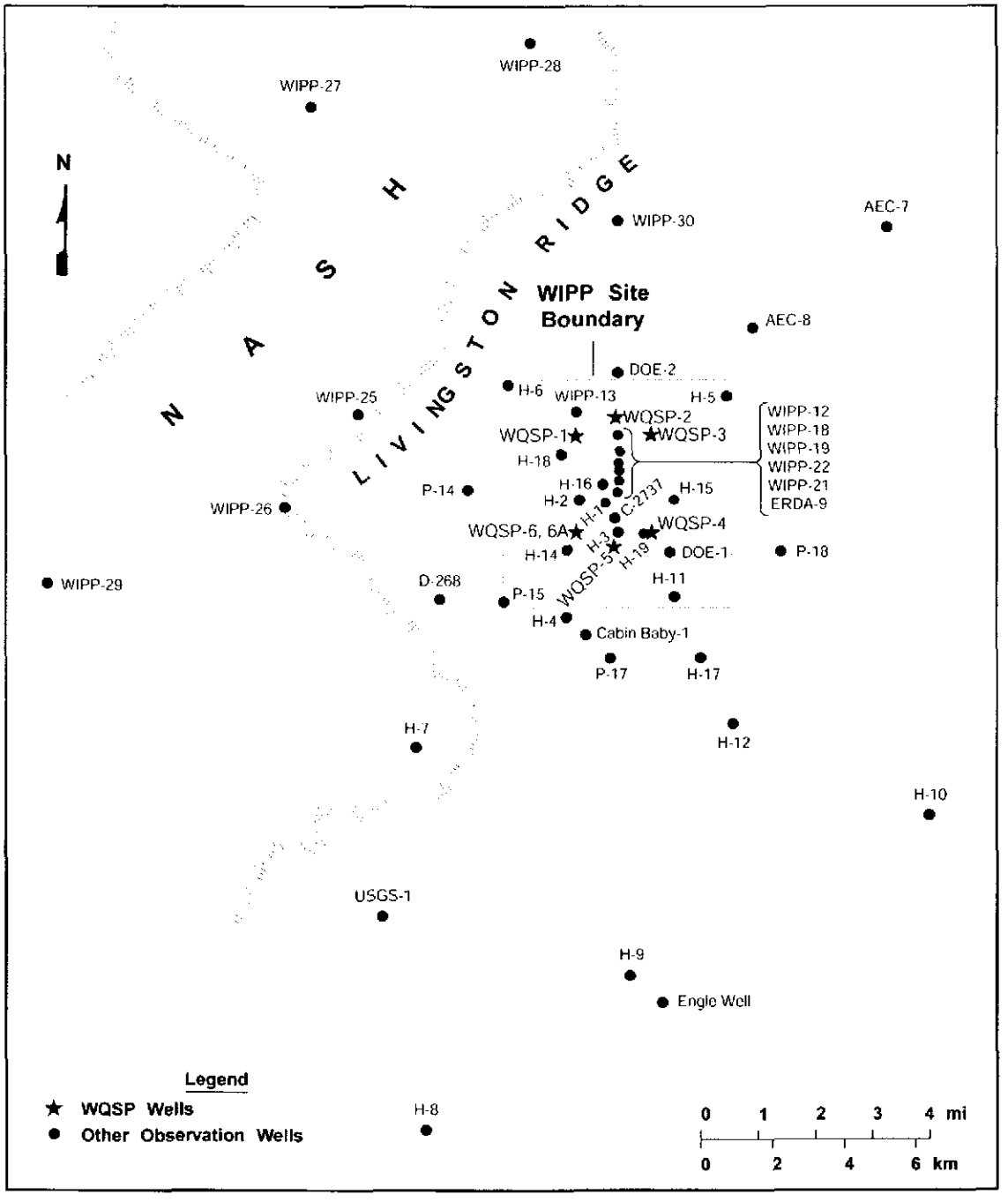

Figure 1. Location map for WIPP monitoring wells.

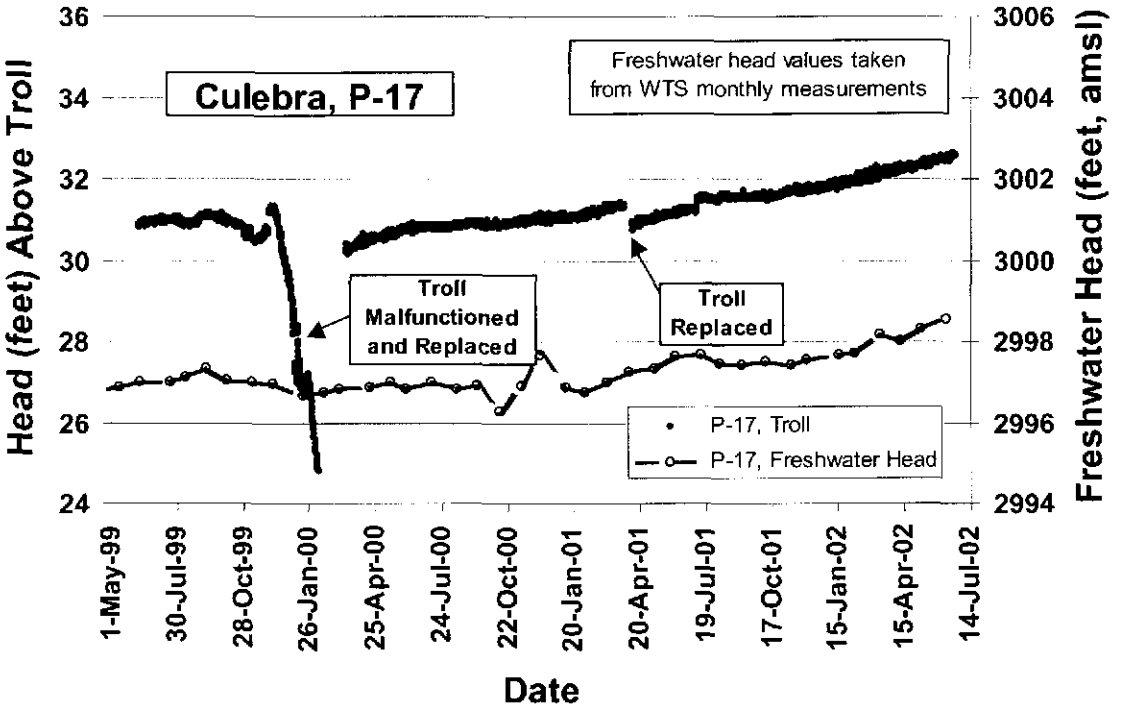

Figure 2. Culebra head levels measured in P-17.

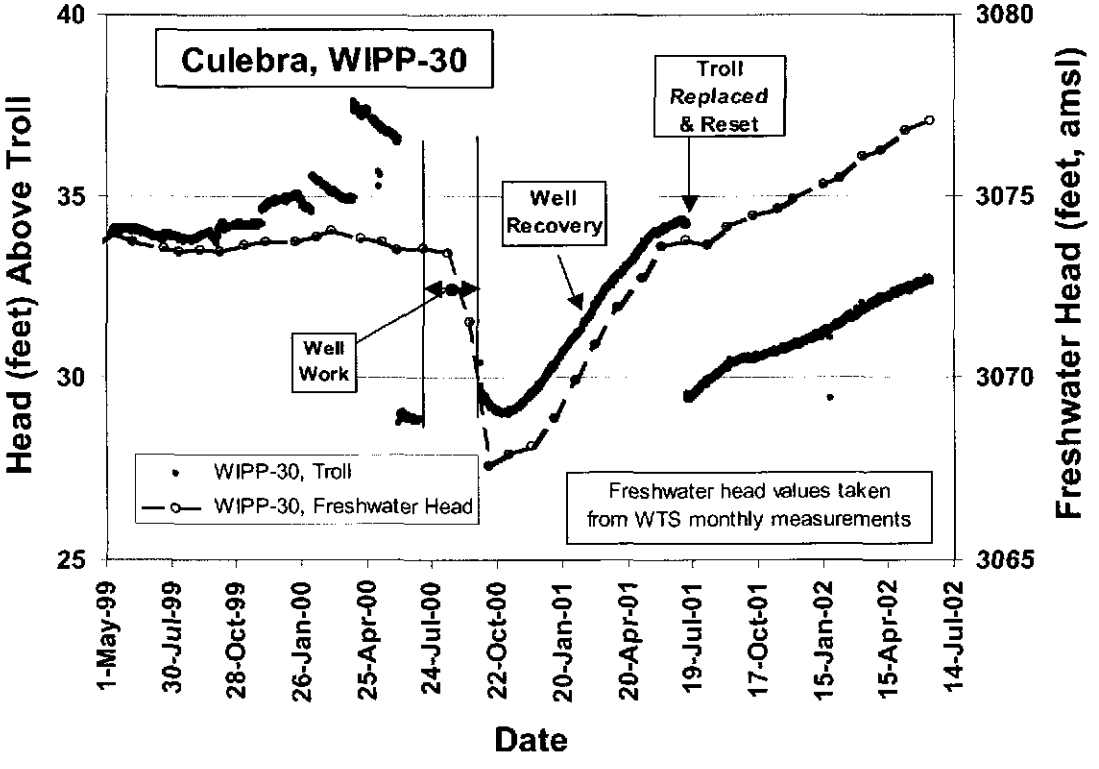

Figure 3. Culebra head levels measured in WIPP-30.

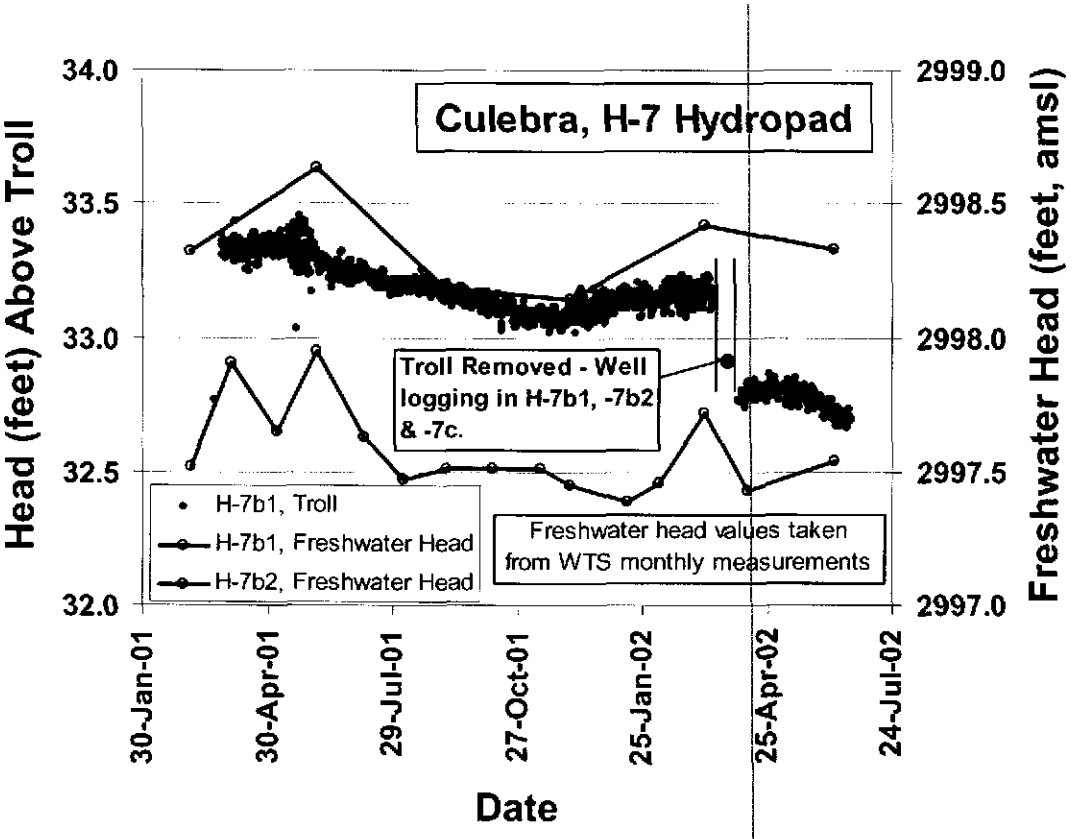

Figure 4. Culebra head levels measured at the H-7 well pad.

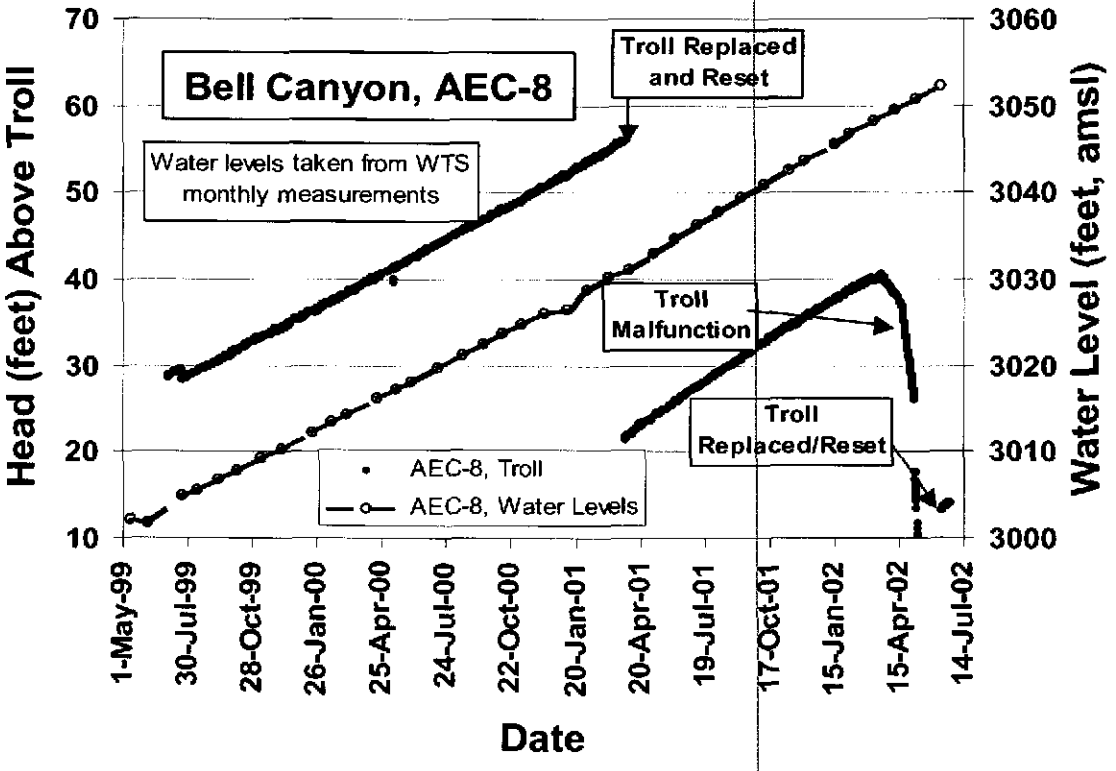

Figure 5. Bell Canyon head levels measured in AEC-8.

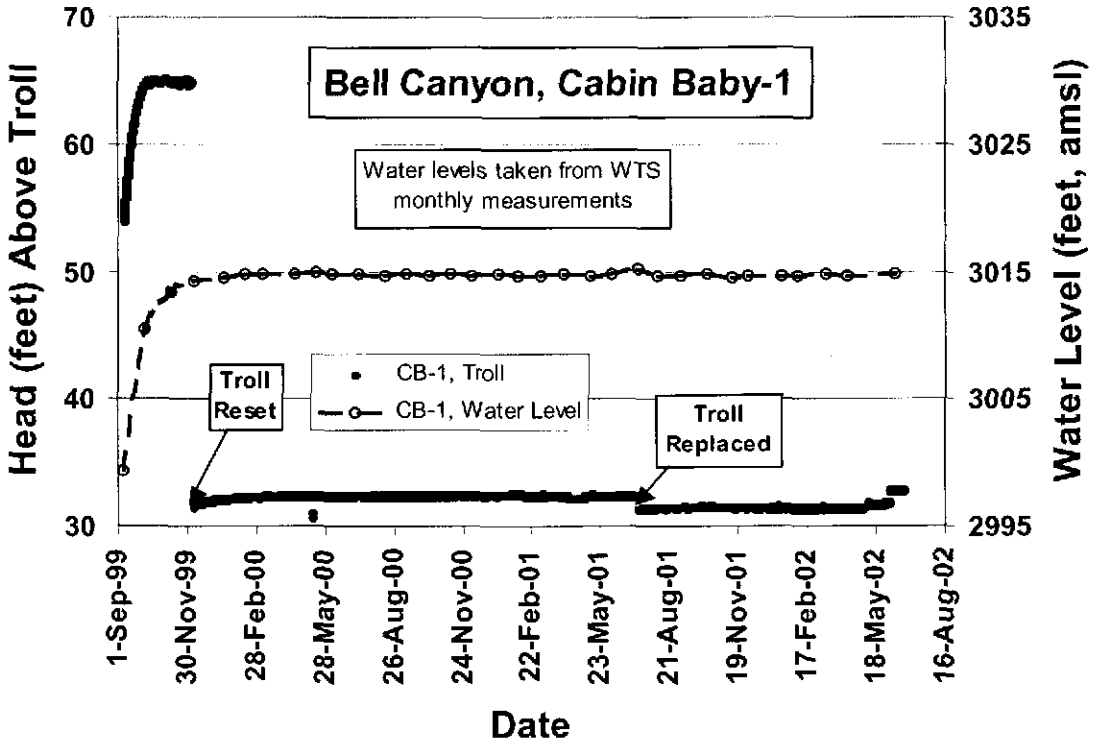

Figure 6. Bell Canyon head levels measured in Cabin Baby-1.

The TROLL measurements of Culebra water levels in H-7b1 were initiated in May 2001 using the TROLL removed from WIPP-13. These TROLL measurements, together with manual water-level measurements made by WTS in H-7b1 and H-7b2, are shown in Figure 4. H-7b1 and H-7b2 are two of the four wells located at the H-7 well pad and are separated horizontally by approximately 100 feet. The four wells are configured in a diamond pattern with wells located at the corners. The other wells at the H-7 well pad are H-7a (plugged and abandoned) and H-7c (inactive). From late March through early April 2002, the TROLL in H-7b1 was removed while WTS logged the wells on the well pad. This logging activity likely affected the water levels in the wells, but little evidence of the activity is seen in Figure 4. In general, the water levels at the H-7 well pad are stable with perhaps a slight downward trend during the last 3 months of monitoring.

The Bell Canyon water levels measured in AEC-8 (Figure 5) and Cabin Baby-1 (Figure 6) show contrasting trends over the May 1999 through June 2002 monitoring period. Although the Bell Canyon water level in Cabin Baby-1 rose initially in response to recovery from previous well work, it has been stable for more than 2.5 years at a level of 3015 feet, amsl. In early May 2002, the TROLL in Cabin Baby-1 was removed to permit access for other well activities, and then replaced in the well six days later. At AEC-8, the Bell Canyon water level has risen steadily at a rate of about 1.6 feet/month or more than a 50-foot rise since the TROLL monitoring was initiated. At the end of June 2002, the Bell Canyon water level in AEC-8 was approximately 3051 feet amsl. As described in Section 2.3 of this report, the rise in AEC-8 water levels may be related to a problem with the well (possibly, a split casing). The TROLLs are in good agreement with the manual water-level measurements made in both wells except for

the large offsets in head attributable to re-positioning of the TROLL and/or malfunctioning of the TROLL (April 2002, AEC-8).

The continuous monitoring of water levels in the Culebra and Bell Canyon using TROLLs will be maintained at least through the next reporting period. TROLL data will be compared with direct measurements of water levels to evaluate the long-term performance of the TROLLs and will be converted to true freshwater elevation heads when well-specific density data become available. A TROLL was recently installed in C 2737 to monitor Culebra water levels (and also Magenta water levels) at this location and these water levels will be included in the next status report.

METEOROLOGICAL DATA

Although the WIPP site comprises only 16 square miles, the WIPP well monitoring network encompasses an area of approximately 250 square miles. Weather patterns within this relatively large area can produce significant variability in precipitation on a local scale. Precipitation recharge has been postulated as a possible mechanism to explain changes in Culebra water levels so measurement of precipitation at or near individual monitoring wells is necessary to determine if such a mechanism is important. The H-7 and H-9 well pads are two monitoring locations considered to be good candidates for testing the precipitation recharge postulate; however, the nearest meteorological station to the H-7 and H-9 well pads is located at the WIPP site, approximately 5 miles and 8 miles from the H-7 and H-9 well pads, respectively. Therefore, SNL instrumented both the H-7 and H-9 well pads with stand-alone, remote tip-bucket rain gauges and data loggers to record precipitation directly at the well pads. The H-9 well pad was instrumented in late February 2000, while the H-7 well pad was instrumented in mid-May 2001.

Monthly precipitation totals measured at the H-9 well pad from March 2000 through July 2002 are shown in Figure 7. Precipitation at this site is highly variable ranging from 0 to more than 5 inches/month. Monthly precipitation totals measured at the H-7 well pad from June 2001 through July 2002 are shown in Figure 8 and range from near 0 to approximately 2.2 inches/month. For comparison, the differences in monthly precipitation totals at the two sites range from approximately 5 to 50 %.

As described elsewhere in this report (i.e., Section 2.3), the Culebra groundwater-monitoring well (i.e., H-9b) located on the H-9 well pad was lost so a direct comparison of rainfall and Culebra water levels is not possible. A second well, H-9c, located on the H-9 well pad was recently re-completed as a Magenta groundwater monitoring well; however, water levels in this well have been disturbed because of the re-completion activities and well development and water-quality sampling that occurred subsequent to re-completion. Therefore, correlation between rainfall and Magenta water levels was not attempted. Figure 9 plots rainfall events at the H-7 well pad and Culebra water levels in H-7b1 from April 1, 2001 through July 1, 2002. No clear correlation between rainfall and water levels is apparent from this comparison; however, this apparent lack of correlation could also mean head levels in the Culebra lag rainfall events. Longer-term data are needed to investigate possible correlations including the effect of time lag.

Precipitation measurements will be continued at least through the next reporting period.

INJECTION WELL MONITORING NEAR THE H-9 WELL PAD

Private resource exploration companies are currently involved in deep-well injection activities (specifically, injection of produced oil-field brines into the Bell Canyon Formation) that are being conducted outside, but near, the WIPP site boundary area. WIPP stakeholders have suggested that a hydrological connection may exist between these injection activities and the changes in water levels measured in some of the Culebra monitoring wells. The premise for such a hydrological connection is vertical flow from the Bell Canyon to the Culebra induced by a change in hydraulic gradient between the two formations during brine injection. Possible vertical flow paths include:

1. Poorly cemented and/or leaking injection wells.
2. Old abandoned wells that extend through the Culebra to the Bell Canyon or deeper.
3. Porous media flow from the Bell Canyon up through the Castile and Salado Formations (a highly unlikely scenario given the low hydraulic conductivity of the Castile and Salado and the relatively long flow path - a distance of more than 3,600 feet).

To investigate the various hydrological connection scenarios, inflow data for six injection wells located near the H-9 well pad are being collected by WTS for comparison with the water levels measured at the H-9 well pad. The location of the H-9 well pad is approximately 6.5 miles south of the WIPP site boundary as shown in Figure 1.

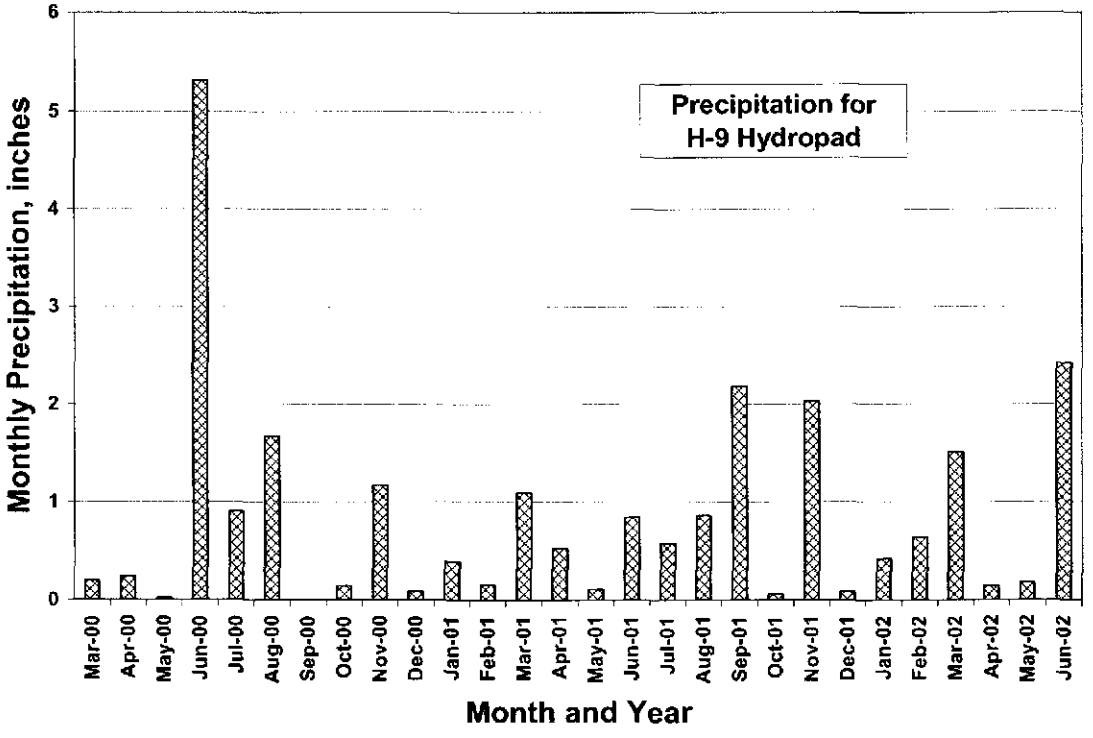

Figure 7. Monthly precipitation totals for the H-9 well pad.

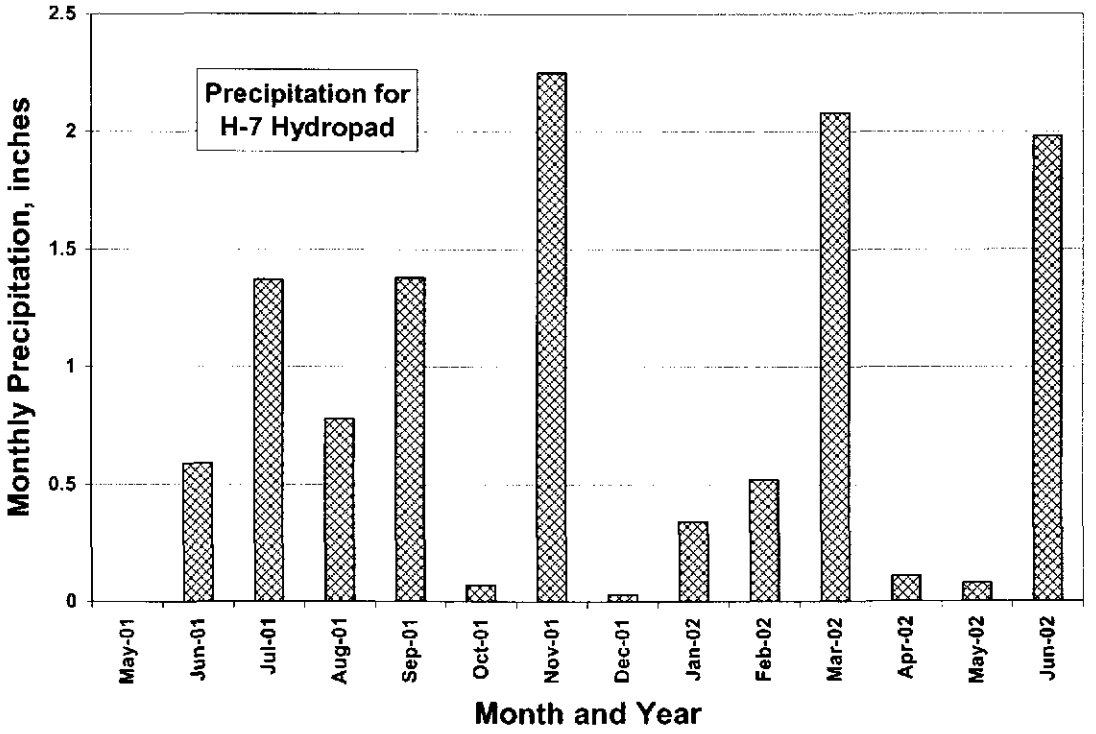

Figure 8. Monthly precipitation totals for the H-7 well pad.

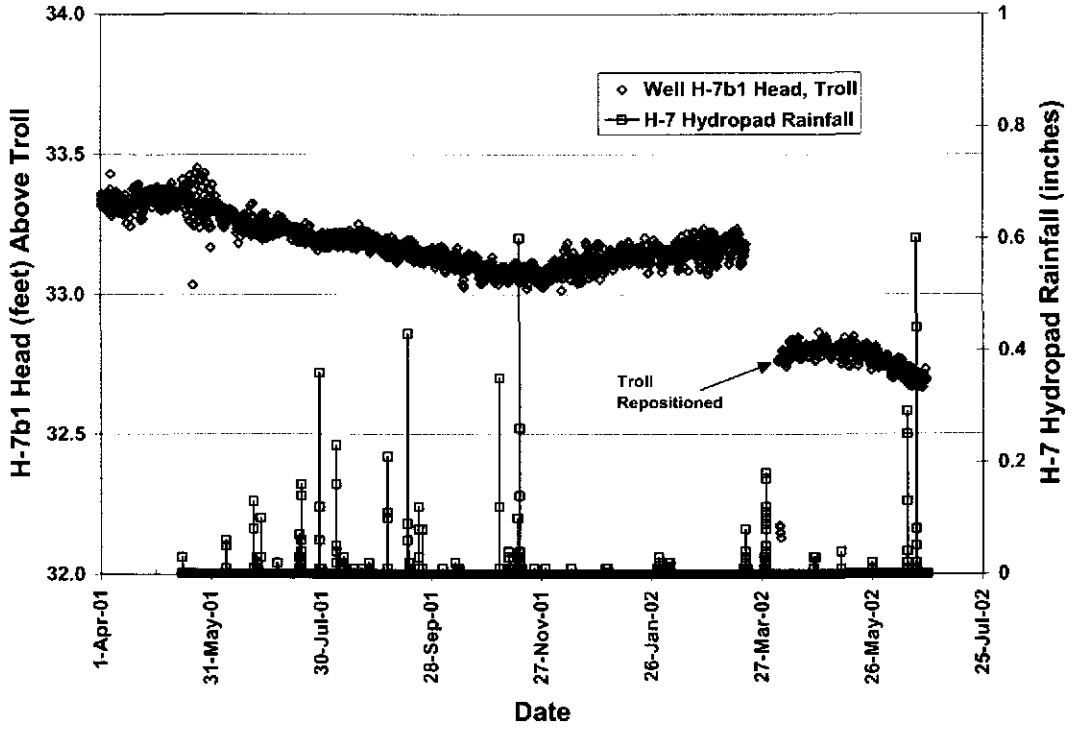

Figure 9. Temporal comparison of rainfall events and Culebra water levels at the H-7 well pad

The six injection wells monitored by WTS are Cal Mon #5, Sand Dunes 28F#1, Pure Gold B F#20, Todd 26F#2, Todd 26F#3, and Todd 27F#16. These wells are located from 1.5 to 3 miles northeast of (and up-Culebra-head gradient from, down-gradient in the Bell Canyon) the H-9 well pad (Figure 10). The injection zones for all six wells are shown in Table 1. With the exception of Pure Gold B F#20, the injection zones are located in the Bell Canyon Formation at depths typically between 4,500 to 5,500 feet (below ground surface, bgs). The injection zone for Pure Gold B F#20 is in the Brushy Canyon Formation at a depth of 7,740 to 7,774 feet bgs. Injection data for the wells are being collected daily by WTS during non-weekend and non-holiday periods (except during August 23, 2001, through October 8, 2001, when no data were collected). The data collected include total cumulative injection volume as read on the injection meter for each well, well injection pressure, and the date and time each meter was read.

As part of the current investigations, an average daily injection rate for each well was calculated by dividing the difference in injection volumes for consecutive meter readings by the elapsed time (in days) between readings. With the exception of the Pure Gold B F#20, the average daily injection rates for each of the six wells are shown in Figure 11 for the entire monitoring period beginning in July 1999. Pure Gold B F#20 was recently added to the injection well cluster so the data for this well are shown only for the period from June 1, 2001, through June 30, 2002.

The current average daily injection rate for Todd 26F#2 is approximately 700 barrels/day, about the same rate reported in January 2002. The average daily injection rate for Todd 26F#3 has dropped consistently over the past year and is currently less than 500 barrels/day. The average daily injection rate for Todd 27F#16 is currently about 1,700 barrels/day, about the same rate reported in January 2002, but is well below a high of 2,800 barrels/day recorded in April and May 2000. With the exception of a few short time intervals, the average daily injection rate for Cal Mon #5 ranges from 500 to 1,000 barrels/day.

The injection rates for Sand Dunes 28F#1 are highly variable, but have typically ranged between 0 and 500 barrels/day during the reporting period. At the beginning of June 2001, Pure Gold B F#20 was added to the Sand Dunes 28F#1 brine manifold. As a result, the injection rate at Sand Dunes 28F#1 dropped to zero and the initial injection rates for Pure Gold B F#20 ranged between 1,000 and 1,500 barrels/day. The injection rates at Sand Dunes 28F#1 remained zero until October 2001 when they increased to 500 to 1,000 barrels/day. During this same time, the injection rates at Pure Gold B F#20 were highly variable with rates as high as 2,500 barrels/day and as low as 500 barrels/day. Over the last six months, the rates of injection at Pure Gold B F#20 have increased from about 750 barrels/day to nearly 1,000 barrels/day. The sum of the injection rates for Sand Dunes 28F#1 and Pure Gold B F#20 is currently equivalent to the rates for Sand Dunes 28F#1 immediately before Pure Gold B F#20 was added to the brine manifold.

Table 1. Injection Zone Depth Intervals for the Injection Wells Located Near the H-9 Well Pad

Well No.	Injection Zone Depth, feet[(a)]
Cal Mon #5	4484 – 5780
Sand Dunes 28F#1	4295 – 5570
Pure Gold B F#20	7740 – 7774
Todd 26F#2	4460 – 5134
Todd 26F#3	4390 – 6048
Todd 27F#16	4694 – 5284

(a) below ground surface, bgs

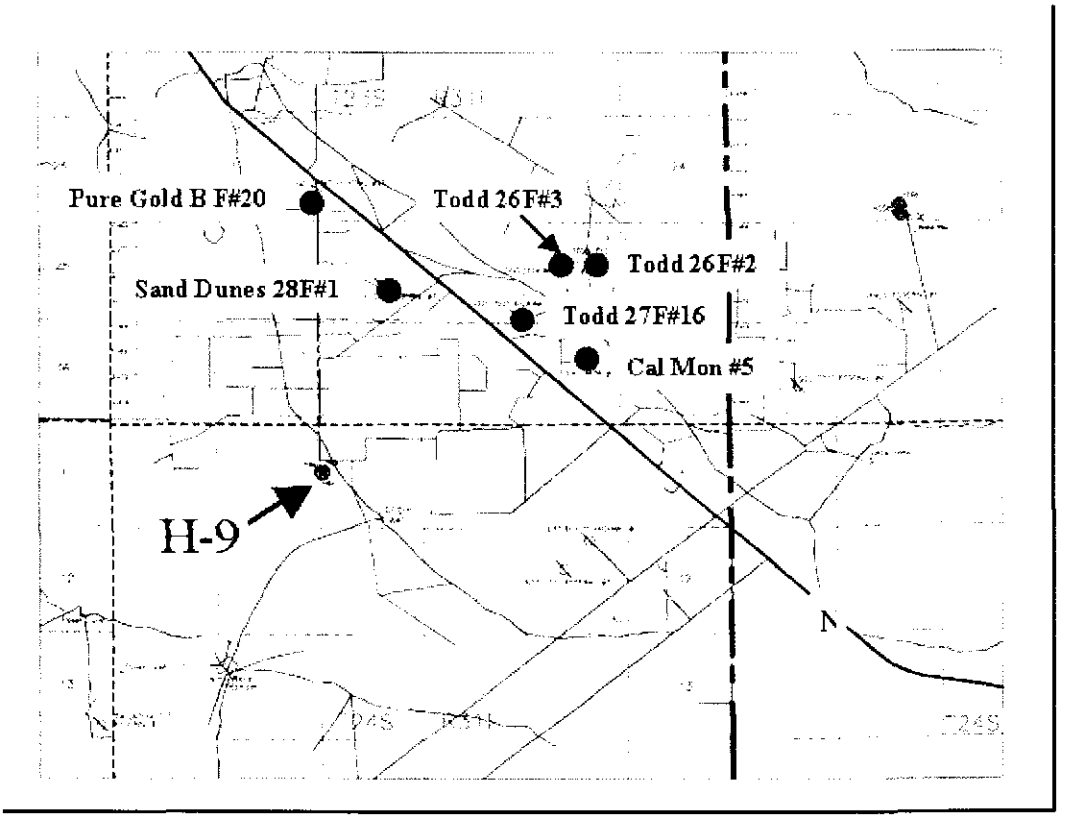

Figure 10. Location of injection wells relative to the H-9 well pad.

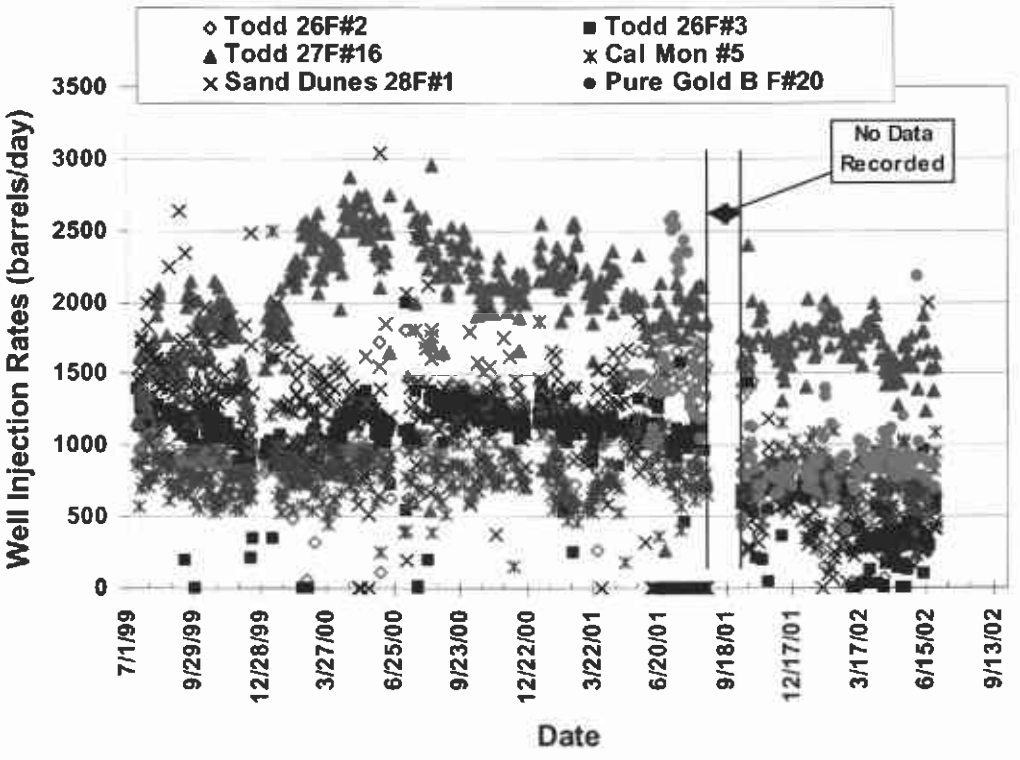

Figure 11. History of daily injection rates for six wells located near the H-9 well pad.

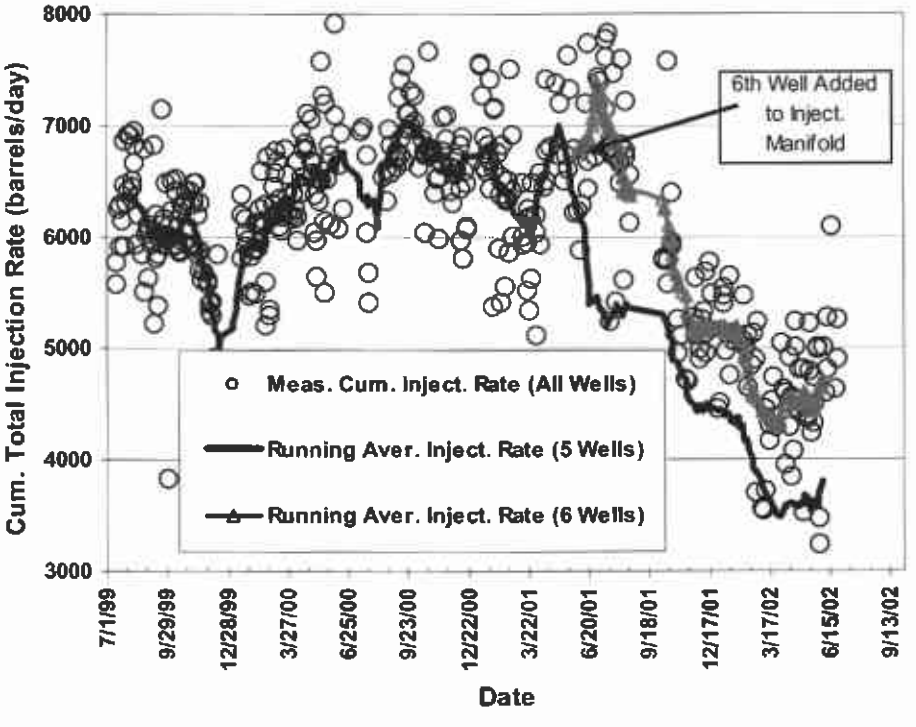

Figure 12. History of cumulative daily injection rates for injection wells located near the H-9 well pad.

As shown previously in Table 1, the injection zones for five of the six wells cover approximately the same depth interval (between 4,500 and 5,500 feet bgs). In addition, because the wells are located near one another (1 to 3 miles) in a horizontal plane, the injection can be approximated as a point source on the regional scale. Using this assumption, the total injection rate at the point source is simply the cumulative total of the injection rates of the five individual wells. Figure 12 gives the total cumulative injection rate as a function of time for all six wells.

Because of the large variability in the cumulative rates, two running-average injection rates were calculated. One running average included the data from all six wells, while the second included data only from the five wells injecting at the same depth interval. Both of these running-average injection rates are plotted in Figure 12 for comparison with the measured cumulative rate. Each running-average rate is calculated as the average total injection rate for all of the data falling inside a sliding "time window." Subsequent rates are determined by simultaneously adding and dropping a data point from either end of the time window, until all of the data have eventually been included in one of the time windows. The average rates are then plotted at the midpoints of their respective time windows. As shown in Figure 12, this technique "smooths" the measured data so that local trends and/or peaks and valleys become obvious. The running-average injection rates for the six wells parallel the rates for the five wells, but are offset in magnitude as expected. Both the five-well and six-well cumulative daily injection rates have fallen steadily for nearly a year and are now about half of what they were in July 2001; however, since March 2002, the cumulative rates appear to have stabilized at approximately constant values.

Because of the apparent loss of the Culebra groundwater monitoring well (i.e., H-9b) at the H-9 well pad (see Section 2.3 for additional details), no Culebra water levels are currently available for comparison with injection rates. Injection rate monitoring will continue at least through the next reporting period, while a plan is developed to assess if valid Culebra water levels can once again be measured at the H-9 well pad.

Development of Well Test Data Interpretation Software – nSIGHTS

Since the CCA was submitted in 1996, advances have been made in the interpretation of results derived from well-test analyses. In particular, it is now possible to quantify accurately the uncertainty in fitting parameters estimated from the analyses of hydraulic field tests. Thus, parameters such as transmissivity and storativity that were previously treated as single-valued estimates in the CCA can now be treated more realistically as probabilistic variables and their uncertainty can be accurately quantified. SNL is incorporating these advances into the new well-test data interpretation software know as nSIGHTS or **n**-dimensional **S**tatistical **I**nverse **G**raphical **H**ydraulic **T**est **S**imulator. When the software has been completed and documented, it will be used to re-analyze historical well-test data to characterize better both the parameter estimates and their uncertainty and to interpret new data from well tests to be performed at several new locations on or near the WIPP site. The discussion below provides a general description of the approach used in the nSIGHTS software and gives the status of its development.

Well-test analysis is the process by which hydraulic parameters of interest such as transmissivity (T) and storativity (S) are estimated from measured pressure and flow-rate data. This problem of inferring T, S, etc. from a measured response is generally known as an inverse problem. An inherent quality of inverse problems is that the parameters estimated via this process have some degree of uncertainty associated with their values.

The well-test analysis code nSIGHTS is being developed to quantify the uncertainty in parameters such as transmissivity that are estimated from WIPP field tests. To demonstrate how this uncertainty originates, how it is relevant to the WIPP project, and to better understand the well-test analysis process, the following simple example is considered:

Assume that the values of two parameters, A and B, which cannot be measured directly in controlled tests, are required to characterize a process or develop a model. Furthermore, assume a related parameter, C, can be measured directly and the total system response – call it D – can also be measured. After measuring C and D, some analysis indicates that the relationship among the three parameters A, B, and C, and the response D is described by the following equation: $A + B + C = D$. In an attempt to estimate A and B, their values will be adjusted and combined with the measured value C such that $A + B + C$ matches the measured response D.

No discipline, including well-test analysis, is complete without some specialized terminology. In the language of inverse problems, A and B are *fitting parameters*, C is a *non-fitting parameter*, and D is a *constraint*. The equation $A + B + C = D$ is the *conceptual model*. The constraint D serves to limit the possible values of A and B. Obviously, without information on the constraint, no unique estimates of A and B can be made. Constraints used in well-tests analysis are typically some combination of pressure and flow-rate measurements. The non-fitting parameters in well-test analysis (C in this example) include geometric and/or fluid properties such as wellbore radius and volume, length of the tested interval, fluid density, etc.

Given that values for C and D have been obtained, a problem of uniqueness in determining the values for A and B still exists. To understand the lack of uniqueness, assume that C has a value of 5 and that D has a value of 50. Then, further assume that A and B can only vary between values of 0 and 100 (note that this range restriction is an additional constraint). The area within Figure 13 contains all the possible solutions to the problem (given that A and B are limited to values between 0 and 100) and is known as the *parameter* or *solution space*. However, not all of the A and B combinations within this parameter space will satisfy the constraint that $A + B + 5 = 50$. The optimal solutions, i.e., those solutions that satisfy both constraints fall within the red region in Figure 13 – a line segment in this example. This region of optimal solutions is typically referred to as the *minimum*.

Why the term "minimum?" When the A and B combinations contained within the minimum are input into the model, the difference between the model output (the estimated value of D) and the measured D value are minimal relative to other A and B combinations within the parameter space. Hence, the term "minimum." nSIGHTS quantifies the quality of the fit to the constraint as the *sum of the squared errors (SSE)*. The difference between each constraint data point (pressures and flow rates) and its simulated value is squared and these squared differences are then summed. The SSE value is sometimes referred to as the value of the ***objective function***.

nSIGHTS utilizes a non-linear regression algorithm to search for optimal solutions, i.e., to best satisfy the stated objective function by minimizing the SSE.

The minimum is not a single-valued combination of A and B – instead there is a range of possible values. This range is the result of the correlation that exists between the fitting parameters A and B. A change in the estimate of A can be compensated by a corresponding change in the estimate of B such that the constraints are still satisfied and the minimal value of the objective function (SSE) is unchanged. For a given conceptual model, this correlation among fitting parameters is typically the largest source of uncertainty in the estimate of the fitting parameters.

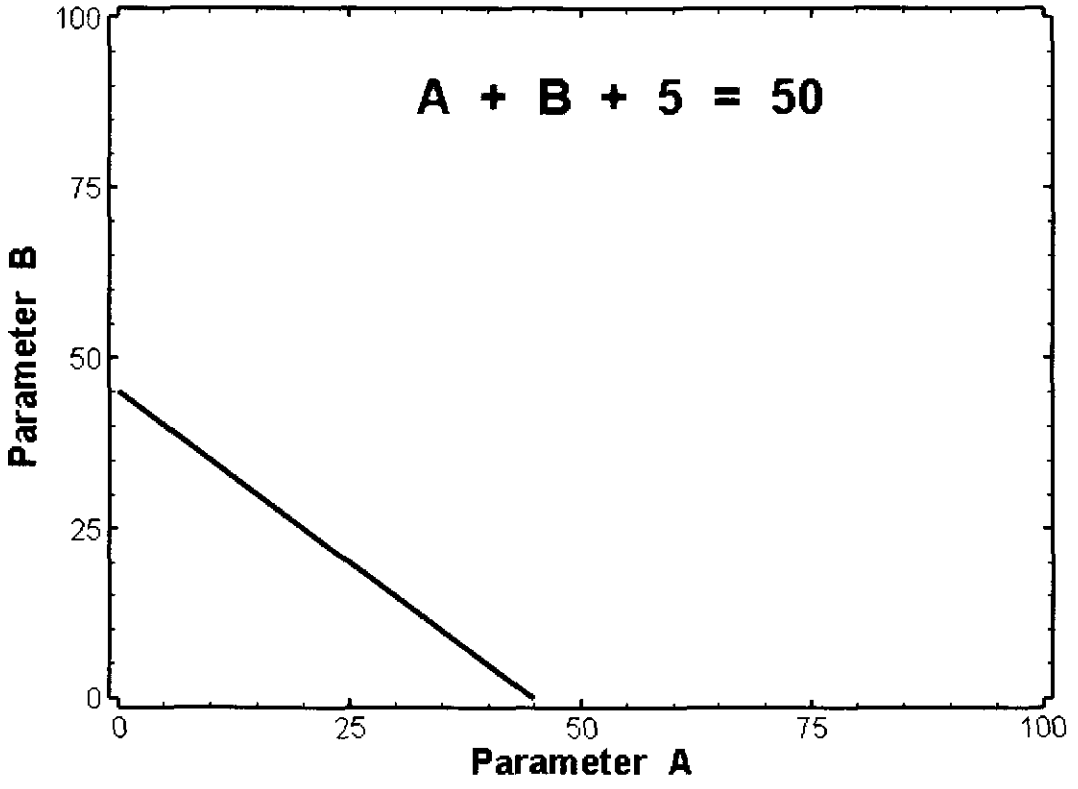

Figure 13. Solution space for hypothetical example denoting optimal solution region where the uncertainty results from correlation between the fitting parameters.

Noise in the data is another source of uncertainty. Assume that measurements of D can only be resolved to a value somewhere between 45 and 55, i.e., the constraint becomes $45 < A + B + 5 < 55$. The new minimum is the area between the blue lines shown in Figure 14 – the uncertainty is slightly increased. Now assume that C cannot be measured exactly, say that it's 5 ± 1. The situation then becomes $45 < A + B + (5 \pm 1) < 55$. The possible solutions are now contained between the green lines in Figure 15. This additional uncertainty results from the correlation between the fitting and non-fitting parameters.

In review, for a given conceptual model, uncertainty can result from correlation among fitting parameters, noise in the data, and correlation among fitting and non-fitting parameters.

Also note that dramatic changes in the estimates of the fitting parameters can result by changing the conceptual model itself. If it were decided that $A + (B \times C) = D$ better represented what was observed in the system, then the values of A and B estimated using the new model might be very different than those obtained using the previous conceptual model.

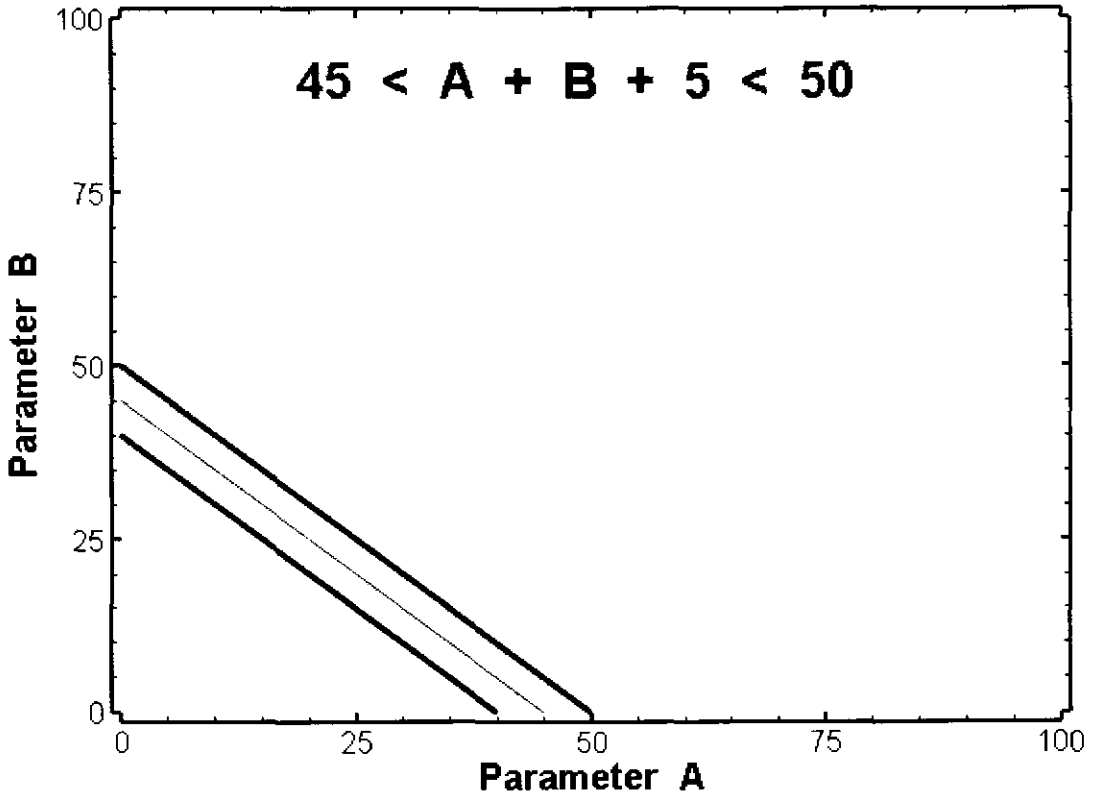

Figure 14. Solution space for hypothetical example denoting optimal solution region and range in uncertainty attributed to errors in the measured constraint.

Given that uncertainty in the estimates of the fitting parameters is an inherent part of the well-test analysis process, it is important that this uncertainty be quantified. Calculations of probabilistic transmissivity fields used for Culebra transport calculations are currently constrained in part by single-valued estimates of T obtained from previous analyses of hydraulic tests. New analyses of the existing Culebra data will be performed using nSIGHTS to quantify the uncertainty in T at each well location. These T distributions will then be used to generate T fields that better incorporate the overall uncertainty in the current understanding of the Culebra.

STATUS

QA testing of the nSIGHTS code is proceeding as per the nuclear waste management procedure NP 19-1 Rev. 9, *Software Requirements* (Chavez, 2002), and will be completed in November 2002. The Requirements Document, Design Document, and User's Manual are currently in review. The Verification and Validation Plan is in process and is about 75%

complete. Tests for various code functions are being taken from the existing GTFM 6.2 documentation (the DOS precursor to nSIGHTS) where possible.

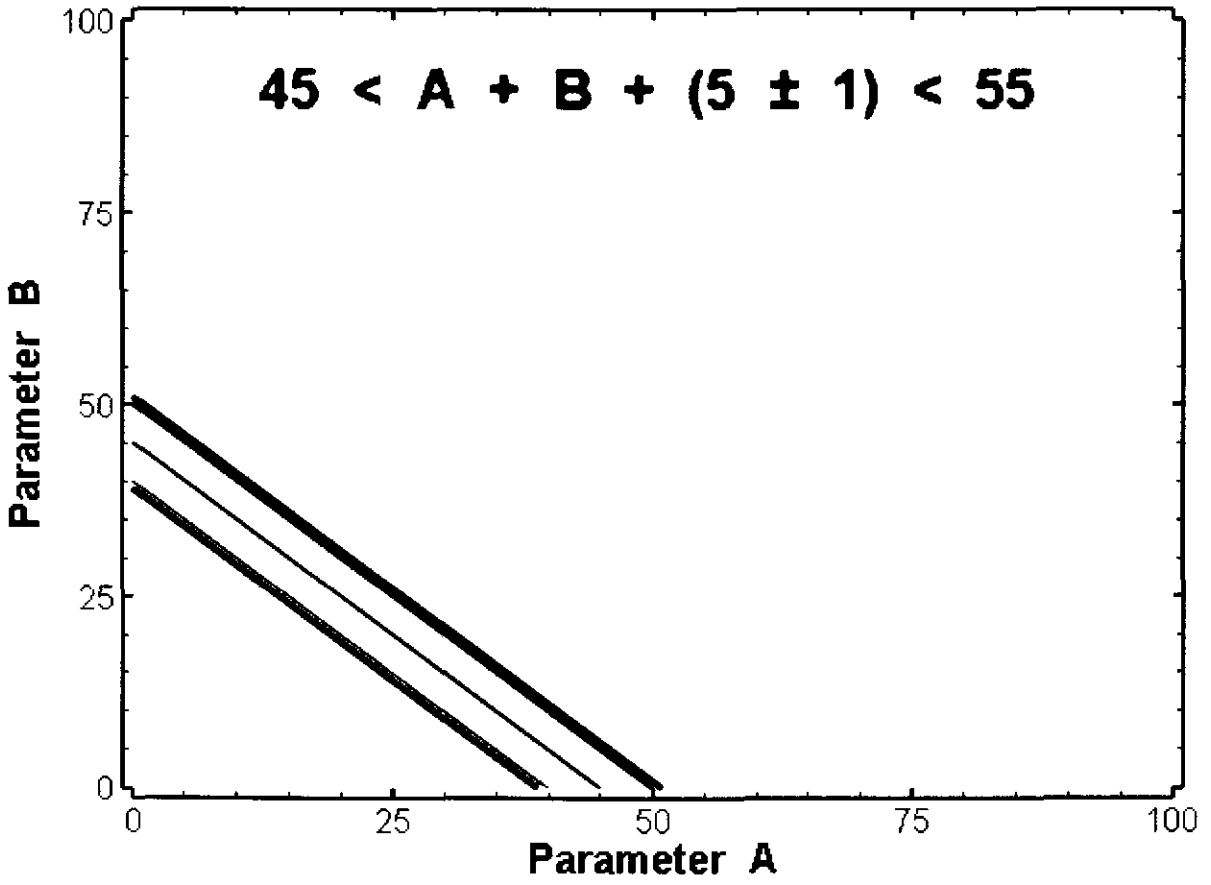

Figure 15. Solution space for hypothetical example denoting optimal solution region and ranges in uncertainty attributed to errors in the measured constraint and correlation among fitting and non-fitting parameters.

Culebra Water-Level Rise Scenario Development

Powers (2001) is a starting point for the investigation of water-level changes. This test plan outlines the following activities:

1. Review of hydrograph features and contributing events.
2. Scenario and hypothesis development.
3. Review of field and drillhole evidence for events and processes.
4. Sensitivity analyses.
5. Scenario and hypothesis testing.

The examination of water-level records (hydrographs) from the WIPP wells revealed a general long-term rise in both Culebra and Magenta water levels (e.g., Figure 16), as well as short-term fluctuations of unknown origin in Culebra water levels in specific areas (e.g.,

Figure 17). Based on knowledge of human activities around the WIPP site and recent geologic observations of increased subsidence fracturing in Nash Draw, seven scenarios were initially defined that were thought to have the potential to affect water levels. The matrix given as Table 2 summarizes the SNL evaluation of the plausibility of the scenarios, and steps that might be taken to investigate them further. The scenarios that are considered worth investigating further are:

1. Leakage from the Mississippi East tailings pond north of the WIPP site causing locally elevated Culebra and Magenta heads, which then propagate to the south.
2. Leakage through boreholes penetrating other water-bearing units above the Salado that are poorly cased or improperly plugged and abandoned.
3. High-T conduits extending from Nash Draw to the (south)east allowing heads in Nash Draw to affect heads under Livingston Ridge (including the WIPP site) more than previously thought.

Note that these scenarios are not mutually exclusive, and may all be contributing to the observed water-level fluctuations.

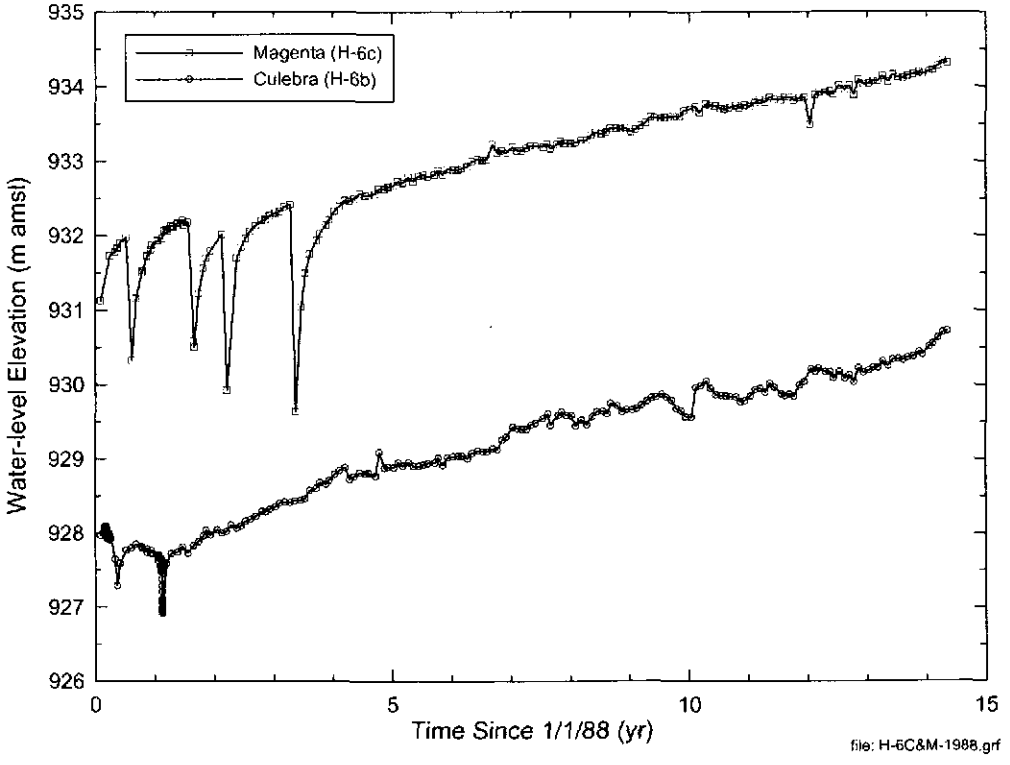

Figure 16. Rising Culebra and Magenta water levels at H-6.

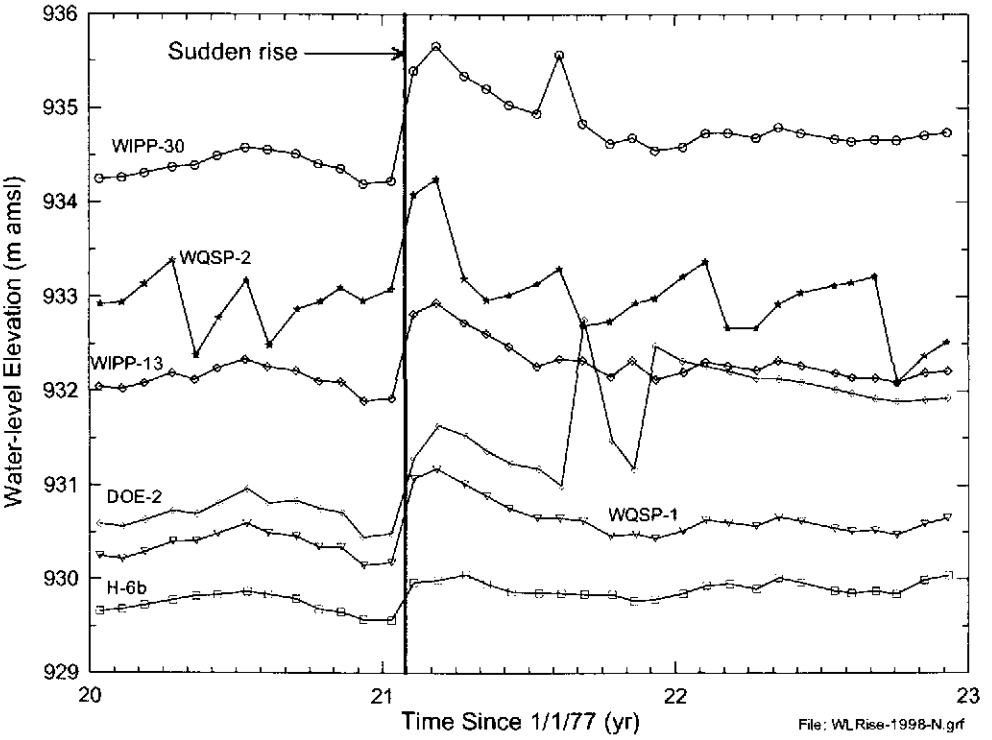

Figure 17. Example of short-term water-level fluctuation north of WIPP.

Factors Causing Water Level Changes and Effects of Changes on Calibration of T-Fields

A two-pronged strategy has now been developed to address water-level issues. The elements of this strategy are:

1. Evaluation of whether T fields calibrated to different sets of historically observed heads are significantly different (in terms of groundwater flow directions and velocities) from the T fields calibrated for the CCA.
2. Identification of the factors causing Culebra water-level fluctuations and revise Culebra models as appropriate.

EFFECTS OF CHANGING WATER LEVELS ON T-FIELD CALIBRATION

To carry out the first element of this strategy, Beauheim, (2002) wrote the analysis plan describing the four principal tasks:

1. Construction of geologic contour maps.
2. Estimation of base transmissivity fields.
3. Conditioning of base T fields to equilibrium heads.
4. Conditioning of base T fields to transient heads.

Table 2. Evaluation of Scenarios Potentially Capable of Affecting WIPP Water Levels

Scenario	Capable of producing observed long-term rise?	Capable of producing observed short-term fluctuations?	Which wells would it affect the most?	Would this effect still be significant in 1000 years?	How can it be evaluated?
Recharge (leakage) from Mississippi East tailings pond	Yes (tailings pond has existed for ~50 years)	No	Northern wells	No (lifetime of tailings pond too short)	Model simulations; well south of pond on Livingston Ridge
Leakage through wells from shallower units	Yes	Yes	Wells nearest to leaking well(s)—most likely potash holes north or west of WIPP site	Yes	3D model simulations; evaluation of presence of shallow water north of site
Leakage through wells from deeper units (including injection)	No (not yet—wells north of site haven't been there long enough)	Perhaps from loss of circu-lation during drilling—very short-term	Off-site wells closest to leaking wells	Yes	Injection data collection and monitoring
Precipitation/ "Natural" recharge	Doubtful (if current understanding of recharge areas is correct)	No	Shallow wells, then propagate to others	Yes	3D modeling
High-T conduits from Nash Draw	Yes	No	Northwestern wells (e.g., H-6)	Yes	Well NW of site; geolo-gical and geophysical evaluation; Magenta evaluation and modeling
Mine subsidence	No	No	None are very close to mines	NA	Difficult--seismic data?
Subsidence related to oil and gas production	No	No	Wells outside site closest to production wells	NA	Calculations of induced strain

Four sets of 100 T fields are being generated, each using different values of "steady-state" or "equilibrium" heads. The heads used represent snapshots in time of the heads observed in 1980, 1990, and 2000, as well as the head values used for the CCA modeling. Whereas the CCA T fields relied simply on kriging of measured T values to define the base T fields that were then calibrated, the new base T fields have been developed using a statistical correlation between measured T and geologic factors, including thickness of overburden above the Culebra and whether or not halite has been dissolved from the upper Salado at that location.

Once the four sets of T fields have been calibrated only to steady-state heads, comparisons will be made of the calculated flow paths and travel times from a position above the WIPP waste panels to the site boundary. These results will also be compared to those obtained for the CCA. Selected T fields will then be calibrated to transient heads as well, and the results again compared to those obtained for the CCA. If the travel times calculated for the new T fields fall within the cumulative distribution function (CDF) of travel times developed for the CCA, then current water levels should not produce travel times inconsistent with the modeling done for the CCA.

The groundwater flow model being used for this activity is MODFLOW 2000, and PEST is being used to optimize the conditioning of the model to heads. A model domain was defined extending 30,600 m north-south and 22,300 m east-west, approximately centered on the WIPP site, to include all WIPP wells (except for WIPP-29), the Mississippi East tailings pond north of the WIPP site, and the portions of Nash Draw believed relevant to WIPP hydrology (Figure 18). A uniform MODFLOW grid with 50-m X 50-m elements was created for the modeling domain.

At the present time, all necessary geologic information has been collected and compiled in a GIS database that can be used to produce any desired maps, the statistical correlation between T and geologic factors has been established and used to create 100 equally probable base T fields (e.g., Figure 19), equilibrium head values at the WIPP wells have been defined for the three snapshots in time (Table 3), and boundary conditions have been defined for the four sets of T fields. Conditioning of the base T fields to equilibrium and transient heads will be performed in the second half of 2002.

IDENTIFICATION OF FACTORS CAUSING CHANGING WATER LEVELS

A variety of activities are underway to identify the factors causing Culebra water-level fluctuations and revise Culebra models as appropriate. Records have been assembled documenting how potash exploration boreholes have been plugged and abandoned, and specific boreholes have been identified as potential leakage candidates. As part of the compilation of geologic information for the new T fields, logs from old and recently drilled wells have been reviewed for evidence of dissolution of the upper Salado, leading to the tentative identification of two dissolution tongues extending from Nash Draw to the southeast (see Figure 19). In the near future, potash mine water-production records will be obtained that will provide insight into how much water has historically been pumped into the Mississippi East tailings pond.

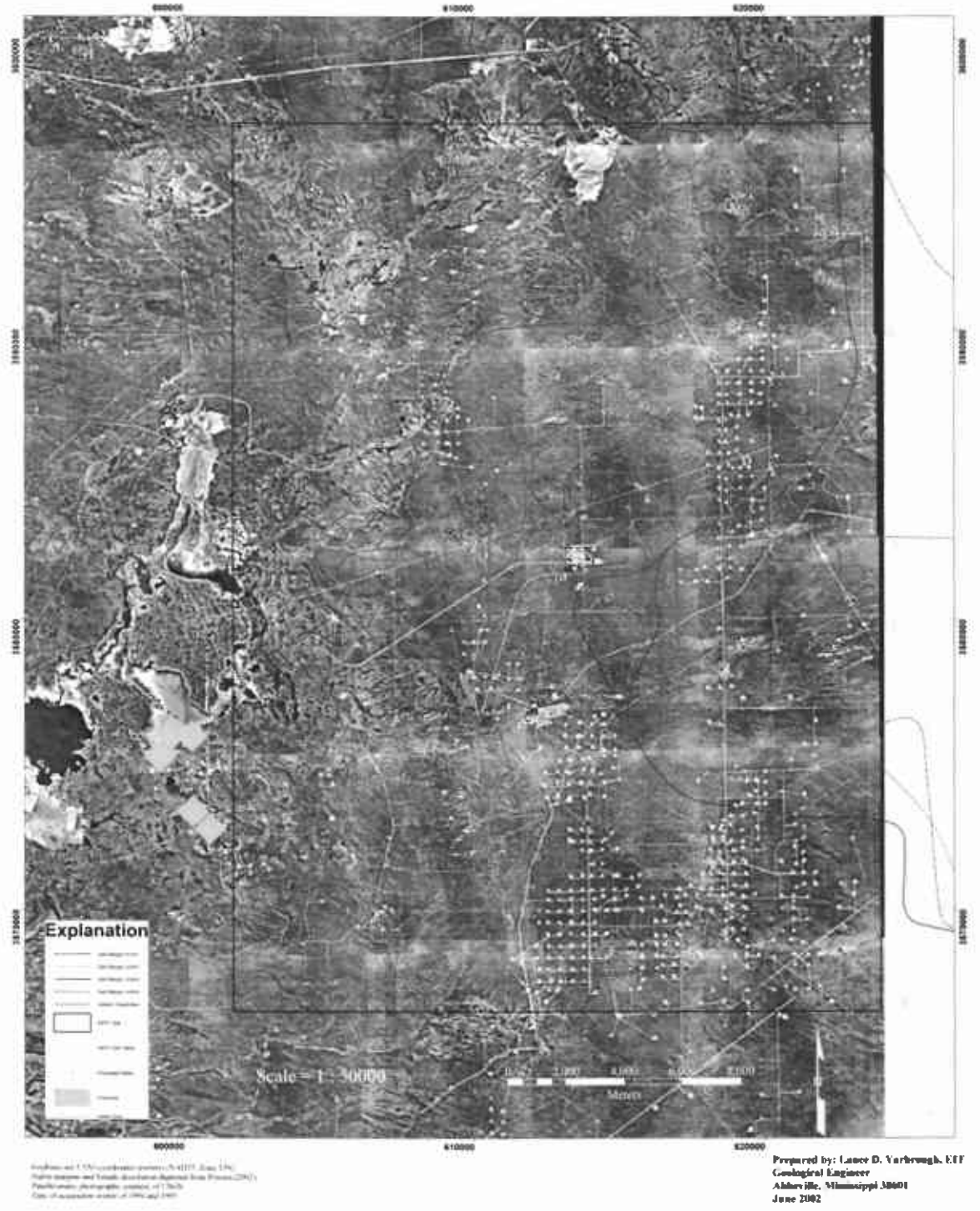

Figure 18. Model domain (black rectangle) for new Culebra T fields.

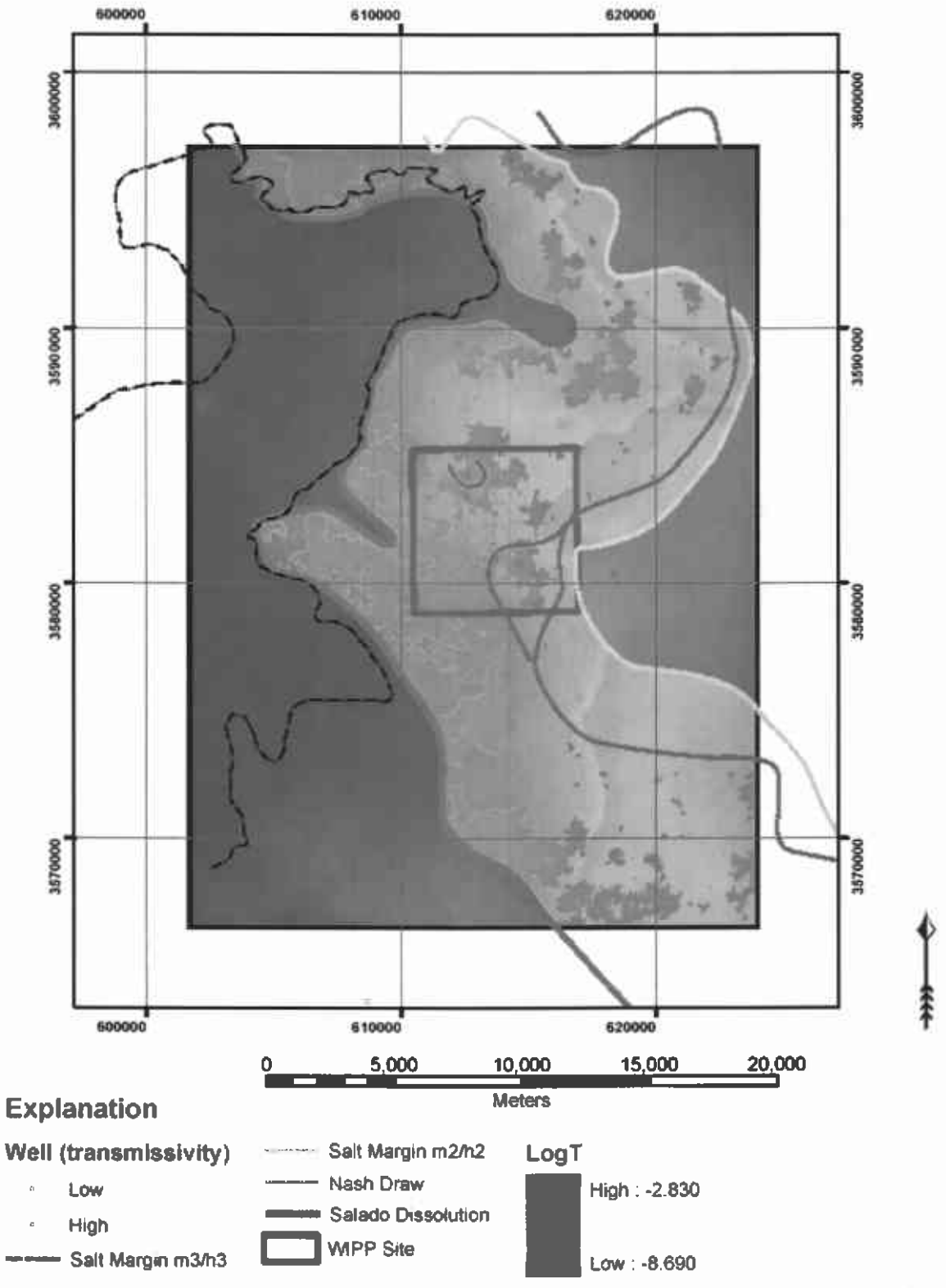

Figure 19. Example of base T fields generated using geologic data.

Table 3. Heads to Be Used in Water-Level-Rise Impact Assessment.

Well	CCA Freshwater Head Range (m amsl)	1980 Freshwater Head Range (m amsl)	1990 Freshwater Head Range (m amsl)	2000 Freshwater Head Range (m amsl)
AEC-7	931.2-932.8	NA	930.7-933.4	931.8-934.6
CB-1	910.4-911.8	NA	911.6-913.8	NA
D-268	915.1-915.6	NA	914.7-916.2	P&A
DOE-1	912.1-918.6	NA	913.1-918.4	914.9-918.2
DOE-2	933.2-936.2	NA	933.1-937.1	**938.0-942.0**
H-1	919.6-923.6	920.5-925.4	NA	**925.6-928.7**
H-2b2	924.7-926.6	NA	NA	925.6-927.6
H-3	912.9-916.7	914.2-918.9	NA	915.7-918.6
H-4b	910.8-912.0	911.1-914.2	**914.1-916.3**	**914.5-916.6**
H-5b	932.8-935.6	932.1-935.8	932.1-935.8	934.4-938.2
H-6b	931.0-933.0	931.4-934.4	930.4-933.5	932.7-935.7
H-7b1	912.6-913.2	911.8-913.2	912.6-914.0	**913.3-914.7**
H-9b	906.3-907.6	**908.0-909.8**	**911.1-913.0**	**910.6-912.5**
H-10b	919.1-923.5	918.3-923.6	918.2-923.4	P&A
H-11	911.4-915.4	NA	912.9-916.0	914.0-917.0
H-12	912.3-914.7	NA	914.0-917.5	912.4-917.0
H-14	916.8-920.8	NA	915.2-916.9	919.0-921.5
H-15	916.0-920.3	NA	914.7-918.0	918.2-921.5
H-17	910.1-911.9	NA	**912.7-915.7**	**914.3-916.4**
H-18	931.3-934.9	NA	932.1-935.3	**935.6-938.8**
P-14	926.0-927.8	926.1-928.8	926.2-928.9	P&A
P-15	917.0-918.6	915.7-920.5	917.2-918.7	P&A
P-17	908.6-910.0	NA	**912.7-915.1**	**914.0-916.4**
WIPP-12	933.5-935.8	NA	930.0-933.4	932.4-935.9
WIPP-13	932.4-935.2	NA	932.3-935.7	933.5-936.8
WIPP-18	929.3-933.5	NA	NA	**934.4-937.8**
WIPP-25	927.7-929.7	925.9-930.5	928.7-931.7	**931.2-934.2**
WIPP-26	918.4-918.9	**915.4-917.1**	**919.2-920.5**	**920.5-921.8**
WIPP-27	937.4-938.8	**940.6-944.2**	938.0-940.3	**939.8-942.2**
WIPP-28	936.3-938.4	934.1-937.1	NA	P&A
WIPP-30	932.8-935.0	NA	934.0-936.8	**935.5-938.3**
USGS-1	909.7-910.2	NA	NA	NA

NA: data not available
Bold red signifies range is completely outside CCA range.
P&A: plugged and abandoned

Once new Culebra T fields are available that have been calibrated to transient heads, the three scenarios described above will be modeled using existing data. Plans are also being made to install a number of new Culebra wells to provide information needed to validate these scenarios and model them in greater detail. Because Magenta water levels are also rising and because leaking boreholes may interconnect the Culebra and Magenta, additional information on the Magenta will be collected. Over the next few years, hydraulic testing will be performed in eight wells recently recompleted to the Magenta and several new Magenta wells planned for installation north of the WIPP site. The information from these wells will be used to develop a groundwater-flow model for the Magenta that can then be linked to the Culebra model. At the conclusion of these activities, new Culebra conceptual and numerical models consistent with all observations will be developed.

Dewey Lake Geohydrological Investigations

At least one scenario that explains Culebra water-level rises identifies leakage from shallow water-bearing zones to the Culebra through poorly plugged or cased boreholes. Testing of this scenario requires knowledge of the geohydrology of the shallow water-bearing units, e.g., the Dewey Lake Formation. In anticipation of the need for this information, SNL is preparing a test plan that describes the methods that will be used to characterize better the hydrology of the Dewey Lake. This test plan has been drafted and is currently undergoing SNL management, technical, and quality assurance review. The plan is expected to be finalized in August 2002 and will be submitted with the next status report.

References

Beauheim, R.L. 2000. "*Compliance Monitoring Program: Recompletion and Testing of Wells for Evaluation of Monitoring Data from the Magenta Member of the Rustler Formation on the WIPP Sit.*" TP-00-03. Carlsbad, NM: Sandia National Laboratories.

Beauheim, RL. 2002. "*Analysis Plan for Evaluation of the Effects of Head Changes on Calibration of Culebra Transmissivity Fields.*" AP-088. Carlsbad, NM: Sandia National Laboratories.

Chavez, M. 2002. "*Software Requirements.*" NP 19-1, Rev. 9. Carlsbad, NM: Sandia National Laboratories.

Jepsen, R.A. 2000. "*Groundwater Monitoring Activities: TROLL Measurements, Bell Canyon Injection Well Monitoring Near H-9, and Meteorological Monitoring at H-9.*" TP 99-10. Carlsbad, NM: Sandia National Laboratories.

Powers, D.W. 2001. "*Examining Culebra Water Levels.*" TP 01-01. Carlsbad, NM: Sandia National Laboratories.

2.3 WIPP Hydrologic Data Assessment[1]

D. A. Chace, T. W. Pfeifle and T. L. MacDonald
Sandia National Laboratories, MS 1395
4100 National Parks Highway
Carlsbad, NM USA 88220

Abstract

Groundwater monitoring activities at the Waste Isolation Pilot Plant (WIPP) are an integral part of the US Department of Energy's (DOE) broader requirement to ensure protection of the environment, the health and safety of workers and the public, proper characterization of the disposal system, and compliance of the WIPP with applicable regulations. This commitment is not only for the current operational phase of the WIPP, but extends through the post-closure phase to meet regulatory requirements. Groundwater monitoring at the WIPP is driven by regulatory requirements, in particular, requirements to measure both water quality and water levels. These measurements are currently made manually in approximately 70 wells located within and near the WIPP site boundary.

Westinghouse TRU Solutions (WTS), the DOE's Management and Operating Contractor, is responsible for collecting the manual groundwater measurements and maintenance of the well network. Sandia National Laboratories (SNL), DOE's Science Advisor, is responsible for evaluating the acquired groundwater data, comparing the data against regulatory compliance requirements and making recommendations to improve the effectiveness and efficiency of the monitoring systems. SNL activities conducted between January 1, 2002 and June 30, 2002 to assess current groundwater monitoring data and to evaluate new technologies (i.e., remote monitoring water-level instrumentation) are described. Evaluation of data for regulatory compliance is performed on an annual basis using other process requirements and, thus, is not included within the context of this work scope.

Background Information

The primary objective of the current WIPP groundwater-monitoring program (GWMP) is to meet regulatory compliance requirements (e.g., DOE Compliance Certification Application, or CCA, DOE 1996; DOE Hazardous Waste Facility Permit, or HWFP, New Mexico Environment Department, or NMED, 1999) by measuring water quality in seven wells, known as Water Quality Sampling Program (WQSP) wells and water levels in approximately 70 wells located within or outside the WIPP Land Withdrawal Act (LWA) boundary. A secondary objective is to maintain a well network that provides for these measurements. The focus of the GWMP is the Culebra Member of the Rustler Formation because it is the most transmissive saturated unit at the WIPP site. Other formations, e.g., the Magenta Member of the Rustler and the Dewey Lake and Bell Canyon Formations, are monitored where access is available. Data collection and well maintenance are the responsibility of WTS. Water-quality data are collected semi-annually, in the spring and fall. Water-level measurements are made monthly in all primary wells and quarterly in redundant wells (wells located on the same well pad and completed to the same hydrologic unit as the primary well). In addition, WTS regularly performs well maintenance including well logging and integrity testing, replacement of wells as required, and plugging and

[1] This work is covered by WBS #1.3.5.3.1.1 and #1.3.5.3.1.2

abandonment (P&A) of wells that are unreliable for monitoring because of some well-related problem (e.g., corroded casing or poor cement) found during integrity testing.

SNL assesses the groundwater monitoring data concurrently as they are received from WTS and annually evaluates the data against regulatory compliance requirements. SNL's responsibilities and technical scope are provided both in DOE documents and in SNL analysis plans, e.g., DOE (1999), SNL (2000). The assessment includes preparation and review of updated hydrographs, analysis of new well configurations, review of data trends, and identification of deviations from normal or expected groundwater behavior. In addition, as directed by DOE or requested by WTS, SNL personnel also monitor WTS hydrologic field activities through instrumentation of and, in some cases, testing in monitoring wells. Data assessments also include evaluating new monitoring techniques and technologies to ensure that the monitoring program is effective in meeting requirements and efficient in terms of cost and resource allocation. SNL groundwater data-assessment activities performed between January 1, 2002 and June 30, 2002, described below, include:

- Assessment of WIPP groundwater levels.
- Observations of WIPP groundwater levels during WTS well maintenance activities.
- Remote monitoring system demonstration at WIPP C 2737.

The annual evaluation of data against regulatory compliance requirements will be conducted by SNL in October 2002 and results reported in a separate document.

Assessment of WIPP Groundwater Levels

WIPP groundwater-level measurements focus primarily on the Culebra because this hydrogeologic unit has been determined to be the most transmissive saturated unit of the stratigraphic sequence within which the WIPP is sited. Monthly groundwater level measurements are made in the seven WQSP wells plus other wells completed in the Culebra (quarterly measurements are made in the case of redundant wells located on the same well pad where measurements are made monthly). The Culebra wells included in the groundwater-level-monitoring network are shown in Figures 1 and 2. In addition to measurements of the water levels in the Culebra, water levels in the Dewey Lake, Magenta, Rustler-Salado (Los Medanos) contact, and Bell Canyon are measured at a limited number of locations to aid in the characterization of site hydrology. Figures 3 and 4 show the Magenta groundwater-level-monitoring network and all other wells in the groundwater-level-monitoring well network, respectively. Some wells have multiple completions so that more than one hydrologic unit can be measured in the same well. In the past, the groundwater-level-monitoring network was made up of 71 wells in which 80 water-bearing intervals were monitored. However, in the past six months, several of these wells have been P&A subsequent to the performance of a well integrity evaluation.

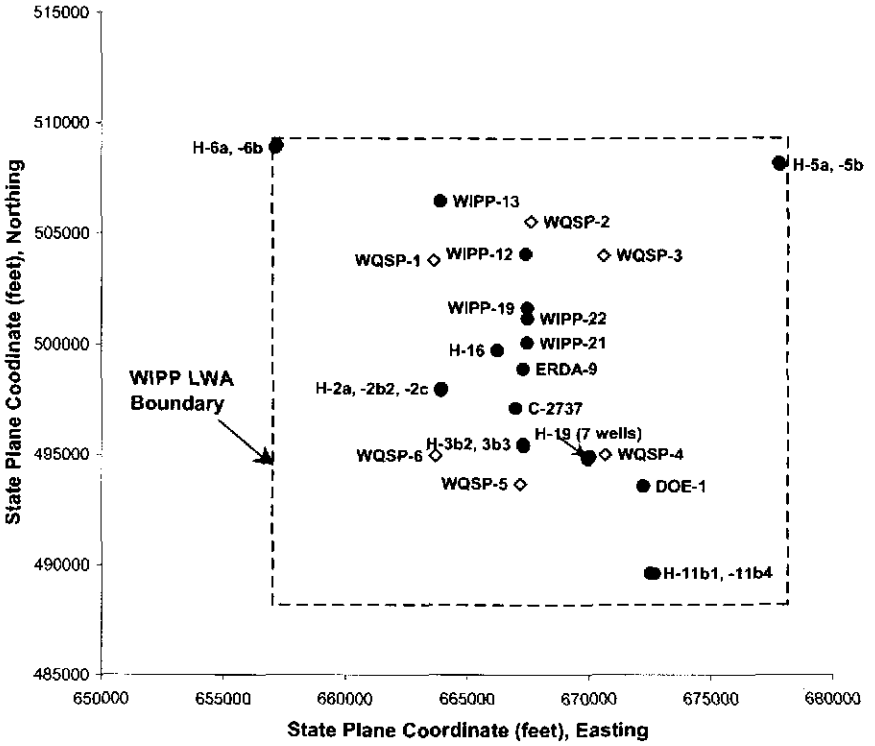

Figure 1. Culebra monitoring well locations inside the WIPP LWA boundary.

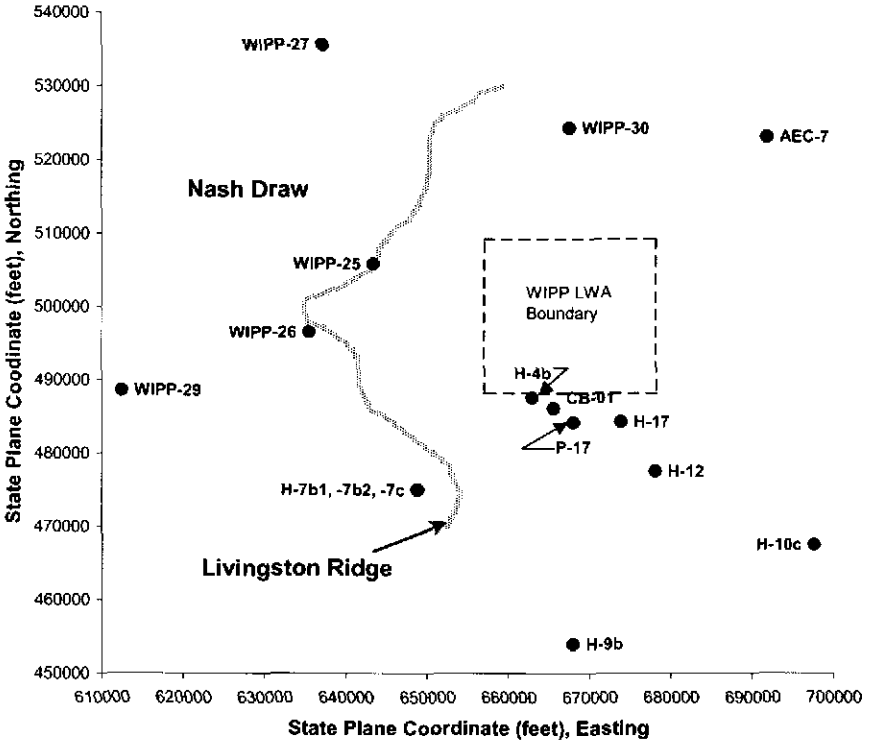

Figure 2. Culebra monitoring well locations outside the WIPP LWA boundary.

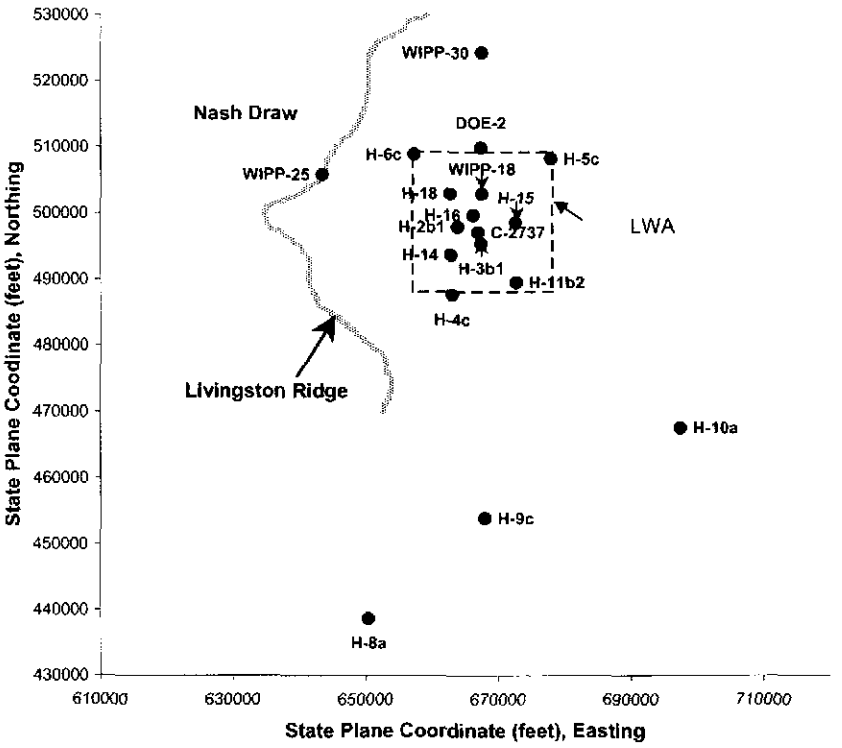

Figure 3. Magenta monitoring well locations on and around the WIPP site.

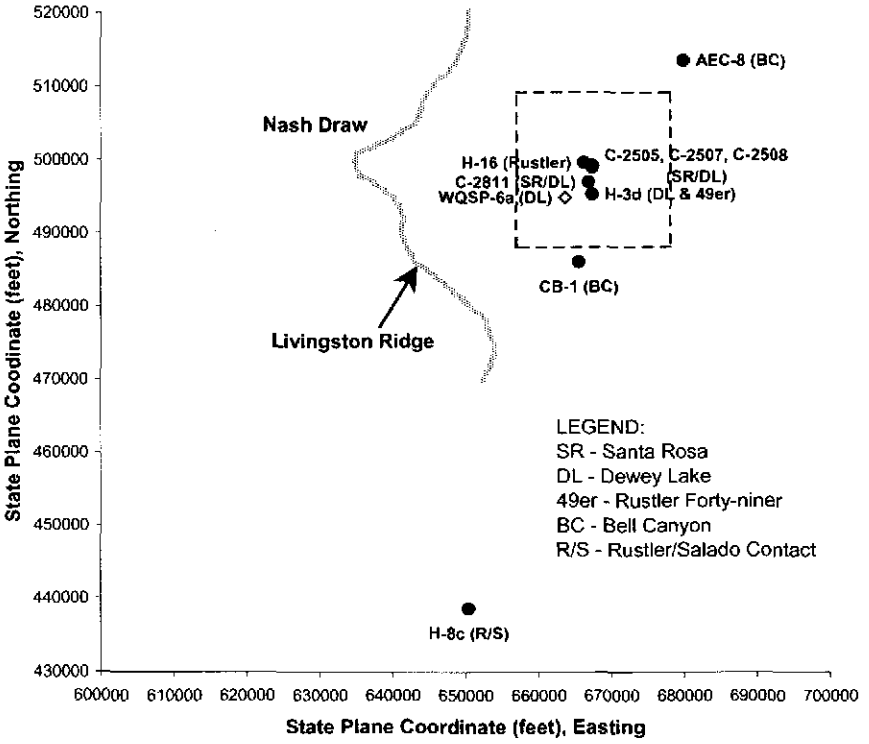

Figure 4. Other monitoring well locations on and around the WIPP site.

Table 1 provides information regarding the current status of the water-level-monitoring network including well, monitored zone, type and frequency of measurements, and change in status (P&A, recompleted, etc). The WTS well-integrity evaluation is an ongoing process and not all of the wells listed in Table 1 have received such an evaluation. Therefore, it is expected that additional wells in the groundwater-level-monitoring network will be deemed unusable upon the performance of a well integrity evaluation and will be P&A. During the current reporting period, four wells were P&A, one well is in the process of being P&A, one well (H-9c) was inadvertently lost when it was plugged with cement during the P&A of another well (see subsequent discussion), two wells were re-completed, and one well (C 2737) was equipped with a remote-monitoring system to monitor automatically and remotely the Culebra and Magenta water levels in the well. In addition to these routine maintenance activities, WTS also pumped the annulus of well Cabin Baby-1 to reduce the Culebra water level in this well (also see subsequent discussion). Some deviations from normal or expected performance are briefly described below.

DEVIATIONS FROM NORMAL

Deviations from normal water level trends in individual wells that occurred between January 1, 2002 and June 30, 2002 (the reporting period for this technical baseline report) are described below.

Cabin Baby-1 (Culebra)

The Culebra water level in Cabin Baby-1 continued to rise during the reporting period until May 2002 when the DOE Carlsbad Field Office (CBFO) instructed WTS to pump the water level down as an interim action to prevent the possibility of commingling of groundwater from separate water-bearing units. WTS pumped approximately 105 barrels of fluid dropping the water level approximately 500 feet. The suspected cause for the water level rise in Cabin Baby-1 is a leaking packer. Remediation alternatives are currently being evaluated by DOE/CBFO. Additional detail on the pumping activity is provided later in this report.

H-3b3 (Culebra)

H-3b3 showed a water level increase in March 2002 (quarterly measurement) in response to scheduled well maintenance activities. The reason for the increase is probably a fluid-density change caused when different water was added to the well during the maintenance activities.

The water level increase in H-9b observed in March 2002 is a direct result of P&A activities in H-9a during the same time demonstrating communication between the two wells through the Culebra (see subsequent discussion). Following the P&A activities in H-9a, cement was found to exist in H-9b at a level above the top of the Culebra. In an effort to verify that the Culebra had been plugged in H-9b as a result of the H-9a P&A activities, the water level in H-9b was pumped down and observed. Currently, the H-9b water level remains well below the known Culebra static water level on the H-9 well pad. Therefore, H-9b was removed from the Culebra groundwater-level-monitoring network, but may be recompleted as a Magenta groundwater-level-monitoring well in the future and then placed back into service in the well network.

Table 1. WIPP Groundwater-Monitoring Well Network Information

Well I.D.	Zone Monitored	Type of Measurement	Measurement Frequency	Status
AEC-7	Culebra	Manual	Monthly	
C 2737 (PIP)	Culebra	Manual/Electronic	Monthly/Variable	Equipped with remote monitoring system, May 2002
CB-1	Culebra	Manual/Electronic	Monthly/Variable	Annulus water pumped, May 2002
DOE-1	Culebra	Manual	Monthly	
ERDA-9	Culebra	Manual	Monthly	
H-2a	Culebra	Manual	Quarterly	
H-2b2	Culebra	Manual	Monthly	
H-2c	Culebra	Manual	Quarterly	
H-3b2	Culebra	Manual	Monthly	
H-3b3	Culebra	Manual	Quarterly	
H-4b	Culebra	Manual	Monthly	
H-5a	Culebra	Manual	Quarterly	
H-5b	Culebra	Manual	Monthly	
H-6a	Culebra	Manual	Quarterly	
H-6b	Culebra	Manual	Monthly	
H-7b1	Culebra	Manual/Electronic	Quarterly/Variable	
H-7b2	Culebra	Manual	Monthly	
H-9a	Culebra	Manual	Monthly	P&A on February 11, 2002
H-9b	Culebra	Manual	Monthly	Determined to have been plugged in the Culebra during H-9a plugging activities
H-10b	Culebra	Manual	Monthly	P&A on January 31, 2002
H-10c	Culebra	Manual	N/A	Recompleted to Culebra on February 19, 2002
H-11b1	Culebra	Manual	Quarterly	
H-11b3	Culebra	Manual	Quarterly	In the process of being P&A
H-11b4	Culebra	Manual	Monthly	
H-12	Culebra	Manual	Monthly	
H-16	Rustler	Electronic	Continuous	Lost 49er pressure gage
H-17	Culebra	Manual	Monthly	
H-19b0	Culebra	Manual	Monthly	
H-19b2	Culebra	Manual	Quarterly	
H-19b3	Culebra	Manual	Quarterly	
H-19b4	Culebra	Manual	Quarterly	
H-19b5	Culebra	Manual	Quarterly	
H-19b6	Culebra	Manual	Quarterly	
H-19b7	Culebra	Manual	Quarterly	
P-15	Culebra	Manual	Monthly	P&A on February 11, 2002
P-17	Culebra	Manual/Electronic	Monthly/Variable	
P-18	Culebra	Manual	Monthly	P&A on February 25, 2002
WIPP-12	Culebra	Manual	Monthly	
WIPP-13	Culebra	Manual	Monthly	
WIPP-19	Culebra	Manual	Monthly	

Table 1. WIPP Groundwater-Monitoring Well Network Information (continued)

Well I.D.	Zone Monitored	Type of Measurement	Measurement Frequency	Status
WIPP-21	Culebra	Manual	Monthly	
WIPP-22	Culebra	Manual	Monthly	
WIPP-25 (PIP)	Culebra	Manual	Monthly	
WIPP-26	Culebra	Manual	Monthly	
WIPP-27 (PIP)	Culebra	Manual	Monthly	
WIPP-29	Culebra	Manual	Monthly	
WIPP-30 (PIP)	Culebra	Manual	Monthly	
WQSP-1	Culebra	Manual	Monthly	
WQSP-2	Culebra	Manual	Monthly	
WQSP-3	Culebra	Manual	Monthly	
WQSP-4	Culebra	Manual	Monthly	
WQSP-5	Culebra	Manual	Monthly	
WQSP-6	Culebra	Manual	Monthly	
C 2737 (annulus)	Magenta	Manual/Electronic	Monthly/Variable	Equipped with remote monitoring system, May 2002
DOE-2	Magenta	Electronic	Variable	
H-2b1	Magenta	Manual	Monthly	
H-3b1	Magenta	Manual	Monthly	
H-4c	Magenta	Manual	Monthly	
H-5c	Magenta	Manual	Monthly	
H-6c	Magenta	Manual	Monthly	
H-8a	Magenta	Manual	Monthly	
H-9c	Magenta	Electronic	Variable	Recompleted to Magenta on February 19, 2002.
H-10a	Magenta	Manual	Monthly	
H-11b2	Magenta	Electronic	Variable	
H-14	Magenta	Electronic	Variable	
H-15	Magenta	Electronic	Variable	
H-18	Magenta	Electronic	Variable	
WIPP-18	Magenta	Electronic	Variable	
WIPP-25 (annulus)	Magenta	Manual	Monthly	
WIPP-30 (annulus)	Magenta	Manual	Monthly	
H-3d (PVC)	Dewey Lake	Manual	Monthly	
WQSP-6a	Dewey Lake	Manual	Monthly	
H-8c	Los Medanos	Manual	Monthly	
AEC-8	Bell Canyon	Manual/Electronic	Monthly/Variable	
CB-1 (PIP)	Bell Canyon	Manual	Monthly	Annulus water pumped, May 2002
H-3d (PIP)	Forty-niner	Manual	Monthly	

H-11b4 (Culebra)

The water level decrease in H-11b4 in March 2002 and subsequent increase in April 2002 is a response to well maintenance activities and the associated partial recovery. Additional detail is provided later is this report.

H-16 (Rustler)

The well head at H-16, located adjacent to the WIPP air intake shaft, has not been accessible for a number of years so WTS does not currently include the well in its monitoring network. SNL, however, configured the well with a multiple-packer system to isolate the five members of the Rustler Formation, i.e., the Forty-niner, Magenta, Tamarisk, Culebra, and Los Medanos. Pressure transducers were placed in the five zones during installation of the packer system and measure, on a continuous basis, the hydraulic pressure in each zone. Figure 5 summarizes the pressures in each hydrologic zone for the time period from March 31, 1998 to June 30, 2002. The zone pressure is the highest in the Los Medanos Member (~190 psi) and, in order decreases for the Culebra (~145 psi), Magenta (~ 140 psi), Tamarisk (~100 psi) and Forty-niner (~60 psi) Members. Several of the pressure-response curves (e.g., Tamarisk and Forty-niner) have a sinusoidal shape. An explanation for this behavior is not available, but could be explained by seasonal changes in temperature in the air intake shaft.

During the reporting period, the signal from the pressure transducer monitoring the Forty-niner interval was lost. The cause of the problem has not yet been determined, but investigations to be performed during the next reporting period will examine the electrical connectors and cabling for the transducer near the ground surface.

WIPP-25 (Culebra)

The water level in WIPP-25 continued to rise for the duration of this reporting period. The cause of the water level rise in this well, along with others in the Nash Draw area, continues to be investigated.

WIPP-27 (Culebra)

The water level in WIPP-27 continued to rise through March 2002, at which time it appeared to stabilize. The cause of the water level rise in this well, along with others in the Nash Draw area, continues to be investigated.

WIPP-30 (Magenta/Culebra)

Both the Culebra and Magenta water levels in WIPP-30 continued to rise during this reporting period. The Magenta water level appeared to stabilize in March 2002, but will continue to be observed. The cause of the water level rise in this well, along with others in the Nash Draw area, continues to be investigated.

WQSP-3 (Culebra)

WQSP-3 showed a decreased water level in April 2002 followed by an increase of similar magnitude in May 2002. This water level fluctuation was the result of semi-annual pumping for water-quality sampling and the associated partial recovery.

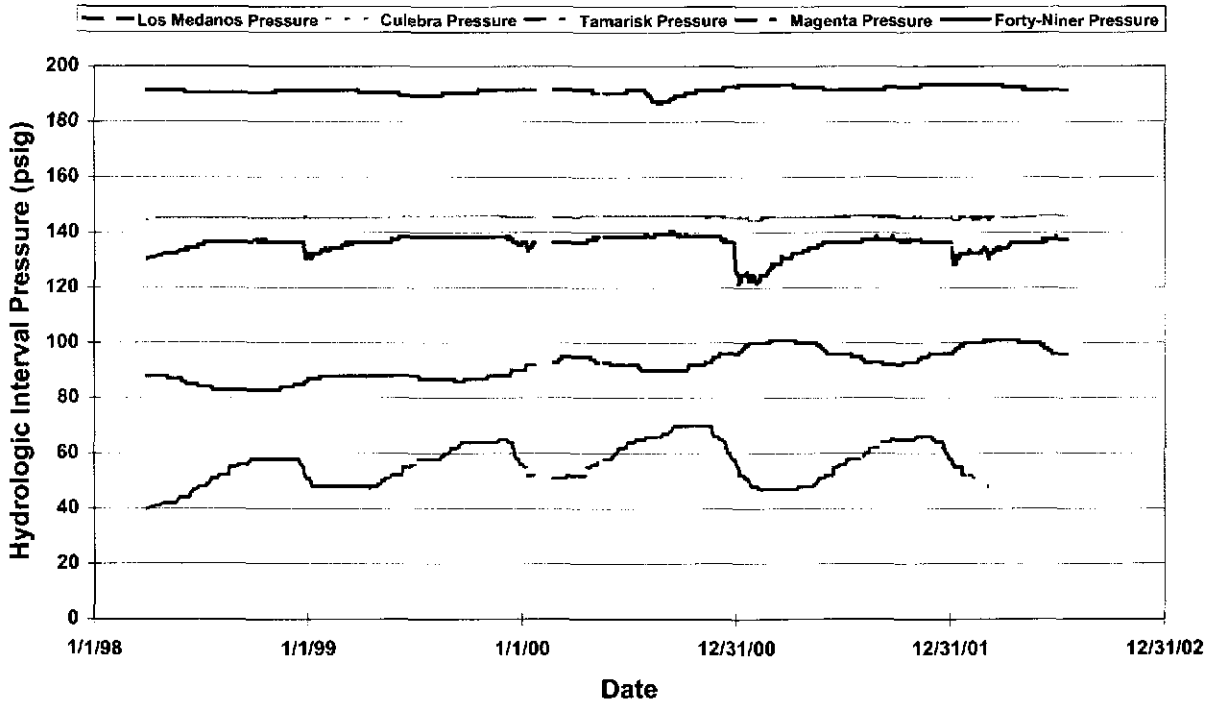

Figure 5. Hydraulic pressures in the Rustler members at H-16 near the WIPP air intake shaft.

H-3b1 (Magenta)

H-3b1 showed a dramatic water level decrease in March 2002 that continued in April 2002. In May 2002 the H-3b1 water level began to increase again. This water-level fluctuation is the result of scheduled well maintenance activities and the associated partial recovery.

H-10a (Magenta)

H-10a showed a dramatic Magenta water level increase of approximately 45 feet in February 2002 and the water level continued to rise an additional 15 feet in March 2002. Since that time, the water level has stabilized at this elevated level. This sustained water level rise is suspected to be a result of density differences between the formation fluid and the fluid used during scheduled well maintenance (the fluid used during well maintenance being of lower density). Similar water level responses have been observed in this well following previous well maintenance activities.

The water level in AEC-8 continued to rise during the reporting period and has risen by more than 90 feet since 1993. The well is configured using two casing strings having diameters of 8.625 inches and 5.5 inches. The outer casing is cemented over its entire extent from 874 feet to ground surface. The inner casing is cemented from 4907 feet to 868.5 feet so the annulus between the two casing strings is open from the surface to 868.5 feet. One explanation for the rising water level in the well is a leaking inner casing. SNL has recommended to the DOE that the annulus between the two casings be fully cemented to the surface and that an integrity test be performed in the well to evaluate its condition. Assuming the well annulus is cemented and casing integrity is proven, AEC-8 could be returned to service as a Bell Canyon monitoring well. If well integrity cannot be proven, then SNL will recommend that AEC-8 be P&A and that DOE-2 be converted to a Bell Canyon monitoring well to retain Bell Canyon water-level monitoring north of the WIPP site.

Observations of WIPP Groundwater Levels During WTS Well Activities

As discussed above, WTS personnel and their contractors conducted well logging, pumping, and P&A activities at several of the WIPP monitoring well locations. SNL personnel monitored these activities either through TROLL measurements or manual measurements of water levels in the tested wells and/or other wells on the well pad. Well activities monitored included those at the Cabin Baby-1, H-7, H-9, H-10, and H-11 well pads. A brief summary of the monitoring activities for each well activity is described below.

CABIN BABY-1 WELL ACTIVITIES

Cabin Baby-1 is a dual-completion well that monitors both Bell Canyon and Culebra water levels. The well has a cemented steel casing extending from ground surface to the top of the Salado and is open-hole below the casing down to TD (total depth). Two production-injection packers (PIPs) are set in the well, one in the lower anhydrite of the Castile immediately overlying the Bell Canyon and one in the casing just below the Culebra Member of the Rustler. The PIPs are connected via tubing that extends to the ground surface. Bell Canyon water levels are measured in the tubing, while Culebra water levels are measured in the annulus between the tubing and cemented steel casing. The casing is perforated through the entire Culebra interval. While Bell Canyon water levels have been stable in Cabin Baby-1, Culebra water levels have been rising since the double-PIP system was installed more than two years ago. These rises, approximately 3 to 4 feet/month, were attributed to water leakage by the upper PIP with water originating from the uncased open-hole section of the well between the two PIPs.

In April 2002, the annulus water level in Cabin Baby-1 was found to be within 35 feet of the ground surface. Assuming the water in the well annulus was brine-saturated (having originated from the open-hole section rather than the Culebra interval), the DOE directed WTS to pump the well annulus to ensure that the net hydraulic gradient in the Culebra was toward the well rather than away from the well. In early May 2002, WTS personnel pumped approximately 100 barrels of water from the annulus lowering the water level nearly 500 feet as shown in Figure 6. Water level measurements made after the well was pumped indicate the level in the annulus is currently rising at a rate of approximately 25 ft/month. This high rate is likely influenced by both Culebra water recharge to the well and continual leakage of water by the upper PIP. The rise is expected to decrease with time as the head in the well increases.

Bell Canyon water levels were monitored during the pumping of the well annulus. These data are also shown in Figure 6 and indicate the Bell Canyon water level was unaffected by the pumping of water from the annulus. The small excursion in Bell Canyon water levels was caused by the re-installation of a TROLL in the tubing.

H-7 WELL PAD ACTIVITIES

As part of its well logging and integrity testing program, WTS and Schlumberger (its support services contractor) logged H-7b2 using an ultrasonic imaging (USI) tool to determine the competency of the well casing and cement. The USI tool requires sufficient positive fluid pressure in the wellbore to operate effectively. Water was added to the well to provide the required positive fluid pressure on the tool. Following log completion, approximately 300 barrels of water were removed from the well to recover the tool cushion water and sufficient native water to ensure the water in the well was representative of formation waters. During loading of the well with water and subsequent pumping, SNL personnel monitored the water level in H-7b1, another well located on the H-7 well pad approximately 100 feet from H-7b2. Figure 7 plots the water-level response in H-7b1 during the loading, logging, and pumping of H-7b2. As shown, water levels initially increased as cushion water was added to H-7b2, then decreased rapidly as the cushion water was pumped out of H-7b2. The fluctuations in water levels during loading and pumping the well were less than 1 foot. Full recovery of water levels from the well activities required less than one month.

H-9 WELL PAD ACTIVITIES

In November 2001, WTS and Schlumberger also logged and tested the three Culebra groundwater-monitoring wells located on the H-9 well pad. Following recommendations by SNL, DOE instructed WTS to P&A H-9a, retain H-9b as a Culebra groundwater-monitoring well, and convert H-9c to a Magenta groundwater-monitoring well.

In early February 2002, H-9c was converted to a Magenta monitoring well by setting a bridge plug between the Culebra and Magenta intervals (a bridge plug was also set below the Culebra) and perforating the casing through the entire Magenta interval using four shots per lineal foot of casing length. This well was subsequently pumped to remove perforation-gun cushion water and sampled to determine water quality. Later in February 2002, WTS mobilized on the well pad to begin the P&A activities at H-9a. Because of the highly transmissive nature of the Culebra at the H-9 well pad, WTS and Schlumberger designed a cement containing charcoal and Celoflake additives that would limit cement migration. In addition, WTS requested that SNL monitor water levels in the other Culebra monitoring well at the well pad, i.e., H-9b.

On February 11, 2002, WTS initiated the P&A activity at H-9a by injecting the tailored cement into the well, while SNL monitored water levels in H-9b using a TROLL. Immediately following the introduction of cement into H-9a, water levels in H-9b increased rapidly by more than 150 feet as shown in Figure 8. Because water levels then stopped rising and cement pressures increased to near normal levels, the cementing process continued at H-9a until the well was cemented from TD to surface. Water-level monitoring was continued at H-9b even after H-9a was plugged to determine if the water level rise would dissipate with time. These water level measurements were verified by manual water level measurements as shown in Figure 8.

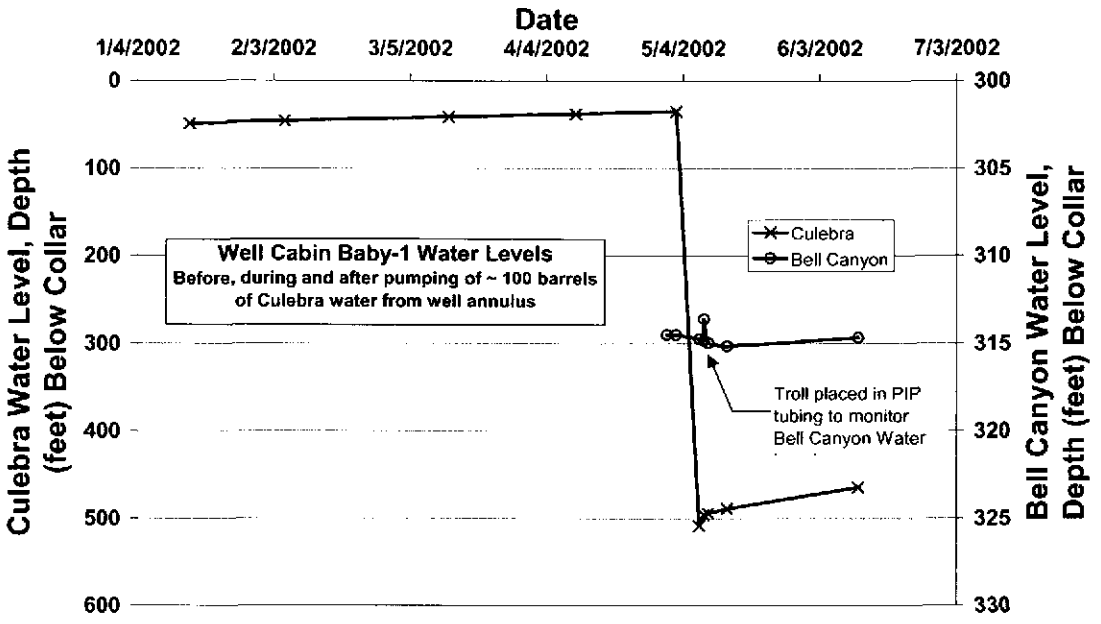

Figure 6. Culebra and Bell Canyon water levels in Cabin Baby-1 during pumping of the well annulus.

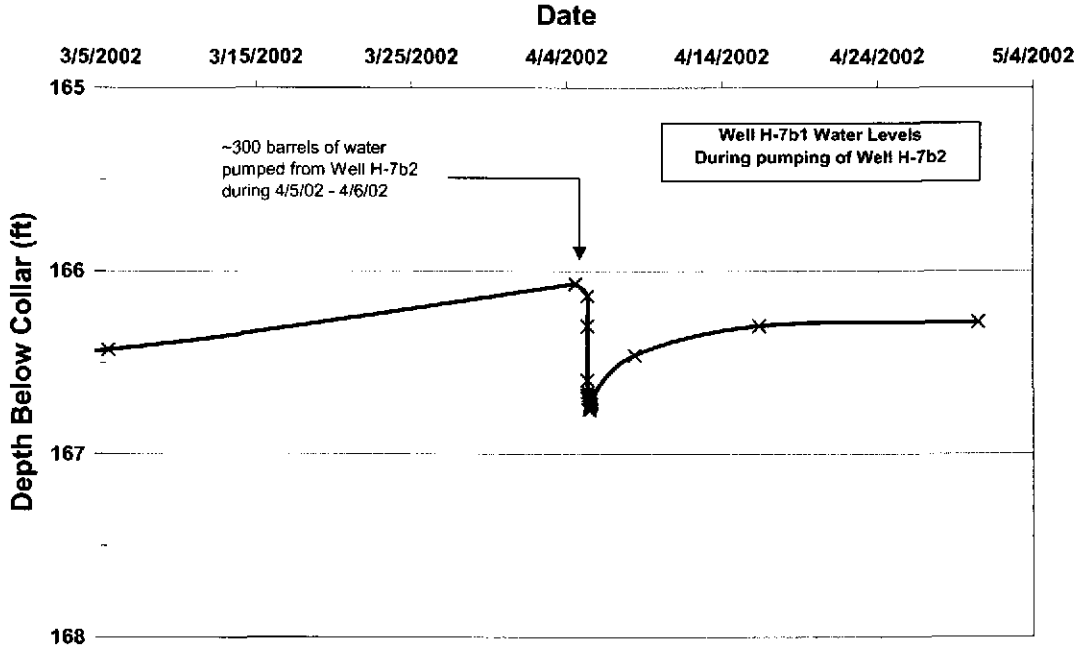

Figure 7. Depth to Culebra water level in H-7b1 during logging and pumping of H-7b2.

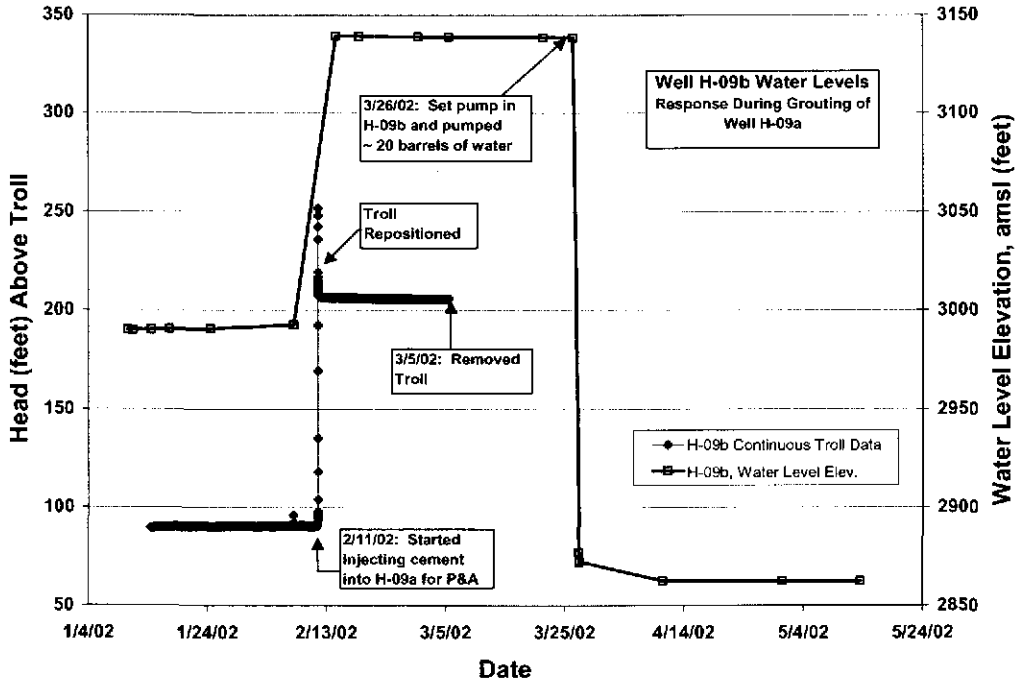

Figure 8. Culebra water level elevation and heads (above TROLL) in H-9b during plugging and abandonment of H-9c.

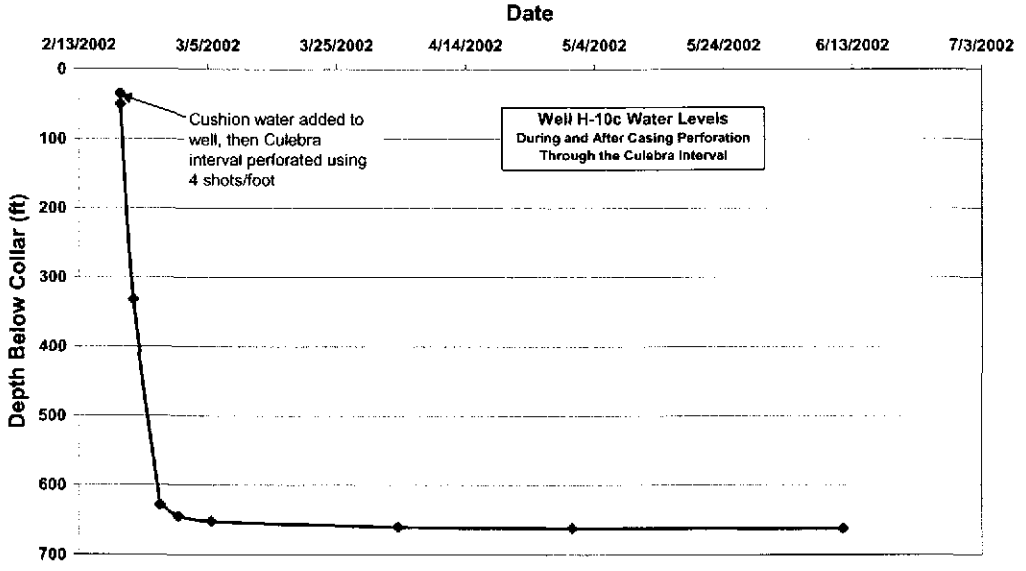

Figure 9. Depth to water in H-10c before and after perforation of the well casing through the Culebra interval.

When the water levels did not fall but remained constant instead, a bailer was lowered into H-9b and retrieved cement containing charcoal and Celoflake indicating cement had migrated through the Culebra from H-9a to H-9b.

Water level monitoring at H-9b was continued for approximately six weeks after P&A of H-9a. No changes in water level were observed during this period so the well was pumped to determine if hydraulic connection with the Culebra unit could be re-established by inducing a hydraulic gradient toward rather than away from the well. Approximately 20 barrels of water were removed from the well with a corresponding water-level drop of nearly 300 feet. Water-level monitoring was resumed after pumping and continued for nearly 2 months. During this period, water levels in H-9b remained constant, indicating that hydraulic connection could not be re-established.

With the P&A of H-9a, the apparent loss of H-9b, and the conversion of H-9c to a Magenta well, Culebra groundwater monitoring at the H-9 well pad is no longer possible. Options for re-initiating Culebra monitoring at the H-9 well pad are currently being investigated.

H-10 WELL PAD ACTIVITIES

In January 2002, WTS and Schlumberger logged and tested the integrity of H-10a (Magenta well) and H-10b (Culebra well) and intended to P&A H-10c (Rustler/Salado well) because it no longer provided information required for site hydrologic assessments. The integrity of H-10a was established and, therefore, the well was returned to service as a Magenta groundwater-monitoring well. In contrast, H-10b was determined to be in poor condition (corroded casing). Based on these results, SNL recommended that H-10b rather than H-10c be P&A and that H-10c be converted to a Culebra groundwater-monitoring well. The DOE accepted this recommendation and instructed WTS to recomplete H-10c to a Culebra well.

In February 2002, H-10b was P&A. No special precautions were taken to prevent cement migration because the Culebra at this location has relatively low transmissivity. During the same month, H-10c was cemented from TD to approximately 35 feet below the Culebra interval. The casing through the Culebra interval was then perforated using four shots per lineal foot of casing length. As with the USI tool described above, the gun used to perforate the casing required a high positive fluid pressure in the well to cushion the blast of the gun. Therefore, the well was filled nearly to the ground surface with cushion water before the casing perforation was performed. Figure 9 shows the depth to water immediately after the cushion water was added to the well and also the temporal depths following perforation of the casing. As shown, all of the cushion water rapidly flowed out of the well and into the Culebra unit adjacent to the well. The flow stopped only when the head within the well and the areal Culebra head equilibrated. Because no attempt was made to develop the well by pumping after the casing was perforated, cushion water has been introduced into the Culebra unit and is likely continuing to disperse away from the well. In the future, this well will need to be pumped for a long period of time to re-establish native Culebra water in the well.

WTS and Schlumberger also logged and tested the integrity of three Culebra groundwater-monitoring wells at the H-11 well pad (H-11b1, H-11b3, and H-11b4). Results of the logging and testing indicated the need to P&A H-11b3. To prevent the migration of cement from H-11b3 to other wells at the H-11 well pad (as was the case at the H-9 well pad), WTS used a cement dump bailer rather than a cement pump to install the cement plug. As an additional precaution, WTS requested that SNL monitor the Culebra water levels in H-11b1 and H-11b4 during the cementing of H-11b3.

Cement was placed in H-11b3 in two stages. The first stage was performed on March 25, 2002, and the second stage two days later. SNL monitored Culebra water levels in both H-11b1 and H-11b4 during this period using TROLLs. As shown in Figure 10, the water levels in both wells fluctuated less than 0.5 feet during the placement of the cement indicating that cement did not migrate from H-11b3 as had occurred at the H-9 well pad.

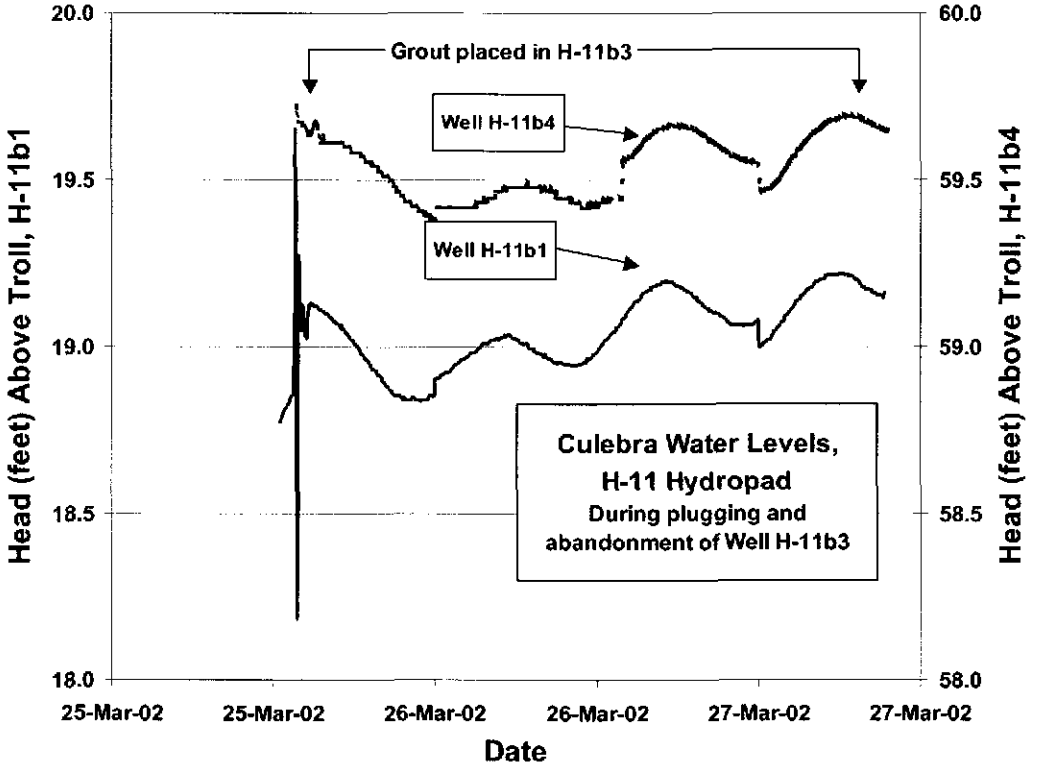

Figure 10. Culebra heads (above TROLLs) in H-11b1 and H-11b4 during the Plugging and Abandonment of H-11b3.

Remote Monitoring System Demonstration at C 2737

BACKGROUND INFORMATION

On November 15, 2001 the Groundwater Task Force (GWTF), including members from DOE, WTS, and SNL, initiated discussions regarding the automation of water level measurements that are currently being taken manually at approximately 63 wells on a monthly basis. The desire expressed in the GWTF meeting was to be able to access remotely "smart" down-hole gages via modem. The term "smart" refers to programmable (the rate at which measurements are taken is user defined and can be controlled by the behavior of the water level in the well) gages that can collect at least pressure and temperature data and have on-board nonvolatile memory. Additional parameters that can be measured with optional instrumentation include:

- Dissolved oxygen (DO)
- Conductivity
- pH
- Oxidation reduction potential (ORP)
- Salinity
- Nitrate
- Chloride
- Ammonium
- Turbidity

The manpower required to collect water-level measurements from these wells on a monthly basis is significant and the data density has proven to be insufficient to capture many of the subtle water level changes as well as the actual timing of some of the more significant water level changes. The use of "smart" down-hole gages accessed remotely via cellular phone and modem will not only reduce costs associated with monitoring water levels (and other parameters if so desired), but also optimize data density such that more data are recorded when the water level in a given well is changing and less data are recorded when the water level is relatively stable. This feature allows the precise timing and magnitude of events to be determined so that these water-level changes might be correlated with potential events, whereas manual monthly water-level measurements clearly miss such events. The reduction in the cost of the data is realized as a result of a reduction in manpower required to collect the data. Access to the data via cellular phone and modem eliminates the need for monthly manual water-level measurements. However, to confirm the integrity of the electronically recorded data, regular but infrequent manual water-level measurements should be taken as a means of verifying the accuracy of the electronic data.

The GWTF decided that the relatively new C 2737 location would be the most desirable location for a pilot installation of a remote telemetry system. At this location, both the Magenta and the Culebra are accessible at the same wellhead. Therefore, information from both intervals could be obtained from a single system installation, thereby reducing the cost of data collection even further. Figure 11 shows the location of the C 2737 well pad.

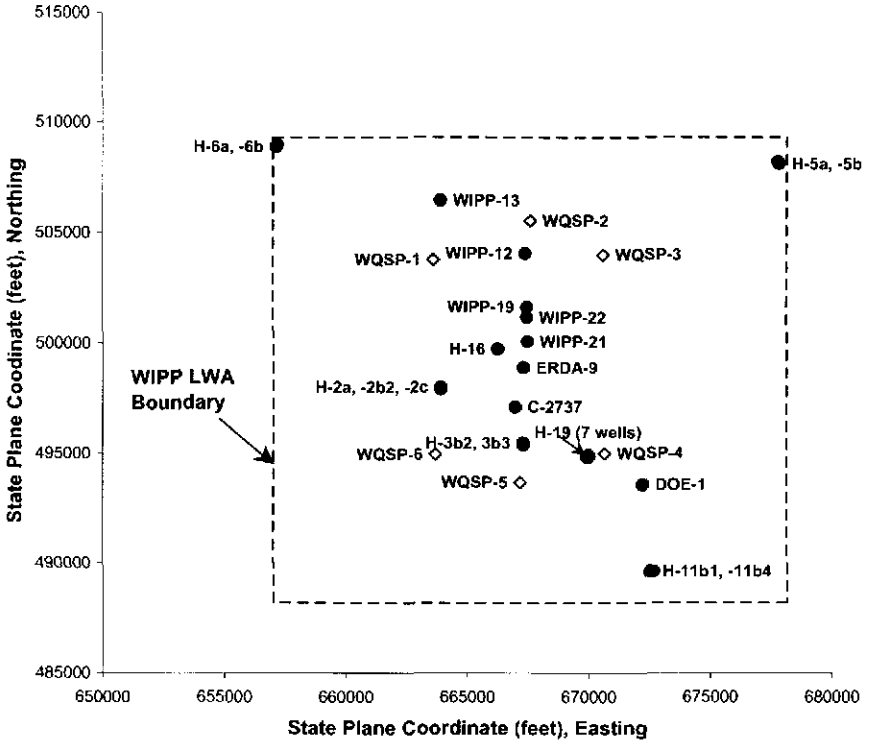

Figure 11. Location of C 2737 well pad.

SYSTEM CONFIGURATION

The entire remote telemetry system was provided by In-Situ, Inc. and consists of the following items:

- Two, 100-psig miniTROLL pro pressure/temperature "smart" gages.
- A solar panel and gel-cell battery as the power source.
- A cellular modem and associated interface hardware and software to provide real-time remote access to the down-hole equipment.

As part of the remote telemetry system installation, a metal frame was constructed and anchored to the C 2737 wellhead. This metal frame served as a mounting structure for both the solar-power panel and the cellular modem/interface enclosure. Figure 12 illustrates the wellhead configuration, the remote telemetry system installation, and the individual system components identified for reference.

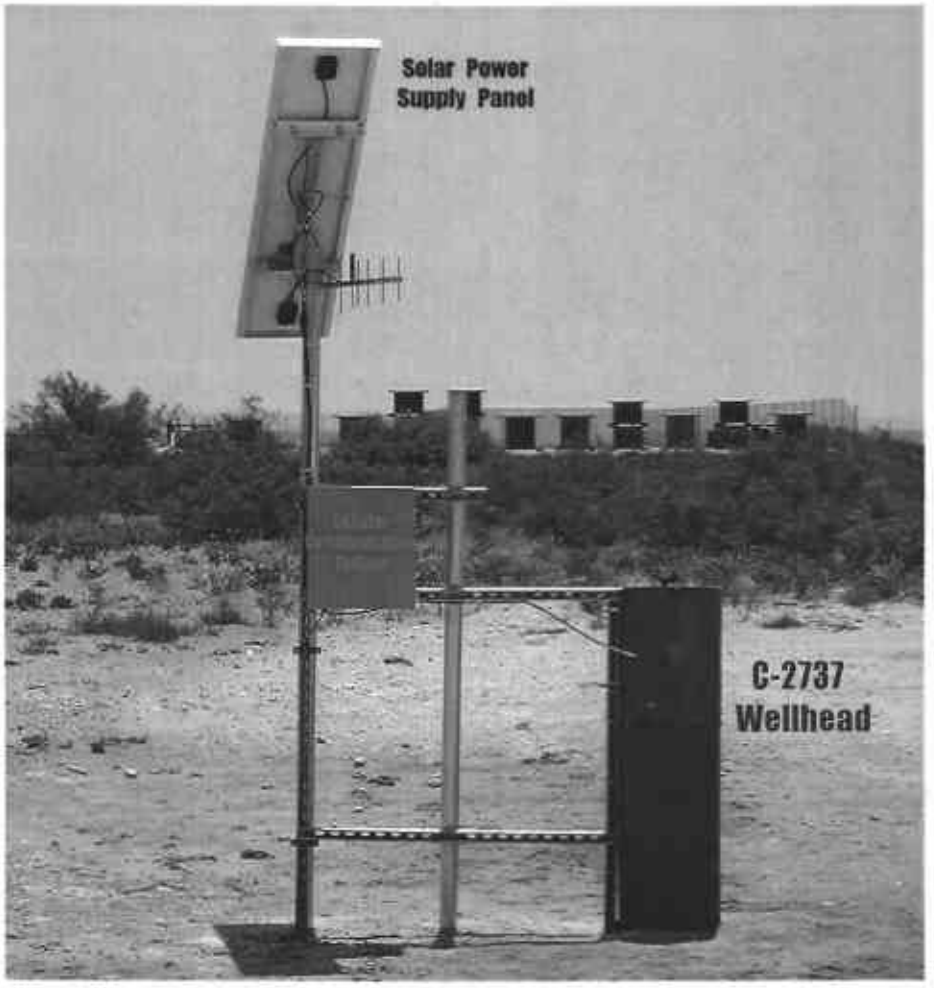

Figure 12. C 2737 wellhead configuration with telemetry system installation.

MiniTROLL pro pressure/temperature gages were installed in both the tubing (Culebra) and the annulus (Magenta) of C 2737. Table 2 provides all of the pertinent information regarding the installation of the pressure/temperature gages in C 2737.

At the top of the wellhead, but contained inside the surface casing for security purposes, resides a junction box which serves as the interface between both of the pressure/temperature gages and the cellular communication hardware. Figures 13, 14, and 15 show the junction box within the C 2737 wellhead, the cellular communication system, and the solar (power supply) panel, respectively.

Table 2. C 2737 Remote-Monitoring System Installation Information[(a)]

Well I.D.	Interval	Depth to Water (ft amsl)	MiniTROLL Installation Depth (ft amsl)	Gage Serial #
C 2737	Magenta	3141.99	2949.30	8268
C 2737	Culebra	3016.29	2903.05	7861

(a) Information taken from TROLL Scientific Notebook. Duplicate copies of notebook are filed in the Sandia National Laboratories Records Center.

Figure 13. C 2737 interface hardware linking the down-hole gages to the communication system.

Figure 14. C 2737 cellular communication system.

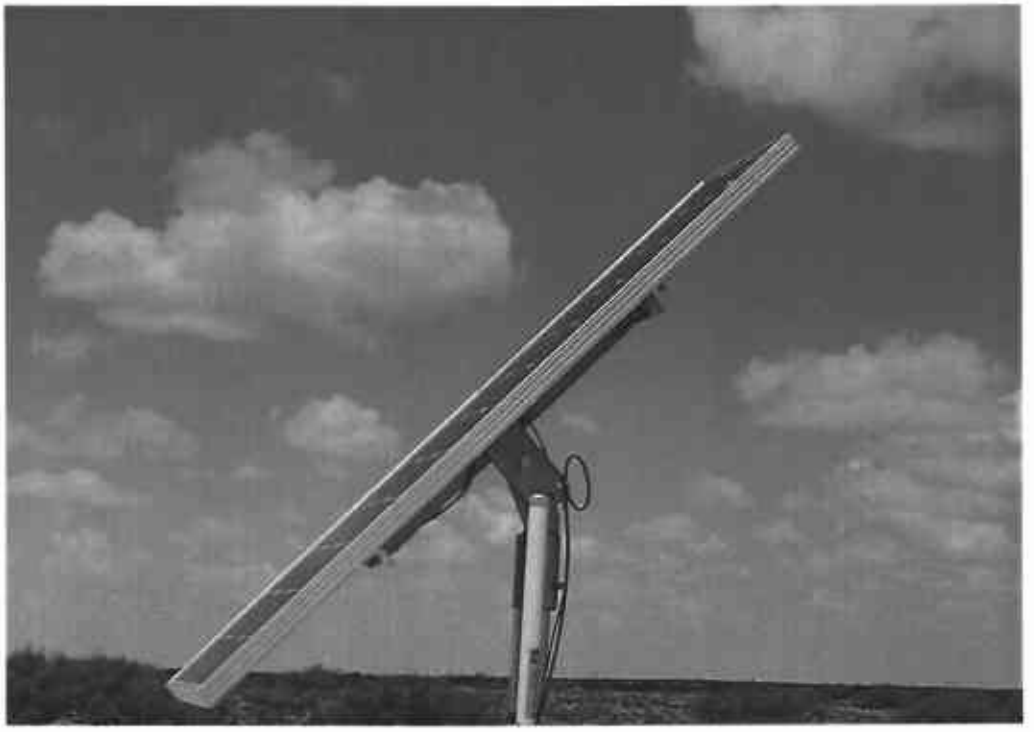

Figure 15. C 2737 solar (power supply) panel.

C 2737 DATA

The remote telemetry data-collection system accessed via cellular phone and modem, described, was installed at C 2737 on May 29, 2002. C 2737 is a dual-completion well providing access to both the Magenta and Culebra. The remote telemetry system monitors and records both pressure and temperature associated with these two water-bearing intervals. Figures 16 and 17 illustrate the Magenta and Culebra water levels and water temperatures at C 2737 from the time of installation on May 29, 2002 through June 25, 2002. The initial decrease in both the Magenta and Culebra water levels is attributed to water-level equilibration following the disturbance caused by the installation of the TROLLs.

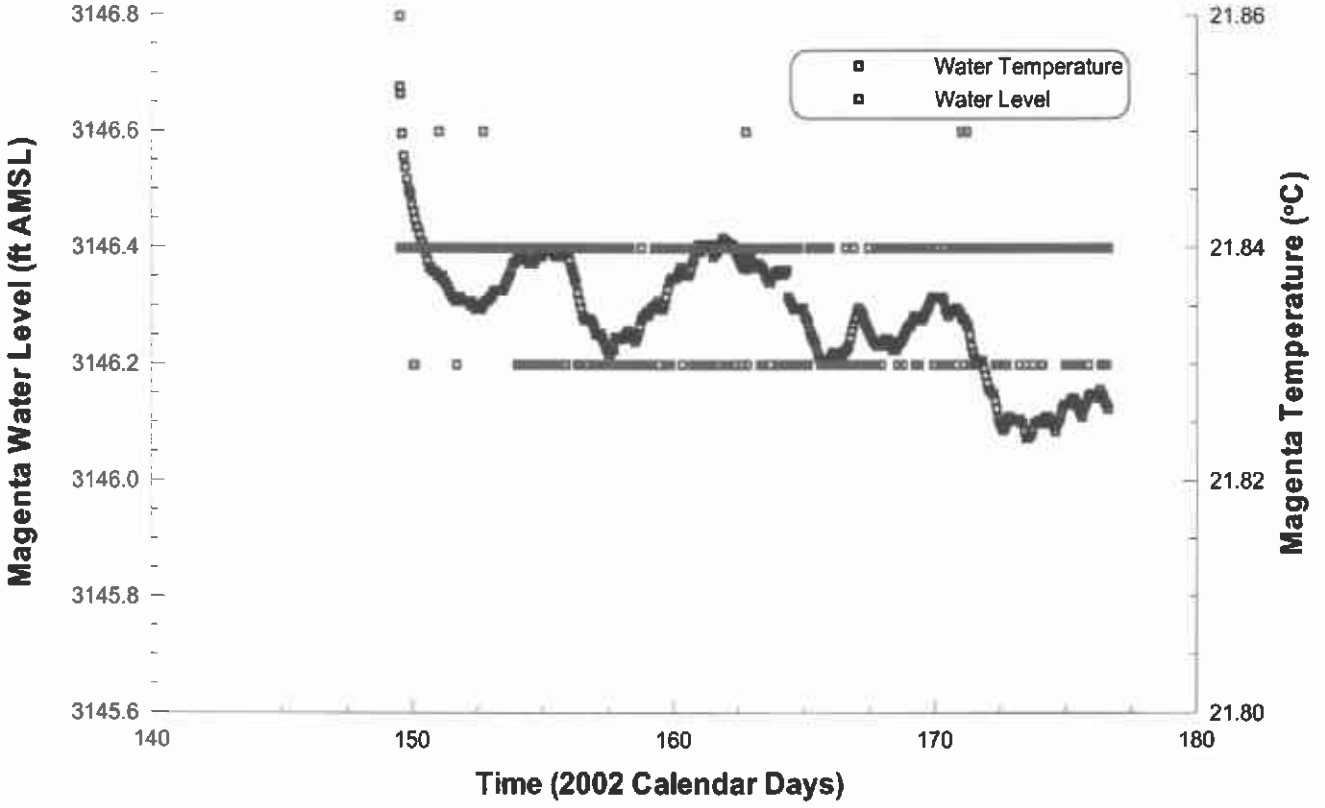

Figure 16. C 2737 Magenta water level and water temperature.

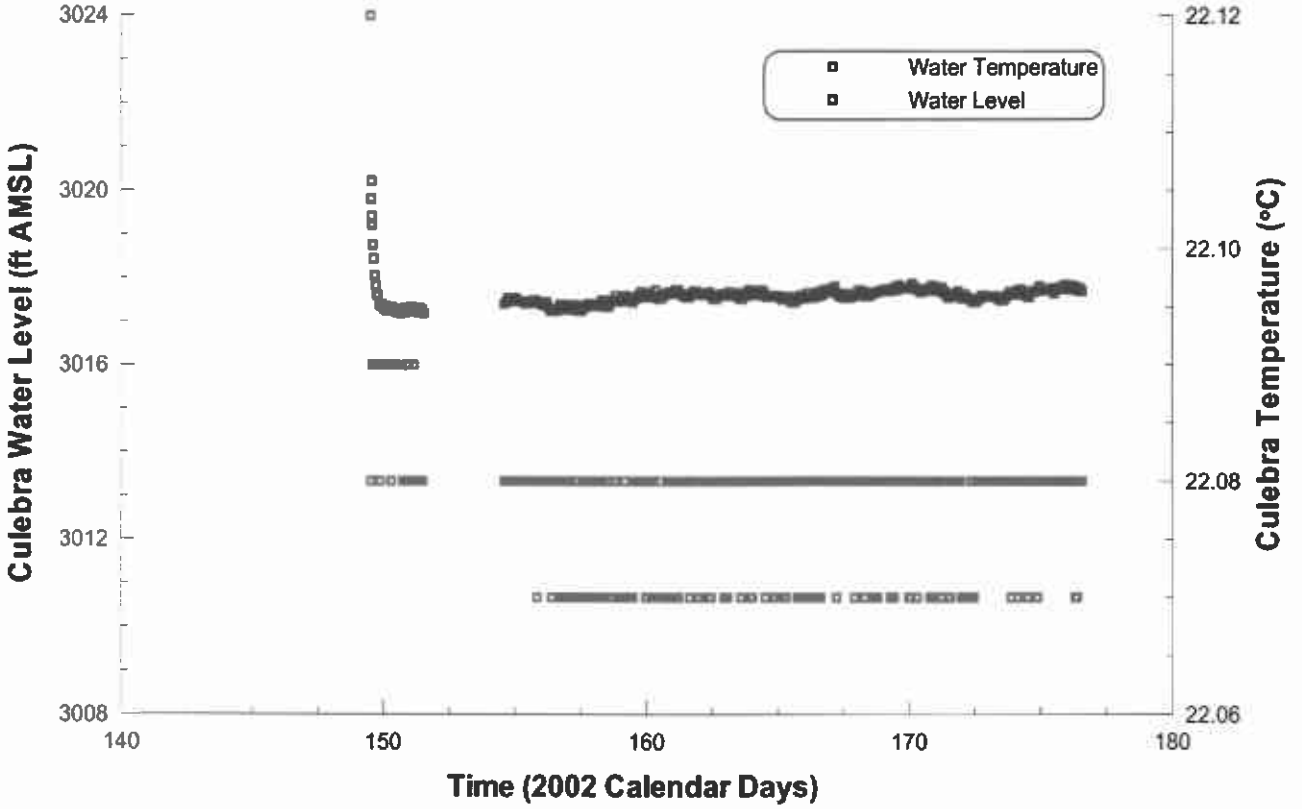

Figure 17. C 2737 Culebra water level and water temperature.

References

New Mexico Environment Department. 1999. *Hazardous Waste Facility Permit, Waste Isolation Pilot Plant EPA No. NM4890139088.* Santa Fe, NM: New Mexico Environment Department.

Sandia National Laboratories. 2000. "An Analysis Plan for Annually Deriving Compliance Monitoring Parameters and their Assessment Against Performance Expectations to Meet the Requirements of 40 CFR 194.42e." AP-069. Carlsbad, NM: Sandia National Laboratories.

US Department of Energy, 1996. *Title 40 CFR Part 191 Compliance Certification Application for the Waste Isolation Pilot Plant.* DOE/CAO-1996-2184. Carlsbad, NM: US Department of Energy, Carlsbad Area Office.

US Department of Energy. 1999. *40 CFR Parts 191 and 194 Compliance Monitoring Implementation Plan.* DOE/WIPP-99-3119. Carlsbad, NM: US Department of Energy Carlsbad Area Office.

3 GEOCHEMISTRY

3.1 Re-Evaluation of Microbial Gas Generation under Expected Waste Isolation Pilot Plant Conditions[1]

Data Summary and Progress Report (February 1 – July 15, 2002)
July 18, 2002

J. B. Gillow and A. J. Francis
Environmental Sciences Department,
Brookhaven National Laboratory
Upton, NY USA 11973

Abstract

Gas generation from the microbial degradation of the organic constituents of transuranic waste under conditions expected in the WIPP repository is being investigated at Brookhaven National Laboratory (BNL). This report summarizes progress from the period February 1 – July 15, 2002. During this period, we analyzed total gas and carbon dioxide (CO_2) production in initially aerobic and anaerobic humid samples at 3334 and 2945 days incubation (9.1 and 8.1 years), respectively. Carbon dioxide production in unamended inoculated and amended inoculated samples, initially aerobic and anaerobic, without bentonite, has leveled off, consistent with analyses over the past two years. Initially aerobic, unamended inoculated samples with bentonite continue to produce CO_2, from 244 ± 180 μmoles CO_2 g^{-1} cellulose at 3009 days to 300 ± 228 μmoles CO_2 g^{-1} cellulose at 3334 days (0.17 μmol CO_2 g^{-1} cellulose day^{-1} for the last 325 days); an increase in the rate of CO_2 production has been continuing in these samples since 804 days incubation. This treatment shows the stimulatory effect of bentonite on biodegradation of cellulose under humid conditions. Methane (CH_4) was analyzed in anaerobic humid samples and was below the minimum detectable amount (0.1 nmol ml^{-1}) in all treatments except those containing bentonite. Unamended inoculated samples with bentonite produced 25.5 ± 1.2 nmol CH_4 g^{-1} cellulose at 2653 days (7.3 years) incubation and amended inoculated samples produced 32.6 ± 9.3 nmol CH_4 g^{-1} cellulose. This finding verifies the presence of viable methanogenic bacteria in the humid samples. The extent of biodegradability of plastic and rubber materials, both unirradiated and irradiated, under WIPP-repository relevant conditions are being evaluated. The results for CH_4 analyses at 3070 days (8.4 years) incubation for polyethylene, polyvinylchloride, and neoprene and 2926 (8 years) for unleaded hypalon are summarized. Over a period of 2230 days incubation (6.1 years since CH_4 was last analyzed) the concentration of CH_4 in almost all samples did not increase but remained nearly equal to that measured at 840 days incubation. The exception to this was the unirradiated polyethylene, which increased from 2.14 ± 1.52 μmol $sample^{-1}$ at 840 days incubation to 2.50 ± 0.26 μmol

[1] This work is covered by WBS #1.3.5.4.1.1

sample^{-1} at 3070 days; however, this does not appear to be significant. Experiments performed at a relative humidity (RH) of 70% may no longer appropriately simulate WIPP disposal rooms post-closure due to the fact that magnesium oxide (MgO) is being emplaced. Experiments were initiated this period that employ radiolabelled carbon substrate (^{14}C) to examine microbial gas generation at 10, 40, 60, and 70% RH. The extreme sensitivity of this method for detecting CO_2 production will provide a means of assessing and quantifying microbial activity under the MgO-constrained water (H_2O) activity that simulates the current WIPP repository design.

BNL Project Objectives

1. Re-evaluation of the existing microbial gas data and development of appropriate technical approaches to improve the conservatism in the current gas generation model.
2. Re-examination and improvement of the experiment for cellulose degradation under humid conditions to derive a more realistic rate for humid microbial degradation.
3. Determination of the effect of MgO on the rate and extent of gas generation under humid conditions.
4. Clarification with scooping experiments of the factors that have caused a diminishing microbial gas generation rate with time in the ongoing experiments, including testing the effect of crystallinity on cellulose degradation under hypersaline conditions.
5. Determination of the rate and extent of methanogenesis by halophilic microorganisms. Due to the fact that methanogenesis is the terminal electron-accepting process in any system, it is important to understand the occurrence and rate of this process.

Progress Report

Long-term experiments designed to examine gas generation due to biodegradation of the organic fraction of transuranic wastes under WIPP repository-relevant conditions have been ongoing at BNL. Table A provides information about the status of these studies as of July 15, 2002.

Table A. Status of Microbial Gas Generation Experiments at BNL

Experiment	Start Date	Most Recent Analyses (Days/Years)	Data Reported (this report) (Days/Years)
Long-Term Inundated Cellulose	1/29/92	3462 / 9.5 aqueous metabolite analysis: 3561 / 9.9	(CO_2 analysis planned for FY02)
Initially Aerobic Humid Cellulose	4/7/93	3009 / 8.2	3334 / 9.1
Anaerobic Humid Cellulose	5/4/94	2616 / 7.2	2945 / 8.1 (methane at 2653 / 7.3)
Inundated PE, PVC, and Neoprene	3/9/93	2612 / 7.2	(methane at 3070 / 8.4) (CO_2 planned for FY02)
Inundated Hypalon	8/3/93	2464 / 6.8	(methane at 2926 / 8.0) (CO_2 analysis planned for FY02)

Research performed during this reporting period was conducted according to procedures specified by Francis et al. (2001) under contract AT-8739. Note that the SNL-approved BNL QA Program remained in effect during this reporting period, and is effectively implemented to date. During this period (February 1 – July 15, 2002) the following tasks were completed:

1. Total gas, CO_2, and CH_4 analysis of samples from the initially aerobic and anaerobic humid cellulose biodegradation experiment.
2. Methane analysis of samples from the plastic and rubber biodegradation experiment.
3. Experiments were started that will quantify gas generation due to microbial activity under conditions of MgO-constrained H_2O activity.
4. A planning meeting was held at Sandia Carlsbad on April 3, 2002, to discuss the status of ongoing studies and plans for this fiscal year. This meeting was attended by A.J. Francis and Jeff Gillow, BNL, and Yifeng Wang and Laurence Brush, SNL.
5. More complete details of the progress made during this reporting period are provided below.

QUALITY ASSURANCE PROGRAM

The program was approved by the SNL QA Team Lead on February 23, 2001 and remains in effect.

GAS ANALYSIS OF HUMID SAMPLES

Tables 1-4, Appendix A, provide data for total gas and CO_2 produced in initially aerobic humid cellulose samples incubated for 3334 days (9.1 years). All samples contain 1 g of cellulosic material. Table 5 provides data that has been corrected for CO_2 produced in the absence of cellulose due to metabolism of any dissolved organic carbon in the mixed inoculum. Table 6-9 provide data for total gas and CO_2 produced in anaerobic humid samples incubated for 2945 days (8.1 years); Table 10 provides corrected data for CO_2 production. All data are reported as gas produced g^{-1} cellulose and are the mean ± standard error of the mean of the analysis of triplicate samples. In all cases samples prepared to determine inoculum viability (succinate or glucose amended treatments) were not analyzed during this time period.

Initially Aerobic Treatments

Initially aerobic humid treatments with and without bentonite have ceased to produce gas as indicated by the decrease in total gas produced at 3334 days (Table 1 and 2). These samples have not produced any gas since the previous analysis period. The concentration of CO_2 in the samples is consistent with the previous analysis specifically in all of the control samples; e.g., the "No cellulose" control showed 2.89 ± 0.08 μmoles CO_2 $sample^{-1}$ at 3009 days and now shows 2.87 ± 0 μmoles CO_2 $sample^{-1}$. Carbon dioxide production in unamended inoculated and amended inoculated samples without bentonite has leveled off (Table 3 and 5), consistent with the analysis over the past two years. This observation is indicative of a limited capability for microbial growth on cellulose under initially aerobic humid conditions (RH = 70%). Unamended inoculated samples with bentonite continue to produce CO_2 (Table 4 and 5) from 244 μmoles CO_2 g^{-1} cellulose at 3009 days to 300 μmoles CO_2 g^{-1} cellulose at 3334 days (0.17 μmol CO_2 g^{-1} cellulose day^{-1} for the last 325 days); an increase in the rate of CO_2 production has been continuing in these samples since 804 days incubation (Table 5). This treatment shows the stimulatory effect of bentonite on biodegradation of cellulose under humid conditions. In addition, the treatment shows the viability of the microbial community over 9.1 years. Therefore the lack of gas production in samples without bentonite, which are relevant to the WIPP repository environment, is not due to a loss of microbial viability. Amended samples, however, have not produced CO_2 since 804 days. The unamended inoculated samples without bentonite showed 6.09 ± 2.41 μmol CO_2 g^{-1} cellulose at 3334 days and amended inoculated samples showed 0.48 ± 0.29 μmol CO_2 g^{-1} cellulose. Unamended inoculated samples with bentonite showed 300 ± 228 μmol CO_2 g^{-1} cellulose at 3334 days and amended inoculated samples showed 615 ± 250 μmol CO_2 g^{-1} cellulose. This is a decrease of 1.4, and 0.6, an increase of 56, and a decrease of 229 μmol, respectively, over 325 days since the last analysis. The changes in CO_2 production over this time period are not significant given the large variation (error) in CO_2 values between triplicate samples.

Anaerobic Treatments

Total gas produced in anaerobic humid samples is presented in Tables 6 and 7; the amended inoculated samples without bentonite showed an increase of 1.29 ml gas sample^{-1} (Table 6) and the unamended inoculated samples with bentonite showed an increase of 1.04 ml gas sample^{-1}; there was no increase in total gas in the other treatments at 2945 days. Carbon dioxide production has not increased at 2945 days in samples without bentonite and similar to initially aerobic samples continues to level off (Table 8). Samples with bentonite have also leveled in terms of CO_2 production (Table 9). After correcting for gas production in the absence of cellulose (Table 10), the unamended inoculated samples without bentonite showed 115 ± 20 μmol CO_2 g^{-1} cellulose at 2945 days and amended inoculated samples showed 21.9 ± 3.3 μmol CO_2 g^{-1} cellulose. Unamended inoculated samples with bentonite showed 541 ± 135 μmol CO_2 g^{-1} cellulose at 2945 days and amended inoculated samples showed 618 ± 125 μmol CO_2 g^{-1} cellulose. This is a decrease of 20, 4.9, 50, and 55 μmoles CO_2, respectively, over 329 days since the last analysis. It is important to note that samples that show a larger deviation from the mean generally show evidence of microbial activity (trending toward positive gas production). The larger spread in the data is indicative of microbial processes that may be occurring at slightly different rates in the active samples due to differences in overall microbial population or metabolic capability. Samples with a smaller variation in values between triplicate bottles have generally ceased to show additional microbial gas production.

ANALYSIS OF METHANE IN ANAEROBIC HUMID SAMPLES

Methanogenesis is a potential gas-consuming microbial process that may occur under repository conditions. In addition, methanogenic bacteria are extremely sensitive to changes in pH, Eh, the presence of oxygen (O_2), and have seldom been found to metabolize complex organic substrates under hypersaline conditions (Oren, 1999). The entire set of samples from the anaerobic humid cellulose biodegradation experiment was analyzed for the presence of methane at 2653 days (7.3 years) incubation. Methane was analyzed by gas chromatography using flame ionization detection and a set of National Institute of Standards and Technology-traceable calibration gases ranging in concentration from 5 to 100 ppm. Methane was detected in unamended inoculated samples with bentonite and amended inoculated samples with bentonite, but was below detectable (<0.1 nmol ml^{-1}) in all other samples. Table B summarizes the results of this analysis.

Table B. Methane Analysis of Anaerobic Humid Samples at 2653 Days Incubation

Sample	Methane (nmol g^{-1} cellulose)
Unamended inoculated + bentonite	25.5 ± 1.2
Amended inoculated + bentonite	32.6 ± 9.3

Gillow and Francis (2002) provided data for methane produced under inundated conditions; in these samples at 3462 days incubation (9.5 years), unamended inoculated sample with bentonite showed 4.51 ± 0.06 nmol CH_4 g^{-1} cellulose and amended inoculated samples with bentonite showed 3.41 ± 0.13 nmol CH_4 g^{-1} cellulose. Under humid conditions, and in the presence of bentonite, the production of methane appears more favorable; in unamended samples methane production was 6x greater than under inundated conditions and almost 10x greater for amended humid samples. This is further evidence of the stimulatory effect of bentonite on microbial activity and also verifies the presence of viable methanogenic bacteria, which should be capable of methanogenesis in all of the samples if conditions are favorable. In addition, the maintenance of strictly anaerobic conditions is verified by methanogenic bacterial activity which cannot occur even in the presence of trace O_2 (Ramakrishnan et al., 2000). The potential remains for the consumption of CO_2 by methanogenic bacteria and additional analyses will provide a suitable data set to compare CO_2 consumption with methane production.

ANALYSIS OF METHANE IN SAMPLES CONTAINING PLASTIC AND RUBBER MATERIALS

Plastic and rubber materials consist of long repeating single bonded carbon chains and are usually quite resistant to biodegradation. Irradiation causes the polymer to break down due to free radical formation, in addition there can be cross-linking of the polymer chain after free radical formation and reduction of the molecular mass of the polymer (Woods and Pikaev, 1994). The extent of biodegradability of plastic and rubber materials, both unirradiated and radiation-damaged, under WIPP-repository relevant conditions are being evaluated in studies initiated in 1993. Details of the experiment are provided elsewhere (Francis et al., 1997). Briefly, sheets of polyethylene (PE), polyvinylchloride (PVC), neoprene (NE), hypalon (HY) and leaded hypalon (LHE) were subject to electron-beam irradiation at Argonne National Laboratory's linear accelerator to create lower absorbed dose (700 Mrad, or 7 MGy) and high absorbed dose (4000-6000 Mrad (40-60 Mgy)) samples for study. Unirradiated and irradiated material was prepared to 2 cm^2 sub samples and these were added to serum bottles and inundated with mixed inoculum/G-Seep brine mixture. Samples were capped with butyl rubber stoppers and have been assessed for total gas, CO_2, H_2, N_2O, and CH_4 attributable to biodegradation of the polymer. Previously, at 7.2 years incubation, total gas and CO_2 was analyzed in these samples. Methane was last analyzed in samples containing PE, PVC, and HY at 840 days incubation, and in samples containing HY at 664 days incubation. Here results for CH_4 analyses at 3070 days (8.4 years) incubation for PE, PVC, and NE and 2926 (8 years) for HY are summarized in Table C (anaerobic treatments only).

Table C. Analysis of Methane in Samples Containing Plastic and Rubber Materials. Nd = Not Detected.

Anaerobic Treatment	Incubation Time	
	T=840 days	T=3070 days
	Methane (μmol sample^{-1})	
Samples without polymer (no irradiation)		
Unamended	0.91 ± 0.14	0.99 ± 0.20
Amended	4.03 ± 0.17	3.65 ± 0.11
Polyethylene		
Unirradiated – Unamended	0.85	0.53
Amended	2.14 ± 1.52	2.50 ± 0.26
Lower-Dose- Unamended	1.01	0.72
Amended	4.13 ± 0.02	3.04 ± 0.11
High-Dose – Unamended	1.02	0.70
Amended	4.29 ± 0.13	1.73 ± 1.20
Polyvinylchloride		
Unirradiated – Unamended	1.27	1.00
Amended	4.88 ± 0.11	3.50 ± 0.37
Lower-Dose-Unamended	nd	nd
Amended	nd	0.004 ± 0.004
High-Dose – Unamended	nd	0.01
Amended	0.03 ± 0.02	0.04 ± 0.04
Neoprene		
Unirradiated – Unamended	0.03	0.02
Amended	4.03 ± 0.22	2.64 ± 0.34
Lower-Dose- Unamended	nd	0.01
Amended	3.87 ± 0.23	3.05 ± 0.14
High-Dose – Unamended	nd	2.79
Amended	4.91 ± 0.04	3.71 ± 0.01

Anaerobic Treatment		Incubation Time	
		T=840 days	T=3070 days
		Methane (μmol sample^{-1})	
Hypalon		*T=664 days*	*T=2926 days*
Unirradiated –	Unamended	nd	0.01
	Amended	0.02 ± 0.00	0.02 ± 0.01
Lower-Dose-	Unamended	nd	0.02
	Amended	0.01 ± 0.00	0.02 ± 0.01

Over a period of 2230 days incubation (6.1 years) the concentration of CH_4 in almost all samples containing polyethylene, polyvinylchloride, and neoprene did not increase but remained nearly equal to that measured at 840 days incubation. The exception to this was the unirradiated polyethylene, which increased from 2.14 ± 1.52 μmol sample^{-1} at 840 days incubation to 2.50 ± 0.26 μmol sample^{-1} at 3070 days; however, this does not appear to be statistically significant. In addition, samples containing hypalon did not show any increase in CH_4 over 2262 days incubation (6.2 years). The concentrations of methane detected at 664 and 840 days and at 2926 and 3070 days are extremely consistent indicating that no further methanogenesis has occurred in these samples. The CH_4 detected is most likely the result of metabolism of dissolved organic C in the mixed inoculum/inundation fluid; however, additional methane production due to biodegradation of the polymer is not evident. The inhibitory effect of irradiated PVC remained after 6.1 years indicating that the degradation products produced due to irradiation continue to be toxic to the microbial consortium in the samples. Additional analyses, including quantification of CO_2 in the samples since the last time period of this analysis (7.2 years), is planned. Characterization of the polymer using solid-state techniques (infrared spectroscopy), specifically in the case of PE, at this stage of incubation is also planned and will provide a more sensitive means of assessing the extent of biodegradation of the polymer.

MICROBIAL GAS GENERATION UNDER CONDITIONS OF MgO-CONSTRAINED WATER ACTIVITY

The two experiments in-progress at BNL are examining gas generation due to cellulose biodegradation under humid conditions. Samples were prepared to maintain a 70% RH environment. Most of the samples in these experiments received 2.0 to 2.5 ml of liquid (2.0 ml of liquid inoculum or 2.0 ml of liquid inoculum and 0.5 ml of a nutrient solution). Experiments performed at an RH of 70% may no longer appropriately simulate WIPP disposal rooms post-closure due to the fact that MgO is being emplaced. Microbial gas generation rates under MgO-constrained humid conditions may be much lower due to sequestering of water, which is necessary for microbial activity. An

experiment procedure has been prepared that tests microbial activity under more relevant MgO-constrained water activity conditions. In order to obtain relevant gas generation data rapidly and accurately, the following was used: (1) a "dry" inoculum; (2) ^{14}C-labeled substrate (for metabolism and growth); (3) extremely sensitive techniques for capturing and quantifying microbially produced CO_2 (alkaline trapping and $^{14}CO_2$ liquid scintillation counting). The experiment is described briefly.

Inoculum Preparation

The facultative anaerobe *Halomonas* sp. (WIPP-1A) was grown in the following media for 48 hours:

WDn Medium	($g\ L^{-1}$)
Sodium succinate	5
Potassium nitrate	1
Potassium phosphate monobasic	0.25
Yeast extract	0.25
Sodium chloride	200
pH	6.8-7.0
Filter sterilized	0.45 μm

The optical density (o.d.) of the culture at 48 hours was 0.8 (measured at 600 nm). The culture was centrifuged at 5,000 xg for 20 minutes, the supernatant decanted, and resuspended in sterile WDn medium diluted 1-4 and centrifuged again at 5,000 xg for 20 minutes. The supernatant was decanted and the cell pellet was resuspended in 20 ml of sterile WDn medium to prepare the inoculum. The o.d. of the inoculum was measured (1.0) and 1.0 ml was preserved with formalin (10% v/v) for direct counting by microscopy. The sample was split into two 10-ml aliquots and air-dried for 1-week followed by final drying in an oven at 30°C.

Sample Preparation

Glass serum bottles (60 ml) were acid washed (10% HCl), rinsed with DI water, autoclaved at 120°C, 20 psi, and air-dried at 80°C overnight. Once dried, 2 ml of WDn medium was added to each of 24 bottles. To six bottles, 40 ml of medium was added. Radiolabelled succinic acid, obtained from PerkinElmer Life Sciences, was added to each of the bottles. Exactly 5 μl of a 3.7 MBq ml^{-1} 1,4-^{14}C-succinic acid solution was pipetted into each bottle for a total of 1.1×10^6 dpm of ^{14}C in each. Sample bottles containing 2 ml of solution were placed in a desiccator along with a 20 ml sterile glass vial containing 10 ml of 0.5 N NaOH to trap, and quantify, any ^{14}C-CO_2 evolved during drying. Samples remained in the desiccator for seven days during which time ^{14}C-CO_2 was not evolved, followed by final drying in an oven at 30°C until dry at which time 12 bottles received air-dried inoculum (0.1 g inoculum $bottle^{-1}$). Tubes (13 x 120 mm, glass, sterile) of saturated salt solutions were added to the bottles in order to maintain the relative humidity at a desired level. An additional 12 bottles received the WDn nutrient

solution but not the ^{14}C substrate and were air-dried. These bottles were used to prepare triplicate samples for humidity testing during the course of the experiment to verify the humidity inside of the bottles using a portable digital humidity meter (Rotronic, Switzerland). The treatment matrix for these experiments is summarized in Table D.

Table D. Treatment Matrix For C-14 Humid Study

Treatment	Relative Humidity				
	Inundated	70 % (G-Seep)	60% (NaBr)	40% (NaI)	10% (LiI)
	Number of Sample Bottles				
Inoculated	3	3	3	3	3
Uninoculated	3	3	3	3	3
Humidity test	3	3	3	3	3

Samples were capped with thick butyl rubber stoppers (Bellco, NJ) affixed with 1-ml sterile glass tubes by running a sterile stainless steel (Nichrome V) wire through the stopper and wrapping the tube to hang it within the bottle. The samples were placed into an incubator set at 30 ± 2°C and alarmed for temperature excursions. The inundated samples serve as a test for inoculum viability and it is expected that CO_2 production will be detected in these samples after a short amount of time relative to humid samples. At approximately 2 months 1.0 ml of sterile 0.5 N NaOH will be added to the hanging-tube within the bottles by using a sterile needle and syringe. The NaOH will be left in the bottle for 1 hour (reaction time is currently being optimized) in order to capture the ^{14}C-CO_2 that is produced in the bottle. The NaOH will then be withdrawn and added to 10 ml of Ultima Gold XR (Packard Instrument Corp.) scintillation fluid for analysis by liquid scintillation counting (LSC). The LSC has a minimum detectable amount of 20 dpm ^{14}C, which will correlate with metabolism of 7.2×10^{-14} mol of ^{14}C-succinate (1.74×10^{-6} mol of ^{14}C-succinate will be present in each bottle). The extreme sensitivity of this method to succinate metabolism and CO_2 production will provide a means of assessing and quantifying microbial activity under the MgO-constrained water activity that simulates the current WIPP repository design. Results of the first round of analyses of these samples will be provided prior to the end of FY'02.

ONGOING WORK

- A draft manuscript, planned for submittal to a peer-reviewed journal, has been prepared that details gas production due to cellulose biodegradation under hypersaline conditions; this is currently undergoing review and revision at SNL and BNL.
- The experiment to examine microbial growth and gas production under conditions of MgO-constrained water activity is underway and analyses continue.

FUTURE WORK

- Total gas, CO_2, and CH_4 will be analyzed in samples prepared to examine gas generation due biodegradation of cellulose under inundated conditions.
- Total gas and CO_2 will be analyzed in samples containing plastic and rubber materials.
- Material characterization techniques including infrared and x-ray spectroscopy will be used to assess the extent of biopolymer degradation due to microbial activity in samples containing cellulose and plastic and rubber materials thus providing an assessment of polymer crystallinity and its relation to the extent and rate of gas generation
- A manuscript concerned with methanogenesis under hypersaline conditions will be prepared for submittal to a peer-reviewed journal.
- A manuscript detailing the effect of bentonite on microbial activity will be prepared for submittal to a peer-reviewed journal.

References

Francis, A.J., J.B. Gillow, and M.R. Giles, M. R. 1997. *Microbial Gas Generation Under Expected Waste Isolation Pilot Plant Repository Conditions.* SAND96-2582. Albuquerque, NM: Sandia National Laboratories. 20-23.

Francis, A.J., J.B. Gillow, and Y. Wang. 2001. "Re-Evaluation of Microbial Gas Generation Under Expected Waste Isolation Pilot Plant Conditions." TP-99-01. Carlsbad, NM: Sandia National Laboratories.

Gillow, J.B., and A.J. Francis. 2002. "Re-Evaluation of Microbial Gas Generation under Expected Waste Isolation Pilot Plant Conditions." In Sandia National Laboratories, "Sandia National Laboratories Technical Baseline Reports, January 31, 2002." Carlsbad, NM: Sandia National Laboratories. 2.1-1 - 2.1-26.

Oren, A. 1999. "Bioenergetic Aspects of Halophilism," *Microbiology and Molecular Biology Reviews.* Vol. 63, no. 2, 334-348.

Ramakrishnan, B., T. Lueder, R. Conrad, and M. Friedrich. 2000. "Effect of Soil Aggregate Size on Methanogenesis and Archael Community Structure in Anoxic Rice Field Soil," *FEMS Microbiology Ecology.* Vol. 32, 361-270.

Woods, R.J., and A.K. Pikaev. 1994. *Applied Radiation Chemistry: Radiation Processing.* New York: John Wiley and Sons.

Brookhaven National Laboratory
WIPP Gas Generation Project

Data Summary and Progress Report
February 1 – July 15, 2002
Appendix

Data Tables

Total Gas and CO_2 Produced in Samples of the Initially Aerobic and Anaerobic Humid Cellulose Biodegradation Experiment

Tables 1-10

Table 1. Total Volume of Gas Produced in Initially Aerobic Humid Treatments (without bentonite)

Treatments (without bentonite)	Volume of Gas Produced (ml/sample)								
	Incubation Time (Days)								
	6	120	317	399	593	804	2553	3009	3334
Control									
Empty bottle	7.15	-0.22	0.28	1.08	1.19	2.51	0.73	3.37	1.24
Blank (tube+brine only)	5.74	-2.27	-0.68	0.14	0.52	0.32	-0.89	1.88	-1.18
No cellulose (salt/ inoculum/ tube+brine)	6.23 ± 0.09	-2.36 ± 0.04	-0.21 ± 0.07	0.73 ± 0.07	0.23 ± 0.04	3.01 ± 0.22	-0.48 ± 0.87	0.20 ± 0.02	-0.62 ± 0.05
Carbon Source: Cellulose Only									
Unamended uninoculated	6.87 ± 0.11	-0.03 ± 1.85	-0.41 ± 0.09	-0.20 ± 0.14	0.12 ± 0.03	1.10 ± 0.17	0.77 ± 0.16	3.84 0.38	-0.73 ± 0.12
Unamended inoculated	7.50 ± 0.33	-0.31 ± 1.62	0.19 ± 0.33	-0.61 ± 0.25	0.31 ± 0.05	1.29 ± 0.25	1.15 ± 0.39	2.91 ± 0.49	-0.96 ± 0.14
Amended uninoculated	6.98 ± 0.18	-0.03 ± 1.68	-0.23 ± 0.10	-0.29 ± 0.13	0.20 ± 0.10	0.50 ± 0.21	1.26 ± 0.24	2.12 ± 0.36	-0.73 ± 0.07
Amended inoculated	7.39 ± 0.11	-0.21 ± 1.57	-0.02 ± 0.18	-0.39 ± 0.07	0.13 ± 0.17	0.77 ± 0.18	0.91 ± 0.12	1.33 ± 0.27	-0.46 ± 0.40
Carbon Source: Cellulose + Glucose									
Amended uninoculated	6.45 ± 0.11	-2.08	0.75 ± 0.00	-0.06 ± 0.21	0.02 ± 0.14	0.13 ± 0.28	1.05 ± 0.22	1.10 ± 0.77	NA
Amended inoculated	7.03 ± 0.07	-1.92 ± 0.11	0.79 ± 0.33	0.35 ± 0.23	0.15 ± 0.04	0.50 ± 0.22	1.15 ± 0.00	1.31 ± 0.40	NA
Amended uninoculated (RG salt)	NA	3.12	1.99 ± 1.90	-0.80 ± 0.11	-0.34 ± 0.33	0.18 ± 0.40	2.87 ± 0.99	2.09 ± 0.29	NA
Carbon Source: Cellulose + Succinate									
Amended uninoculated (w/ acetylene)	19.5	NA	0.64	-0.10	1.66	-0.10	1.98	1.05	NA
Amended uninoculated (w/o acetylene)	5.15	-2.08	0.98	-0.37	-0.08	0.72	0.74	0.22	NA
Amended inoculated (w/ acetylene)	12.9	NA	1.17	0.35	-0.34	-0.10	NA	NA	NA
Amended inoculated (w/o acetylene)	5.88	-2.29	1.27	0.05	0.17	0.72	2.18	1.25	NA

RG salt = reagent grade NaCl was used in this treatment in place of WIPP salt
NA=not analyzed
3334 day data from notebook JG121101

Table 2. Total Volume of Gas Produced in Initially Aerobic Humid Treatments (with bentonite)

Treatments (with bentonite)	Volume of Gas Produced (ml/sample) Incubation Time (Days)								
	6	120	317	399	593	804	2553	3009	3334
Control									
Empty bottle	7.15	-0.22	0.28	1.08	1.19	2.51	0.73	3.37	1.24
Blank (tube+brine only)	5.74	-2.27	-0.68	0.14	0.52	0.32	-0.89	1.88	-1.18
No cellulose (salt/ inoculum/ tube+brine)	7.25 ± 0.03	-2.42 ± 0.08	-0.42 ± 0.07	0.52 ± 0.18	0.33 ± 0.04	1.68 ± 0.95	1.47 ± 0.51	1.11 ± 0.48	-0.80 ± 0.14
Carbon Source: Cellulose Only									
Unamended uninoculated	5.67 ± 0.00	1.03 ± 1.41	-0.62 ± 0.17	-0.39 ± 0.15	0.31 ± 0.05	-0.01 ± 0.10	1.36 ± 0.25	4.67 ± 0.34	2.21 ± 0.16
Unamended inoculated	6.35 ± 0.48	-0.59 ± 1.52	0.11 ± 0.13	-0.40 ± 0.08	0.06 ± 0.12	0.02 ± 0.32	1.05 ± 0.30	2.39 ± 0.69	0.76 ± 0.15
Amended uninoculated	6.09 ± 0.00	0.08 ± 1.85	0.01 ± 0.13	-0.15 ± 0.13	0.11 ± 0.05	0.19 ± 0.27	2.05 ± 0.99	1.36 ± 0.29	-0.46 ± 0.03
Amended inoculated	7.81 ± 0.26	0.78 ± 1.56	0.35 ± 0.31	0.02 ± 0.24	0.11 ± 0.14	0.51 ± 0.19	1.15 ± 0.18	0.43 ± 0.48	0.02 ± 0.00
Carbon Source: Cellulose + Glucose									
Amended uninoculated	6.35 ± 0.04	-1.98	-1.45 ± 0.29	-0.09 ± 0.25	0.07 ± 0.07	1.03 ± 0.76	1.41 ± 0.40	3.38 ± 0.76	NA
Amended inoculated	7.29 ± 0.11	-1.45 ± 0.07	-0.42 ± 0.07	0.23 ± 0.11	0.20 ± 0.04	1.28 ± 0.83	1.20 ± 0.04	NA	NA
Amended uninoculated (RG salt)	NA	2.60	1.78 ± 1.57	-0.82 ± 0.21	0.13 ± 0.04	1.59 ± 0.76	1.26 ± 0.37	4.06 ± 0.22	NA
Carbon Source: Cellulose + Succinate									
Amended uninoculated (w/ acetylene)	18.7	NA	0.74	-0.15	0.07	-0.63	1.46	2.18	NA
Amended uninoculated (w/o acetylene)	5.56	-1.98	1.71	-0.76	0.27	-0.33	0.84	2.30	NA
Amended inoculated (w/ acetylene)	18.0	NA	2.00	0.05	0.10	0.55	NA	NA	NA
Amended inoculated (w/o acetylene)	6.82	-2.29	2.30	0.67	-0.11	1.16	0.74	-0.19	NA

RG salt = reagent grade NaCl was used in this treatment in place of WIPP salt
NA=not analyzed
3334 day data from notebook JG121101

Table 3. Production of Carbon Dioxide in Initially Aerobic Humid Treatments (without bentonite)

Treatments (without bentonite)	Carbon Dioxide (µmoles/sample) Incubation Time (Days)								
	6	120	317	399	593	804	2553	3009	3334
Control									
Empty bottle	4.05	4.97	4.96	4.94	4.87	2.71	2.68	2.94	3.07
Blank (tube+brine only)	4.18	4.64	4.54	4.63	3.00	2.76	2.74	3.50	3.48
No cellulose (salt / inoculum/ tube+brine)	7.93 ± 0.19	14.0 ± 0.1	10.7 ± 0.3	9.21 ± 0.06	6.28 ± 0.22	3.61 ± 0.18	3.55 ± 0.2	2.89 ± 0.08	2.87 ± 0
Carbon Source: Cellulose Only									
Unamended uninoculated	7.45 ± 0.21	10.7 ± 0.2	12.2 ± 0.7	12.2 ± 0.9	11.2 ± 1.5	8.96 ± 1.82	8.73 ± 2.43	7.40 ± 1.66	5.99 ± 1.14
Unamended inoculated	11.7 ± 0.1	56.0 ± 4.4	72.6 ± 11.4	65.5 ± 11.5	45.3 ± 8.1	27.6 ± 5.3	12 ± 3.25	10.4 ± 2.68	8.96 ± 2.41
Amended uninoculated	14.0 ± 1.1	28.1 ± 0.8	24.1 ± 1.8	22.9 ± 2.6	17.4 ± 3.1	12.2 ± 2.7	6.08 ± 1.78	6.23 ± 1.88	5.94 ± 1.88
Amended inoculated	35.9 ± 1.3	42.4 ± 1.5	31.1 ± 2.4	24.8 ± 2.9	14.7 ± 2.4	8.21 ± 1.75	4.48 ± 1.09	3.96 ± 0.56	3.35 ± 0.29
Carbon Source: Cellulose + Glucose									
Amended uninoculated	12.7 ± 0.4	32.7	39.7 ± 0.6	38.6 ± 1.2	35.0 ± 3.07	26.5 ± 4.5	29.83 ± 5.84	28.4 ± 10	NA
Amended inoculated	28.3 ± 1.6	183 ± 98	236 ± 140	166 ± 96	79.8 ± 39.8	28.2 ± 9.0	9.1 ± 1.46	8.41 ± 2.77	NA
Amended uninoculated (RG salt)	NA	36.0	44.8 ± 0.1	46.5 ± 0.1	47.4 ± 2.6	39.4 ± 5.6	56.81 ± 3.99	61.0 ± 5.8	NA
Carbon Source: Cellulose + Succinate									
Amended uninoculated (w/ acetylene)	15.1	NA	28.8	27.7	21.0	16.8	22.12	NA	NA
Amended uninoculated (w/o acetylene)	15.7	26.0	22.7	19.7	14.4	7.06	4.75	3.25	NA
Amended inoculated (w/ acetylene)	14.5	NA	1384	1450	1470	1270	NA	NA	NA
Amended inoculated (w/o acetylene)	15.8	42.4	40.0	38.2	29.5	23.6	16.86	11.3	NA

RG salt = reagent grade NaCl was used in this treatment in place of WIPP salt
NA=not analyzed
3334 day data from notebook JG121101

Table 4. Production of Carbon Dioxide in Initially Aerobic Humid Treatments (with bentonite)

Treatments (with bentonite)	Carbon Dioxide (µmoles/sample) Incubation Time (Days)								
	6	120	317	399	593	804	2553	3009	3334
Control									
Empty bottle	4.05	4.97	4.96	4.94	4.87	2.71	2.68	2.94	3.07
Blank (tube+brine only)	4.18	4.64	4.54	4.63	3.00	2.76	2.74	3.50	3.48
No cellulose (salt / inoculum/ tube+brine)	34.2 ± 0.8	164 ± 1	168 ± 8	144 ± 4	89.1 ± 0.8	42.3 ± 3.0	16.13 ± 4.52	13.6 ± 4	10.6 ± 2.5
Carbon Source: Cellulose Only									
Unamended uninoculated	9.15 ± 0.58	12.1 ± 0.6	13.2 ± 0.6	13.1 ± 0.3	11.0 ± 0.5	9.82 ± 0.15	9.98 ± 1.15	10.5 ± 0.3	10.2 ± 0.3
Unamended inoculated	20.7 ± 0.0	172 ± 5	273 ± 25	268 ± 44	219 ± 61	184 ± 76	233 ± 152	258 ± 180	311 ± 228
Amended uninoculated	15.2 ± 0.9	52.2 ± 1.8	49.9 ± 1.1	45.1 ± 2.4	33.2 ± 4.2	23.1 ± 5.5	22.1 ± 6.29	15.1 ± 6.9	12.0 ± 6.0
Amended inoculated	53.7 ± 2.4	1030 ± 80	1620 ± 30	1600 ± 40	1520 ± 40	1469.8 ± 40	1059 ± 207	858 ± 219	626 ± 250
Carbon Source: Cellulose + Glucose									
Amended uninoculated	14.8 ± 0.5	46.3	590 ± 364	625 ± 394	694 ± 438	631 ± 401	53.8 ± 26.3	50.5 ± 27.5	NA
Amended inoculated	44.9 ± 2.6	1590 ± 40	1240 ± 20	1250 ± 160	1240 ± 240	816 ± 355	964 ± 230	n/a ±	NA
Amended uninoculated (RG salt)	NA	39.5	50.9 ± 1.3	54.6 ± 2.4	55.7 ± 6.7	45.7 ± 8.6	82.0 ± 37.0	90.7 ± 45.3	NA
Carbon Source: Cellulose + Succinate									
Amended uninoculated (w/ acetylene)	22.9	NA	50.0	50.8	46.1	38.9	27.8	27.7	NA
Amended uninoculated (w/o acetylene)	21.7	47.7	50.4	46.8	43.6	37.3	34.0	30.3	NA
Amended inoculated (w/ acetylene)	38.5	NA	1430	1470	1540	1460	NA	NA	NA
Amended inoculated (w/o acetylene)	52.8	1130	1460	1500	1520	1400	631	320	NA

RG salt = reagent grade NaCl was used in this treatment in place of WIPP salt
NA=not analyzed
3334 day data from notebook JG121101

Table 5. Summary of Carbon Dioxide Production per gram Cellulose in Initially Aerobic Humid Treatments (including corrected data)

Treatments ***without bentonite***	Carbon Dioxide (µmoles/ gram cellulose) Incubation Time (Days) 6	120	317	399	593	804	2553	3009	3334
Control									
No cellulose (salt/ inoculum/ tube+brine)	7.93 ± 0.19	14.0 ± 0.1	10.7 ± 0.3	9.21 ± 0.06	6.38 ± 0.22	3.61 ± 0.18	3.55 ± 0.2	2.89 ± 0.08	2.87 ± 0
Carbon Source: Cellulose									
Unamended inoculated	11.7 ± 0.1	56.0 ± 4.4	72.6 ± 11.4	65.5 ± 11.5	45.3 ± 8.1	27.6 ± 5.3	12.0 ± 3.25	10.4 ± 2.68	8.96 ± 2.41
Amended Inoculated	35.9 ± 1.3	42.4 ± 1.5	31.1 ± 2.4	24.8 ± 2.9	14.7 ± 2.4	8.21 ± 1.75	4.48 ± 1.09	3.96 ± 0.56	3.35 ± 0.29
*Unamended inoculated (corrected)**	3.77 ± 0.22	42.1 ± 4.4	62.0 ± 11.4	56.3 ± 11.5	38.9 ± 8.1	24.0 ± 5.3	8.45 ± 3.26	7.51 ± 2.68	6.09 ± 2.41
*Amended inoculated (corrected)**	28.0 ± 1.3	28.5 ± 1.5	20.5 ± 2.4	15.6 ± 2.9	8.32 ± 2.41	4.60 ± 1.76	0.93 ± 1.11	1.07 ± 0.57	0.48 ± 0.29

Treatments ***with bentonite***	Carbon Dioxide (µmoles/ gram cellulose) Incubation Time (Days) 6	120	317	399	593	804	2553	3009	3334
Control									
No cellulose (salt/ inoculum/ tube+brine)	34.2 ± 0.8	164 ± 1	168 ± 8	144 ± 4	89.1 ± 0.8	42.3 ± 3	16.13 ± 4.52	13.6 ± 4.0	10.6 ± 2.5
Carbon Source: Cellulose									
Unamended inoculated	20.7 ± 0.0	172 ± 5	273 ± 25	268 ± 44	219 ± 61	184 ± 76	233 ± 152	258 ± 180	311 ± 228
Amended inoculated	53.7 ± 2.4	1033 ± 76	1623 ± 26	1600 ± 44	1520 ± 40	1470 ± 40	1059 ± 207	858 ± 219	626 ± 250
*Unamended inoculated (corrected)**	-13.5 ± 0.8	8.00 ± 5.41	105 ± 26	124 ± 44	130 ± 61	142 ± 76	217 ± 152	244 ± 180	300 ± 228
*Amended inoculated (corrected)**	19.5 ± 2.5	869 ± 76	1455 ± 28	1456 ± 44	1431 ± 40	1428 ± 40	1043 ± 207	844 ± 219	615 ± 250

** These samples have been corrected with the appropriate control for gas production in the absence of cellulose*

Table 6. Total Volume of Gas Produced in Anaerobic Humid Treatments (without bentonite)

Treatments (without bentonite)	Total Volume of Gas Produced (ml/sample)													
	Days													
	6	*100*	gas produced* (94 d)	*140*	gas produced (40d)	*415*	gas produced (275 d)	*2156*	gas produced (1741 d)	*2616*	gas produced (460 d)	*2945*	gas produced (329 d)
Control													
Empty bottle	7.98 ± 0.59	4.82 ± 0.54	-3.36	3.61 ± 0.66	-1.01	2.01 ± 1.04	-1.60	0.72	-1.29	0.29	-0.43	2.51 ± 0.46	2.22
Blank (tube+brine only)	6.85 ± 0.38	3.81 ± 0.34	-3.04	2.80 ± 0.27	-1.01	0.37 ± 1.02	-2.43	-0.89	-1.26	n/a		-0.85 ± 0.11	
No cellulose (salt/ inoculum/ tube+brine)	6.49 ± 0.04	3.07 ± 0.07	-3.42	1.56 ± 0.63	-1.51	2.76 ± 0.88	1.20	5.53	2.77	2.33	-3.20	-0.57 ± 0.93	-2.90
Carbon Source: Cellulose Only													
Unamended uninoculated	7.33 ± 0.80	1.59 ± 1.25	-5.74	0.01 ± 1.07	-1.58	-2.26 ± 0.17	-2.27	0.09 ± 0.18	2.35	2.51 ± 0.59	2.42	-0.84 ± 0.73	-3.15
Unamended inoculated	9.49 ± 0.45	2.40 ± 1.23	-7.09	1.17 ± 1.39	-1.23	-0.28 ± 1.23	-1.45	2.00 ± 1.02	2.28	1.42 ± 0.58	-0.58	-0.50 ± 0.31	-1.92
Amended uninoculated	7.50 ± 0.13	0.93 ± 1.25	-6.57	-0.92 ± 1.12	-1.85	-1.87 ± 0.24	-0.95	1.70 ± 1.05	3.57	1.86 ± 1.01	0.16	-0.57 ± 0.74	-2.43
Amended inoculated	7.64 ± 0.37	0.89 ± 0.69	-6.75	-0.54 ± 1.03	-1.43	-1.07 ± 1.15	-0.53	0.43 ± 0.00	1.50	0.19 ± 0.15	-0.24	1.48 ± 1.14	1.29
Amended inoculated (w/ acetylene)	20.4 ± 0.1	16.6 ± 0.6	-3.87	14.95 ± 0.48	-1.61	7.15 ± 5.15	-7.80	0.32 ± 0.08	-6.83	0.25 ± 0.23	-0.07	NA	
Carbon Source: Cellulose + Glucose													
Amended uninoculated	6.55 ± 0.63	3.82 ± 0.73	-2.73	2.07 ± 0.86	-1.75	-0.51 ± 0.44	-2.58	2.50 ± 0.62	3.01	1.57 ± 0.62	-0.93	NA	
Amended inoculated	7.18 ± 0.04	4.83 ± 0.11	-2.35	1.77 ± 1.10	-3.06	0.68 ± 1.90	-1.09	3.27 ± 1.74	2.59	2.34 ± 1.89	-0.93	NA	
Amended uninoculated (RG salt)	6.60 ± 0.00	2.35 ± 1.90	-4.25	0.18 ± 2.28	-2.17	0.09 ± 1.48	-0.09	3.83 ± 0.51	3.74	1.27 ± 0.15	-2.56	NA	
Carbon Source: Cellulose + Succinate													
Amended uninoculated (w/ acetylene)	18.9 ± 0.1	10.8 ± 4.1	-8.11	3.66 ± 1.90	-7.15	8.11 ± 5.24	4.45	NA	NA	1.60		NA	
Amended uninoculated (w/o acetylene)	8.30 ± 0.19	4.50 ± 0.29	-1.80	4.21 ± 0.37	-0.29	2.49 ± 1.80	-1.72	8.69	6.20	NA		NA	
Amended inoculated (w/ acetylene)	18.7 ± 0.1	7.27 ± 6.63	-11.46	6.83 ± 6.43	-0.44	6.46 ± 4.32	-0.37	5.70 ± 3.19	-0.76	3.25	-2.45	NA	
Amended inoculated (w/o acetylene)	5.67 ± 0.04	1.70 ± 1.72	-3.97	0.67 ± 1.71	-1.03	2.46 ± 1.61	1.79	7.05	4.59	NA		NA	

RG salt = reagent grade NaCl was used in this treatment in place of WIPP salt
NA=not analyzed
*net gas produced between two time periods (duration between analyses given in parentheses).
2945 day data from notebook JG121101

Table 7. Total Volume of Gas Produced in Anaerobic Humid Treatments (with bentonite)

Treatments (with bentonite)	Total Volume of Gas Produced (ml/sample)													
	Days													
	6	100	gas produced* (94 d)	140	gas produced (40 d)	415	gas produced (275 d)	2156	gas produced (1741 d)	2616	gas produced (460 d)	2945	gas produced (329 d)
Control													
Empty bottle	7.98 ± 0.59	4.62 ± 0.54	-3.36	3.61 ± 0.66	-1.01	2.01 ± 1.04	-1.60	0.72	-1.29	0.29	-0.43	2.51 ± 0.46	2.22
Blank (tube+brine only)	6.85 ± 0.38	3.81 ± 0.34	-3.04	2.80 ± 0.27	-1.01	0.37 ± 1.02	-2.43	-0.89	-1.26	n/a		-0.85 ± 0.11	
No cellulose (salt/ inoculum/ tube+brine)	6.18 ± 0.19	4.60 ± 0.37	-1.58	0.87 ± 1.85	-3.73	1.93 ± 0.37	1.06	-1.79	-3.72	0.78	2.57	-0.83 ± 0.11	-1.61
Carbon Source: Cellulose Only													
Unamended uninoculated	7.22 ± 0.25	2.91 ± 0.90	-4.31	1.40 ± 1.22	-1.51	-0.65 ± 1.05	-2.05	0.98 ± 0.52	1.63	-1.04 ± 0.28	-2.02	0.00 ± 0.79	1.04
Unamended inoculated	6.63 ± 0.03	6.36 ± 1.22	-0.27	5.86 ± 3.11	-0.50	11.22 ± 5.42	5.36	6.37 ± 2.06	-4.85	-0.59 ± 0.62	-6.96	-3.09 ± 0.50	-2.50
Amended uninoculated	6.18 ± 0.08	3.72 ± 0.51	-2.46	1.57 ± 1.11	-2.15	-0.79 ± 1.06	-2.36	1.05 ± 0.47	1.84	2.92 ± 0.56	1.87	-1.24 ± 0.63	-4.16
Amended inoculated	6.81 ± 0.12	10.4 ± 1.7	3.59	15.31 ± 1.70	4.91	8.60 ± 2.97	-6.71	2.58 ± 1.49	-6.02	1.52 ± 0.20	-1.06	-2.19 ± 1.18	-3.71
Amended inoculated (w/ acetylene)	18.2 0.3	17.2 ± 0.3	-1.02	15.54 ± 0.74	-1.61	7.32 ± 5.11	-8.22	8.16 ± 4.20	0.84	6.22 ± 2.44	-1.94	NA	
Carbon Source: Cellulose + Glucose													
Amended uninoculated	7.18 ± 0.04	3.18 ± 1.10	-4.00	-0.39 ± 0.77	-3.57	-1.91 ± 0.00	-1.52	0.19	2.10	-0.43	-0.62	NA	
Amended inoculated	6.97 ± 0.11	9.79 ± 3.73	2.82	7.87 ± 4.78	-1.92	7.46 ± 6.62	-0.41	7.73 ± 4.82	0.27	7.73 ± 4.53	0.00	NA	
Amended uninoculated (RG salt)	7.18 ± 0.14	5.51 ± 0.04	-1.67	3.27 ± 0.29	-2.24	2.43 ± 0.95	-0.84	6.23 ± 1.15	3.80	5.01 ± 0.94	-1.22	NA	
Carbon Source: Cellulose + Succinate													
Amended uninoculated (w/ acetylene)	19.9 ± 0.4	8.36 ± 2.14	-11.52	4.75 ± 3.05	-3.61	-1.54 ± 0.03	-6.29	2.34 ± 0.62	3.88	1.51 ± 0.10	-0.83	NA	
Amended uninoculated (w/o acetylene)	7.91 ± 0.48	4.26 ± 1.10	-3.65	3.20 ± 1.03	-1.06	3.86 ± 0.24	0.66	3.37 ± 2.03	-0.49	2.86 ± 1.60	-0.51	NA	
Amended inoculated (w/ acetylene)	19.6 ± 0.1	16.7 ± 0.5	-2.89	8.59 ± 4.01	-8.12	5.36 ± 5.00	-3.23	10.04	4.68	1.46	-8.58	NA	
Amended inoculated (w/o acetylene)	6.76 ± 0.18	10.2 ± 0.3	3.42	10.41 ± 1.22	0.23	3.84 ± 1.94	-6.57	-0.53	-4.37	0.50	1.03	NA	

RG salt = reagent grade NaCl was used in this treatment in place of WIPP salt
NA=not analyzed
*net gas produced between two time periods (duration between analyses given in parentheses).
2945 day data from notebook JG121101

Table 8. Production of Carbon Dioxide in Anaerobic Humid Samples (without bentonite)

Treatments (without bentonite)	µmoles CO_2/Sample						
	Days						
	6	100	140	415	2156	2616	2945
Control							
Empty bottle	0.00 ± 0.00	0.68 ± 0.48	1.34 ± 0.95	0.00 ± 0.00	4.13	1.84	1.80 ± 0.09
Blank (tube+brine only)	0.00 ± 0.00	0.32 ± 0.22	0.00 ± 0.00	0.00 ± 0.00	2.14	2.39	2.37 ± 0.04
Salt / inoculum/ tube+brine (no cellulose)	3.60 ± 0.01	5.90 ± 0.11	7.63 ± 1.08	16.4 ± 0.6	8.35	6.81	5.38 ± 1.97
Carbon Source: Cellulose Only							
Unamended uninoculated	4.07 ± 0.09	5.44 ± 0.10	6.22 ± 0.82	8.05 ± 0.18	15.8 ± 0.46	17.7 ± 0.3	16.5 ± 0.8
Unamended inoculated	11.3 ± 0.12	25.9 ± 3.8	36.1 ± 7.0	89.0 ± 24.4	163 ± 36	142 ± 28	120 ± 20
Amended uninoculated	3.34 ± 0.22	34.3 ± 1.44	39.8 ± 0.9	32.3 ± 1.5	13.5 ± 2.76	31.2 ± 7.0	25.1 ± 8.0
Amended inoculated	16.9 ± 1.15	36.4 ± 0.8	40.4 ± 0.8	34.7 ± 0.9	18.2 ± 1	33.6 ± 1.0	27.3 ± 2.7
Amended inoculated (w/ acetylene)	13.7 ± 1.3	38.5 ± 2.2	42.7 ± 2.5	61.0 ± 16.9	47.3 ± 17	76.5 ± 27.0	n/a
Carbon Source: Cellulose + Glucose							
Amended uninoculated	3.34 ± 0.27	23.5 ± 1.6	31.3 ± 0.0	38.6 ± 2.1	42.9 ± 5.2	54.9 ± 8.9	NA
Amended inoculated	17.7 ± 0.47	39.8 ± 0.2	42.2 ± 0.9	41.8 ± 4.2	52.8 ± 10.8	58.9 ± 12.2	NA
Amended uninoculated (RG salt)	4.07 ± 0.37	19.8 ± 2.4	28.9 ± 0.6	26.3 ± 2.9	47.8 ± 12.3	48.2 ± 19.7	NA
Carbon Source: Cellulose + Succinate							
Amended uninoculated (w/ acetylene)	3.21 ± 0.04	22.5 ± 0.8	29.4 ± 2.5	28.8 ± 3.0	NA	33.8 ± 7.2	NA
Amended uninoculated (w/o acetylene)	3.19 ± 0.18	21.4 ± 0.2	27.9 ± 0.5	34.1 ± 2.5	984	NA	NA
Amended inoculated (w/ acetylene)	13.5 ± 0.7	78.1 ± 33.4	123 ± 63	308 ± 175	99.8	133 ± 79	NA
Amended inoculated (w/o acetylene)	14.8 ± 0.2	60.5 ± 16.0	106 ± 21	328 ± 78	1034	NA	NA

RG salt = reagent grade NaCl was used in this treatment in place of WIPP salt
n/a =not analyzed
2945 day data from notebook JG121101

Table 9. Production of Carbon Dioxide in Anaerobic Humid Samples (with bentonite)

Treatments (with bentonite)	µmoles CO_2/Sample						
	Days						
	6	100	140	415	2156	2616	2945
Control							
Empty bottle	0.00 ± 0.00	0.68 ± 0.48	1.34 ± 0.95	0.00 ± 0.00	4.13	1.84	1.80 ± 0.09
Blank (tube+brine only)	0.00 ± 0.00	0.32 ± 0.22	0.00 ± 0.00	0.00 ± 0.00	2.14	2.39	2.37 ± 0.04
Salt / inoculum/ tube+brine (no cellulose)	14.2 ± 0.51	36.6 ± 6.1	39.8 ± 5.5	51.6 ± 3.4	93.8	59.21 ± 14.1	63.9 ± 11.8
Carbon Source: Cellulose Only							
Unamended uninoculated	5.04 ± 0.15	12.1 ± 3.2	14.4 ± 3.6	26.5 ± 8.9	37.6 ± 19.1	70.5 ± 36.4	80.7 ± 40.6
Unamended inoculated	20.3 ± 0.2	93.7 ± 2.6	186 ± 6	434 ± 39	483 ± 133	650 ± 175	605 ± 134
Amended uninoculated	6.65 ± 0.80	39.2 ± 1.5	45.5 ± 1.5	49.6 ± 1.6	41.7 ± 3.2	70.3 ± 4.3	67.1 ± 10.1
Amended inoculated	32.2 ± 1.1	250 ± 30	473 ± 25	442 ± 152	554 ± 35.7	732 ± 47	682 ± 124.0
Amended inoculated (w/ acetylene)	26.8 ± 0.7	94.0 ± 18.6	123 ± 30	251 ± 92	558 ± 270	609 ± 273	NA
Carbon Source: Cellulose + Glucose							
Amended uninoculated	6.71 ± 0.12	44.5 ± 0.2	53.1 ± 0.4	64.3 ± 1.0	177	201 ± 4	NA
Amended inoculated	31.4 ± 0.7	396 ± 13	487 ± 1	584 ± 28	754 ± 94	641 ± 16	NA
Amended uninoculated (RG salt)	5.28 ± 0.45	45.9 ± 0.7	55.1 ± 1.4	74.9 ± 2.2	178 ± 3	209 ± 1	NA
Carbon Source: Cellulose + Succinate							
Amended uninoculated (w/ acetylene)	5.77 ± 0.60	0.00 ± 0.00	41.5 ± 3.1	36.7 ± 0.9	48.5 ± 0.5	75.0 ± 6.3	NA
Amended uninoculated (w/o acetylene)	8.58 ± 0.74	44.9 ± 1.6	51.5 ± 1.0	54.0 ± 2.0	79.4 ± 3.4	44.8 ± 0.6	NA
Amended inoculated (w/ acetylene)	27.7 ± 0.27	70.3 ± 2.7	114 ± 0	324 ± 30	447	568	NA
Amended inoculated (w/o acetylene)	28.0 ± 0.82	237 ± 2	317 ± 6	516 ± 0	1356	944 ± 110	NA

RG salt = reagent grade NaCl was used in this treatment in place of WIPP salt
NA=not analyzed
2945 day data from notebook JG121101

Table 10. Summary of Carbon Dioxide Production per gram Cellulose in Anaerobic Humid Samples

Treatments ***without bentonite***	*Carbon dioxide (µmoles/ gram cellulose)* Days						
	6	100	140	415	2156	2616	2945
Control							
No cellulose (salt/ inoculum/ tube+brine)	3.60 ± 0.01	5.9 ± 0.1	7.64 ± 1.08	16.4 ± 0.6	8.35	6.81	5.38 ± 1.97
Carbon Source: Cellulose							
Unamended inoculated	11.3 ± 0.1	25.9 ± 3.8	36.1 ± 7	89 ± 24.4	163 ± 36	142 ± 28	120 ± 20
Amended inoculated	16.9 ± 1.2	36.4 ± 0.8	40.4 ± 0.8	34.7 ± 0.9	18.2 ± 1.0	33.6 ± 1.0	27.3 ± 2.7
*Unamended inoculated (corrected)**	7.70 ± 0.12	20.0 ± 3.8	28.5 ± 7.1	72.6 ± 24.4	155 ± 36	135 ± 28	115 ± 20
*Amended inoculated (corrected)**	13.3 ± 1.2	30.5 ± 0.8	32.8 ± 1.3	18.3 ± 1.1	9.9 ± 1.0	26.8 ± 1.0	21.9 ± 3.3

Treatments ***with bentonite***	*Carbon dioxide (µmoles/ gram cellulose)* Days						
	6	100	140	415	2156	2616	2945
Control							
No cellulose (salt/ inoculum/ tube+brine)	14.2 ± 0.5	36.6 ± 6.1	39.8 ± 5.5	51.6 ± 3.4	93.8	59.2 ± 14.1	63.9 ± 11.8
Carbon Source: Cellulose							
Unamended inoculated	20.3 ± 0.2	94 ± 3	186 ± 6	434 ± 39	483 ± 133	650 ± 175	605 ± 134
Amended inoculated	32.2 ± 1.1	250 ± 30	473 ± 25	442 ± 152	554 ± 35.7	732 ± 47	682 ± 124
*Unamended inoculated (corrected)**	6.10 ± 0.55	57.1 ± 6.6	146 ± 8	382 ± 39	389 ± 133	591 ± 176	541 ± 135
*Amended inoculated (corrected)**	18.0 ± 1.2	213 ± 31	433 ± 26	390 ± 152	460 ± 36	673 ± 49	618 ± 125

** These samples have been corrected with the appropriate control for gas production in the absence of cellulose*

3.2 Experimental Study of Microbial Gas Generation Under WIPP-Relevant Humid Conditions[1]

Yifeng Wang
Sandia National Laboratories, MS 1395
4100 National Parks Highway
Carlsbad, NM 88220 USA

This test plan, which appears on the SNL NWMP website as TP-02-06, describes humid microbial gas-generation experiments to be carried at SNL in Carlsbad.

[1] This work is covered by WBS #1.3.5.4.1.1

Sandia National Laboratories
Waste Isolation Pilot Plant
Test Plan TP-02-06

Experimental Study of Microbial Gas Generation Under WIPP-Relevant Humid Conditions

WBS 1.3.5.4.1

Revision 1

Effective Date: 07/25/02

Prepared by:

Y. Wang, 6822
Principal Investigator
WIPP Repository Performance
& Certification Department

WIPP:1.3.5.4.1:TD:QA:DPRP1:NF:CHEMISTRY:MICROBIAL GAS GENERATION; TP-02-06

APPROVAL PAGE

Prepared by:	*Original signed by Yifeng Wang* Y. Wang, 6822 WIPP Repository Performance & Certification Department	*7/24/02* Date
Technical Reviewer	*Original signed by Nathalie Wall* Nathalie Anne Wall, 6822 WIPP Repository Performance & Certification Department	*7/24/02* Date
QA Reviewer	*Original signed by M. Mitchell* Marty Mitchell, 6820 Carlsbad Programs Group	*7/24/02* Date
Responsible NWMP Manager	*Original signed by F.D. Hansen* F. D. Hansen, 6822 Acting Manager WIPP Repository Performance & Certification Department	*7/24/02* Date

TABLE OF CONTENTS

1.0 DEFINITION OF ACRONYMS

ASTM	American Society for Testing and Materials
BNL	Brookhaven National Laboratory
CCA	Compliance Certification Application
CBFO	Carlsbad Field Office
CRA	Compliance Recertification Application
DAS	Data acquisition system
DOE	Department of Energy
EPA	Environmental Protection Agency
GC-MS	Gas chromatography – mass spectrometer
ICP-OES	Inductively coupled plasma optical emission spectrometer
MGGP	Microbial Gas Generation Program
M&TE	Measuring and test equipment
NIST	National Institute of Standards and Technology
NWMP	Nuclear Waste Management Program
NP	Nuclear Waste Management Program Procedure
PA	Performance assessment
QA	Quality assurance
SNL	Sandia National Laboratories
SOP	Standard Operating Procedure
SP	NWMP Activity/Project Specific Procedure
TOP	Technical Operating Procedure
TP	Test plan
WIPP	Waste Isolation Pilot Plant

2.0 REVISION HISTORY

The original test plan was issued on June 28, 2002. This is the first revision of the test plan. This revision includes a more detailed description of microbe cell counting methods.

3.0 PURPOSE AND WORK SCOPE

The transuranic wastes destined to the Waste Isolation Pilot Plant (WIPP) contain a large quantity of cellulosics, plastics, and rubbers, which may potentially be degraded by microorganisms in the repository over a regulatory time period of 10,000 years via the following sequential reactions (Wang and Brush, 1996):

$$C_6H_{10}O_5 + 4.8H^+ + 4.8NO_3^- \rightarrow 7.4H_2O + 6CO_2 + 2.4N_2 \quad (1)$$

$$C_6H_{10}O_5 + 6H^+ + 3SO_4^{2-} \rightarrow 5H_2O + 6CO_2 + 3H_2S \quad (2)$$

$$C_6H_{10}O_5 + H_2O \rightarrow 3CH_4 + 3CO_2. \quad (3)$$

Gas generation from biodegradation and metal corrosion would pressurize the WIPP repository, which could lead to an increase in spalling and direct release of radionuclides in the event of human intrusions (Helton et al., 1998). The CO_2 generated from microbial reactions will reduce the pH of WIPP brines and provide additional carbonate ions for actinide complexation, thus resulting in the potential for increased actinide mobility in the repository. To mitigate the effect of microbial gas generation on brine chemistry, an MgO engineered barrier has been designed to sequester CO_2 from aqueous and gaseous phases in the repository (Wang et al., 1997).

The WIPP microbial gas generation program (MGGP) was designed to establish defensible microbial degradation rates for the WIPP Compliance Certification Application (CCA), which was submitted to the Environmental Protection Agency (EPA) in 1996 and approved in 1998. After the CCA submission, the Department of Energy Carlsbad Field Office (DOE/CBFO) decided to continue the MGGP with an objective to increase confidence in the CCA gas generation model and provide more realistic long-term rates for WIPP Compliance Recertification Applications (CRA), because a sensitivity analysis based on the CCA calculations has shown that microbial gas generation rates are among the most sensitive parameters for WIPP long-term performance (Helton et al., 1998). Over the last 10 years, Brookhaven National Laboratory (BNL) has been responsible for the experimental part of the MGGP, while Sandia National Laboratories (SNL) has provided the overall technical guidance and the integration of the experimental data into the performance assessment (PA) models. More background information can be found in two test plans (Brush, 1990; Francis et al., 2001) and various technical reports (Francis and Gillow, 1994, 2000; Wang and Brush, 1996; Francis et al., 1997; Wang et al., 1997; Gillow and Francis, 2001a, 2001b, 2002).

The rate of microbial degradation under humid conditions is an important parameter for the prediction of gas generation for a time period when the repository is not inundated. The existing rate was derived from the BNL "humid" experiments, in which liquid inocula were directly added to cellulosic materials and the humidity of the samples was maintained by placing a glass tube containing G-Seep brine (water activity $a_w = 0.73$, Francis et al., 1997, p. 17) inside each incubation bottle (Francis et al., 1997). The addition of liquid inocula might have artificially increased the water content in cellulosic materials and thus induced a high humid biodegradation rate as observed. A high rate for humid microbial gas generation currently implemented in performance assessment calculations contributes, to a large extent, to the calculated pressure buildup in the repository before a human intrusion and therefore to the spalling and direct release of radionuclides. The spalling release requires the gas pressure to be higher than ~ 80 atm.

In reality, the humid degradation rate is expected to be very low, if not zero. A preliminary natural analog study indicates that the cellulosic materials that have been placed in the Eddy Potash Mine for over 40 years have experienced practically no biodegradation at all under humid conditions (Xu, 2001). For the WIPP, the emplacement of MgO backfill will significantly reduce the water vapor pressure in waste disposal rooms by hydration reaction:

$$MgO + H_2O = Mg(OH)_2. \quad (4)$$

The water activity (a_w) buffered by this reaction is calculated to be $10^{-6.3}$ atm, based on thermodynamic data from Robie et al. (1978). The actual water activity in the repository, which will ultimately be controlled by the relative rates of both brine inflow and MgO hydration, is expected to be much lower than that established by WIPP brines, about 0.7 (Brush, 1990). An abundance of laboratory and field data imply that the minimum water activity required by microorganisms in soils is about 0.6, below which microbial activities are significantly inhibited (Kral and Cousin, 1981; Donnelly et al., 1990; Nizovtseva et al., 1995; Barros et al., 1995; Stark and Firestone, 1995; Cattaneo et al., 1997). Based on all these considerations, it is believed that the humid rate for a WIPP environment should be close to zero and thus the gas generation under humid conditions has been overestimated in the existing PA calculations.

The experiments described in this test plan will focus on the further determination of the rate of microbial gas generation under WIPP-relevant humid conditions by improving the previous experimental procedure. Two major improvements will be made: (1) the extra water introduced into samples by adding liquid inocula will be removed before the start of the incubation experiments; (2) the samples will be maintained at various levels of humidity by using different salt-saturated brines. The results obtained from these experiments will directly support the DOE-proposed modifications to microbial gas generation rates for WIPP CRA.

The work described in this test plan is a natural extension of the existing BNL gas generation studies and will be conducted at SNL-Carlsbad Geochemical Laboratory. Over the past 10 years, BNL has gained a great deal of experience in dealing with WIPP-

related microbial issues. Therefore, the technical assistance from the BNL personnel (A.J. Francis and Jeff Gillow) will be essential for the success of the planned work. The assistance will include the development of appropriate inocula, microbial characterization, experimental design, and data interpretation.

4.0 EXPERIMENTAL PROCESS DESCRIPTION

4.1 Overall Strategy and Process

The following experimental setup and procedure are modified from the BNL microbial gas generation experiments (Francis and Gillow, 1994; Francis et al., 1997).

Experimental setup. The experimental setup for humid incubation will consist of a 160-mL serum bottle and a glass tube placed inside the bottle[1]. The glass tube in each sample will contain an equal volume of salt-saturated brine to maintain a constant humidity in the serum bottle. Cellulosic materials will be placed on the bottom of the bottle. Caution will be taken to avoid any spills of the brine onto the cellulosic materials. The serum bottles will be closed with butyl rubber stoppers. The headspace volume of the samples will be determined by measuring the volume of water needed to fill the whole bottle.

It is anticipated that the WIPP repository will become anoxic shortly after room closure. To simulate the repository condition, all samples need to be incubated under anaerobic conditions. All solutions will be purged with Ar gas before use. The headspace of each sample will be purged with Ar gas before it is tightly sealed. All of the samples will be prepared and sampled inside a glove box purged with Ar gas.

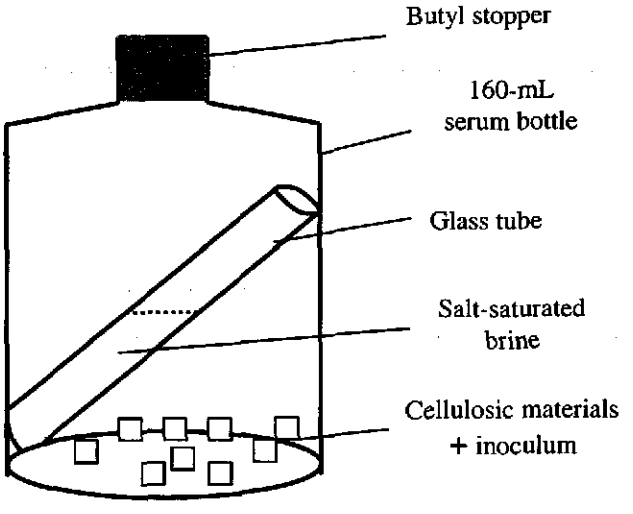

Figure 1. Experimental setup for determining the rate of microbial gas generation under humid conditions.

[1] Other size bottles can be used if 160 mL ones are not available.

Substrates. Cellulosic materials in WIPP wastes consist of ~ 70% of papers and ~ 26% of various woods (Brush, 1990, p. 54). A mixture of four types of papers will be used in the majority of incubation samples: filter paper (Whatman #1™), white paper towel (Fort Howard), brown paper towel, and Kimwipes™ (Kimberly-Clark, lintless tissue wipes). These four types of materials are identical to those used in the BNL experiments. The papers will be shredded into 1-cm-x-1-cm squares. Each type of paper will be weighed (0.25 g), mixed thoroughly, and transferred to serum bottles that have been acid-washed (10% HCl) and sterilized (autoclaved at 120°C for 20 min). A small set of samples will use shredded woods (e.g., saw dust) (1.0 g/sample) rather than papers for a comparison of the biodegradability of papers and woods. In each sample, 1.0 g of cellulosic materials will be mixed with 5.0 g of either crushed WIPP muck pile salt or reagent-grade NaCl.

Inocula. The same inocula will be used as those developed for the BNL experiments. These inocula were prepared from a mixture of a variety of WIPP-relevant samples (Francis et al., 1997). The use of a mixed inoculum instead of a pure culture ensures that a host of microorganisms are present in the experiment and prevents bias toward one potential gas-generating microbial process. Two mL of the mixed inocula will be pipetted onto cellulosic materials in each sample with a calibrated pipette. Each uninoculated sample will instead receive an equal volume of filter-sterilized (0.2 μm) reagent-grade NaCl solution (20% w/v deionized water). The samples will be dried in a desiccator. An appropriate desiccant (e.g., $CaSO_4$) and the duration of the desiccation will be chosen to ensure the viability of microorganisms after the desiccation. The viability of microorganisms will be tested by first rewetting the sample and then checking if microbes can still grow (Gillow, 1996; Gillow, 1998). A small number of samples will be prepared without desiccation of inocula for clarification of the effect of additional water introduced into samples by adding liquid inocula.

Nutrients and electron acceptors. The samples will be prepared with and without added nutrients. The nutrients added will consist of 0.5 mL of solution containing ammonium nitrate (0.1% w/v), potassium phosphate (0.1% w/v), and yeast extract (0.05%w/v). Unamended samples will receive 0.5 mL of filtered, sterilized reagent-grade salt solution (20% w/v). The nutrient solution will be added to samples before the desiccation of inocula. All samples will be prepared in triplicate. See the treatment matrix for sample preparation in Figure 2.

As shown in Reactions 1 and 2, nitrate and sulfate can serve as electron acceptors for microbial degradation. To bound the concentrations of these components in actual wastes, an extra amount of nitrate and sulfate may need to be added to a selected number of nutrient-amended samples.

Humidity control. A constant humidity will be maintained in the samples by glass tubes containing saturated salt solutions (Figure 1). The following salts will be used to buffer the samples at different humidity levels (Lide, 2002; Brush, 1990):

Relative Humidities of Saturated Salt Solutions

Salt	Relative humidity (%) at 25 °C
WIPP brine	~70
$NaBr.2H_2O$	58
$NaI.2H_2O$	38
$LiCl.H_2O$	11

Ca and Mg salts are excluded because of possible formation of carbonate minerals, which may affect the measurement of CO_2 in the headspace. To minimize the CO_2 uptake by the solution, the pH of the solution will be adjusted to a mildly acid value (e.g., ~ 5). The partition coefficients of gaseous species between the solution and the headspace will be measured and used for the correction for gas dissolution in the solutions.

Incubation. All of the samples will be incubated at ~ 30°C in a temperature-controlled oven over a time period of 3 years.

Inundated samples. A small number of brine-inundated samples will be also prepared. These samples will serve two purposes: (1) one set of these samples will mimic experimental conditions at BNL to provide a consistency check for the data obtained from the work described in this test plan as compared to those obtained at BNL, which is important for deriving a defensible scaling factor for microbial gas generation rates between humid and inundated conditions; (2) by appropriate control of nitrate and sulfate concentrations in synthetic brines, the inundated samples prepared in this work will allow better demonstration of the dependence of the microbial gas generation rate on the identity of the electron acceptor. The treatments of the inundated samples include: (1) 5 g of mixed cellulosic materials, and (2) 100 mL of brine with or without dissolved sulfate. Most of the samples will be amended with nutrients or excess nitrate; some will be unamended for comparison. The amounts of nitrate and sulfate added to the samples will reflect and bound the concentrations of these components in actual wastes. Synthetic G-Seep brine will be used (Brush, 1990):

Composition of G-Seep brine

Major ion	g/L	M
Na^+	95.0	4.11
Cl^-	181	5.10
Mg^{2+}	15.3	0.63
K^+	13.7	0.35
Ca^{2+}	0.32	0.01
SO_4^{2-}	29.1	0.30
HCO_3^-	0.73	0.01

All the samples will be prepared under anoxic conditions.

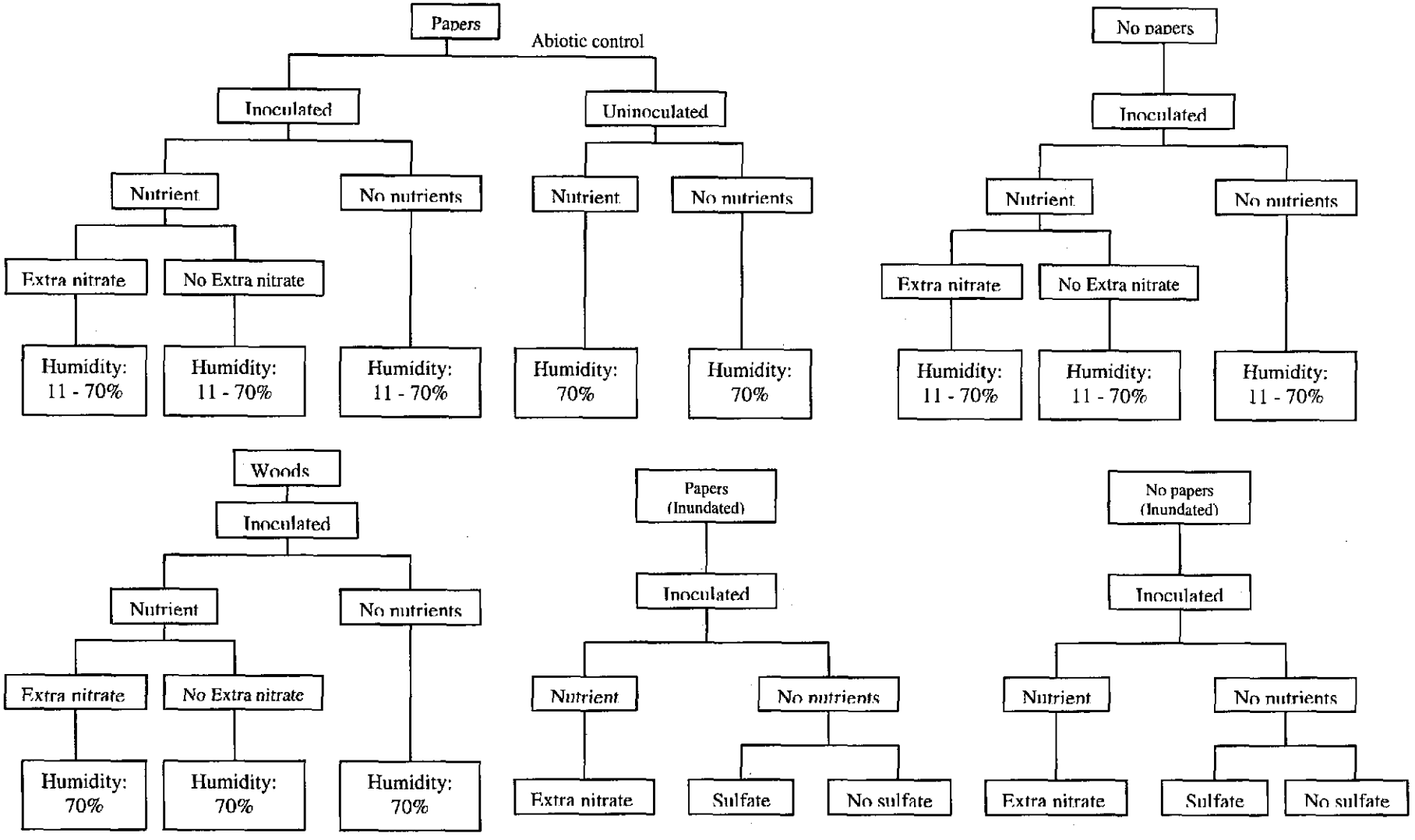

Figure 2. Treatment matrix for samples. Each sample will be prepared in triplicates. At minimum, a total of 105 samples are needed.

Abiotic controls. Samples containing sterilized, reagent-grade NaCl without inoculum will serve as abiotic controls. Cellulosic materials in these samples will be sterilized prior to the experiments. Formalin may also be used for the abiotic controls.

Gas sampling and analysis. The composition of the headspace gas of each sample will be monitored over time. The headspace gas will be sampled at least once a month for the first year and less frequently thereafter depending on the overall gas generation rate. For each sampling, the butyl rubber septum on the serum bottle will be pierced with a sterile, 22-gauge needle (Becton Dickenson) attached to a digital pressure gauge to measure the headspace gas pressure for the calculation of total generated gas. Immediately after this, a gas-tight syringe (Pressure-Lok™, Precision Instrument Corp.) fitted with a stainless-steel side-port needle will be used to take 10 μL of headspace gas to determine the various gases (Ar, CH_4, CO_2, H_2, H_2S, N_2, and O_2) quantitatively by Varian 3900 Gas Chromatography (GC) with a Saturn 2100T Ion Trap Mass Spectrometer (MS). The Rubber stopper will not be replaced after each sampling. It is expected that the gas leakage, if any, from the pierced rubber stopper is negligible, as long as the bottle is not overly pressurized. Ar will be used as an inert gas to check for gas leakage from the serum bottles during the experiments, and its initial concentration will be analyzed immediately after the bottle is closed.

Bacterial counting. Bacterial direct counting will be needed to check the viability of microbes in dried inocula. Microbial cells will be stained with the DNA-specific stain 4'6-diamidino-2-phenylindole (DAPI, Polysciences, Inc.) and will be examined by epi-fluorescence microscopy using Olympus BX60 Polarizing Microscope and UV light source (Kepner and Pratt, 1994; Gillow, 1996, 1998). Alternatively, green-fluorescent nucleic-acid dyes will be used in conjunction with aluminum oxide filters if particulate matter in the dried inoculum complicates microscopic visualization (Weinbauer, 1998). Direct counting may be used as the experiment progresses to detect increases in the microbial population.

Data reduction. Gas generation rates will be determined from total gas volume and individual gas concentrations accumulated with time. The total amount of gas in the headspace determined from the pressure measurement will be compared with that determined from GC-MS to ensure data quality.

4.2 Sample Control

The sample control for the work under this test plan will follow WIPP Nuclear Waste Management Program (NWMP) Procedure NP 13-1. Each sample will be appropriately labeled. Sample preparation, utilization, and final disposition will be documented in scientific notebooks. When samples are not in the possession of individual designated with their custody, they will be stored in a secure area with associated documentation (chain of custody).

4.3 Data Quality Control

Measuring and Test Equipment (M&TE). A calibration program will be implemented for the work described in this test plan in accordance with NP 12-1, "Control of Measuring and Test Equipment." This M&TE calibration program will meet the requirements in NWMP procedure NP 12-1 for: (1) receiving and testing M&TE; (2) technical operating procedures for M&TE; (3) the traceability of standards to nationally recognized standards such as those from the National Institute of Standards and Technology; (4) maintaining calibration records. In addition, NP 13-1 and SP 13-1 identify requirements and appropriate forms for documenting and tracking sample possession.

Data Acquisition Plan. Data collection procedures are specific to individual instruments. For details of the data acquisition for a particular instrument, see the specific procedures (SP) or users manual for that instrument. Any data acquired by a data acquisition system (DAS) will be attached directly to the scientific notebook or compiled in separate loose-leaf binders with identifying labels to allow cross reference to the appropriate Scientific Notebook. If the instrument allows data to be recorded electronically, copies of the data disks will be submitted to the NWMP Records Center according to NWMP procedure NP 17-1, "Records." For instruments that do not have direct data printout, the instrument readings will be recorded directly into the scientific notebook. Current versions of the DAS software will be included in the SNL WIPP Baseline Software List, as appropriate.

Quality control of the scientific notebooks will be established by procedures described in NWMP procedure NP 20-2, "Scientific Notebooks." Methods for justification, evaluation, approval, and documentation of deviation from test standards and establishment of specially prepared test procedures will be documented in the Scientific Notebooks. Procedures including use of replicates, spikes, split samples, control charts, blanks and reagent controls will be determined during the development of experimental techniques.

The numerical data will be transferred from data printouts and scientific notebooks to Microsoft Excel (Office 97 version or later) spreadsheets. Data transfer and reduction will be performed in such a way to ensure that data transfer is accurate, that no information is lost in the transfer, and that the input is completely recoverable. Data transfer and reduction will be controlled to permit independent reproducibility by other qualified individuals. A copy of each spreadsheet will be taped into the scientific notebook, and a second person will compare the data recorded in the notebook and that on the spreadsheet to verify that no transcription errors have occurred during technical and/or QA review of the notebook. This verification will be documented in the notebook when signed by the reviewer.

Data Identification and Use. The details about the data to be obtained and the use of these data can be found in Section 4.1. All calculations performed as part of the activities of TP 02-06 will be documented in a scientific notebook. The notebook will be technically reviewed periodically by a second person, who will note concurrence by co-signing the examined material. If a discrepancy is found, that discrepancy and its

resolution will be documented in the notebook. In addition, there will be periodic quality assurance reviews of the notebook to ensure that the requirements of NWMP procedure NP 20-2, "Scientific Notebooks" are addressed.

4.4 Equipment

A variety of measuring and analytical equipment will be used for the work described in this test plan. A complete equipment list, including serial numbers, will be maintained in the scientific notebook. For a newly purchased instrument, if the operating procedure has not yet been developed or written, scientific notebooks will be used to record all laboratory work activities.

Weighing Equipment. Several balances are present in the facility and may be used for this project. These include a Mettler AT-261 five-decimal-place electronic balance, an ANC three-decimal-place balance, and top-loading balances and scales with maximum ranges of 2 to 30 kilograms. Balance calibration checks will be performed routinely using the following NIST-traceable weight sets, which, in turn, are calibrated by the SNL Calibration Laboratory every three years:

- *Troemner Calibration weight set*, ASTM Class 1, Serial number 22803, 1 mg – 100 g, calibration expires 12/16/02.
- *Troemner Calibration weight*, NIST Class 1, Serial number 42795, 100 g, calibration expires 11/19/02.
- *Troemner Calibration weight*, NIST Class 1, Serial number 42797, 100 g, calibration expires 11/19/02.
- *Troemner Calibration weight*, NIST Class 1, Serial number 42799, 100 g, calibration expires 11/19/01.
- *Troemner Calibration weight*, NIST Class 1, Serial number 42800, 100 g, calibration expires 11/19/01.
- *Troemner Calibration weight*, ASTM Class 1, Serial number 47824, 200 g, calibration expires 11/19/02.
- *Troemner Calibration weight*, ASTM Class 1, Serial number 55335, 1000 g, calibration expires 11/19/02.
- *Troemner Calibration weight*, ASTM Class 2, Serial number I-12, 10 kg, calibration expires 12/17/02.

Additional calibrated NIST-traceable weight sets that would be purchased at a later date may also be used. Balance accuracy and precision will be checked daily or prior to use (whichever is less frequent), using the calibration weight sets listed above. Calibration checks will be recorded in the scientific notebook.

Liquid Measuring Equipment. Standard Laboratory Class A glassware (pipettes, volumetric flasks, etc.) will be used at all times. In addition, several adjustable Eppendorf pipettes are available for use in the laboratory. The calibration of pipettes will

be checked routinely against a calibrated balance, and will be recorded in the scientific notebook.

Gas Analysis Equipment. Varian 3900 Gas Chromatography (GC) with Saturn 2100T Ion Trap Mass Spectrometer (MS) will be used to analyze headspace gas compositions. This is a newly purchased equipment, and the operating procedure needs to be developed.

Gas Sampling Equipment. 22-gauge needles (Becton Dickenson), a digital pressure gauge, and a gas-tight syringe (Pressure-Lok™, Precision Instrument Corp.) fitted with a stainless-steel side-port needle.

Gas Calibration Standards. Appropriate concentrations of analyte gases CO_2, CH_4, H_2, H_2S, N_2, and O_2 will be obtained from commercial sources. Primary calibration standards, specifically for CO_2, will be certified traceable to NIST.

Atmosphere Control Equipment. A glove box will be used for sample preparation and sampling.

Temperature Control Equipment. All samples will be incubated in a temperature-controlled incubator. Temperature will be monitored using instruments that have been calibrated with temperature standards traceable to NIST.

Other Analytical Equipment.

- *pH Meters and Autotitrators* – Solution pH may be measured using pH meters and/or autotitrators. A Mettler Model MA235 pH/Ion Analyzer and a Mettler Model DL25 Autotitrator will be used for this purpose. The range for all pH meters is 0.00 to 14.00. Electrodes will be calibrated before each use or daily (whichever is less frequent) with pH 4, 7, and 10 buffers manufactured by Fisher Scientific with unique lot numbers and expiration dates; traceable to the National Institute of Standards and Technology (NIST). The accuracy of the buffers is ±0.01 pH units; buffer values will be adjusted for laboratory temperatures as per buffer instruction sheets if necessary. Calibration checks will be recorded in the scientific notebook. Measuring pH in concentrated brines is difficult, and a procedure will be developed to calibrate pH meters.
- *Equipment for Chemical Analysis* – Three instruments may be used for chemical analyses. The first is a Perkin Elmer Optima 3300 DV inductively coupled plasma optical emission spectrometer (ICP); the second is a Cary 300 UV-visible spectrophotometer; and the third, is a UIC, Inc. carbon analyzer, consisting of an acidification module, a furnace module, and a CO_2 coulometer. These instruments will be user-calibrated each time they are used and documented in the scientific notebook.
- *Equipment for microbe counting/sizing* – An Olympus BX60 polarizing microscope will be used for observation of microbe preparations and for counting/sizing. The counting grid will be standardized with a Wild stage micrometer, serial # 2660 (or

equivalent), calibrated every five years by Klarman Rulings (NIST-traceable). Sizing accuracy checked using Bangs Laboratories NIST-traceable uniform microspheres (0.538 and 1.900 μm).

NMWP Activity/Project Specific Procedures (SPs) will be written for these instruments as necessary. Until that time, detailed procedure descriptions will be documented in laboratory notebooks.

5.0 TRAINING

All personnel involved in the experiments described in this test plan will be trained and qualified for their assigned work. This requirement will be implemented through NWMP procedure NP 2-1, "Qualification and Training." Evidence of training to assigned NPs, SPs, TOPs, TP 00-07, ES&H procedures, and any other required training will be documented through Form NP 2-1-1, "Qualification and Training." Annual Refresher QA training will ensure on-site personnel are trained to the NWMP QA Program. Specifically, the following Nuclear Waste Management Program Procedures (NPs) and Activity/Project Specific Procedures (SPs) are applicable:

- SOP-C001, "Standard Operating Procedure for Activities in the SNL/Carlsbad Laboratory Facility,"
- SP 12-1, "Use of Laboratory Balances and Scales,"
- SP 12-2, "Use and Maintenance of the UIC, Inc. Model CM5014 CO2 Coulometer, CM5130 Acidification Module and CM5120 Furnace Apparatus,"
- SP 13-1, "Chain of Custody,"
- NP 2-1, "Qualification and Training,"
- NP 6-1, "Document Review Process,"
- NP 12-1, "Control Of Measuring And Test Equipment,"
- NP 13-1, "Sample Control,"
- NP 17-1, "Records,"
- NP 20-2, "Scientific Notebooks."

In addition, SPs will be written for use of the GC-MS, ICP-OES, UV-Vis Spectrophotometer. Sample preparation procedures, which may vary from sample to sample as work scope evolves, will be detailed in scientific notebooks in accordance with NWMP procedure NP 20-2.

6.0 HEALTH AND SAFETY

All of the health and safety requirements relevant to the work described in this test plan and the procedures that will be used to satisfy these requirements are described in ES&H standard operating procedures. SOP-C001 describes the non-radiological hazards associated with these experiments and describes the procedures to deal with those hazards, including all the training requirements for personnel involved in conducting the

experiments. Additional SPs may be mandated by SNL ES&H requirements and their issuance will not require revision of this test plan.

7.0 PERMITTING/LICENSING

There are no special licenses or permit requirements for the work described in this Test Plan.

8.0 REFERENCES

Barros N., I. Gomez-Orellana, S. Feijoo, and R. Balsa. 1995. "The effect of soil moisture on soil microbial activity studied by microcalorimetry,." *Thermochimica Acta.* Vol. 249, pp. 161-168.

Brush, L.H. 1990. *Test Plan For Laboratory and Modeling Studies of Repository and Radionuclide Chemistry for the Waste Isolation Pilot Plant.* SAND90-0266. Albuquerque, NM: Sandia National Laboratories.

Cattaneo, M.V., C. Mason, and C.W. Greer. 1997. "The influence of moisture on microbial transport, survival and 2,4-D biodegradation with generally marked *Burkholderia cepacia* in unsaturated soil columns," *Biodegradation.* Vol. 8, pp. 87-96.

Donnelly, P.K., J.A Entry, D.L. Crawford, and K. Cromack Jr. 1990. "Cellulose and lignin degradation in forest soils: response to moisture, temperature, and acidity," *Microbial Ecology.* Vol. 20, pp. 289-295.

Francis, A.J., and J.B. Gillow. 1994. *Effects of Microbial Processes on Gas Generation under Expected WIPP Repository Conditions: Progress Report through 1992.* SAND93-7036. Albuquerque, NM: Sandia National Laboratories.

Francis, A.J., and J.B. Gillow. 2000. "Progress report: microbial gas generation program." Unpublished memo to Y. Wang, January 6, 2000. Carlsbad, NM: Sandia National Laboratories.

Francis, A.J., J.B Gillow, and M.R. Giles. 1997. *Microbial Gas Generation under Expected Waste Isolation Pilot Plant Repository Conditions.* SAND96-2582. Albuquerque, NM: Sandia National Laboratories.

Francis, A.J., J.B Gillow, and Y. Wang. 2001. "Re-Evaluation of Microbial Gas Generation under Expected Waste Isolation Pilot Plant Conditions." TP-99-01, Rev. 1. Carlsbad, NM: Sandia National Laboratories.

Gillow, J.B. 1996. "BNL-EPI, The Direct Count Method for Enumerating Bacteria," Technical Operating Procedure, Upton, NY: Brookhaven National Laboratory.

Gillow, J.B. 1998. "BNL-UV/Vis-1, Analysis of Optical Density of Biomass by spectrophotometry." Technical Operating Procedure, Upton, NY: Brookhaven National Laboratory.

Gillow, J.B., and A.J. Francis. 2001a. "Re-evaluation of microbial gas generation under expected Waste Isolation Pilot Plant conditions." Unpublished report, January 31, 2001. Carlsbad, NM: Sandia National Laboratories. Pp. 19-46.

Gillow, J.B. and A.J. Francis. 2001b. "Re-evaluation of microbial gas generation under expected Waste Isolation Pilot Plant conditions." Unpublished report, July 31, 2001. Carlsbad, NM: Sandia National Laboratories. Pp. 3.1 to 3.21

Gillow, J.B., and A.J. Francis. 2002. "Re-evaluation of microbial gas generation under expected Waste Isolation Pilot Plant conditions." Unpublished report, January 31, 2002. Carlsbad, NM: Sandia National Laboratories. Pp. 2.1-1 to 2.1-25.

Helton J.C., J.E. Bean, J.W. Berglund, F.J. Davis, K. Economy, J.W. Garner, J.D. Johnson, R.J. Mackinnon, J. Miller, D.G. O'Brien, J.L. Ramsey, J.D. Schreiber, A. Shinta, L.N. Smith, D.M. Stoelzel, C.T. Stockman, and P. Vaughn. 1998. *Uncertainty and Sensitivity Analysis Results Obtained in the 1996 Performance Assessment for the Waste Isolation Pilot Plant.* SAND98-0365. Albuquerque, NM: Sandia National Laboratories.

Kepner, R.L., Jr, Pratt, J.R. 1994. "Use of fluorochromes for direct enumeration of total bacteria in environmental samples: past and present." Microbiological Reviews. Vol. 58, pp. 603-615.

Kral, D.M., and M.K. Cousin. 1981. "Water Potential Relations in Soil Microbiology." SSSA Special Publication no. 9. Soil Science Society of America.

Lide, D.R. 2002. *Handbook of Chemistry and Physics*. Boca Raton, FL: CRC Press.

Nizovtseva, D.V., A.M. Semenov, and N.S. Panikov. 1995 "Influence of humidity on microbial cellulose activity in peat from a raised bog," *Microbiology*. Vol. 64, pp. 701-705.

Robie, R.A., B.S. Hemingway, and J.R. Fisher. 1978. *Thermodynamic Properties of Minerals and Related Substances at 298.15 K and 1 Bar (10^5 Pascals) Pressure and at Higher Temperatures*. U.S. Ge0ological Survey Bulletin no. 1452.

Stark, J.M., and M.K. Firestone. 1995. "Mechanism for soil moisture effects on activity of nitrifying bacteria," *Applied and Environmental Microbiology*. Vol. 61, pp. 218-221.

Wang, Y., and L.H. Brush. 1996. "Estimates of gas-generation parameters for the long-term WIPP performance assessment. Unpublished memo to M.S. Tierney, January 26, 1996. WPO #30819. Albuquerque, MM: Sandia National Laboratories.

Wang, Y., L.H. Brush, and R.V. Bynum. 1997. "Use of MgO to mitigate the effect of microbial CO_2 production in the Waste Isolation Pilot Plant." *WM'97*, March 2-6, 1997, Tucson, Arizona.

Weinbauer, M. G., Beckmann, C., Hofle, M. G. 1998. "Utility of gree fluorescent nucleic acid dyes and aluminum oxide membrane filters for rapid epifluorescence enumeration of soil and sediment bacteria." Applied and Environmental Microbiology. Vol. 64, pp. 5000-5003.

Xu, H. 2001. "Microstructure investigation of cellulosic materials from the Eddy Potash Mine." Unpublished report, January 31, 2001. Carlsbad, NM: Sandia National Laboratories. Pp. 47-54.

3.3 Effect of Actinide Complexation by Organic Ligands on WIPP Performance Assessment[1]

Donald E. Wall
Sandia National Laboratories, MS 1395
4100 National Parks Highway
Carlsbad, NM 88220 USA

This paper was presented as a poster at the 223rd National American Chemical Society Meeting, April 7-11, 2002, in Orlando, FL (SAND2001-3400P). The format of the poster has been modified for inclusion in this report.

[1] This work is covered by WBS #1.3.5.1.2.1

Effect of Actinide Complexation by Organic Ligands on WIPP Performance Assessment

Donald E. Wall
Sandia National Laboratories – Carlsbad Programs Group, 4100 National Parks Highway – Carlsbad, NM 88220 - USA

The Waste Isolation Pilot Plant (WIPP)

- WIPP received the 500th shipment of TRU waste on January 5, 2002, bringing the total number of waste containers disposed at WIPP to just over 14,000.
- During its operational phase the WIPP is projected to receive about 844,000 drums (55 gallon) of TRU waste. The repository will consist of 56 disposal rooms configured in 8 panels, with 7 rooms per panel. Access drifts will provide additional disposal capacity equivalent to 14 rooms.
- The layout of the WIPP and a cross section of the stratigraphic horizon are presented in Figures 1 & 2.

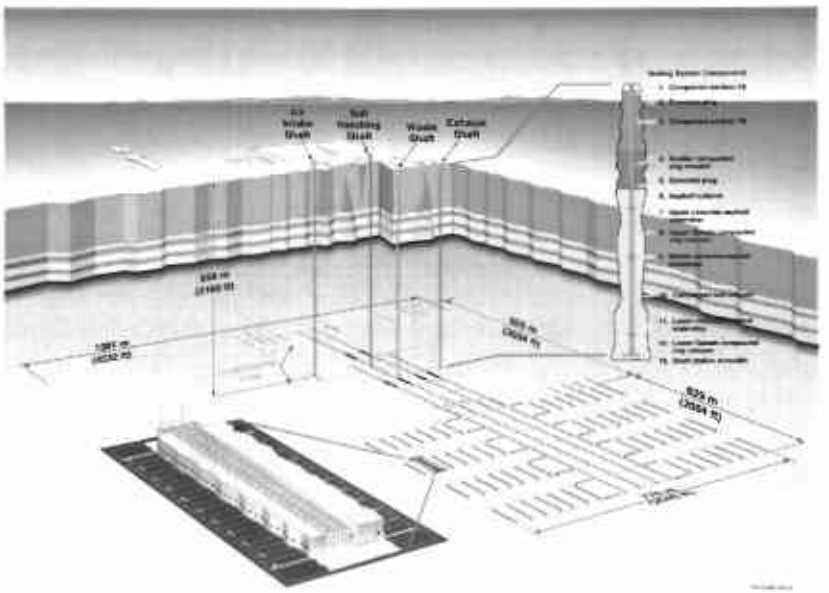

Figure 1: Layout of the Waste Isolation Pilot Plant

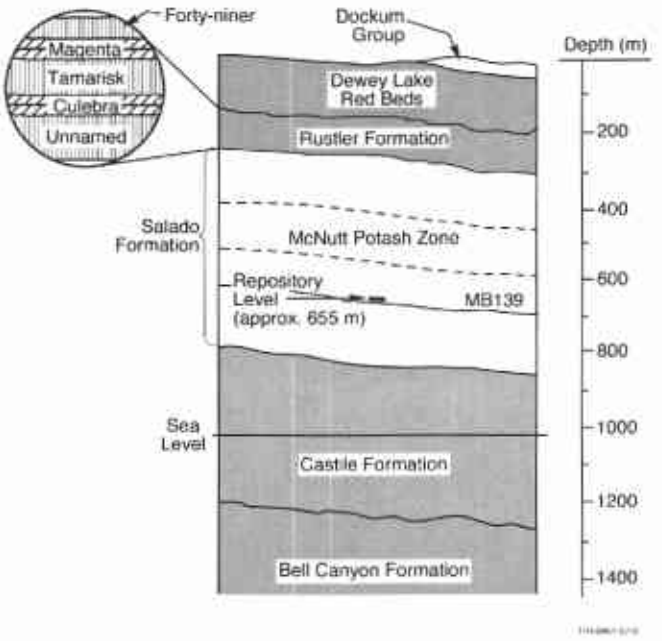

Figure 2: Stratigraphic horizon of the WIPP within the Delaware Basin

Performance Assessment

- WIPP Performance Assessment evaluates the risk associated with occurrence of scenarios, which are classified as the following general types: 1. Undisturbed 2. Mining. 3. Drilling-no Castile hit 4. Drilling with Castile hit 5. Multiple intrusions
- Releases in the undisturbed scenario are essentially non-existent. Potential release pathways, such as through the disturbed rock zone, or up a sealed shaft and through the fractured dolomite of the Culebra Formation, are negligible and do not impact repository performance. The release scenario that most affects performance assessment is due to human intrusion as a result of a drilling intrusion. The drilling rate used in performance assessment is based upon historical drilling rates within the Delaware Basin during the previous 100 years.
- The drilling rate used in the Compliance Certification Application was 46.8 boreholes/km^2/10,000 years. The current rate is 52.7 boreholes/km^2/10,000 years. It is expected that the rate used in recertification will be changed from 46.8 boreholes/km^2/10,000 years to another value yet to be determined.
- Releases from the repository are categorized as:
    - Cuttings-Solid material abstracted by the rotating drilling bit. Cuttings volume is calculated using an average drill bit diameter of 12.25 inches.
    - Cavings-Solid material eroded from the borehole wall during the drilling operation. The magnitude of cavings releases is a function of shear stress imparted by drilling fluids and shear strength of the waste.

- Spallings-Solid material transferred to the borehole due to pressure buildup within the repository. Gas generation due to waste degradation may lead to pressure buildup.
- Direct Brine Release (DBR)-Movement to the accessible environment of brine carrying dissolved or colloidal radioactive material as the immediate result of a drilling intrusion.
- Long-Term Brine Release- Contaminated brine carrying dissolved or colloidal radioactive material, to the accessible environment over a long period of time.

Release Scenarios

TRU waste has greater than 100 nCi of TRU radionuclides per gram of waste, with TRU radionuclides defined as having Z > 92 and half-life > 20 years. The Waste Unit Factor (WUF), which is used to determine release limits, is the number of millions of curies of TRU waste. According to the Transuranic Waste Baseline Inventory Report (TWBIR) the WUF is 3.44, corresponding to 3.44 x 10^6 Ci of TRU waste. Additional inventory has been documented and the inventory has been recalculated with correction for radioactive decay to a projected closing date of 2033. A recommendation for an updated WUF of 3.59 has been made in the Technical Baseline Migration Parameter Report (1)

Scenarios that contribute to releases are designated as: E1, single penetration of a panel by drilling intrusion that intersects a brine reservoir, E2 a single penetration of a panel that does not intersect a brine reservoir, E1E2, two penetrations of a panel, one that intersects a brine reservoir, and one that does not. The E1E2 scenario may lead to increased brine releases if the brine reservoir is pressurized. Brine releases may also follow an E1 or E2 scenario if the repository is pressurized for another reason, such as gas generation.

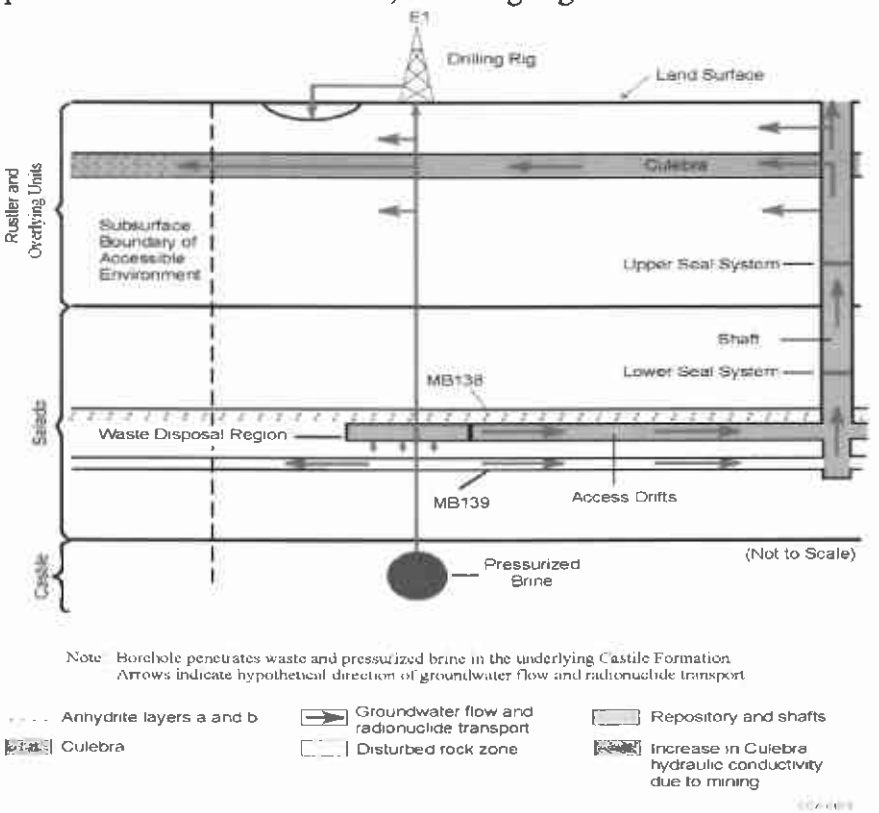

Figure 3: Conceptual Release Pathways for the Disturbed Performance Deep Drilling Scenario E1

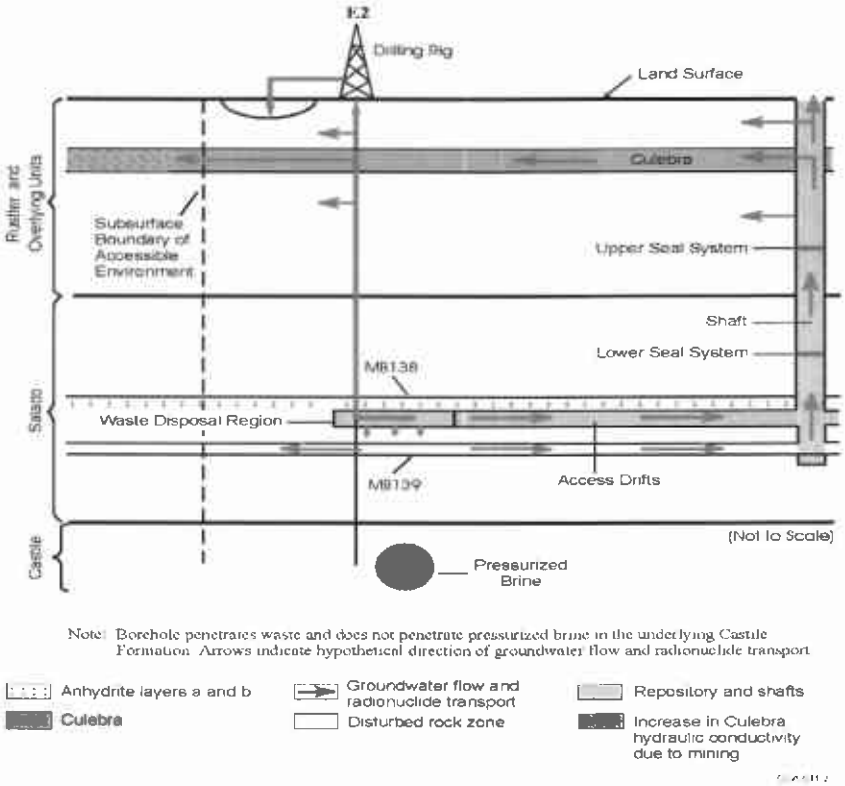

Figure 4: Conceptual Release Pathways for the Disturbed Performance Deep Drilling E2 Scenario

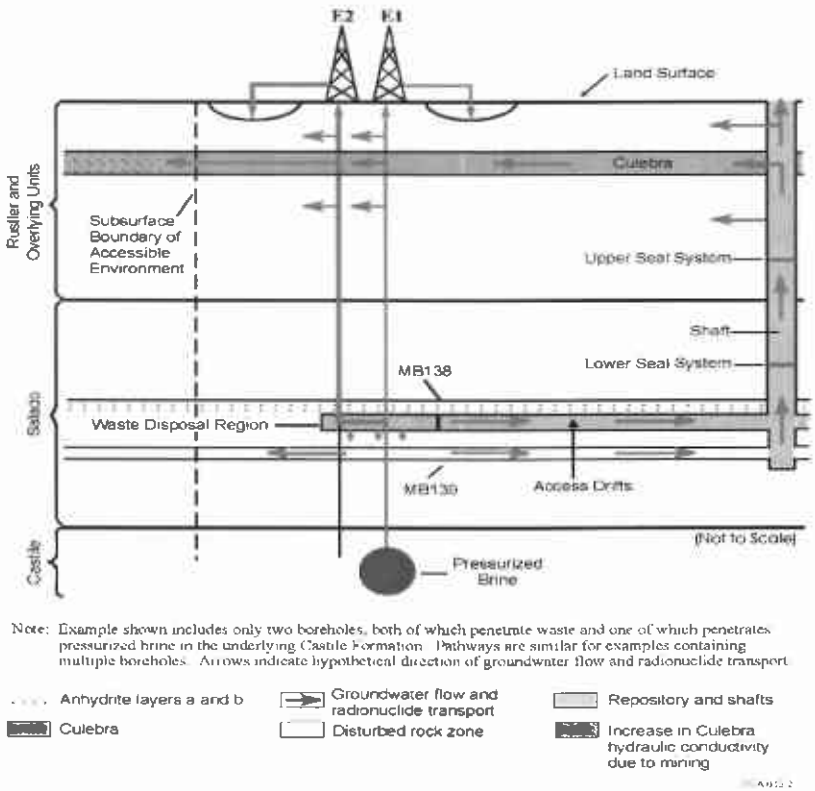

Figure 5: Conceptual Release Pathways for the Disturbed Performance Deep Drilling Scenario E1E2

Regulatory Compliance

- Containment Requirements: Disposal systems for spent nuclear fuel or high-level or transuranic waste shall be designed to provide a reasonable expectation, based upon performance assessments, that the cumulative releases of radionuclides to the accessible environment for 10,000 years after disposal from all significant processes and events that may affect the disposal system shall:

    - Have a likelihood of less than one chance in 10 of exceeding the release limit
    - Have a likelihood of less than one chance in 1,000 of exceeding ten times the release limit

- Probabilistic analysis is expressed as a Complementary Cumulative Distribution Function (CCDF), that describes the relationship between the likelihood of cumulative releases and the regulatory limits. Release limits and projected WIPP radionuclide inventory are presented in Table I and II.

Release Limits and Inventory

Table I: Normalized Release Limits

Radionuclide	Release Limit per Million Curies of TRU Radionuclides	Release Limit for the WIPP Normalized By Total Waste Unit Factor
Am-241 or 243	100	344
C-14	100	344
Cs-135 or 137	1000	3440
I-129	100	344
Np-237	100	344
Pu-238, 239, 240, 242	100	344
Ra-226	100	344
Sr-90	1000	3440
Tc-99	10000	34400
Th-230 or 232	10	34.4
Sn-126	1000	3440
U-233, 234, 235, 236, or 238	100	3440
Any other α emitting radionuclide with half-life greater than 20 years	100	3440

Table II: Radionuclide Inventory

Nuclide	Inventory	% of Waste Unit
^{241}Am	4.48×10^{5}	11
^{243}Am	32.6	8.0×10^{-4}
^{249}Cf	0.687	1.7×10^{-6}
^{251}Cf	3.78×10^{-3}	9.8×10^{-6}
^{243}Cm	101.7	2.5×10^{-3}
^{245}Cm	115	2.8×10^{-3}
^{246}Cm	0.102	2.5×10^{-6}
^{247}Cm	3.21×10^{-9}	7.9×10^{-14}
^{248}Cm	0.0369	9.1×10^{-7}
^{237}Np	56.4	1.4×10^{-3}
^{238}Pu	2.61×10^{6}	64.1
^{239}Pu	7.95×10^{5}	19.5
^{240}Pu	2.15×10^{5}	5.28
^{242}Pu	1170	2.87×10^{-2}
^{244}Pu	1.50×10^{-6}	3.7×10^{-11}

Experimental Work

Complexation data for interaction of actinides with organic ligands was generated in the Actinide Chemistry Program at Florida State University. Complexation constants with inorganic ligands, (OH^-, CO_3^{2-}) and organic ligands (acetate, citrate, oxalate, EDTA) were used to calculate solubilities of actinides in the III and IV oxidation states. Solubilities are used to assess the impact of direct brine releases on WIPP regulatory compliance.

Table III. Organic Ligand Inventory in the WIPP

Ligand	Inventory (grams)	Projected Concentration (M)
acetate	1.3×10^{6}	1.1×10^{-3}
oxalate	1.6×10^{6}	4.7×10^{-4}
citrate	1.4×10^{8}	7.4×10^{-3}
EDTA	2.3×10^{4}	4.2×10^{-6}

Table IV: Actinide Stability Constants with Predominant Organic Ligands in the WIPP (a)

Ligand	Th(IV)	U(VI)	Np(V)	Am(III)
acetate	4.51 (2)	3.14 (2)	1.80 (2)	2.20 (2)
citrate	10.18 (3)	7.10 (4)	2.56 (4)	8.8 (7)
oxalate	7.47 (5)	5.82 (5)	4.63 (5)	4.57 (5)
EDTA	23.73 (7)	10.48 (5)	5.45 (5)	18.97 (7)

(a) values are log β_{101} in 5 m NaCl solution at 25° C
References are in parentheses.

Complementary Cumulative Distribution Function

The total CCDF is the contribution of the average CCDF's for each of the potential release pathways. The summed normalized release on the abscissa of Figure 6 is given in EPA units, which are used to define the containment requirements for the repository. EPA units are defined as the number of curies of a particular radionuclide in the WIPP inventory divided by the release limit for that radionuclide. For example, ^{239}Pu has a projected inventory at closure of 7.95×10^5 Ci, and a release limit of 344 Ci, which may be expressed in EPA units as:

$$7.95 \times 10^5 \text{Ci}/344\text{Ci} = 2311 \text{ EPA units}$$

Cuttings and cavings make the largest contribution the the overall CCDF, with spallings also making a substantial contribution. The contribution to the overall CCDF by the direct brine release scenario is about 1 order of magnitude less than either cuttings and cavings or spallings. Although a feature, event or process that affects actinide solubility could move the CCDF for the DBR, the smaller contribution of DBR to the total CCDF means that relatively large errors in determination of actinide solubilities do not sufficiently propagate to greatly affect the total CCDF.

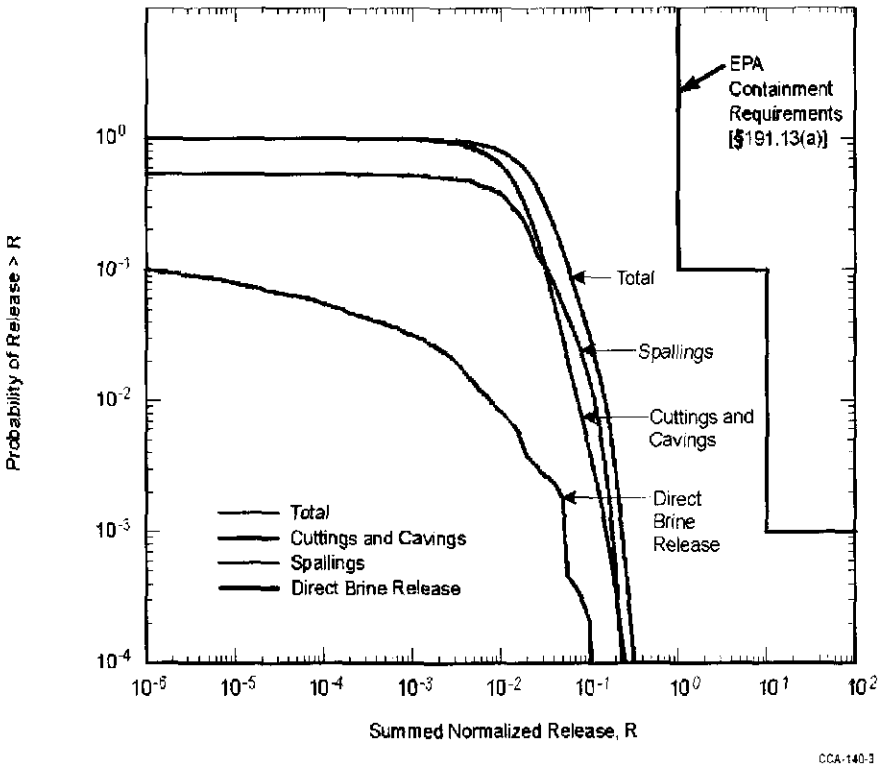

Note: Mean CCDFs are shown for the total normalized release (this curve is also shown in Figure 6-40 and is the mean of the family shown in Figure 6-35) and for the normalized releases resulting from cuttings and cavings, spallings, and direct brine release. The mean CCDF for subsurface releases resulting from groundwater transport is not shown because those releases were less then 10-6 EPA units and the CCDF cannot be shown at the scale of this figure.

Figure 6: Mean CCDFs for Specific Release Modes, Replicate 1

References

(1) Wall D., 2001, Technical Baseline Migration Parameter Report Rev. 0, ERMS 519513, Sandia National Laboratories, Carlsbad, NM.

(2) Moore R.C., Borkowski M., Bronikowski M.G., Chen J., Pokrovsky O.S., Xia Y., and Choppin G.R., J. Sol. Chem. 28, 521, 1999, Thermodynamic Modeling of Actinide Complexation with Acetate and Lactate at High Ionic Strength.

(3)Choppin G.R., Erten H., and Xia Y., Radiochim. Acta 74, 123, 1996, Variation of Stability Constants of Thorium Citrate Complexes with Ionic Strength.

(4)Bronikowski M., Pokrovsky O., Borkowski M, and Choppin G.R., UO22+ and NpO2+ Complexation with Citrate in Brine Solutions, Actinide Speciation in High Ionic Strength Media, Reed, D. ed., Kluwer Academic/Plenum Publishers, N.Y., 1999, 177-185

(5)Pokrovsky O., Bronikowski M, Moore R, and Choppin G.R., Radiochim. Acta 80, 23, 1998, Interaction of Neptunyl (V) and Uranyl (VI) with EDTA in NaCl Media: Experimental Study and Pitzer Modeling

(6)Borkowski M., Moore R., Bronikowski M., Chen J., Pokrovsky O., Xia Y. and Choppin G.R., J. Radioanal. Nucl. Chem. 248(2), 467, 2001

(7) Choppin G.R., Bond A.H., Borkowski M., Bronikowski M.G., Chen J.F., Lis S., Mizera J., Pokrovsky O., Wall N.A., Xia Y.X., and Moore R.C., 2001, SAND99-0943, Waste Isolation Pilot Plant Actinide Source Term Test Program: Solubility Studies and Development of Modeling Parameters. SNL WIPP Library.

3.4 Chemical Behavior of Hypochlorite In High Ionic Strength Solutions[1]

Donald E. Wall
Sandia National Laboratories, MS 1395
4100 National Parks Highway
Carlsbad, NM 88220 USA

This test plan, which appears on the SNL NWMP website as TP-02-01, describes non-radioactive experiments on the decomposition of hypochlorite underway at SNL in Carlsbad.

[1] This work is covered by WBS #1.3.5.1.2.1

SANDIA NATIONAL LABORATORIES
WASTE ISOLATION PILOT PLANT
TEST PLAN, TP 02-01

Chemical Behavior of Hypochlorite in High Ionic Strength Solutions

Revision 1
(The title of this test plan has been changed. The original title is: Complexation Behavior of Hypochlorite with Metal Ions)

Task 1.3.5.4.1.2

Effective Date: TBA

Prepared by:
Donald Wall (6822)

Sandia National Laboratories
Carlsbad, NM

WIPP:1.3.5.4.1.2:TD:QA:DPRP1:NF:Test Plan for Complexation Behavior of Hypochlorite with Metal Ions, TP 02-01

APPROVAL PAGE

Author:	*Original signed by Donald Wall* Donald Wall (6822)	*07/31/02* Date
Technical Reviewer:	*Original signed by E. R. Giambalvo* Emily R. Giambalvo (6822)	*07/31/02* Date
Management Reviewer	*Original signed by M.K. Knowles* M. Kathryn Knowles (6821)	*07/31/02* Date
QA Reviewer	*Original signed by Marty Mitchell* Marty Mitchell (6820)	*07/31/02* Date

CONTENTS

1.0 LIST OF ACRONYMS

$\mathcal{A}_n$	thermodynamic activity
ACS	American Chemical Society
An	actinide
An(III)	actinide in the +III oxidation state
An(IV)	actinide in the +IV oxidation state
An(V)	actinide in the +V oxidation state
An(VI)	actinide in the +VI oxidation state
Ar	argon
B	boron
Br	bromine
C	Coulomb
Ca	calcium
CCA	Compliance Certification Application
Ce	cerium
$Cl^{\bullet}$	atomic chlorine free radical
$Cl_2^{\bullet-}$	molecular chlorine free radical
ClO_3^-	chlorate
Co	cobalt
DBR	Direct Brine Release
DOE CBFO	Department of Energy Carlsbad Field Office
E^0	Standard reduction potential
EDTA	ethylenediaminetetraacetic acid
ERDA-6	Descriptive label applied to a Castile brine composition
F	The faraday constant, (96,485 coulombs/mole)
Fe	iron
GWB	Generic weep brine
H^+	hydrogen ion
$H^{\bullet}$	Atomic hydrogen free radical
HCl	hydrochloric acid
HOCl	hypochlorous acid
$HOCl^{\bullet-}$	hypochlorous acid, anionic free radical
ICP-OES	Inductively coupled plasma optical emission spectroscopy
J	Joule
K	potassium
Ln	lanthanide
Mn	manganese
NaOH	sodium hydroxide
Nd	neodymium
Ni	nickel
NIST	National Institute of Standards and Technology
$OH^{\bullet}$	hydroxyl free radical
OCl^-	hypochlorite

OH^-	hydroxide
pcH	negative logarithm of the hydrogen ion concentration of a solution
pH	negative logarithm of the hydrogen ion thermodynamic activity of a solution
pK_a	negative base 10 logarithm of an acid dissociation constant
R	ideal gas constant, 8.314 J/molK
SO_4^{2-}	sulfate
T	temperature, in degrees Celsius or kelvins
UV-VIS	ultraviolet-visible (spectroscopy)
WIPP	Waste Isolation Pilot Plant
ΔG	Gibbs free energy of reaction
α-particle	high energy particle expelled from a nucleus during an α-decay process
β-particle	a positron or negatron expelled from a nucleus during a β-decay process
β_{pqr}	stability constant for a metal/ligand complex
γ	activity coefficient (not related to γ-ray)
γ-rays	high-energy photons emanating from a nucleus due to a nuclear decay process
μ	ionic strength

2.0 REVISION HISTORY

This is a revised version, Revision 1, of this test plan. Subsequent revisions will be done in accordance with the Sandia National Laboratories Nuclear Waste Management Program Procedures: NP 20-1 Test Plans, NP 6-1 Document Review Process and NP 6-2 Document Control Process.

3.0 PURPOSE & SCOPE

3.1 Introduction

The position put forth in the Compliance Certification Application (CCA) is that the presence of large amounts of iron, in the form of both waste and waste containers, emplaced within the Waste Isolation Pilot Plant (WIPP) will provide sufficient electrochemically reducing conditions to maintain plutonium as Pu(III) and Pu(IV) (DOE, 1996). The Source Term Test Program (STTP) was initiated at Los Alamos National Laboratory in order to make an examination of the behavior of actinides, particularly Pu, in brines that were in contact with actual waste forms (Villarreal, 1996). During the course of the experimental program, there was evidence of the appearance of Pu(VI) in some of the test containers. It was proposed that the generation and persistence of radiolysis products in brine solutions exposed to α-radiation was responsible for affecting the solution redox conditions, and that Pu(VI) appeared in response to alteration of a reducing state imposed by the presence of metallic iron (Villarreal et al. 2000) The appearance of Pu(VI) has been commented upon by Oversby (2000) and Brush et al. (2001). Generation of hypochlorite (OCl^-) and hydrogen

peroxide (H_2O_2) as a result of α-particle induced radiolysis of brine was suggested as the probable mechanism for oxidation of Pu, but was not experimentally observed or measured (Villarreal et al. 2000). While it is true that OCl^- is a sufficiently strong oxidant to oxidize Pu to Pu(VI) under basic conditions, H_2O_2 can act as an electron donor, and reduces Pu(VI), also under basic conditions. However, both OCl^- and H_2O_2 are highly reactive and unstable in aqueous solutions. For example, the iron-catalyzed decomposition of H_2O_2 is well known and particularly rapid (Greenwood and Earnshaw, 1989a). In fact, both OCl^- and H_2O_2 may be catalytically decomposed by metal ions that have more than one accessible oxidation state in aqueous solution, such as Fe and Pu. Additionally, OCl^- and H_2O_2 react with each other, so cannot coexist to a great extent within the same solution. Hence, solutions containing OCl^- and H_2O_2, redox active metals, and radioactive materials may result in a plethora of experimental variables to be monitored and controlled. Due to the multiple interactions that simultaneously take place, any attempt to study the redox behavior of Pu with radiolysis products requires *exceedingly* careful experimental design and control, lest erroneous conclusions be made as a result of either failure to control or monitor critical variables.

There are different, but widely applied approaches to the examination of complex systems, that may be broadly described as the "top-down" and the "bottom-up" approaches. The former is primarily concerned with observation of the total behavior of a system, without regard to the fundamental reasons for the behavior. The limitation inherent in this method is that predictive capability is not developed, no matter how similar the alternative systems are to the studied system. Such a method acknowledges a lack of control of critical experimental variables, and even fails to recognize their identity. The "bottom-up" approach is profitably used when it is necessary to develop a fundamental understanding of a system in order to take into account the relative impacts that variations in experimental variables impart to the overall system behavior. In carrying out the "bottom-up" approach it is necessary to identify, isolate, control and quantify the experimental variables. Neglect of a single one of these four activities constitutes a critical failure of experimental design. Additionally, the "bottom-up" approach may be used to quantify the influence of a variable on system behavior, and evaluate its overall relative importance. The work described in this test plan is patterned after the "bottom-up" approach, in an attempt to determine whether generation of radiolysis products may have a significant impact on the total system performance of the WIPP. Production of OCl^- in NaCl-based brine solutions exposed to α-radiation does occur. The question to be addressed is whether the process can have a significant impact upon the oxidation-states and solubilities of actinides within the WIPP. Examination of the chemical behavior of OCl^- does not require use of any radioactive materials, but can be used to determine the stability and reactivity of OCl^- under WIPP representative conditions.

The Environmental Evaluation Group has expressed concern over the report of the appearance of Pu(VI) in some containers in the STTP project, and has expressed its opinion in a report, EEG-77 (Oversby 2000). In EEG-77 Oversby briefly quotes EEG-68, describing laboratory observations of Pu(V), (Oversby 2000, Neill et al. 1998):

"...Pu(V) is observed as a long-lived transient in many laboratory experiments. Pu(V) may be formed as a result of radiolysis reactions in brine, and while its total abundance in the repository is likely to be low, it might be significant as a transient species in some waste containers."

In the above statement, Oversby describes the radiolysis effects as possible reasons for appearance of oxidized Pu. It is not possible to produce Pu(V) by direct oxidation of either Pu(III) or Pu(IV) in solution due to the overvoltage required to carry out the oxidation steps. The exact reasons for this behavior will be presented later in this test plan. Presently, it should be borne in mind that the chemical behavior of Pu is rather complex, requiring strict control over experimental variables.

3.2 Radiolysis in Brines

The effect of radioactive decay on aqueous solutions is markedly dependent upon the type and energy of radiation involved. For example, β-particles, with a charge of $\pm$ 1.602 x 10^{-19} C and a mass of 9.11 x 10^{-31} kg, have much larger rates of energy transfer to target material than high energy photons, such as γ-rays, which have neither charge nor mass. The α-particles, with charges of +3.204 x 10^{-19} C and masses of 6.647 x 10^{-27} kg, exhibit much larger rates of linear energy transfer than β particles, leaving intense tracks of ionized target material, including many atomic and molecular species in highly excited states. In general, α-particles travel 30-70 μm in water (Ganguly et al. 1956). The ionization tracks of α-particles in aqueous solutions include numerous hydrogen, oxygen, and hydroxyl free radicals. Ordinarily, free radicals have very short lifetimes in solution due to rapid reaction with solute and solvent molecules. Combination processes become increasingly important in the diffusion limited environment surrounding particle tracks of high linear energy transfer species. H_2 and O_2 are two well-known gas generation products due to radiolysis of water and recombination of the hydrogen free radicals, $H^{\bullet}$, or the oxygen free radical, $O^{\bullet}$, although the mechanisms and products of brine radiolysis may be quite different. The superscript dot indicates a free radical species. Recombination processes may also yield H_2O_2 as a product of the reaction of two hydroxyl radicals. Also significant, but dependent upon the solution composition, are generation of molecular chlorine (Cl_2), hypochlorous acid (HOCl) and OCl^-.

In the following discussion, the symbol "→" denotes a thermodynamically irreversible process, while the symbol "⇌" indicates a thermodynamically reversible process. Water radiolysis in the tracks of α-particles leads to generation of numerous species, such as:

$$H_2O \xrightarrow{\alpha} e^-_{aq}, OH^{\bullet}, H^{\bullet}\ H_2O_2, H_2, O_2, H^+, OH^- \qquad (1)$$

Aquated electrons (e^-_{aq}) and free radical species are very reactive, rapidly combining with

many other dissolved species. Additional reactions take place in the presence of significant concentrations of other solute species, such as Cl^-. Participation of Cl^- in radiolytically initiated reactions leads to generation of additional chemical species due to subsequent oxidation-reduction reactions. For example, the hydroxyl radical can oxidize chloride, yielding the hypochlorous acid anion $HOCl^{\bullet-}$

$$OH^\bullet + Cl^- \rightarrow HOCl^{\bullet-} \quad (2)$$

The hypochlorous acid anion is also a radical species that equilibrates rapidly with H^+ to give the chlorine radical

$$HOCl^{\bullet-} + H^+ \rightleftharpoons Cl^\bullet + H_2O \quad (3)$$

The likelihood of the chlorine radical combining with chloride is greater in solutions with high chloride content:

$$Cl^\bullet + Cl^- \rightleftharpoons Cl_2^{\bullet-} \quad (4)$$

$Cl_2^{\bullet-}$ reacts rapidly to produce Cl_3^-, which is more stable than $Cl_2^{\bullet-}$,(Kim et al. 1987)

$$Cl_2^{\bullet-} + Cl_2^{\bullet-} \rightarrow Cl_3^- + Cl^- \quad (5)$$

The Cl_3^- species is in equilibrium with other chlorine species, ultimately producing hypochlorite:

$$Cl_3^- \rightleftharpoons Cl_2 + Cl^- \quad (6)$$

$$Cl_2 + H_2O \rightleftharpoons HOCl + Cl^- + H^+ \quad (7)$$

$$HOCl \rightleftharpoons H^+ + OCl^- \quad (8)$$

It has been reported that the production of HOCl and OCl^- depends on the Cl^- concentration (Kim et al. 1987). The dependence of OCl^- concentration on NaCl concentration is illustrated in Figure 1. Data used to generate this figure were taken from Kelm et al. (1999). Each sample contained 1 Ci/L of ^{238}Pu introduced as finely divided precipitate of Pu(VI) hydroxide. The solutions were adjusted to a pH of ~12. No error bars are included because the literature reference includes insufficient data to estimate or evaluate the uncertainty. The equation for the linear best-fit line is $y = 0.0059x - 0.0105$.

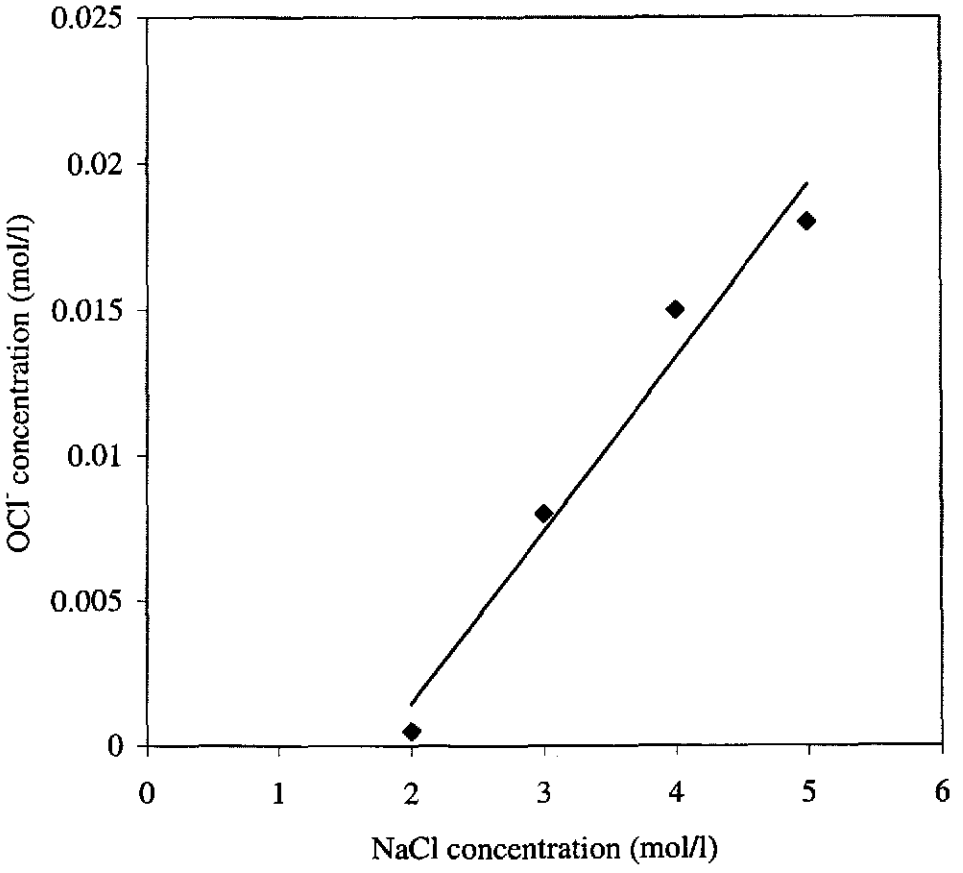

Figure 1. Generation of hypochlorite as a function of aqueous NaCl concentration.

Production of OCl^- is not a significant process for Cl^- concentrations less than ca. 1.8 molar at radioactivity levels of 1 Ci/L. The minimum concentration of Cl^- required for OCl^- hypochlorite generation most likely reflects the decreased probability of reactions 4 and 5 taking place. Conversely, the data indicate that the reactions leading to HOCl production in 5 M NaCl solution produce significant quantities of OCl^-, (nearly 20 mM), in the presence of 1Ci/L of α-emitting radionuclides. The pK_a value of HOCl is 7.43 (μ=1.0 $NaClO_4$, T= 25° C), indicating that at pH relevant to WIPP conditions (pH≈9-10) the conjugate base (OCl^-) will be the predominant form (Martell et al. 1998). The symbol "μ" indicates ionic strength. Decomposition rate constants, determined by measurement of the kinetics of decomposition in high ionic strength solutions, may be used together with kinetic data of radiolytic production to calculate steady state concentrations of hypochlorite under conditions expected to exist within the WIPP. The steady state concentrations may be used to calculate the oxidation/reduction potentials and capacities in brines as a result of radiolytic production of OCl^-.

3.3 Thermodynamic Relationships

Various thermodynamic relationships are discussed in the text of this test plan, therefore, it is appropriate to commence with an introduction to the meanings and use of these relationships. The Gibbs free energy (ΔG) of a system describes whether the reaction under consideration is a thermodynamically favorable process. Reactions that have negative values of ΔG will spontaneously proceed as written, whereas, reactions that have positive values of ΔG will spontaneously proceed in the reverse direction. Oxidation/reduction reactions may be written as half-reactions which have specific values for the associated thermodynamic driving force, sometimes written in terms of electromotive force (e.m.f), usually expressed in volts. The relationship between the ΔG of a reaction and the e.m.f is shown by equation 9:

$$\Delta G = -nFE \qquad (9)$$

n is the number of electrons exchanged in the reaction, F is the Faraday constant (96,485 coulombs/mole) and E is the e.m.f., in volts, for the reaction. Equation 9 shows that a reaction that features a positive value for the e.m.f. will have a negative value for ΔG, and will proceed spontaneously as written. Conversely, a reaction with a negative e.m.f. value will proceed in the reverse direction. Oxidation/reduction reactions with negative e.m.f. values may be coupled with other reactions that have positive e.m.f. values, and if the combination of the two reactions yields a positive e.m.f. value, the reaction will proceed. In other words, a strongly favorable half-reaction may supply the thermodynamic driving force necessary to drive another less favorable half-reaction.

The e.m.f. potentials for many reactions may be found in tables of standard reduction potentials, which are tabulated for standard state conditions of 25°C, a partial pressure of one atmosphere for gas phase reactants, such as O_2, and thermodynamic activity equal to one for all other reactants. However, the reaction potential differs under non-standard state conditions; equation 10 is used in an example:

$$aA + bB \rightleftharpoons cC + dD \qquad (10)$$

In equation 10, a moles of reactant A combine with b moles of reactant B to yield c moles of product C and d moles of product D. It should be noted that the reactants, products and coefficients in equation 10 indicate an equilibrium condition. The Nernst equation, which is used to calculate reaction potentials for non-standard state conditions, is illustrated using the reactants and products from equation 10. The concentrations of the reactants and products in equation 11 are not necessarily those at equilibrium, and in fact may be far from equilibrium. For simplicity of expression and mathematical treatment, concentrations rather than activities are used in the present discussion.

$$E = E^0 - \frac{RT}{nF} \ln \frac{[C]^c[D]^d}{[A]^a[B]^b} \quad (11)$$

E^0 is the standard state reaction potential, n is the number of electrons exchanged in the reaction, R is the ideal gas constant (8.314 $Jmol^{-1}K^{-1}$), T is the temperature in kelvins, and F is the Faraday constant. Equation 11 may be simplified for T = 298 K, and converting to base 10 logarithms:

$$E = E^0 - \frac{0.059}{n} \log \frac{[C]^c[D]^d}{[A]^a[B]^b} \quad (12)$$

It is apparent that the e.m.f. for a chemical system is greatly dependent on the concentrations of the reactants, which may be affected by other parameters, such as solubility or presence of organic ligands. Complexation by organic ligands has a twofold effect on the redox potential for metals; it changes the concentration of free metal in solution and changes the electron density around the metal ion in a manner that depends on the nature of orbital overlap and the electronic configuration of the metal and ligand. A description of the effects on redox potentials of these two types of effects will be provided in this test plan for Pu and Fe.

The reaction in equation 10 may also be rewritten in terms of the equilibrium constant, K. The ratio in equation 13 should not be confused with the ratio in equation 12. Equations 10 and 13 are for equilibrium conditions, whereas equations 11 and 12 may indicate non-equilibrium concentrations:

$$K = \frac{[C]^c[D]^d}{[A]^a[B]^b} \quad (13)$$

The equilibrium constant is related to the ΔG of the reaction through the following thermodynamic relationship:

$$\Delta G = -RT\ln K \quad (14)$$

A positive value for the equilibrium constant, indicating that the reaction favors the products, yields a negative value for ΔG, consistent with a thermodynamically favorable reaction. The interconnections among the thermodynamic relationships allow determination of parameters, such as the e.m.f. values for redox couples, by numerous and sometimes simpler experimental means. For example, experimental measurements of equilibrium constants are often simpler and more reliable than direct e.m.f. measurements. On the other hand, tables of e.m.f. values are very useful to predict states of thermodynamic equilibrium.

3.4 HOCl/OCl^- and H_2O Redox Behavior

HOCl and its conjugate base, OCl^-, are strong oxidizing reagents, and react vigorously with many materials. The strong thermodynamic driving force for HOCl and OCl^- oxidation reactions are clearly indicated by the standard reduction potentials that are listed in Table 1:

Table 1. Standard Reduction Potentials for Reactions of HOCl and OCl^-

Reaction	E^0 (volts)
$HClO + H^+ + e^- \rightarrow \frac{1}{2} Cl_2 + H_2O$	1.61
$HClO + H^+ + 2e^- \rightarrow Cl^- + H_2O$	1.48
$OCl^- + H_2O + 2e^- \rightarrow Cl^- + 2OH^-$	0.81

Values of 1.61 and 1.48 volts exceed the thermodynamic limit for the stability of water. Both oxidation potentials are sufficiently high that solutions of HOCl in water are not stable, and result in the oxidation of water to O_2. It is useful to consult a Latimer diagram for the standard reduction potentials of water to gain an understanding of the fundamental thermodynamic limitations on the behavior of HOCl and OCl^- in an aqueous solution. Simplified versions of Latimer diagrams for water adapted from Greenwood and Earnshaw (1989a) are presented below:

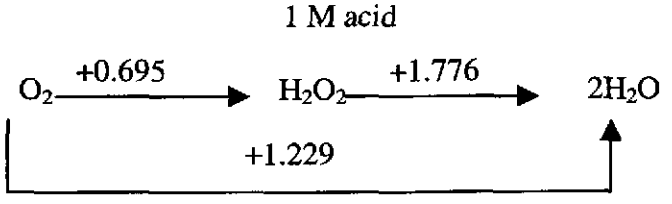

Figure 2. Latimer diagram for oxidation of water.

The data in Figure 2 may be used to prepare a Poubaix diagram that illustrates the stability fields for water under various pH and redox conditions. The reactions for the standard reductions that are used to generate the Poubaix diagram are provided in Table 2.

Table 2. Oxidation/reduction reactions of water

Reaction	E^0 (volts)
$O_2 + 4H^+ + 4e^- \rightleftharpoons 2H_2O$	+1.229
$O_2 + 2H^+ + 2e^- \rightleftharpoons H_2O_2$	+0.695
$H_2O_2 + 2H^+ + 2e^- \rightleftharpoons 2\ H_2O$	+1.776
$H^+ + 1e^- \rightleftharpoons ½\ H_2$	0.000

The stability fields, i.e. combinations of redox and pH conditions are presented in Figure 3.

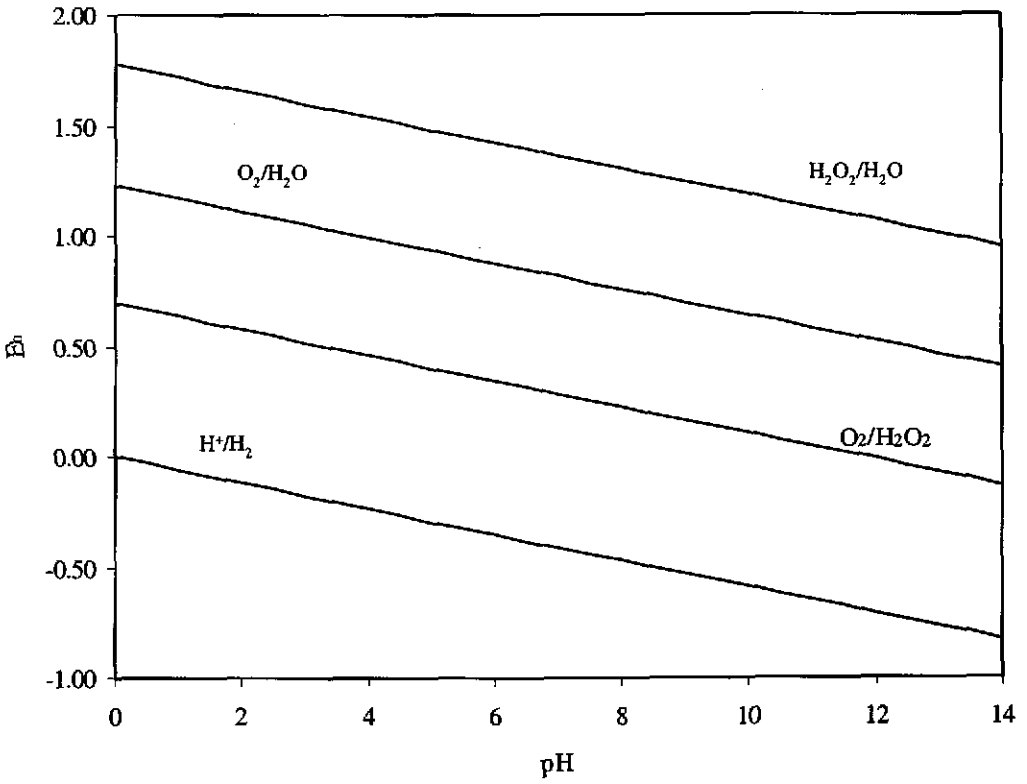

Figure 3. Poubaix diagram illustrating oxidation/reduction stability fields for water.

The line designated by the H_2O_2/H_2O couple indicates the potential at which water is oxidized to H_2O_2 (or H_2O_2 is reduced to water). Water is the more stable species at combinations of half-cell reduction potential (E_h) and pH below the line, although H_2O_2 may still form slowly to satisfy equilibrium conditions. When conditions are sufficiently oxidizing, as occurs above the line, H_2O_2 is the more stable species, and water is spontaneously oxidized to H_2O_2. The line designated by O_2/H_2O_2 delineates the equilibrium condition at which H_2O_2 is further oxidized to O_2 (or O_2 is reduced to H_2O_2). At pH = 9 the

value for the oxidation of H_2O_2 to O_2 is -0.16 volts, which, although negative, may be coupled with a reaction in which Pu is reduced from Pu(VI) to Pu(V), where the stronger thermodynamic driving force for the reduction of Pu is the dominant force (vide infra). The line designated by the O_2/H_2O couple indicates the overall limit of thermodynamic stability for water, which results from the combination of the reactions for the oxidation of H_2O to H_2O_2 and further oxidation of H_2O_2 to O_2.

Some macromolecular electron transfer catalysts, such as enzymes, can catalyze the synchronous four-electron reduction of O_2. However, the reduction of O_2 in water occurs in successive steps in the absence of such catalysts. The initial two-electron oxidation of water to H_2O_2, with an oxidation potential of –1.776 volts, is very unfavorable thermodynamically, and provides the kinetic barrier to the rapid oxidation of water for solution compositions that have oxidation potentials that lie in the region between the lines established by the reactions for the four electron O_2/H_2O couple, and the two electron H_2O_2/H_2O couple. In other words, an aqueous solution of a strong oxidant may be metastable in water, even if oxidation of water is thermodynamically favorable, due to the high oxidation potential required by the initial oxidation of water to H_2O_2. As a result, it is possible to prepare solutions of OCl^- or H_2O_2 that are metastable with respect to oxidation of water.

Under acidic conditions, the reaction for the oxidation of HOCl to Cl_2 and H_2O may be combined with the reaction for the oxidation of water to oxygen, as shown in Table 3.

Table 3. Reaction of hypochlorous acid in water

$4HClO + 4H^+ + 4e^- \rightarrow 2Cl_2 + 4H_2O$	1.61
$2H_2O \rightarrow O_2 + 4e^- + 4H^+$	- 1.229
$4HClO + \rightarrow 2Cl_2 + O_2 + 2H_2O$	0.381

The positive value for the reaction of HOCl with water indicates that a solution of HOCl in acid is thermodynamically unstable, and that HOCl will spontaneously react with water to produce Cl_2 and O_2. However, the reaction may be kinetically slow due to the large positive overvoltage for the oxidation of water to O_2. Nevertheless, the volatility and relatively low aqueous solubility of both Cl_2 and O_2 may act as an additional driving force for the oxidation of water by HOCl. Like HOCl, OCl^- is thermodynamically unstable with respect to oxidation of water, but the reaction is also kinetically hindered due to the overvoltage required for oxidation of water to oxygen. Consequently, it is possible to prepare solutions containing OCl^- that are metastable, although such solutions do eventually decompose.

The redox lability of OCl^- is well known, and has been discussed by other authors (Greenwood and Earnshaw 1989b, Cotton et al., 1999). Both HOCl and OCl^-, as strong oxidants, react very readily with numerous materials, such as metallic iron. There have also

been reports of the observation of decomposition of OCl^- in aqueous solutions (Lister 1952, Adam et al. 1992, Church 1994, Wang and Margerum 1994, Adam and Gordon 1999). Decomposition pathways include a reaction of HOCl with OCl^- in addition to reaction with water. Additionally, HOCl and OCl^- may undergo catalyzed decomposition reactions in the presence of redox active metals, such as Fe or Pu. The generation rates of HOCl and OCl^- in NaCl brine exposed to α-radiation have been studied, and generation rate constants may be determined based upon data already existing in the chemical literature. Hence, some statements may be made about the expected persistence of HOCl and OCl^- in aqueous solutions:

- HOCl is thermodynamically unstable in acid and neutral solutions, and OCl^- is unstable in basic solutions
- HOCl and OCl^- in solution spontaneously decompose either by reaction with each other or with water
- HOCl and OCl^- decomposition reactions act as a pathway to limit their uppermost concentrations that may be reached under conditions of continuous generation
- Bounding conditions for upper limits of OCl^- concentrations due to radiolytic generation may be determined from knowledge of production and decomposition rates

3.5 Redox Behavior of Pu

Ultimately, it is the objective of the experimental work described in this test plan to determine whether HOCl or OCl^- generation in irradiated brines can produce conditions sufficiently oxidizing to affect the oxidation state distribution of Pu. It has been previously documented in the chemical literature that OCl^- oxidizes Pu to Pu(VI) (Choppin and Morgenstern, 2000); the question at hand is whether the process can become an important one in the WIPP environment. It is necessary to understand the redox behavior of Pu in order to determine the potential impact that the presence of OCl^- can have on Pu, both as an oxidant, and potentially as a complexing agent. The effect of acidity and complexation may be seen in Latimer diagrams for the reduction potentials of Pu under acidic, neutral, and basic conditions are presented as Figure 4, which is adapted from Weigel et al., (1986). An introductory discussion of Pu redox chemistry is based in part on these Latimer diagrams.

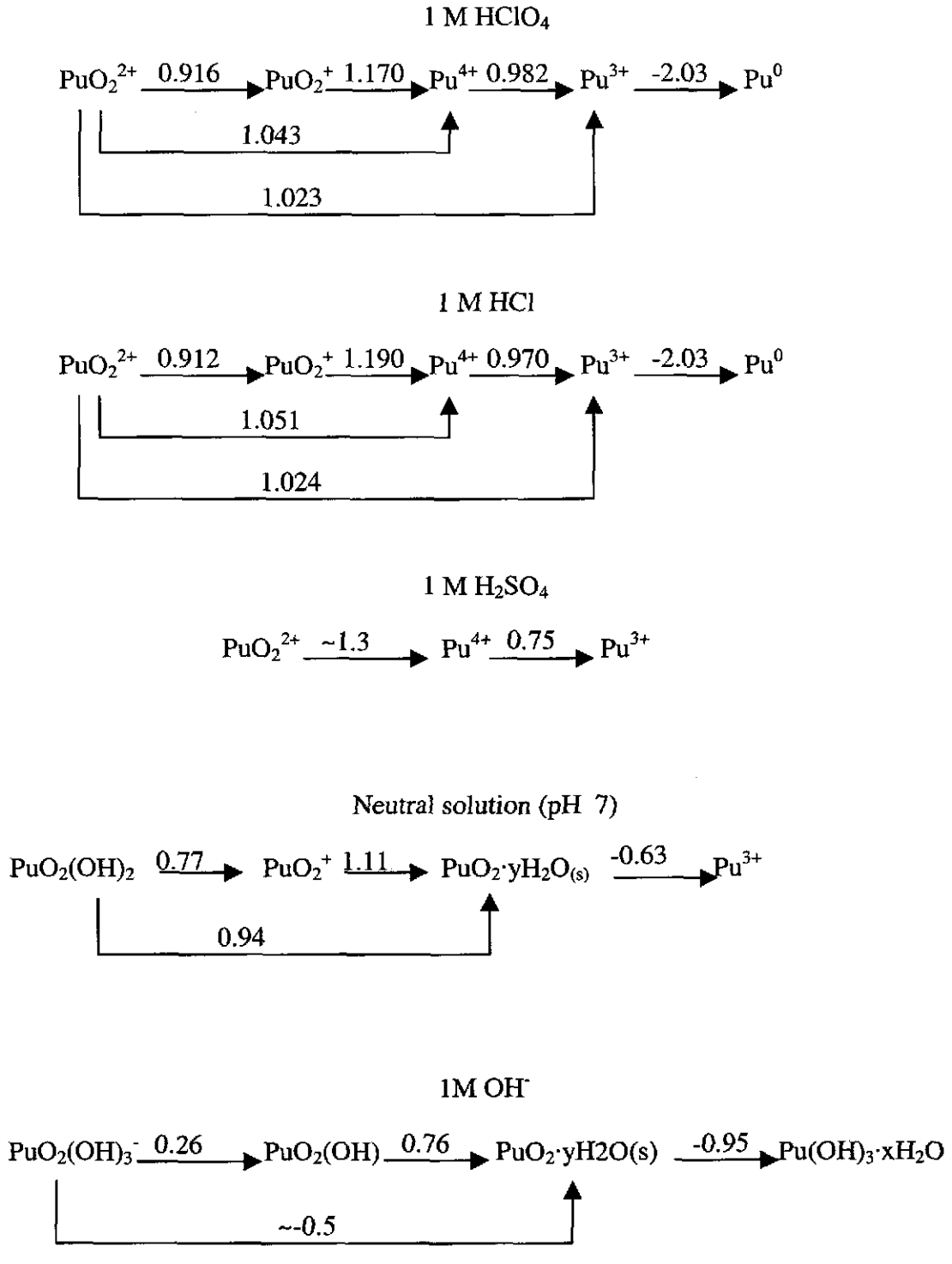

Figure 4. Latimer diagrams for oxidation/reduction behavior of plutonium.

The Latimer diagrams illustrated in Figure 4 are based on total concentrations of Pu at each respective oxidation state, not concentrations of the free metal ion. Since a positive e.m.f. indicates a thermodynamically favored reaction, the voltage values indicated on the Latimer diagrams for Pu shows that Pu^{3+} is strongly favored in acidic solutions. Comparison of the voltage values in $HClO_4$, HCl, and H_2SO_4 provide an illustration of the way that complexing and non-complexing media can affect the redox potentials. For example, the reaction:

$$PuO_2^{2+} + 4H^+ + 2e^- \rightleftharpoons Pu^{4+} + 2H_2O \qquad (15)$$

has potentials that are 1.043, 1.051, and ~1.3 volts, in $HClO_4$, HCl, and H_2SO_4, respectively. The differences among the potentials may be explained by the fact that for a given ligand the order of strength of complexation for the four oxidation states of Pu usually is given by

$$Pu^{4+} > PuO_2^{2+} > Pu^{3+} > PuO_2^{+} \qquad (16)$$

The conjugate bases ClO_4^-, Cl^-, and SO_4^{2-} form complexes with a given oxidation state of Pu that have relative stabilities occurring in the same order as the charge densities on the ligands, i.e.

$$SO_4^{2-} > Cl^- > ClO_4^- \qquad (17)$$

For this series of Lewis bases, complexation with Pu^{4+} is stronger than with PuO_2^{2+}. As a result, for the reduction of Pu(VI) to Pu(IV), the reaction that takes place in the more complexing medium tends to stabilize Pu(IV) relative to Pu(VI), and with increasing degrees of complexing ability further favoring the oxidation state that forms the strongest complexes, i.e. Pu(IV). Consideration of the relative abilities of SO_4^{2-}, Cl^- and ClO_4^- leads to the prediction that the reduction potential should be the most positive in H_2SO_4, and the least positive in $HClO_4$, which is confirmed by experimental measurements.

Pu(IV) has a very strong affinity for oxygen, so much so that it is capable of displacing protons from water, even under acidic conditions. In effect, the waters of hydration that are within the inner coordination sphere of Pu(IV) become very acidic. The tendency of coordinated water to lose a proton, referred to as hydrolysis, may be illustrated in the following reaction (with $n \approx 9$):

$$Pu(H_2O)_n^{4+} \rightleftharpoons PuOH(H_2O)_{n-1}^{3+} + H^+ \qquad (18)$$

The first hydrolysis of coordinated water becomes an important mechanism at about pH = 1, and is followed by subsequent hydrolysis reactions until, in the neutral pH region, PuO_2 has formed due to the loss of four protons from two water molecules. PuO_2, which is very insoluble, may have additional waters of coordination associated with it, and is sometimes written as $PuO_2 \cdot yH_2O_{(s)}$. It is the insolubility of Pu(IV) oxides, or hydrous

oxides that shifts the reaction equilibria for Pu in neutral and basic solution to favor the Pu(IV) oxidation state. Examination of the Latimer diagram for Pu in neutral solution reveals that the reduction potential for the reduction of Pu(VI) to Pu(IV) is 0.94 volts, which implies that in order to oxidize Pu(IV) to Pu(VI) in near neutral solutions it would be necessary to employ a strong oxidant that has a rather large oxidation potential. However, the situation is further complicated by the fact that the presence of any complexing ligand will have an impact upon the redox couples of Pu. For example, in strongly basic media (pH 14) Pu(VI) has about the same stability as Pu(IV), due to formation of anionic Pu(VI) complexes with hydroxide. It is generally true that for Pu, higher pH favors the higher oxidation states.

There are other aspects of Pu solution chemistry that may be discerned by examination of the Latimer diagrams for Pu. For example, it is apparent that it is not possible to prepare a solution of PuO_2^+ by direct oxidation of an acidic or neutral solution of Pu(III) or Pu(IV). This is due to the fact that the voltage required to oxidize Pu(IV) to Pu(V) is greater than the voltage required to oxidize Pu(IV) to Pu(VI). As a result, application of an oxidizing condition, either chemical or electrical, invariably results in quantitative oxidation of Pu to Pu(VI). In order to obtain Pu(V) in solution, it is necessary to oxidize all Pu to Pu(VI), then gently reduce the Pu(VI) to Pu(V). For that reason, oxidizing solution conditions will usually result in the presence of Pu(VI), but not Pu(V). Additionally, it should be noted that it is not possible to obtain large concentrations of Pu(V) in acidic solutions due to the Pu(V) disproportionation reaction, as illustrated for 1 M solutions of HCl in Table 4:

Table 4. Disproportionation of PuO_2^+

Reaction	E^0
$PuO_2^+ + 4H^+ + 1e^- \rightarrow Pu^{4+}$	1.190
$PuO_2^+ \rightarrow PuO_2^{2+} + 1e^-$	-0.912
$2\ PuO_2^+ + 4H^+ \rightarrow Pu^{4+} + PuO_2^{2+}$	0.278

However, there are ways to explore Pu(V) chemistry in acidic solutions, such as using classic radiotracer methods with ^{238}Pu. The short half-life of ^{238}Pu (87.7 years) allows the possibility of working with very dilute solutions of Pu, effectively quenching the disproportionation reaction by slowing the reaction kinetics.

As described earlier, Oversby has stated that (Neill 1998, Oversby 2000):

> "...Pu(V) is observed as a long-lived transient in many laboratory experiments. Pu(V) may be formed as a result of radiolysis reactions in brine, and while its total abundance in the repository is likely to be low, it might be significant as a transient species in some waste containers."

Oversby describes the possible reasons for appearance of oxidized Pu due to radiolysis effects. It is impossible to produce Pu(V) by direct oxidation of either Pu(III) or Pu(IV) in solution due to the overvoltage required to carry out the oxidation steps. Pu(VI) is the resultant oxidation state whenever direct oxidations of Pu(III) or Pu(IV) are carried out in solution. Pu(V) may then be produced by gentle reduction of Pu(VI). Observations of Pu(V) in brine solutions that are significantly affected by radiolysis may be due to initial oxidation of Pu(III,IV) to Pu(VI), by OCl^-, followed by reduction of Pu(VI) to Pu(V) by a reducing agent such as H_2O_2. Further reduction of Pu(V) to Pu(IV), or disproportionation of Pu(V), in basic solutions is kinetically hindered by the inverse fourth power dependence upon the hydrogen ion concentration.

This discussion is intended to introduce the reader to some of the subtleties of Pu solution chemistry, and describe some of the difficulties inherent in experimental work with Pu. It should be apparent that qualitative observations may be of little use when not obtained in conjunction with careful experimental design, vigilant control of numerous experimental variables, and judicious interpretation of data.

3.6 Redox Behavior of Fe

The corrosion of iron, present within the waste and as the waste containers, is expected to have a significant impact on the oxidation/reduction conditions within the WIPP. Iron corrosion under anoxic conditions should provide a source of electrochemical reductive capacity, which is expected to maintain Pu in a reduced state, as Pu(III) or Pu(IV). The standard reduction potentials for iron are presented in Table 5.

Table 5. Reduction reactions of iron

Reaction	E^0 (volts)
$Fe^{2+} + 2e^- \rightarrow Fe^0$	-0.447
$Fe^{3+} + 3e^- \rightarrow Fe^0$	-0.037
$Fe^{3+} + 1e^- \rightarrow Fe^{2+}$	0.77

The standard reduction potentials are for standard conditions of activity, and are not pH dependent in the range below which hydrolysis becomes an important feature. It is apparent that the Fe^0 to Fe^{2+} oxidation that occurs during corrosion of iron can provide a thermodynamic driving force of +0.447 volts, which, when coupled with other redox reactions, allows metallic iron to behave as a reducing agent. For example, coupling the oxidation of iron with the reduction of Pu^{4+} to Pu^{3+} in 1 M HCl solution is illustrated in Table 6.

Table 6. Reduction of Pu by metallic Fe

Reaction	Volt-equivalent
$Fe^0 \rightarrow Fe^{2+} + 2e^-$	+0.447
$2Pu^{4+} + 4e^- \rightarrow 2Pu^{3+}$	+1.94
$Fe^0 + 2Pu^{4+} \rightarrow Fe^{2+} + 2Pu^{3+}$	+2.387

An equilibrium constant for the reduction of Pu^{4+} by iron can be written as

$$K = \frac{[Fe^{2+}][Pu^{3+}]^2}{[Pu^{4+}]^2} \qquad (19)$$

Combining equations 9 and 14 and rearranging gives

$$\ln K = nFE/RT \qquad (20)$$

When the volt-equivalent is used, n = 1, T = 298, equation 20 yields a value of 2.4 x 10^{40} for the equilibrium constant. The large value of the equilibrium constant shows that Pu^{3+} is much more stable that Pu^{4+} in acid solutions containing iron. It is important to note that Fe^{2+} is the stable oxidation state of iron in acid systems, but the situation is quite different in neutral or basic solutions. The redox behavior of iron in neutral solutions is affected by the strong tendency of Fe^{3+} to form insoluble hydrolysis products, which tends to shift the equilibrium position between Fe^{2+} and Fe^{3+} in favor of Fe^{3+}. The reactions for complexation and precipitation of Fe^{2+} and Fe^{3+} by hydroxide may be respectively written as

$$Fe^{2+} + 2OH^- \quad Fe(OH)_{2,(s)} \qquad (21)$$

$$Fe^{3+} + 3OH^- \quad Fe(OH)_{3,(s)} \qquad (22)$$

The solubility product constants, K_{sp}, for iron hydroxide precipitates are written as (Baes and Mesmer, 1986):

$$K_{sp,Fe(OH)_2} = [Fe^{2+}][OH^-]^2 = 10^{-15} \qquad (23)$$

$$K_{sp,Fe(OH)_3} = [Fe^{3+}][OH^-]^3 = 10^{-38} \qquad (24)$$

The standard reduction potential for the reduction of Fe^{3+} to Fe^{2+}, 0.77 volts, may be used in the Nernst equation, along with the values for the solubility product constants of ferrous and ferric hydroxide precipitates to calculate a value of the reduction potential in

neutral and basic solutions. For example, using the Nernst equation and the K_{sp} values to solve for iron concentrations yields the reduction potential of Fe^{3+} to Fe^{2+} at pH = 9:

$$E = E^0 - 0.059 \log \left(\frac{\frac{K_{sp,Fe(OH)_2}}{[OH^-]^2}}{\frac{K_{sp,Fe(OH)_3}}{[OH^-]^3}} \right) \quad (25)$$

$$E = 0.77 - 0.059 \log(10^{18}) \quad (26)$$

$$= -0.292 \text{ volts} \quad (27)$$

The relatively large negative value for the reduction potential of Fe^{3+} to Fe^{2+} indicates that the reaction has a strong tendency to go in the reverse direction, i.e. Fe(III) is the stable oxidation state of iron in basic solutions, and Fe(II) will readily give up an electron in basic solutions. Perusal of the Latimer diagrams for Pu suggests that the dominant oxidation state of Pu in basic solution will probably be Pu(III) or Pu(IV), when coupled with the oxidation of iron from Fe(II) to Fe(III), although it is clear that milder oxidizing conditions can generate Pu(V) and Pu(VI) more easily in basic solutions than in acidic conditions. Additionally, as has been previously noted, complexing solutes will also affect the redox couples, and concomitantly, the redox speciation of Pu. Therefore a complete determination of the redox couples of Pu under WIPP conditions would require carefully designed and controlled experiments. The stability of these respective oxidation states depends upon attainment of a state of thermodynamic equilibrium.

The previous discussion on the redox properties of Pu illustrates the effect that ligands can have on the oxidation state distribution of Pu. In addition to affecting the redox couples, ligands also may affect solubilities, e.g. complexation of actinide ions with organic ligands solubilizes the metal ions, and must be quantified to make meaningful predictions of dissolved actinide concentrations. Well-defined values for complexation constants (commonly called stability constants) as well as solubility product constants are necessary to calculate actinide solubilities

3.7 Complexation Behavior of OCl^-

3.7.1 OCl^- as a Ligand

The complexing ability of OCl^- with actinide ions has not been systematically studied, although Kim has reported formation of OCl^- complexes with PuO_2^{2+} (Pashalidis et al. 1993). Experimentally observed OCl^- concentrations, and a brief summary of likely complexation properties are discussed within this test plan. Previous reports suggest that

OCl^- may be present in millimolar concentrations in the immediate vicinity of α-emitting radioactive material.(Kim et al. 1987, Pashalidis et al. 1993) OCl- may affect solution behavior of Pu; as an oxidant it may affect redox speciation, and as a ligand it may affect solubility. Hypochlorite complexes with PuO_2^{2+} are illustrated in equations (28) and (29):

$$PuO_2^{2+} + OH^- + OCl^- \rightleftharpoons PuO_2(OH)(OCl) \quad (28)$$

$$PuO_2^{2+} + 2OCl^- \rightleftharpoons PuO_2(OCl)_2 \quad (29)$$

Stability constants for reaction (28) have been reported as log $\beta_{1\text{-}11}$ = 14.0 at pH=6.7 and log $\beta_{1\text{-}11}$ = 14.5 at pH= 8.4 (μ=0.55 M, T=22° C). The stability constant for reaction (29) is log β_{102} = 10.3 (μ=0.55, T=22° C) (Pashalidis, 1993).

The short range of α-particles in solution can cause chemical environments that feature greater concentrations of radiolysis products in the immediate vicinity of radioactive sources than in the bulk solution, i.e. the actinides and ligands will occur together in close proximity. In fact it is likely that dissolution processes in localized heterogeneous microenvironments in a steady-state, non-equilibrium condition will be governed not by average solution concentrations of complexing ligands, but by concentration gradients that increase in magnitude as a function of proximity to the surface of the radiation-emitting solid. Figure 1 demonstrates that significant amounts of hypochlorite may be generated in NaCl solutions, especially brines. It is not necessary for multiple curie levels to be dispersed in brine to generate high local concentrations of hypochlorite because localized solution conditions will be established in the environs of the α-emitting radioactive source.

Figure 4 illustrates the steady state concentration of OCl^- generated as a function of radioactivity in 5 molal NaCl solution. The data used to generate the data points in this figure were taken from Kelm et al. (1999). The data points at ca. 6 and 12 Ci/L had not reached their respective steady state concentrations, therefore, there is not enough data to determine the type of function that correctly defines hypochlorite generation. However, the high-radioactivity solutions are not generally representative of conditions expected to persist within the WIPP.

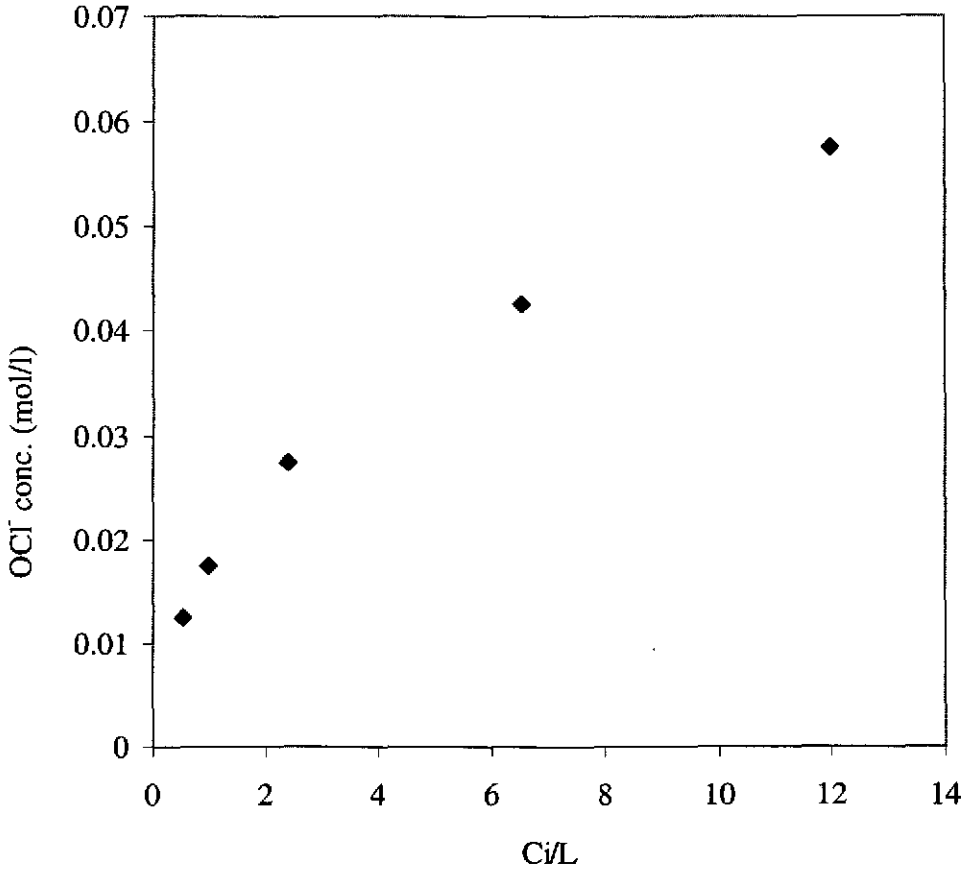

Figure 4. Generation of hypochlorite as a function of radioactivity in 5 mol/L NaCl at pH ca. 12.

3.7.2 Prediction of log β

The actinide ions (An(III,IV,V,VI)), which behave as hard acids due to their relatively low polarizability and high ionization potentials, interact with ligands primarily by electrostatic interaction (Pearson, 1963). As a result, an extended form of the Born equation, which relates electrostatic attraction to the Gibbs free energy of formation, may be used to make an approximate prediction of the magnitude of the stability constant for trivalent actinides or lanthanide analogs when the stability constant for another actinide/ligand pair is known (Choppin and Rizkalla, 1994). The relationship is illustrated by equation 30:

$$\Delta G = \frac{-N_A e^2 Z_1 Z_2}{418.7 D_e d_{12}} - \nu RT55.5 + \sum \ln f(I) \qquad (30)$$

where ΔG is the Gibbs free energy of complex formation, N_A is Avogadro's number, e is the fundamental unit of charge, Z_1 is the charge on the metal ion, Z_2 is the charge on the ligand, D_e is the effective dielectric constant (57 for An^{3+} or Ln^{3+}, 40 for An^{4+}, 65 for AnO_2^{+}, 55 for AnO_2^{2+}), d_{12} is the distance between the metal and ligand, m is the change in number of the reacting species, and $\Sigma \ln f(I)$ is the activity coefficient term to correct for effect of ionic strength (Choppin and Rizkalla, 1994). The relationship between the Gibbs free energy and the stability constant, β, is:

$$\Delta G = -RT\ln\beta \qquad (31)$$

where R is the ideal gas constant, 8.314 J/molK and T is the absolute temperature in kelvins. Substituting equation 31 into equation 30 gives:

$$\ln\beta = \frac{N_A e^2 Z_1 Z_2}{RT418.7 D_e d_{12}} - \nu RT55.5 + \sum \ln f(I) \qquad (32)$$

Equation 32 may be simplified for when comparing reactions that have the same number of reacting species and are at constant ionic strength:

$$\log\beta = \frac{AZ_1 Z_2}{D_e d_{12}} + B \qquad (33)$$

A is a constant that encompasses Avogadro's number, the elementary unit of charge, the ideal gas constant, temperature and the proportionality constant 418.7; B is a constant that includes the change in number of reacting species and ionic strength corrections. Equation 33 indicates that a plot of the logarithm of the stability constants vs. charge on the metal ion for complexes of actinides with a given ligand should be linear when corrected for variations in the effective dielectric constant and the metal-ligand distance. A useful modification of equation 33 is given by equation 34 (Choppin, 1999)

$$\log\beta_n(C) = \log \beta_n(D) \times (Z_C/Z_D) \times (D_D/D_C)(d_{D/C}) \qquad (34)$$

C and D are used to
The effective charge on the metal ion for the four common actinide oxidation states may be summarized as (Choppin and Rao, 1984)

$Pu^{4+} > PuO_2^{2+} > Pu^{3+} > PuO_2^{+}$
$Th^{4+} > UO_2^{2+} > Am^{3+} > NpO_2^{+}$
$4 > 3.3 > 3 > 2.3$

Figure 5. Effective charge on actinide cations.

Plutonium follows the pattern for effective charges on the metal atom as in the corresponding oxidation states of Th^{4+}, UO_2^{2+} Am^{3+} and NpO_2^{+}. The larger effective charge on the AnO_2^{2+} ion relative to the An^{3+} ion often causes the magnitude of the logarithm of the stability constants for AnO_2L^{2-n+} complexes to be about 10-30% greater than the respective complexes with An^{3+} when steric effects to not interfere. Therefore, the magnitude of β_{102} for the Am^{3+} (and Nd^{3+}) complexes with OCl^- should be about 8-9 log units, based on the data for the stability constant of OCl^- with PuO_2^{2+} (Pashalidis et al. 1993).

3.7.3 Comparable ligands

A survey of the National Institute of Standards and Technology (NIST) stability constant database reveals a paucity of data for complexes of metals with hypochlorite. Cyanate (OCN^-) may be expected to exhibit similar complexion behavior to hypochlorite since the pseudohalogen cyanide group replaces the chlorine atom. However, since cyanate exhibits linkage isomerism, a comparison would be valid only for coordination through the oxygen atom of the cyanate group. HOCN has $pK_a = 3.48$ (μ=0 M, T=25° C), making it a weaker conjugate base than OCl^-. Therefore OCN^- complexes formed through the oxygen atom should be weaker than corresponding complexes with OCl^-. Unfortunately, the database for complexation with cyanate is limited to Co^{2+} and Ag^+, both of which may coordinate through the nitrogen atom of cyanate, and neither of the metal ions are suitable analogs for lanthanides or actinides.

The halate anion ClO_3^- may also be generated as a result of α-radiolysis in chloride brine. Ligands with higher pK_a values form stronger conjugate bases, with attendant greater affinity for metal cations. In general, the stabilities of complexes are proportional to the pK_a values of the protonated form of a ligand. The pK_a value for $HClO_3$ is –2.7 (μ=0.10 M $NaClO_4$, T=298 K), making ClO_3^- a rather weak base. Most ligands, with $pK_a<2$ (including ClO_3^-) form only outer sphere complexes with actinides, and it has been shown that $LnClO_3^{2+}$ and $UO_2ClO_3^+$ conform to this behavioral model (Choppin et al. 1988). In contrast, OCl^- most likely forms inner-sphere complexes with actinides; with the accompanying differences in the nature of the enthalpy and entropy driving forces of the complexation reaction. As a result, halates do not make useful analogs for hypohalite anions.

3.7.4 Effect of Complexing Agents on Actinide Solubility

The effect of ligand complexation upon actinides under WIPP conditions causes an increase of actinide solubility and mobility. Actinide solubility is controlled by the extent of complexation and by the solubility product constant of actinide precipitates, or actinide bearing solids in which actinides are co-precipitated as members in a non-actinide host phase. The dissolution of actinide precipitates may be generally described by the equation:

$$(An_p^{n+}B_q^{t-})_s \quad \rightleftharpoons \quad pAn^{n+} + sB^{t-} \tag{35}$$

where $np = st$, An represents an actinide cation with overall charge of n+, and B is a counter-ion that participates in formation of a precipitate.

The solubility product constant is generally expressed as

$$K_{sp} = \{An^{n+}\}^p\{B^{t-}\}^s \tag{36}$$

where the braces indicate thermodynamic activities.

Complexation of the actinide ion in solution will cause further dissolution of the solid phase to compensate for perturbation of the equilibrium expressed in equation (35). Formation of actinide/ligand complexes is described by equation (37), where charges on the metal and ligand are omitted for simplicity:

$$pAn + H_qL_r \quad \rightleftharpoons \quad An_pH_qL_r \tag{37}$$

The thermodynamic stability constant for such a complex is defined as

$$\beta_{pqr} = \frac{\{An_pH_qL_r\}}{\{An\}^p\{H_qL\}^r} \tag{38}$$

The relationship between the solubility product constant of an actinide bearing solid and the solubilizing effect of complexation is illustrated by substituting equation (38) into equation (36):

$$\frac{K_{sp}}{\{B^{t-}\}^s} = \frac{\{An_pH_qL_r\}}{\beta_{pqr}\{H_qL\}^r} \tag{39}$$

The total solubility of an actinide ion is the sum of the free metal ion concentration and the concentrations of all other soluble species. The sum of concentrations of all soluble species

is described by

$$An^{n+} + \sum_{q=0}^{q'} \sum_{r=1}^{r'} [AnH_qL_r] \qquad (40)$$

where q' and r' are the maximum possible values of q and r, and L is the only ligand in the system. Accordingly, addition of complexing ligands will lead to greater total solubility of metal ions.

3.8 Extraction Method for Determination of Stability Constants

Liquid/liquid extraction is a well-developed method and has been extensively used in support of the WIPP actinide science program to determine the stability constants of actinide metal ions and other metal cations with numerous different ligands (Chen et al. 1999, Bronikowski et al. 1999, Choppin and Pokrovsky 1997, Bronikowski et al. 1998, Borkowski et al. 1999, Borkowski et al. 1996, Borkowski et al. 2000). The distribution of a metal ion between two immiscible phases in the presence of an organophilic extractant is described by a distribution coefficient:

$$D = \frac{\sum[M_{org}]}{\sum[M_{aq}]} \qquad (41)$$

where $\Sigma[M_{org}]$ is the sum of the concentrations of all metal species in the organic phase and $\Sigma[M_{aq}]$ is the sum of the concentrations of all metal species in the aqueous phase. An aquophilic complexing agent may exert a competitive influence on the metal distribution that is described by equation 42:

$$\frac{D_0}{D} - 1 = \sum_{1}^{n} \beta'_{10n}[L]^n \qquad (42)$$

where D_0 is the distribution coefficient in the absence of the complexing ligand, β'_{10n} are the successive apparent stability constants, and [L] is the ligand concentration. The apparent stability constant is related to the true stability constant as expressed by equation 43:

$$\beta'_{101} = \beta_{101}/(1 + \sum_{1}^{n} \beta_n^{OH^-}([OH^-])^n + \sum_{1}^{n} \beta_n^{B^-}([B^-])^n) \qquad (43)$$

where $\beta_n^{OH^-}$ is the n^{th} hydrolysis constant, $\beta_n^{B^-}$ is the n^{th} stability constant of the metal with the buffer, [OH^-] is the hydroxide concentration and [B^-] is the free buffer concentration.

In solvent extraction determination of stability constants, it is necessary that the complexing ligand and the metal/ligand complex are much more soluble in the aqueous phase than in the organic phase. This condition is often fulfilled when the metal ligand complex is charged, solvated with water molecules, or has ligands that exhibit aquophilicity through hydrogen bonding. Metal/hypochlorite complexes are expected to satisfy these conditions.

3.9 Use of Analogs

The trivalent lanthanide Nd(III) will be used for stability constant determinations due to its redox stability and to its similarity in charge density to Am(III) and Pu(III). The use of lanthanide cations as analogs for the trivalent actinides is a widely accepted practice, and has been documented elsewhere (Choppin, 1999). Initial determination of the stability constant of OCl^- with Nd is expected to be advantageous because the +3 oxidation state is the only stable oxidation state of Nd. Lack of other accessible oxidation states obviates the necessity of oxidation state control of the metal ion and ensures that it is not possible for the metal ion to cause catalytic decomposition of OCl^-. Moreover, Nd is not a radioactive material, does not present notable toxicity hazards, and may be conveniently handled in experimental work as an ordinary chemical component.

3.10 Brine Compositions

Compositions of WIPP Brine A and ERDA-6 and GWB are given in Table 7. The ionic strengths were calculated from data in Table IV with the equation

$$\mu = 1/2 \sum c_i z^2 \qquad (44)$$

where μ represents the ionic strength, c_i is the concentration of component "i", and z is the charge on the ion. In this case, ionic strength is given in concentration units, rather than activities. The higher ionic strength of Brine A is predominantly due to the higher Mg^{2+} content.

Table 7. Chemical Components of WIPP Brines

Ion or Chemical Property	Brine A (a)	ERDA-6 (a)	GWB (b)
B^{3+} (mM)	63	20	156
Br^- (mM)	11	10	27
Ca^{2+} (mM)	12	20	14
Cl^- (mM)	4800	5350	5610
K^+ (mM)	97	770	467
Mg^{2+} (mM)	19	1440	1020
Na^+ (mM)	4870	1830	3570
SO_4^{2-}	170	40	178
ionic strength (M)	5.57	7.07	6.0

(a) data from Table SOTERM-1, DOE (1996)
(b) data taken from Zhang et al. (1999)

Other metals, such as Fe, Co, Ni, and Mn, will be present in the WIPP as a result of corrosion of waste containers. Steel, composed primarily of iron, with smaller amounts (usually less than 1%) of other components such as Co, Ni and Mn, will provide masses of Fe that far exceed the amounts of the other transition metals. As a result, it is expected that the primary transition metal component in the WIPP environment that can affect the stability of OCl^- will be Fe. It is not anticipated that transition metals other than Fe will exhibit a greater influence than that of Fe.

3.11 Objectives

The objectives of the studies proposed in this test plan are to:

- Determine the rate of decomposition of OCl^- in WIPP-representative brines, including the influence of waste components, such as iron , on decomposition.
- Determine and measure solution conditions that have an impact on complex formation of metal ions with OCl^-
- Determine the stability constants for complex formation of OCl^- with metal ions

Intended use of the data:
Actinide solubility affects the magnitude of the contribution of the direct brine release to the generation of a Complementary Cumulative Distribution Function (CCDF), which is used as an EPA mandated evaluation of regulatory compliance.

The results of this study will be used to:

- Determine OCl^- decomposition rates in order to calculate whether OCl^- generation will be sufficient to affect oxidation/reduction conditions within the repository
- Determine whether complexation by radiolysis products, such as OCl^-, will contribute to increased actinide solubility in the WIPP.

Additionally, of equal importance is a demonstration that processes that are deemed to be significant to repository behavior are quantitatively understood.

4.0 EXPERIMENTAL PROCESS DESCRIPTION

4.1 Sample and Data Control

4.1.1 Critical Variables to be Measured and Controlled

Variables that must be controlled in the types of experiments described within this test plan include:

- pH
- temperature
- sample volume
- sample composition

The decomposition of HOCl or OCl^- may have an effect on the pH of the host solution. Reactions of HOCl and OCl^-, which may affect solution pH values, are listed in Table 1. HOCl is a weak acid, with a pKa $\approx$ 7.5 in low ionic strength solutions, and will probably exhibit an increase of 0.5 to 1 pK unit in high ionic strength solution. There will be some buffering of pH by the acid/base pair of HOCl/OCl^-, although the self-buffering capability will depend upon decomposition pathways and kinetics, which must be experimentally determined. Initially, an attempt will be made to use the self-buffering capacity of the HOCl/OCl^- pair because it is also unknown whether other buffers, such as boric acid/borate will react with either HOCl or OCl^-. The kinetics of decomposition with and without added buffer may be compared to determine whether there is an effect. The representative WIPP brines, ERDA-6, GWB, and WIPP Brine A all contain boric acid/borate, which makes an initial determination of kinetics in a non-boron bearing brine an important first step in the overall examination of the behavior of HOCl and OCl^- in WIPP brines. Solution pH will be controlled by adding small amounts of non-interfering acid or base, such as HCl or NaOH solution. Solution pcH (pcH is the negative logarithm of the hydrogen ion concentration) will be measured with a standard, calibrated pH meter equipped with a combination glass electrode. Any adjustments to solution pH at the beginning or during the course of the experimental work will be recorded in the scientific notebook, along with the measured pH values.

The solution temperatures will be controlled during titrations by performing the experiments in sample vessels immersed in a constant temperature water bath. Refer to the section describing measuring and test equipment for a description of temperature control apparatus.

Sample volumes will be measured with standardized volumetric glassware and calibrated Class A pipets, or calibrated autopipets. Refer to the section describing measuring and test equipment for a description of calibration and control of volumetric glassware and pipets.

Sample composition will be determined by solution preparation using standard laboratory techniques with calibrated equipment. Concentration of HOCl and OCl^- in the decomposition kinetics experiments will be determined by UV-Vis spectroscopy. Concentrations of Nd will be determined by complexometric titration and analysis by atomic emission spectroscopy.

Deviations from these standards, such as allowing sample temperature to equilibrate with ambient temperature rather than remaining under controlled conditions, will be noted in the laboratory notebook, along with descriptions of the acceptability of such deviations and the impact upon the experiment.

4.1.2 Coordination with Organizations Providing Inputs or Using the Results

There are no other organizations providing inputs in terms of data, experimental design, sample analysis, data compilation or interpretation of results. No coordination activities for inputs are planned at the time of the writing of this test plan.

The outcome of the experimental work described herein is unknown at the time of the writing of this test plan, although it may be anticipated that the data will be used to further evaluate the long-term effects of radiolytic generation of oxidants. The results of the experimental work will be provided to the DOE CBFO for further evaluation with regard to screening as a feature, event, or process that may affect the long-term performance of the WIPP.

4.1.3 Procedures to be Used/Developed

It is not necessary to develop new procedures to accomplish the tasks described in this test plan. The procedures that will be used are part of commonly practiced standard laboratory techniques such as titrations and spectrophotometry. The procedures that will be employed are generally described in the section describing reagents and procedures, although specific procedures as applied to a particular experiment will be completely documented in the scientific notebook.

No prerequisites or special controls are specified at the time of the writing of this test plan. No unusual procedures to control specific environmental conditions, such as storage

under controlled atmosphere, are necessary. Controls over other relevant conditions will be recorded in the laboratory notebooks. No unusual processes are anticipated to be employed. The skills developed during the course of work in an analytical or inorganic chemistry laboratory are anticipated to be sufficient to successfully perform the work.

4.1.4 Known Sources of Error and Uncertainty

Sources of error include:
•pH measurement
•volume measurement
•weighing error
•impure reagents
•data transcription error

Errors of pH measurement will be minimized by calibration of measuring equipment with standard buffer solutions and by titration with standardized acid and base solutions. Standard procedures for instrumental pH measurement are widely practiced and published in peer reviewed literature. Procedures will be described in the laboratory notebook and relevant procedural references provided. Volume and weighing measurement error will be minimized by calibration of all volumetric and weighing equipment with accompanying documentation in the laboratory notebooks. All reagents will be A.C.S. reagent grade or better. If necessary, reagents will be purified by standard, documented procedures. Data transcription error will be minimized, and can be traced by attaching hardcopies of instrumental data output within the laboratory notebook.

4.1.5 Data Processing and Mathematical Models

Data processing may be done by hand calculation with the aid of an electronic calculator, or with a standard spreadsheet program, such as Microsoft Excel. Data processing more complicated than simple algebraic manipulations are not anticipated at the time of the writing of this test plan.

4.1.6 Documents to be Maintained as QA Records

Scientific notebooks and hardcopies of instrumental output will be maintained as QA records. Instrument output in electronic format will be preserved on a computer disk or other suitable media, and will be submitted to the Sandia National Laboratories records center along with other QA records.

4.1.7 Sample Handling and Control Requirements

Standard procedures for sample identification, handling, storage, shipping, archiving and disposition have been described in Sandia National Laboratories Nuclear Waste Management Program Procedure NP 13-1. Sample handling will be performed under the guidance of NP 13-1.

Samples will be labeled with unique identification numbers, date, and will be referenced within the laboratory notebook. Solutions, such as standardized stock metal solutions, will be handled and stored in accordance with documented procedures.

Samples will be stored within the working area of the Chemistry and Geochemistry research area at the laboratory of Sandia National Laboratories, Carlsbad. No special precautions are planned to secure the samples.

4.1.8 Sample Disposal

Aqueous solutions of HOCl and OCl^- in brines are non-hazardous, and may be disposed of directly into the sewer, without any special precautions. Organic solutions will be disposed of in accordance with standard operating procedures in place at the Sandia National Laboratories Carlsbad laboratory. Hazardous waste generation is not anticipated at the time of this writing.

4.1.9 Data Acquisition System

Calibrations and calibration checks will be performed on instruments in the manner described in the Measuring and Test Equipment section. Analytical instruments and laboratory equipment will be considered to be exhibiting acceptable performance when the following criteria are met:

- Calibrations for the ICP-OES instrument will be considered successful if initial calibration data exhibit linearity within tolerances established by the instrument manufacturer.
- Initial or continuing calibration of analytical balances will be considered as indicating fitness for use when the instrument indicates that all standard calibration check weights conform within 0.1% of the nominal value.
- Volumetric equipment must exhibit less than 1% relative standard deviation error in order to be considered acceptable for use.
- Calibration of pH measuring apparatus will be considered acceptable if the data exhibit linearity, and the instrument response is greater than 90% efficient (i.e. > 53.1 mV/pH unit).
- Wavelength and percent transmittance calibration of the Cary-300 UV-Vis spectrophotometer will be performed upon instrument start-up, at least one time per day that the instrument is used.

4.1.10 Commercial Software, Not Modified

The commercial software that will be used in the work described in this test plan includes the software that is used to operate the analytical instruments, and spreadsheet software for performing routine calculations.

The IPC-OES is operated by the system software supplied by the instrument manufacturer.

The Cary-300 UV-Vis spectrophotometer is operated by the system software supplied by the instrument manufacturer.

Routine spreadsheet calculations will be performed with Microsoft® Excel 2000 run on a Dell Precision 620 desktop P.C., or equivalent. Use of any other spreadsheet programs will be described and documented in the scientific notebook.

4.1.11 Other Software

No software other than commercial, off-the-shelf software, not modified, will be used in this work.

4.1.12 Methods of justification, evaluation, approval, and documentation of any deviations from test standards

Significant departures from procedures documented in the open scientific literature will require revision of this test plan.

4.1.13 Experimental Controls

Each experimental determination of decomposition rate constants will be repeated in order to reduce likelihood of inadvertent introduction of indeterminate errors. The use of blank spikes, matrix spikes, internal or surrogate standards are not necessary or compatible with the experimental methods used in the kinetics experiments proposed in this test plan.

Each experimental determination of the metal/ligand stability constant will be performed at least three times, with no less than two nominally identical samples used to determine values for each data point. Known quantities of reagents will be introduced into each sample, so mass balances may be calculated from the amount recovered from each phase, making internal and surrogate standard spikes generally unnecessary. It should be noted that experimental procedures may be altered such that spikes are included in experimental procedures if it is necessary to account for variations in instrumental response.

4.1.14 Control and Characterization of Test Media

Test media and samples will be characterized by the analytical methods described elsewhere in this test plan.

4.1.15 Data Identification and Use

Data that is amenable to written recording will be inscribed by hand in appropriate laboratory notebooks. Such information includes, but is not limited to:

- reagent and solution preparation and purification procedures and results
- sample preparation procedures
- sample composition and conditions e.g. pH, reagent volume, reagent concentration, temperature
- sample handling
- sample analysis procedures and results

Instrumental data output, such as tabulated values and parameters, will be stored in a data binder, and appropriate reference to the data location will be made within the laboratory notebook.

4.1.16 Data Transfer and Reduction Controls

Typical data transfer is from instrumental output to laboratory notebook and from laboratory notebook to a spreadsheet program. Printed copies of spreadsheets with full explanations of spreadsheet calculations will be permanently attached to the laboratory notebook or within a data binder specifically designated for the purpose. Data that is stored separately from the laboratory notebook, e.g. in a designated three ring binder, will be appropriately referenced and described with respect to location, within the laboratory notebook.

4.1.17 Identification, Segregation, Disposal of Erroneous Data

Data that is suspected to be erroneous will be tested by comparison to replicate samples or replicate experiments. Statistical justification for rejection of erroneous data will be provided within the laboratory notebook.

4.2 Reagents and Procedures

4.2.1 Measuring and Test Equipment

Measuring and test equipment, including but not limited to, the Sandia National Laboratories Carlsbad laboratory ICP-OES, balance, pipets, pH meter, UV-VIS spectrophotometer will be used in accordance with the Sandia National Laboratories Nuclear Waste Management Program Procedure NP 12-1, Control of Measuring and Test Equipment.

The ICP-OES is an inductively coupled plasma atomic emission spectrometer.

Liquid samples are introduced into the instrument through an autosampler. The samples are aspirated into a plasma ionization chamber, which destroys the sample matrix, atomizes and ionizes the component atoms. Photons of discreet energies are emitted upon transition from the quantized excited to ground electronic states for each component element, which allows quantification by wavelength dispersive analysis of the intensities of the light given off during the de-excitation process. The spectrometer is calibrated by using the measurement of instrument response to plot a calibration curve for a series of samples containing standardized amounts of the analyte of interest. Under ordinary circumstances the instrument has a dynamic range of several orders of magnitude, and features linear response to sample concentration. Second (parabolic) or higher order response in analytical instruments often indicates detector saturation, matrix interference, or other concentration dependent instrumental responses. Evaluation and documentation of calibration, and calibration data will be recorded in the scientific notebook. No use of internal standards is anticipated. Use of surrogate standards, blank spikes, matrix spikes, or other methods of batch control will be documented in the scientific notebook.

Analytical balances will be calibrated before use on a daily basis, at a minimum. Certified, traceable calibration standard weights will be used as calibration standards, continuing calibration check standards, or both.

Solution volumes will be measured either with Class A glass pipets, or autopipets equipped with disposable tips. Calibration of all pipets will be confirmed before use by measuring the volume of water dispensed, which will be determined by mass, as indicated by a calibrated analytical balance. Density conversion factors for water as a function of temperature will be taken from the Handbook of Chemistry and Physics, published by CRC Press, or another reliable, documented source. Atmospheric buoyancy corrections for calibration of volumetric glassware are not required.

Instrument response of potentiometric pH measurement instrumentation will be checked by calibration against traceable standard buffer solutions, or by titration of standardized acid and base solutions. Identity of the calibration solutions will be recorded in the scientific notebook. Constant temperature and atmosphere conditions will be maintained during titrations, if necessary, by immersion of the titration vessel in a thermostated water bath, the temperature of which will be monitored with a thermometer that will be calibrated against a certified, traceable standard thermometer. If necessary, inert atmosphere will be maintained by purging the titration vessel with N_2. Temperature and atmosphere control and conditions will be recorded in the scientific notebook.

The UV-VIS spectrophotometer is a Cary 300 Ultraviolet-Visible Spectrophotometer, equipped with D_2 and tungsten filament lamps. The instrument performs an internal wavelength calibration upon start-up, using emission lines generated by the D_2 lamp. The 100% transmittance calibration is performed by placing a cuvette containing the solvent without the chromophore, and scanning the instrument through the analytical wavelengths. The 0% transmittance calibration is performed by blocking the sample path with an opaque object, such as black painted sheet metal, and scanning the

instrument through the same wavelength region as used in the 100% transmittance measurement. The instrument responses are assigned to the respective 0 and 100% transmittance measurements at each wavelength.

4.2.2 Reagents

Deionized water will be used to prepare all aqueous solutions. All aqueous and organic solutions will be filtered through 0.20 or 0.45 mm pore size membrane filters, as necessary.

High purity OCl^- will be synthesized by one of several methods documented in peer-reviewed literature, or obtained from documented commercial sources. Possible methods include bubbling g Cl_2 gas through carbonate free 0.6 M aqueous NaOH or passing Cl_2 gas through an HgO slurry with subsequent reduced pressure distillation into aqueous NaOH (Adam and Gordon, 1999). Concentration of OCl^- may be determined spectrophotometrically (ε = 350 M^{-1} cm^{-1} at 292 nm), by potentiometric titration, or by other appropriate, documented methods (Vogel 1989, Adam and Gordon 1999).

4.2.3 Metal Solutions

Lanthanide solutions will be standardized by published procedures, such as complexometric titration with volumetric standard EDTA solution and xylenol orange indicator (Vogel, 1989).

4.2.4 Electrolyte Solution Compositions

The proposed work will be conducted in solutions of four different general composition types:

1. NaCl at 5 molal ionic strength
2. Modified WIPP Brine A
3. Modified WIPP ERDA-6
4. Modified GWB

Brine A, ERDA-6 and GWB are saturated solutions, so loss of small amounts of water, (e.g. by evaporation), causes precipitation, and possible formation of lanthanide-bearing solids, either as co-precipitates, or as adsorbates onto the crystal surfaces of solids. Using a diluted form of the brine in order to remain below saturation most easily mitigates the potential for manifestation of such an uncontrolled variable. Consequently, modified forms of Brine A, ERDA-6, and GWB will be prepared that are diluted by 5% on the molar scale. It is possible that preparation of pcH standards will require further modification of the brine compositions. All brine compositions will be documented in the laboratory notebooks, along with explanations for use of a particular brine composition.

4.2.5 Experimental Procedures

4.2.5.1 General Conditions

Sample preparation and analysis procedures, (weighing, pipetting, etc.) are parts of standard laboratory analytical procedures. Instrumental analyses, such as ICP-AES and UV-Vis spectroscopy will be performed in accordance with written procedures that have been supplied by the instrument manufacturer, or other documented procedures that have been demonstrated to be appropriate. Atmospheric components, such as N_2, O_2, Ar and CO_2 have not been reported to affect the decomposition of HOCl/OCl^-, and there is no current evidence that such control is necessary, therefore, controlled atmospheric conditions for complexation and decomposition experiments will not be used. Calibration of pcH measurement instrumentation will be performed under inert (N_2) atmosphere with temperature control. Design of experimental apparatus and method of control of parameters (temperature, atmosphere, etc.) will be fully described in the laboratory notebooks. Temperatures of samples will be monitored and recorded.

4.2.5.2 Decomposition Kinetics

Samples of HOCl and/or OCl^- will be prepared under various conditions of concentration, pcH, brine composition, and added components. A general description of sample preparation will be given here, but complete, detailed, and documented descriptions of sample preparation will be provided in the laboratory notebooks.

Samples of HOCl/OCl^- will be prepared by diluting a stock solution, (either synthesized or obtained from a commercial source) into solutions of various pcH and brine compositions. Samples of specific composition will be large enough (e.g. 250 ml) for repeated sampling and analysis by UV-Vis examination of the HOCl/OCl^- absorbance peaks. Approximately 5-10 ml aliquots will be removed for each analysis, allowing as many as 25 to 50 analyses per sample. Upon preparation, a spectrum of each sample will be obtained. The intensities of the absorbance maxima associated with the electronic transitions attributable to HOCl and OCl^- may be used to determine the respective concentrations of each moiety. The UV-Vis spectra of the samples will be repeatedly obtained over measured time intervals in order to determine the change in concentration of HOCl and OCl^- as a function of time. The time dependence of the change in concentration may be used to derive rate constants that quantitatively describe the kinetic behavior of the decomposition pathways, and their dependence on pcH and solution composition.

There have not been reports of the dependence of the decomposition of HOCl or OCl^- on exposure to light, therefore, some samples will be stored in the dark, and others exposed to room light in order to establish whether exposure to light affects the systems. The appropriate number and type of samples held in the dark and exposed to light will be experimentally determined.

HOCl and OCl^- concentrations will be varied to measure the rate dependence on the concentration of these components. The pcH dependence of decomposition rates will also be determined by preparing samples adjusted to different initial pcH conditions, and measuring change in HOCl/OCl^- concentration as a function of time and acidity in order to develop a predictive model that would be useful under a variety of pcH conditions. It is unknown at this time whether brine components, such as SO_4^{2-} or $B_4O_7^{3-}$ will affect decomposition behavior, therefore, initial measurements will be made in solutions, both with and without SO_4^{2-} or $B_4O_7^{3-}$.

The effect of brine composition on kinetics of decomposition of HOCl/OCl^- will be determined by measuring the changes in concentration over time in a variety of solution matrices. Redox active transition metals, such as iron, may affect decomposition rates, therefore samples will be prepared that include iron, added in metallic and oxidized form (e.g. $FeSO_4$).

4.2.5.3 Stability Constant Determination

The theory of the method has been described in Section 3.8. A general description of the experimental process is supplied here, but it will be necessary to experimentally determine specific parameters, such as appropriate reagent concentrations. In a typical experiment, a series of glass liquid scintillation vials (or other appropriate sample vessels), (≈20 ml) will be filled with 5 ml of the aqueous phase and 5 ml of the organic phase. The aqueous phases will contain varying concentrations of the complexing ligand. Other variables, such as pH, ionic strength, temperature, extractant concentration and volumes of the phases, will be monitored. The vials will be mechanically shaken long enough to ensure equilibration of complex formation and interphase transfer reactions. The length of equilibration time must be experimentally determined, but it usually ranges between 15 minutes and several hours. After equilibrium has been reached, the sample containers may be centrifuged to assist in phase separation, then an aliquot removed from each phase for measurement of distribution ratios of the metal ion. Metal ion concentrations in the sample aliquots may be measured by a variety of techniques, such as UV-VIS spectroscopy, or ICP-OES. ICP-OES or another documented technique will be employed to measure phase distribution of Nd, and other metals that will be systematically added to the solutions, such as Fe, Co, and Ni. UV-VIS spectroscopy will be used to determine whether decomposition of solution components occurs during the course of the experiment.

5.0 TRAINING AND OTHER STANDARD PROCEDURES

5.1 Training

All personnel participating in the work described in this Test Plan will be trained and qualified for the assigned tasks. This requirement will be implemented in accordance with NWMP procedure NP 2-1, "Qualification and Training."

5.2 Standard Procedures

The following NWMP Procedures and Project Specific Procedures are applicable:

SOP-C001: "Standard Operating Procedure for Activities in the SNL/Carlsbad Laboratory Facility."
SP 13-1 "Chain of Custody
NP 6-1 "Document Review Process"
NP 13-1 "Sample Control"
NP 12-1 "Control of Measuring and Test Equipment"
NP 20-1 "Scientific Notebooks"
NP 2-1 "Qualification and Training
NP 17-1 "Records

6.0 HEALTH & SAFETY

There are no unusual health and safety requirements for the work described in this test plan. The health and safety requirements relevant to the tasks for work in this test plan are described in SOP-C001

7.0 PERMITTING/LICENSING

There are no special licenses or permitting requirements for the work described in this test plan.

8.0 REFERENCES

Adam, L.C., I. Fabian, K. Suzuki, G. Gordon. 1992. "Hypochlorous Acid Decomposition in the pH 5-8 Region," Inorganic Chemistry, Vol. 31, 3534

Adam, L.C., G. Gordon. 1999. "Hypochlorite Ion Decomposition: Effects of Temperature, Ionic Strength, and Chloride Ion," Inorganic Chemistry, Vol. 38, 1299

Baes, C.F., R.E. Mesmer. 1986. *The Hydrolysis of Cations.* Malabar, FL: Krieger Publishing Company

Borkowski, M., G.R. Choppin, S. Lis. 1996. "Complexation Study of NpO_2^+ and UO_2^{2+} Ions with Several Organic Ligands and Aqueous Solutions of High Ionic Strength," Radiochimica Acta. Vol. 74, 117

Borkowski, M., M. Bronikowski, J. Chen, G.R. Choppin, R. Moore, O. Pokrovsky, Y. Xia. 1999. "Thermodynamic Modeling of Actinide Complexation with Acetate and Lactate at High Ionic Strength," Journal of Solution Chemistry. Vol 28, no.5, 521

Borkowski, M., G.R. Choppin, R. Moore. 2000. "Thermodynamic Modeling of Metal-Ligand Interactions in High Ionic Strength NaCl Solutions: the Co^{2+}-Oxalate System," Radiochimica Acta, Vol. 88, 599

Bronikowski, M., G.R. Choppin, R. Moore, O. Pokrovsky. 1998. "Interaction of Neptunyl(V) and Uranyl(VI) with EDTA in NaCl Media: Experimental Study and Pitzer Modeling," Radiochimica Acta. Vol. 80, 23

Bronikowski, M., O. Pokrovsky, M. Borkowski, G.R. Choppin. 1999. "UO_2^{2+} and NpO_2^{+} Complexation with Citrate in Brine Solutions," *Proceedings: Actinide Speciation in High Ionic Strength Media*, Ed. D. Reed. New York, NY: Kluwer Academic/Plenum Publishers. 177

Brush, L.H., R.C. Moore, N.A. Wall. 2001. *Response to EEG-77, Plutonium Chemistry Under Conditions Relevant For WIPP Performance Assessment, Review of Experimental Results and Recommendations for Future Work.* ERMS #51737 3 Carlsbad, NM: Sandia National Laboratories

Büppelmann, K., J.I. Kim, Ch. Lierse. 1988. "The Redox-Behavior of Plutonium in Saline Solutions under Radiolysis Effects," Radiochimica Acta, Vol. 44/45, 65

Chen, J., G.R. Choppin, R. Moore. 1999. "Complexation and Ion Interactions in Am(III) ETDA/NaCl Ternary System," *Proceedings: Actinide Speciation in High Ionic Strength Media*, Ed. D. Reed. New York, NY: Kluwer Academic/Plenum Publishers. 187

Choppin, G.R., L. Rao. 1984. "Complexation of Pentavalent and Hexavalent Actinides by Fluoride" Radiochimica Acta, Vol. 37, 143

Choppin, G.R., F. Khalili, E. Rizkalla. 1988. "The Nature of U(VI) Complexation by Halates and Chloroacetates," Inorganic Chemistry, Vol. 143, 131

Choppin, G.R., E.N. Rizkalla. 1994. "Solution Chemistry of the Lanthanides and Actinides," *Handbook on the Physics and Chemistry of the Rare Earths, Vol 18.* Eds., K.A. Geschneidner, L. Eyring, G.R. Choppin, G.H. Lander, Elsevier Science, Ch. 128

Choppin, G.R., O. Pokrovsky. 1997. "Neptunium (V) Complexation by Acetate, Oxalate, and Citrate in $NaClO_4$ Media at 25°C," Radiochimica Acta. Vol. 79, 167

Choppin, G.R., 1999. "Utility of Oxidation State Analogs in the Study of Plutonium Behavior," Radiochimica Acta. Vol. 85, 89

Choppin, G.R., A. Morgenstern. 2000. "Oxidation of Pu(IV) and Pu(V) by sodium hypochlorite," *Plutonium Futures – The Science*,Eds. K.K.S. Pillay, K.C. Kim College Park, MD: American Institute of Physics. 223

Church, J. 1994. "Kinetics of the Uncatalyzed and Cu(II)-Catalyzed Decomposition of Sodium Hypochlorite," Industrial & Engineering Chemistry Research, Vol. 33, 239

Clark, D., W. Runde, M. Neu. 1996. "Neptunium(V) Hydrolysis and Carbonate Complexation: Experimental and Predicted Neptunyl Solubility in Concentrated NaCl Using the Pitzer Approach," Geochimica et Cosmochimica Acta. Vol. 60, no. 12, 2065

Cotton, F.A., G. Wilkinson, C.A. Murillo, M. Bochmann. *Advanced Inorganic Chemistry, 6th Ed.* 1999. New York, NY. Wiley Interscience, John Wiley & Sons, Inc. 547-585

Ganguly, A.K., J.L. Magee. 1956. "Theory of Radiation Chemistry. III. Radical Reaction Mechanism in the Tracks of Ionizing Radiations," Journal of Chemical Physics, Vol. 25 no.1, 129

Greenwood, N.N., A. Earnshaw. 1989a. *Chemistry of the Elements*. New York, NY: Pergamon Press. 698-753

Greenwood, N.N., A. Earnshaw. 1989b. *Chemistry of the Elements*. New York, NY: Pergamon Press. 920-1039

Kelm, M., I. Pashalidis, J.I. Kim. 1999. "Spectroscopic Investigation on the Formation of Hypochlorite by Alpha-Radiolysis in Concentrated NaCl Solutions," Applied Radiation and Isotopes, Vol. 51, 637

Kim, J.I., Ch. Lierse, K. Buppelmann, S. Magirius. 1987 "Radiolytically Induced Oxidation Reactions of Actinide Ions in Concentrated Salt Solutions" Material Research Society Symposium Proceedings, Vol. 84, 603-612

Lister, M.W. 1952. "The Decomposition of Hypochlorous Acid,"; Canadian Journal of Chemistry, Vol. 30, 879

Martell, A.E., R.M. Smith, R.J. Motekaitis. 1998. "Critically Selected Stability Constants of Metal Complexes Database, Version 5.0," College Station, TX: Texas A&M University

Neill, R.H., L. Chatuvedi, D.F. Rucker, M.K. Silva, B.A. Walker, J.K. Channell, T.M. Clemo, 1998. *Evaluation of the WIPP Project's Compliance with the EPA Radiation Protection Standards for Disposal of Transuranic Waste.* EEG-68, Environmental Evaluation Group, Albuquerque, NM

Oversby, V.M.. 2000. *Plutonium Chemistry Under Conditions Relevant For WIPP Performance Assessment, Review of Experimental Results and Recommendations for Future Work.* EEG-77, Environmental Evaluation Group, Albuquerque, NM

Pashalidis, I., J.I. Kim, Ch. Lierse, J.C. Sullivan. 1993. "The Chemistry of Pu in Concentrated NaCl Solution: Effects of Alpha Self-Radiolysis and the Interaction between Hypochlorite and Dioxoplutonium(VI)," Radiochimica Acta, Vol. 60, 99

Pearson, R. 1963. "Hard and Soft Acids and Bases," Journal of the American Chemical Society, Vol. 85, no. 22, 3533

Reed, D., S. Okajima, M. Richmann. 1994. "Stability of Plutonium(VI) in Selected WIPP Brines," Radiochimica Acta. Vol. 66/67, 105

U.S. Department of Energy. 1996. *Appendix SOTERM, Table SOTERM-4, Title 40 CFR 191 Compliance Certification Application*, DOE/CAO-1996-2184, Carlsbad, NM: U.S. Department of Energy

U.S. Department of Energy. 1996. *Appendix SOTERM, Table SOTERM-5, Title 40 CFR 191 Compliance Certification Application*, DOE/CAO-1996-2184, Carlsbad, NM: U.S. Department of Energy

U.S. Department of Energy, 1996 Title 40 CFR Part 191 Compliance Certification Application for the Waste Isolation Pilot Plant. DOE/CAO-1996-2184, October 1996

Villarreal, R., A. Trujillo, C. Scherer, M. Neu, S. Reilly, A. Morzinski, 2000, *A Study of STTP Pyrochemical Salt Tests and Results Featuring Pu(VI)*

Villarreal, R. 1996. *Test Plan for the Actinide Source-Term Waste Test Program (STTP)* MST5-STP-TST1-013/1

Vogel, A.I., Vogel's Textbook of Quantitative Chemical Analysis, 5th ed. p 309-322 John Wiley & Sons, NY (1989)

Wang, T.X., D. W. Margerum. 1994. "Kinetics of Reversible Chlorine Hydrolysis: Temperature Dependence and General-Acid/Base-Assisted Mechanisms," Inorganic Chemistry, Vol. 33, 1050

Weigel, F., J.J. Katz, G.T. Seaborg. 1986. *The Chemistry of the Actinide Elements.* Eds. J.J. Katz, G.T. Seaborg, L.R. Morss. New York, NY: Chapman and Hall

Zhang, P., H. Anderson, J. Kelly, J. Krumhansl, H. Papenguth. 1999. "Kinetics and Mechanisms of Formation of Magnesite from Hydromagnesite in Brine," SAND99-1946J, Carlsbad, NM: Sandia National Laboratories

3.5 Complexation of Am with Humic, Fulvic, and Citric Acids at High Ionic Strength[1]

Nathalie A. Wall, Marian Borkowski, Jian-Feng Chen, and Gregory R. Choppin
Department of Chemistry
Florida State University
Tallahassee, FL 32306-4390 USA

This paper was presented at Migration 01, September 16-21, in Bregenz, Austria (SAND2001-0519P) and has been accepted for publication in *Radiochimica Acta* (SAND2001-0519C).

[1] This work is covered by WBS #1.3.5.1.2.1

Complexation of americium with humic, fulvic and citric acids at high ionic strength[1]

Nathalie A. Wall [2], Marian Borkowski[3], Jian-Feng Chen and Gregory R. Choppin
Department of Chemistry, Florida State University, Tallahassee, FL 32306-4390, USA

Complexation / Humic / Fulvic / Citric / Americium / WIPP

Abstract

The stability constants of the Am^{3+} complexes of humic, fulvic and citric acids (HA, FA and Cit) were determined as a function of ionic strength (NaCl) using a solvent extraction technique. At a HA degree of ionization of 0.7 for the carboxylate groups, the Am-HA binding constant, $\log\beta_1$, varies from 8.3 at I = 0.2 m to 7.2 at I = 6.0 m. The $\log\beta_1$ of Am-Cit varies from 5.9 at I = 0.3 m to 5.10 at I = 5.0 m. Comparison of the binding constants of Am with HA, FA and Cit shows that, at high ionic strength, $\log\beta_1(AmCit) \approx \log\beta_1(AmFA) \approx \{\log\beta_1(AmHA) - 1\}$. Comparison of the values of other metals indicate that the $\log\beta_1$ values for Cit can serve to estimate HA and FA.

Introduction

Knowledge of the speciation and solubility of dissolved actinide species is required to predict actinide release from the Waste Isolation Pilot Plant (WIPP) repository, and this research has provided fundamental thermodynamic parameters for use in modeling such behavior. In the Performance Assessment (PA) calculations described in the Compliance Certification Application (CCA), the US Department of Energy (USDOE) relied on literature and experimental data, and a consideration of the reducing conditions expected in the repository, to assess the likely oxidation states of the actinides of interest. Th, U, Np, Pu and Am were expected to be present as Th(IV), U(IV) or U(VI), Np(IV) or Np(V), Pu(III) or Pu(IV) and Am(III) in all brines present in the WIPP disposal rooms [1]. The actinides Am(III) and Th(IV) were used to predict the behavior of Pu(III) and Pu(IV); the stability constants of the complexes formed between $Am(III)^{3+}$ and $Th(IV)^{4+}$ and a ligand, can be used, after applying suitable small correction, to model the behavior of plutonium in the III and IV oxidation states [2].

Citric acid will be present in WIPP brines, at an estimated amount of 1110 kg [1], when WIPP is filled. Humic and fulvic acids (HA and FA) may also be present in the WIPP from materials placed in the repository, such as soils, and from degradation of cellulosic materials [3]. These ligands can increase the An mobility by forming soluble An complexes. Moreover, the behavior of citrate (Cit) and humic materials towards metals are interesting to compare, as Cit has been considered as a model for certain properties of humic substances associated with their carboxylic groups [4,5].

The stability constants of HA, FA and Cit with actinides such as Th^{4+} [6,7], UO_2^{2+} [8,9], NpO_2^{+} [8,10,11] have been measured as a function of ionic strength. The stability constants of HA with Am^{3+} have been measured at low ionic strength [12,13,14].

In this study the binding constants of HA from Lake Bradford in Florida (designated as LBHA),

[1] This work was supported at Sandia National Laboratories (a multiprogram laboratory operated by Sandia Corporation, a Lockheed Martin Company) by US DOE under contract DEACO4-94AL85000, and at FSU under subcontract AH5590, under a Sandia-approved quality assurance program.

[2] *Present address*: Sandia National Laboratories, 4100 National Parks Highway, Carlsbad, NM 88220, USA
[3] *Present address*: Argonne National Laboratory, 9700 S. Cass Avenue, Argonne, IL 60439, USA

FA from Suwannee River (designated as SRFA) and Cit with Am^{3+} were measured using a solvent extraction technique over a range of ionic strengths (NaCl). The results from this work were used to investigate correlations between the binding constants of HA, FA and Cit.

Experimental

Solutions of NaCl (Fisher ACS grade reagent) were prepared at specific ionic strengths. LBHA and SRFA stock solutions were prepared in NaCl solutions; the characteristics (purity, NMR, pKa and H^+ capacity values) of the LBHA and SRFA are described in reference [9]. The stock solution of Cit was prepared by dissolution of sodium citrate (Aldrich, ACS) in NaCl solutions. ^{241}Am was obtained from Oak Ridge National Laboratory and used to prepare a stock solution in 0.001 M HCl. The radioactive purity of the ^{241}Am was confirmed by γ-ray spectroscopy with a Ge(Li) detector connected to a multichannel analyzer. Stock solutions of 5.0×10^{-5} M HDEHP (di(2-ethylhexyl) phosphate) (Sigma) in n-heptane (Fisher, ACS) and 10^{-5} M HDEHP (Sigma) in toluene (Fisher, ACS) were prepared for use as the organic phase in extraction experiments of ^{241}Am, respectively for the Cit experiments and for the HA and FA experiments; these solutions were pre-equilibrated with the aqueous NaCl solutions, prepared at the ionic strengths to be studied.

All aqueous solutions, except the LBHA and SRFA solutions, were filtered with a 0.2 μm pore size Nalgene Disposable Filter to minimize the possible adsorption of the radioactive tracers by suspended particles. The LBHA and SRFA solutions were not filtered, but the NaCl solutions used to prepare them were.

The solvent extraction experiments were conducted in 20 mL glass vials, previously silanized to minimize metal sorption on the walls [15] Aqueous solutions were prepared from the pre-equilibrated NaCl solution, and contained ^{241}Am (10^{-9} M) plus LBHA, SRFA or Cit. For the HA and FA experiments, acetate buffer (Fisher, ACS grade) at 10^{-2} M was added to control the pcH (= -log H^+ concentration) to 5.0-5.1. The vials were shaken overnight for the HA and FA experiments and for 3-6 hrs for the Cit experiments at constant temperature (25 °C). These times were determined in separate experiments to be sufficient to obtain equilibrium for all the systems. After equilibration, the vials were centrifuged for 3-5 minutes. For the LBHA experiments, the aqueous phase was separated and rapidly filtered through glass wool, to remove a thin film of coagulated HA which formed between the two phases. Duplicate samples, 1.0 mL, were taken from both phases. The count rates of the ^{241}Am in the samples were measured with an ISOFLEX automatic γ counter over an energy window width of 10-70 keV. The LBHA and SRFA concentrations at the end of the experiments were determined by spectrophotometry with a CARY 14 spectrophotometer (with an OLIS Spectroscopy Operating System) at 238 nm based on a calibration curve obtained from freshly prepared LBHA and SRFA solutions at controlled ionic strength and pcH. The pH-meter reading (i.e., pHr) of all the aqueous samples was measured after the extraction using a Corning Semi-Micro Combination glass electrode attached to an Accumet 950 pH/ion Meter. The pHr were converted to pcH values by the equation:

$$pcH = pHr + 0.255 \cdot m_{NaCl} \quad (1)$$

where m_{NaCl} is the molality of NaCl [16].

Data Treatment

The solvent extraction results were interpreted by a modified Schubert method [17]. The general equation of the complexation of a ligand with a metal is:

$$mM^{x+} + hH^+ + nL^{y-} \leftrightarrow M_mH_hL_n^{mx+h-ny} \quad (2)$$

and the stability constant of the complex is defined as:

$$\beta_{mhn} = \frac{\left[M_mH_hL_n^{mx+h-ny}\right]}{\left[M^{x+}\right]^m \cdot \left[H^+\right]^h \cdot \left[L^{y-}\right]^n} \quad (3)$$

Thus, for m = 1 and h = 0, the complex ML_n is designated with a stability constant designated simply as β_n.

For HA and FA, we assume a binding reaction between the carboxylate groups present on the humic substances (RCO_2^-) and the metals. The concentration of deprotonated carboxylate sites, expressed in eq/l, is calculated as the product of the final fulvic or humic concentration in the aqueous phase determined by spectrophotometry, the proton capacity and the degree of ionization (α_{HA} or α_{FA}), that are determined by potentiometric titration, as detailed in [9].

In the case of Cit, $[L^-]$ is the free ligand concentration calculated from the measured pcH (after reaching extraction equilibrium), the total ligand concentrations and the protonation constants [18].

The distribution coefficient is defined by:

$$D = {[M]_{(o)}}/{[M]_{(a)}} \quad (4)$$

where $[M]_{(o)}$ is the metal concentration in the organic phase and $[M]_{(a)}$ is the metal concentration in the aqueous phase. When necessary, the measured D value of individual samples have been corrected to a constant pcH value according to Eq. (5)

$$\log D_{corr} = \log D - n \times (pcH_{aver} - pcH) \quad (5)$$

where n is 3 in 0.1 m NaCl, 2 in 1 m NaCl and 0 in 3 m NaCl and above.
Defining D_0 as the distribution coefficient in the absence of ligand, D_{corr} is calculated by:

$$D_{corr.} = {D_0}\Big/{1 + \left(\sum_{i=1}^{m} \beta_i \times [L^-]^i \Big/ \alpha_M \right)} \quad (6)$$

The value α_M accounts for the hydrolysis and the complexation by carbonate and buffer ion (B) of the metal ion:

$$\alpha_M = 1 + \sum_i {}^{OH}\beta_i \times [OH^-]^i + \sum_j {}^{CO_3}\beta_j \times [CO_3^{2-}]^j + \sum_k {}^{B}\beta_k \times [B^-]^k \quad (7)$$

The values of β_1 and β_2 are determined from the slope of the linear section of the plots $(D_0/D_{corr} - 1)$ vs. $[L^-]$ and $(D_0/D_{corr} - 1)/ [L^-]$ vs. $[L^-]$; the slopes of these plots are respectively β_1/α_M and β_2/α_M. Cm(II) hydrolysis data [19] was used to account for Am(III) hydrolysis. The data necessary for the calculation of the binding constants are presented in Table 1. In the experiments the D values were measured for 10 values of $[L^-]$ and were performed at least twice. The stability constants were calculated as the average values of the data from these separate experiments. Examples of solvent extraction data are presented in Table 2 and the binding constants of Am^{3+} with LBHA, SRFA and Cit are listed in Table 3.

Table 1. Values necessary for stability constant calculations.

	Ionic strength (NaCl)							
	0.1 m	0.3 m	1.0 m	2.0 m	3.0 m	4.0 m	5.0 m	6.0 m
pK_w [20]	13.83	13.71	13.70	13.78	13.93	14.12	14.30	14.47
Acetic acid pKa [20]	4.56	4.51	4.52	4.62	4.77	4.95	5.13	5.31
log $\beta(Am^{3+}$/acetic acid) [21]	1.87	1.73	1.51	1.44	1.62	1.83	2.20	2.44
log $\beta(Am(OH)^{2+})$ [19]	5.76	5.54	5.6	6.06	6.24	6.42	6.60	6.70
log $\beta(Am(OH)_2^{+})$ [19]	11.10	11.12	11.15	12.19	12.57	12.81	13.47	13.89
$\alpha_{Am^{3+}}$, at pcH 5.1 buffered with 10^{-2} M acetic acid	1.58	1.43	1.26	1.21	1.28	1.40	1.77	2.62
$\alpha_{Am^{3+}}$, at pcH 5.0, without buffer	1.00	1.00	1.00	1.00	1.00	1.00	1.00	1.00
LBHA [9]:								
Dissociation coefficient α_{LBHA}, at pcH 5.1 COOH capacity = 3.69 meq/g	0.65	-	0.70	0.70	0.70	-	-	0.64
SRFA [9]:								
Dissociation coefficient α_{SRFA}, at pcH 5.1 COOH capacity = 6.55 meq/g	-	-	-	-	0.91	-	-	0.84
Citric acid pKa_1 [18]	2.93	2.92	2.87	2.84	2.79	2.93	2.96	3.60
Citric acid pKa_2 [18]	4.36	4.25	4.11	4.09	4.12	4.24	4.32	4.41
Citric acid pKa_3 [18]	5.63	5.46	5.18	5.08	5.08	5.20	5.22	5.51

Table 2. Examples of solvent extraction data

A. Am^{3+}-LBHA, pcH 5.1 I= 3m (NaCl)		
Final $[RCO_2^-]$ (eq/L)	D	
0	2.777	Regression:
5.46E-06	1.745	$(D_0/D-1) = 3.07 \cdot 10^{+6} \cdot [RCO_2^-] - 19.13.$
5.80E-06	1.585	Correlation 0.98
6.90E-06	1.087	Log $\beta_1 = 6.60 \pm 0.01$
8.71E-06	0.578	
8.92E-06	0.284	
9.97E-06	0.229	
1.23E-05	0.168	
1.53E-05	0.093	
2.07E-05	0.059	
B. Am^{3+}-SRFA, pcH 5.1 I= 3m (NaCl)		
Final $[RCO_2^-]$ (eq/L)	D	
0	2.336	Regression:
1.19E-05	1.729	$(D_0/D-1) = 3.88 \cdot 10^{+4} \cdot [RCO_2^-] - 0.10.$
1.79E-05	1.967	Correlation 0.95
2.38E-05	1.484	
2.98E-05	1.420	Log $\beta_1 = 4.71 \pm 0.02$
5.96E-05	1.017	
7.15E-05	0.739	
8.34E-05	0.647	
C. Am^{3+}-Cit, pcH 5.0, I= 3 m (NaCl)		
$[L^-]$ (M)	D	
0	0.643928	Regression:
1.18E-06	0.631773	$(D_0/D-1) = 7.15 \cdot 10^{+4} \cdot [L^-] - 0.04.$
2.38E-06	0.523004	Correlation 0.95
2.38E-06	0.522881	
6.01E-06	0.460779	log $\beta_1 = 4.85 \pm 0.04$
4.94E-06	0.489911	
6.01E-06	0.473413	
8.27E-06	0.434401	
8.27E-06	0.39075	

Table 3. Am^{3+}-LBHA, Am^{3+}-SRFA and Am^{3+}-Cit binding constants, pcH 5.1

	Ionic strength	$\log \beta_1$	$\log \beta_2$	Ref.
LBHA	0.1 m (NaCl)	9.8 ± 2.0	13.4 ± 1.3	[13]
LBHA	0.1 m (NaCl)	9.9 ± 1.8	14.0 ± 0.2	[14]
LBHA	0.2 m (NaCl)	8.27 ± 0.04	-	present work
LBHA	1 m (NaCl)	6.2 ± 0.2	11.51 ± 0.04	present work
LBHA	2 m (NaCl)	6.13 ± 0.01	10.97 ± 0.01	present work
LBHA	3 m (NaCl)	6. 6 ± 0.2	11.4 ± 0.3	present work
LBHA	6 m (NaCl)	7.2 ± 0.4	12.3 ± 0.3	present work
LBFA	0.1 m (KCl), pcH 4.5	6.83 ± 1.0	-	[12]
SRFA	3 m (NaCl)	4.7 ± 0.1	-	present work
SRFA	6 m (NaCl)	6.0 ± 0.7	-	present work
Cit	0.3 (NaCl)	5.9 ± 0.1	-	present work
Cit	1.0 (NaCl)	5.2 ± 0.1	-	present work
Cit	2.0 (NaCl)	5.0 ± 0.1	-	present work
Cit	3.0 (NaCl)	4.84 ± 0.04	-	present work
Cit	4.0 (NaCl)	5.38 ± 0.06	-	present work
Cit	5.0 (NaCl)	5.10 ± 0.15	-	present work

Results and Discussion

Only one binding constant was obtained for Am-FA while two were calculated for Am-HA. Fig. 1 shows the influence of the ionic strength on the binding constants of LBHA, SRFA and Cit with Am^{3+}. A value for β_2 for $AmCit_2$ formation was not observed, as the free citrate ion concentrations used in the experiments were too small.

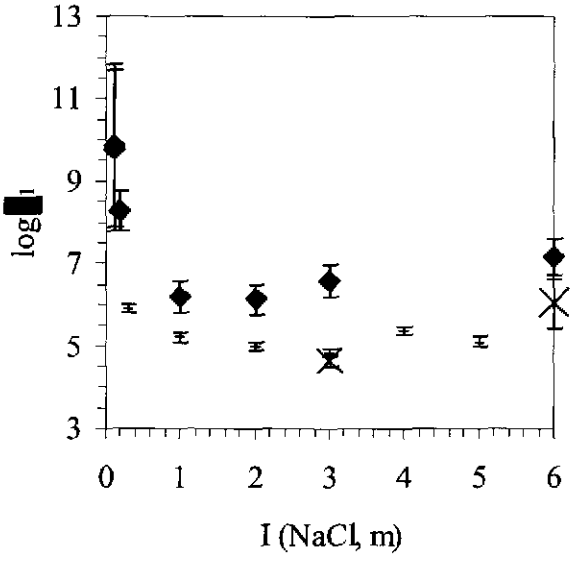

Fig. 1. First stability constant of Am^{3+} with HA (♦), FA (×) and Cit (+).

A variety of models can be applied to determine humic substances binding constants with metals [22,23]. The influence of ionic strength (maintained by $NaClO_4$) on HA binding constants has been determined using the Charge Neutralization Model [25] in a study conducted with much larger concentrations of Am(III) than the present work (10^{-6} M versus 10^{-9} M), while the HA concentration was similar in both works (10^{-5} eq/L). Unlike the results of the present work, the values from [24] show very little influence of the ionic strength on the values of β_1. Such differences for the two models have been discussed in references [25,26]. The data presented in Fig. 1 show that log β_1 values for AmHA are about one order of magnitude higher than the corresponding values for AmFA and AmCit, at high ionic strength (1 m NaCl and above).
Data for UO_2^{2+} complexation with HA are available in the literature [9] while the stability constants of UO_2^{2+}-Cit complexation have been calculated from published apparent stability constants [8], (i.e. β_{app}, calculated as $\beta \times \alpha_{UO_2^{2+}}$) using the Specific Interaction Theory (SIT) approach [27]. Only the stability constants between ionic strengths 0.1-2.0 m have been treated by the SIT model as above 2 m SIT overestimates stability constants [28]. The calculated values of $\alpha_{UO_2^{2+}}$ and the uranyl binding constants are presented in Table 4 and the associated plot is presented in Fig. 2. Unlike for Am^{3+} complexation, the uranyl binding constants with HA are smaller than those with Cit. This difference in binding nature may reflect the greater role of steric effects in the binding to HA.

Table 4. Stability constants of uranium with HA and Cit as a function of ionic strength.

	LBHA [4] pcH 4.9, $\alpha_{HA} = 0.6$ (± 0.1)	Cit [5] pcH 3.3
Ionic strength (m, NaCl)	log β_1	log β_1
0.1	6.4 ± 0.2	7.4
0.3	-	7.30 ± 0.3
0.5	5.9 ± 0.1	-
1.0	5.86 ± 0.06	7.08 ± 0.3
1.5	5.93 ± 0.1	-
2.0	5.90 ± 0.03	7.21 ± 0.3

[4] From reference [9]
[5] From references [29,8]

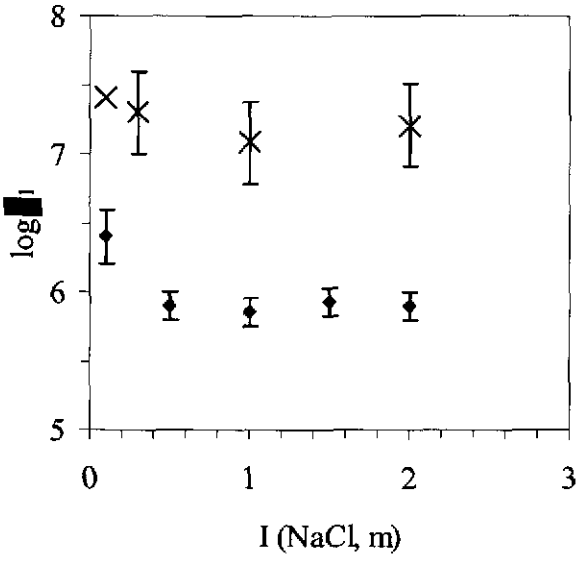

Fig. 2. First stability constant of UO_2^{2+} with HA (♦) and Cit (×).

The ionic nature of the binding has been demonstrated by using a modified Born calculation [30], using the following equation [2]:

$$\log\left(\beta_{1,M_{(1)}L}\right)\cdot\frac{\varepsilon_{M_{(1)}}}{\varepsilon_{M_{(2)}}}\cdot\frac{d_{M_{(1)}L}}{d_{M_{(2)}L}}=\log\left(\beta_{1,M_{(2)}L}\right)\cdot\frac{Z_{M_{(1)}}}{Z_{M_{(2)}}} \qquad (8)$$

where $\beta_{1,M_{(i)}L}$ is the binding constant of the complex $M_{(i)}L$, $Z_{M_{(i)}}$ is the effective charge of the metal ion $M_{(i)}$ (+2.2 for $Np(V)O_2^+$, +3 for Am^{3+}, +3.3 for UO_2^{2+} and +4 for Th^{4+}) [2], $\varepsilon_{M_{(i)}}$ is the effective dielectric constant for the metal ion $M_{(i)}$ and $d_{M_{(i)}L}$ is the distance between the centers of the metal ion and the complexing ligand site.

For complexation of a variety of metal ions with the same ligand, plots of $\log\beta_{ML}\cdot\varepsilon_M/\varepsilon_{UO_2}\cdot d_{ML}/d_{UO_2L}$ versus Z_M should provide a linear correlation if the ligand and the metals have a predominant ionic bonding. The parameters necessary to calculate Eq. 8 are presented elsewhere [2]. The binding constants of different organic ligands (acetate, oxalate, Cit and HA) with actinides, in low ionic strength solutions are presented in Table 5; the values obtained from [29] did not provide any error range. Figure 3 is a plot of $\log\beta_{ML}\cdot\varepsilon_M/\varepsilon_{UO_2}\cdot d_{ML}/d_{UO_2L}$ versus Z_M, for acetate, oxalate, Cit and HA. The expected linear regressions occur for acetate, oxalate, Cit, with the slopes 1.2, 1.4, 2.4 respectively, values close to the theoretical values of $\log\beta_{UO_2L}/Z_{UO_2}$ (respectively 0.8, 1.9 and 2.2), but the value for HA does not fit this linear regression, which we suggest is due to the greater steric effects in the HA bonding.

Table 5. Stability constants ($\log\beta_1$) at 0.1 m ionic strength.

	Th^{4+}	UO_2^{2+}	NpO_2^+	Am^{3+}
HA	-	6.4 ± 0.2 ($\alpha = 0.6$) [9]	-	9.8 ± 2 ($\alpha = 0.6$) [13]
Cit	10.08 ± 0.07 [6]	7.4 [29]	2.97 ± 0.01 [8]	-
Oxalate	8.8 [29]	6.36 [29]	3.40 ± 0.04 [10]	5.25 [29]
Acetate	4.70 ± 0.05 [31]	2.61 [29]	1.20 ± 0.05 [31]	2.0 ± 0.1 [21]

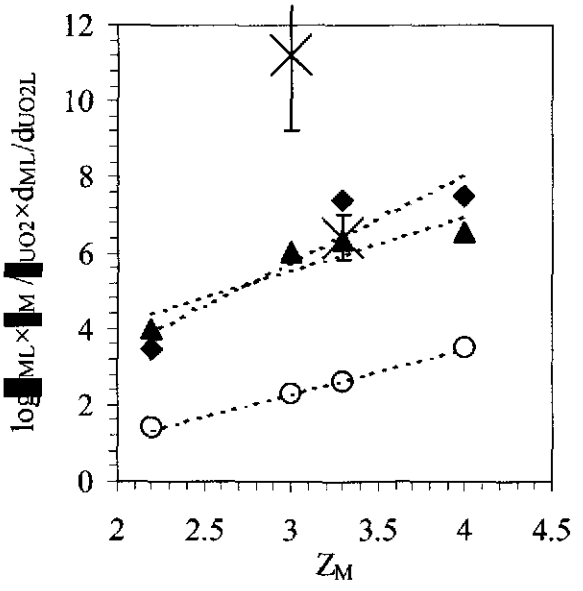

Fig. 3. Correlation between $\log\beta_{ML} \cdot \varepsilon_M / \varepsilon_{UO_2} \cdot d_{ML}/d_{UO_2L}$ and Z_M, for acetate (○), oxalate (▲), Cit (♦) and HA (×)

Conclusion

The numerical values of Cit binding constant can be used as an estimate of the binding to HA and in particular, at pcH ≈ 5 and ionic strengths higher than 1 m NaCl, where the correlation is $\log\beta_1(\text{AmCit}) \approx \log\beta_1(\text{AmFA}) \approx \{\log\beta_1(\text{AmHA}) - 1\}$.

References

1. DOE (US Department of Energy), "Title 40 CFR Part 191 Compliance Certification Application for the Waste Isolation Pilot Plant", DOE/CAO-1996-2184, Vol. 1-21. Carlsbad, NM: US Department of Energy, Carlsbad Area Office 1996.
2. Choppin, G. R.: Utility of Oxidation State Analogs in the Study of Plutonium Behavior, Radiochimica Acta 85 (3-4), 89 (1999).
3. Hayes, M. H. B., MacCarthy, P., Malcom, R. L., Swift, R. S.: Humic Substances II, John Wiley & Sons Ltd 1989, p. 690.

4. Theis, T. L., Singer, P. C.: The Stabilization of Ferrous Iron by Organic Compounds in Natural Waters. In: Trace Metals and Metal-Organic Interactions in Natural Waters (P.C. Singer, ed.) Ann Arbor, MI 1973, p. 303.
5. Bailey, G. W., Shevchenko, S. M., Yu, Y. S., Kamermans, H.: Combining Scanning Tunneling Microscopy and Computer Simulation of Humic Substances: Citric Acid, a Model, Soil Sci. Soc. Am. 61 (1), 92 (1997).
6. Choppin, G. R., Erten, H. N., Xia, Y. X.: Variation of Stability Constants of Thorium Citrate Complexes with Ionic Strength, Radiochim. Acta 74, 123 (1996).
7. Nash, K. L., Choppin, G. R.: Interaction of Humic and Fulvic Acids with Th(IV), J. Inorg. Nucl. Chem. 42 (7), 1045 (1980).
8. Bronikowski, M., Pokrovsky, O. S., Borkowski, M., Choppin, G. R.: UO_2^{2+} and NpO_2^{+} Complexation with Citrate in Brine Solution. In: Actinide Speciation in High Ionic Strength Media: Experimental and Modeling Approaches to Predicting Actinide Speciation and Migration in the Subsurface (D.T. Reed et al., eds.), Plenum Pub., NY 1999, p. 177.
9. Labonne-Wall, N., Choppin, G. R., Lopez, C., Monsallier, J. -M., Interaction of Uranyl with Humic and Fulvic Acids at High Ionic Strength. In: Actinide Speciation in High Ionic Strength Media: Experimental and Modeling Approaches to Predicting Actinide Speciation and Migration in the Subsurface (D.T. Reed et al., eds.), Plenum Pub., NY 1999, p. 199.
10. Pokrovsky, O. S., Choppin, G. R.: Neptunium(V) Complexation by Acetate, Oxalate and Citrate in $NaClO_4$ Media at 25° C, Radiochim. Acta 79 (3), 167 (1997).
11. Rao, L., Choppin, G. R.: Thermodynamic Study of the Complexation of Neptunium(V) with Humic Acids, Radiochim. Acta 69 (2), 87 (1995).
12. Bertha, E. L., Choppin, G.R., Interaction of Humic and Fulvic Acids with Eu(III) and Am(III), J.Inorg. Nucl. Chem. 40 (4), 655 (1978)
13. Torres, R. A., Choppin, G. R.: Europium (III) and Americium (III) Stability Constants with Humic Acid, Radiochim. Acta 35 (3), 143 (1984).
14. Minai, Y., Choppin G. R.: Interaction of Americium with Humic Acids and Two Synthetic Analogues. In: Proceedings of the International Symposium on Advanced Nuclear Energy Research, Oarai, Japan, February 15-16, 1989.
15. Caceci, M. C., Choppin, G. R.: An Improved Technique to Minimize Cation Adsorption in Neutral Solutions, Radiochim. Acta 33 (2-3), 113 (1983).
16. Novak, C. F., Borkowski, M., Choppin, G. R.: Thermodynamic modeling of neptunium (V)-Acetate Complexation in Concentrated NaCl Media, Radiochim. Acta 74, 11 (1996).
17. Schubert, J., The Use of Ion Exchangers for the Determination of Physical-Chemical Properties of Substances, Particularly Radiotracers, in Solution, J. Phys. Chem. 52 (2), 340 (1948).
18. Mizera, J., Bond, A., Choppin, G. R., Moore, R. C.: Dissociation Constants of Carboxylic Acids at High Ionic Strengths. In: Actinide Speciation in High Ionic Strength Media: Experimental and Modeling Approaches to Predicting Actinide Speciation and Migration in the Subsurface (D.T. Reed et al., eds.) Plenum Pub., NY 1999, p. 113.
19. Fanghanel, Th., Kim, J. I., Klenze, R., Hauser, W: Thermodynamics of Radioactive Trace Elements in Concentrated Electrolyte Solutions: Hydrolysis of Cm^{3+} in NaCl-Solutions, Radiochim. Acta 66/67, 81 (1994).
20. Chen, J. F., Xia, Y. X., Choppin, G. R.: Derivative Analysis of Potentiometric Titration Data to Obtain Protonation Constants, Anal. Chem. 68 (22), 373 (1996).
21. Moore, R. C., Borkowski, M., Bronikowski, M. G., Chen, J.-F., Pokrovsky, O. S., Xia, Y., Choppin, G. R.: Thermodynamic Modeling of Actinide Complexation with Acetate and Lactate at High Ionic Strength, J. Sol. Chem. 28 (5), 521 (1999).

22. Hummel, W., Glaus, M. A., Van Loon, L. R.: Trace Metal-Humate Interactions. II. The "Conservative Roof" Model and its Application, Applied Geochem. 15 (7), 975 (2000).
23. Glaus, M. A, Hummel, W., Van Loon, L. R.: Trace Metal-Humate Interactions. I. Experimental Determination of Conditional Stability Constants, Applied Geochem. 15 (7), 953 (2000).
24. Czerwinski, K. R., Kim, J. I., Rhee, D. S., Buckau, G.: Complexation of Trivalent Actinide Ions (Am^{3+}, Cm^{3+}) with Humic Acid: The Effect of Ionic Strength, Radiochim. Acta 72 (4), 179 (1996).
25. Choppin, G. R., Labonne-Wall, N.: Comparison of Two Models for Metal-Humic Interactions, J. Radioanal. Nuc. Chem. 221 (1-2), 67 (1997).
26. Hummel, W., Glaus, M. A., Van Loon, L. R.: Complexation of Radionuclides with Humic Substance: The Metal Concentration Effect, Radiochim. Acta 84 (2), 111 (1999).
27. OECD/NEA: Chemical Thermodynamics of Uranium Volume 1, (I. Grenthe et al.; H. Wanner and I. Forest, eds) Elsevier Publishers B.V. 1992.
28. Du, M., Choppin G. R.: Correlation of Equilibrium Constants with Ionic Strength by SIT, Pitzer and Parabolic Models. In: Actinide Speciation in High Ionic Strength Media: Experimental and Modeling Approaches to Predicting Actinide Speciation and Migration in the Subsurface (D.T. Reed et al., eds.) Plenum Pub., NY 1999, p. 125.
29. Smith, R. M., Martell A. E., Motekaitis, R. J.: NIST Critically selected stability constants of metals complexes database, Version 5.0. User's Guide. U.S. Department of Commerce. Technology Administration , National Institute of Standards and Technology, Standard Reference Data Program, Gaithersburg, MD 1998.
30. Choppin, G. R.: Inner Versus Outer Sphere Complexation of f-Elements, J. of Alloys and Compounds 249 (1-2), 9 (1997).
31. Choppin, G. R, Bond, A., Borkowski, M., Bronikowski, M. G., Chen, J. F., Lis, S., Pokrovsky, O., Wall, N. A., Xia, Y. X., Moore, R. C.: Waste Isolation Pilot Plant Actinide Source Term Test Program: Solubility Studies and Development of Modeling Parameters. Sandia National Laboratories. SAND99-0943. Albuquerque, NM , 2001.

3.6 Use of Oxidation-State Analogs for WIPP Actinide Chemistry[1]

Nathalie A. Wall, Emily R. Giambalvo, Laurence H. Brush, and Donald E. Wall
Sandia National Laboratories, MS 1395
4100 National Parks Highway
Carlsbad, NM 88220 USA

This paper was presented as a poster at the 223rd National American Chemical Society Meeting, April 7-11, 2002, in Orlando, FL (SAND2002-0698P). The format of the poster has been modified for inclusion in this report.

[1] This work is covered by WBS #1.3.5.1.2.1

Use of oxidation-state analogs for WIPP actinide chemistry.

Nathalie A. Wall, Emily R. Giambalvo, Laurence H. Brush, and Donald E. Wall

Sandia National Laboratories – Carlsbad Programs Group, 4100 National Parks Highway – Carlsbad, NM 88220 - USA

Introduction.

The Waste Isolation Pilot Plant (WIPP)

- WIPP has been open since March 1999 as a permanent TRU waste repository.
- First certified deep nuclear geological repository in the world.
- Excavated in a Permian bedded-salt formation.

Performance Assessment

For the Compliance Certification Application performance assessment (CCA PA) (US DOE, 1996), the DOE concluded that Th, U, Np, and Am will speciate in brines present in WIPP disposal rooms as:
Th(IV), U (IV or VI), Np (IV or V), Pu (III or IV), and Am (III).
The DOE also asserted that, because conditions in WIPP disposal rooms will be strongly reducing and the mildly reducing conditions predominant in the Culebra Formation (a fractured dolomite within the Rustler Formation), these elements will also speciate as Th(IV), U(IV or VI), Np(IV) or Np(V), Pu(III) or Pu(IV), Am(III) in the Culebra, which is the most transmissive unit at the WIPP site.

For Performance Assessment, DOE (US DOE, 1996) used:

- experimental data (Pitzer ion-interaction parameters) obtained with Am(III) and the oxidation-state analogy to predict the solubility of Pu(III), and
- experimental data (Pitzer ion-interaction parameters) obtained with Th(IV) and the oxidation-state analogy to predict the solubilities of U(IV), Np(IV), and Pu(IV).

The DOE used literature data to develop a Pitzer-based solubility model for Np(V), but did not use this model for elements other than Np because it maintained that none of the actinides that could affect the long-term performance of the WIPP would speciate in the +V oxidation state.

Reviewers criticize the use of oxidation states analogy

The Environmental Evaluation Group (EEG) provides independent technical review of the Waste Isolation Pilot Plant (WIPP) to ensure the protection of public health and safety, and the environment of New Mexico. EEG (Neill et al. 1998, Oversby 2000) criticized the DOE's use of experimental data for Am(III), and especially Th(IV), and the oxidation-state analogy to predict

the speciation and solubilities of Pu(III) and Pu(IV), respectively. EEG proposes, instead of using the oxidation state analogy, to conduct experiments "using U and Pu at redox conditions that were in the range of those possible for WIPP" (Oversby 2000).

Purpose of this work

The experiments proposed by EEG would be technically difficult and time consuming, as Pu may exist at different oxidation states simultaneously. This work presents an evaluation of the conservatism of using Am(III) to predict the solubility of Pu(III) and of using Th(IV) to predict the solubility of U(IV), Np(IV), and Pu(IV).
Conservatism is viewed by DOE as desirable in the sense that the Th and Am analogies would provide upper bounds for solubility of the An(IV) and An(III) species, respectively. Determination of bounding conditions for use in PA eliminates the need to determine values that lie within the boundaries. The DOE considers determination of values that lie within the boundary conditions established by the use of the oxidation state analogs to be an unnecessary expenditure of resources.

Objectives and Method

The program FMT (SNL, 1997), which is a computer code developed at SNL for calculating actinide concentration limits based on thermodynamic parameters, was used to calculate the solubility of Th(IV) and Am(III) in two different brines: ERDA 6, which is representative of a brine in the Castile Formation and Brine A, which is representative of a brine in the Salado Formation. The composition of the brines are described elsewhere (Brush, 1990). The input data necessary for these calculations were taken from published experimental data.
Similar calculations were performed to determine the solubility of Pu(III), U(IV), Np(IV) and Pu(IV). The Ksp values of the actinide solid phases were taken from published data and the stability constants of the actinides with the ligands of interest were estimated by using a modified Born equation.
The actinide solubilities were compared for each oxidation state.

The present work is intended only to make an evaluation of the utility of Th(IV) and Am(III) as analogs for the respective oxidation states of Pu, in order to establish boundary conditions for the behavior of Pu. It should not be concluded that the solubilities in the present work will be representative of actual WIPP conditions.

Input data

Table 1. Estimated concentrations of the organic ligands that could influence the performance of the repository (US DOE 1996: Appendix SOTERM)

acetate	oxalate	citrate	EDTA
1.1×10^{-3} M	4.7×10^{-4} M	7.4×10^{-3} M	4.2×10^{-6} M

Table 2. Solubility products (0 ionic strength) of the solids controlling An solubility.

	log K_{sp}^{0} *	Reference
$Pu(OH)_{3\ am}$	-26.2	Felmy et al., 1989
$Pu(OH)_{3\ am}$	-22.6	Katz et al., 1986
$Pu(OH)CO_{3\ c}$	unknown	
$Am(OH)_{3\ am}$	-24.5	Rai et al., 1983
$Am(OH)CO_{3\ c}$	-22.5	Felmy et al., 1990
$ThO_{2\ am}$	-45.5	Felmy et al., 1991
$UO_{2\ am}$	-54.5	Neck et al., 2001
$NpO_{2\ am}$	-56.7	Neck et al., 2001
$PuO_{2\ am}$	-58.5	Neck et al., 2001

- $K_{sp}^{0}{}_{(An(OH)n)} = K_{sp}^{0}{}_{(AnOn)} = [An^{n+}]\times[OH^-]^n\times\gamma_{An}\times\gamma_{OHn}$ and
  $K_{sp}^{0}{}_{(An(OH)CO3)} = [An^{n+}]\times[OH^-]\times[CO_3^{2-}]\times\gamma_{An}\times\gamma_{OH}\times\gamma CO_3$
  (where γ_i is the activity coefficient of i)
-

Table 3. Stability constants of the relevant complexes for WIPP, for Th(IV) and Am(III) (0 ionic strength)

Complex	Log β^0	reference
$Th_1(acetate)_1$	7.36	Choppin et al., 2001
$Th_1(citrate)_1$	15.24	Choppin et al., 2001
$Th_1(oxalate)_1$	11.39	Borkowski et al., 2001
$Th_1(EDTA)_1$	23.73	Calc. from Choppin et al., 2001
$Th(OH)_3\ CO_3^-$	38.28	Felmy et al., 1997
$Th(CO_3)_5^{6-}$	27.11	Felmy et al., 1997
Am(acetate)	2.74	Calc. from Choppin et al., 2001
Am(citrate)	8.80	Choppin et al., 2001
Am(oxalate)	6.16	Borkowski et al., 2001
Am(EDTA)	18.97	Choppin et al., 2001
$Am(OH)_{3\ aq}$	14.99	Rai et al., 1983
$Am(OH)_2^+$	10.89	Rai et al., 1983
$Am(OH)^{2+}$	5.80	Rai et al., 1983
$AmCO_3^+$	7.57	Felmy et al., 1990
$Am(CO_3)_2^-$	12.29	Felmy et al., 1990
$Am(CO_3)_3^{3-}$	15.17	Felmy et al., 1990

Table 4. Bond length An-O* (Shannon 1976, David 1986)

	d(An-O) (Å)
Th(IV)	2.40
U(IV)	2.35
Np (IV)	2.33
Pu(III)	2.47
Pu (IV)	2.31
Am(III)	2.44

* Coordination number 8

The stability constants of U(IV), Np(IV), and Pu(III and IV) with acetate, citrate, oxalate, EDTA, OH and CO_3 can be estimated from a modified Born equation (Choppin, 1999), using the data of Table 3 and 4:

$$\log\left(\beta_{An_{(1)}}\right) = \log\left(\beta_{An_{(2)}}\right) \cdot \frac{d_{An_{(2)}-O}}{d_{An_{(1)}-O}}$$

Where An(1) and An(2) are different actinides in the same oxidation state.

Other considerations: MgO is placed in WIPP as a backfill. pH and f_{CO_2} are expected to be controlled by the Mg solid phases brucite [$Mg(OH)_2$] and hydromagnesite [$Mg_4 (CO_3)_3 (OH)_2 . 3 H_2O$].

Results

Table 5: Brine A (Salado brine) parameters:

pH (pcH)	I (m)	log (fCO_2 g)
8.69 (9.37)	7.42	-5.39

Table 6: ERDA 6 (Castile brine) parameters:

pH (pcH)	I (m)	log (fCO_2 g)
9.21 (9.87)	6.68	-5.39

An(III)

Calculations showed that the solid phase controlling the solubility is $AnOH(CO_3)_{am}$, but no experimental data exist on K_{sp} of $PuOH(CO_3)$. Our calculations were run only for $AmOH(CO_3)$. For comparison between Am(III) and Pu(III) solubilities, the solid phase controlling the solubility of An(III) was set as $An(OH)_{3\,am}$.

Table 7: An(III) solubilities in Brine A (Salado brine):

Solid phase	An(III) solubility (m)	Most soluble species (m)
$AmOH(CO_3)_c$	$1.0 \cdot 10^{-6}$	$(Am)_1(EDTA)_1$: $6.9 \cdot 10^{-7}$ $Am(OH)_2^+$: $3.2 \cdot 10^{-7}$
$Am(OH)_{3\ am}$	$1.5 \cdot 10^{-4}$	$Am(OH)_2^+$: $1.4 \cdot 10^{-4}$ $(Am)_1(citrate)_1$: $1.0 \cdot 10^{-5}$
$Pu(OH)_{3\ am}$ based on Felmy (1989) K_{sp}	$4.3 \cdot 10^{-6}$	$(Pu)_1(EDTA)_1$: $2.1 \cdot 10^{-6}$ $Pu(OH)_2^+$: $2.0 \cdot 10^{-6}$
$Pu(OH)_{3\ am}$ based on Katz (1986) K_{sp}	$9.0 \cdot 10^{-3}$	$Pu(OH)_2^+$: $8.2 \cdot 10^{-3}$ $(Pu)_1(citrate)_1$: $6.0 \cdot 10^{-4}$

Table 8: An(III) solubilities in ERDA 6 (Castile brine):

Solid phase	An(III) solubility (m)	Most soluble species (m)
$AmOH(CO_3)_c$	$2.2 \cdot 10^{-7}$	$(Am)_1(EDTA)_1$: $1.7 \cdot 10^{-7}$ $Am(OH)_2^+$: $4.0 \cdot 10^{-8}$
$Am(OH)_{3\ am}$	$2.2 \cdot 10^{-5}$	$Am(OH)_2^+$: $1.6 \cdot 10^{-5}$ $(Am)_1(EDTA)_1$: $4.0 \cdot 10^{-6}$
$Pu(OH)_{3\ am}$ based on Felmy (1989) K_{sp}	$9.8 \cdot 10^{-7}$	$(Pu)_1(EDTA)_1$: $7.2 \cdot 10^{-7}$ $Pu(OH)_2^+$: $2.3 \cdot 10^{-7}$
$Pu(OH)_{3\ am}$ based on Katz (1986) K_{sp}	$1.1 \cdot 10^{-3}$	$Pu(OH)_2^+$: $9.0 \cdot 10^{-4}$

An(IV)

Table 9: An(IV) solubilities in Brine A (Salado brine):

Solid phase	An(IV) solubility (m)	Most soluble species (m)
$ThO_{2\ am}$	$1.6 \cdot 10^{-8}$	$Th(OH)_3(CO_3)^-$: $1.6 \cdot 10^{-8}$
$UO_{2\ am}$	$1.1 \cdot 10^{-16}$	$U(OH)_3(CO_3)^-$: $1.1 \cdot 10^{-16}$
$NpO_{2\ am}$	$1.5 \cdot 10^{-18}$	$Np(OH)_3(CO_3)^-$: $1.5 \cdot 10^{-18}$
$PuO_{2\ am}$	$5.1 \cdot 10^{-20}$	$Pu(OH)_3(CO_3)^-$: $5.1 \cdot 10^{-20}$

Table 10: An(IV) solubilities in ERDA 6 (Castile brine):

Solid phase	An(IV) solubility (m)	Most soluble species (m)
$ThO_{2\,am}$	$5.6 \cdot 10^{-8}$	$Th(OH)_3(CO_3)^-$: $5.6 \cdot 10^{-8}$
$UO_{2\,am}$	$3.7 \cdot 10^{-16}$	$U(OH)_3(CO_3)^-$: $3.7 \cdot 10^{-16}$
$NpO_{2\,am}$	$5.0 \cdot 10^{-18}$	$Np(OH)_3(CO_3)^-$: $5.0 \cdot 10^{-18}$
$PuO_{2\,am}$	$1.7 \cdot 10^{-19}$	$Pu(OH)_3(CO_3)^-$: $1.7 \cdot 10^{-19}$

References

- Borkowki M., Moore R.C., Bronikowski M.G., Chen J., Pokrovsky O., Xia Y., and Choppin G.R., 2001, J. Radioanal. Nuc. Chem. 248, 467-471. Thermodynamic Modeling of Actinide Complexation with Oxalate at High Ionic Strength.
- Brush L.H., 1990, SAND90-0266, Test Plan for Laboratory and Modeling Studies of Repository and Radionuclide Chemistry for the Waste Isolation Pilot Plant. SNL WIPP Library.
- Choppin G.R., 1999, Radiochim. Acta 85, 89-95. Utility of Oxidation State Analogs in the Study of Plutonium Behavior.
- Choppin G.R., Bond A.H., Borkowski M., Bronikowski M.G., Chen J.F., Lis S., Mizera J., Pokrovsky O., Wall N.A., Xia Y.X., and Moore R.C., 2001, SAND99-0943. Waste Isolation Pilot Plant Actinide Source Term Test Program: Solubility Studies and Development of Modeling Parameters. SNL WIPP Library.
- David F., 1986, J. Less-Common Met. 121, 27-42. Thermodynamic Properties of Lanthanide and Actinide Ions in Aqueous Solution.
- Felmy A.R., Rai D., Schramke J.A., and Ryan J.L., 1989, Radiochim. Acta 48, 29-35. The Solubility of Plutonium Hydroxide in Dilute Solution and in High-Ionic-Strength Chloride Brines.
- Felmy A.R., Rai D., and Fulton R. W., 1990, Radiochim. Acta 50, 193-204. The Solubility of AmOHCO3(c) and the Aqueous Thermodynamics of the System Na+-Am3+-HCO3--CO32--OH--H2O.
- Felmy A.R., Rai D., and Mason M.J., 1991, Radiochim. Acta 55, 177-185. The Solubility of hydrous Thorium(IV) Oxide in Chloride Media: Development of an Aqueous Ion-Interaction Model.
- Felmy A.R., Rai D., Sterner S.M., Mason M.J., Hess N.J., and Conradson S.D., 1997, J. Sol. Chem. 26, 233-248. Thermodynamic Models for Highly Charged Aqueous Species: Solubility of Th(IV) Hydrous Oxide in Concentrated NaHCO3 and Na2CO3 Solutions.
- Katz J.J., Seaborg G.T. and Morss L.R., 1986, The Chemistry of the Actinide Elements. Chapman and Hall Ltd. (Vol. 2, p.1289)
- Moore R.C., Borkowski M., Bronikowski M.G., Chen J., Pokrovsky O.S., Xia Y., and Choppin G.R., 1999, J. Sol. Chem. 28, 521-531. Thermodynamic Modeling of Actinide Complexation with Acetate and Lactate at High Ionic Strength.
- Neck V. and Kim J.I., 2001, Radiochim. Acta 89, 1-16. Solubility and Hydrolysis of Tetravalent Actinides.
- Neill R.H, Chaturvedi L., Rucker D.F, Silva M.K, Walker B.A, Channell J.K and Clemo T.M., 1998, EEG-68, Evaluation of the WIPP Project's Compliance with the EPA Radiation Protection Standards for Disposal of Transuranic Waste. Albuquerque, NM: Environmental

Evaluation Group. SNL WIPP Library.

- Oversby V., 2000, EEG-77, Plutonium chemistry under conditions relevant for WIPP performance assessment: Review of experimental results and recommendations for future work. Albuquerque, NM. SNL WIPP Library.
- Rai D., Strickert R.G., Moore D.A., and Ryan J.L., 1983, Radiochim. Acta 33, 201-206. Am(III) Hydrolysis Constants and Solubility of Am(III) Hydroxide.
- Shannon R.D., 1976, Acta Cryst. A32, 751-767. Revised Effective Ionic Radii and Systematic Studies of Interatomic Distances in Halides and Chalcogenides.
- Sandia National Laboratories 1997. FMT(version 2.2). WPO#28119 March 12, 1997. SNL WIPP Library.
- US DOE, 1996, DOE/CAO-1996-2184, Title 40 CFR Part 191 Compliance Certification Application for the Waste Isolation Pilot Plant, Vol. 1-21. Carlsbad, NM: US Department of Energy, Carlsbad Area Office. SNL WIPP Library.

4.1 Carbonation of Magnesium Oxide[1]

Anna C. Snider and Yongliang Xiong
Sandia National Laboratories, MS 1395
4100 National Parks Highway
Carlsbad, NM USA 88220

Abstract

Sandia National Laboratories' (SNL's) Carlsbad Programs Group is currently investigating several issues with respect to the efficacy of magnesium oxide (MgO) under expected repository conditions. Characterization of Premier Chemicals MgO, with respect to both mineralogy and composition, and its ability to absorb water (H_2O) and carbon dioxide (CO_2) under repository conditions continues. Previous work has been described in SNL's (2001a, 2001b, 2002) progress reports to the US Department of Energy (DOE). This section of the status report concentrates on the ability of MgO to sequester CO_2.

MgO carbonation rates are being measured at a CO_2 partial pressure (P_{CO_2}) of about $10^{-3.5}$ atm (ambient atmospheric P_{CO_2}) and at 5% CO_2 ($5x10^{-2}$ atm). In experiments using Premier MgO as the starting material at atmospheric P_{CO_2}, carbonation continues at a slow rate. After 264 days hydromagnesite was identified. (Hydromagnesite can have various compositions; the composition of hydromagnesite formed in these experiments has not been determined yet.) At 5% CO_2, carbonation occurs at a faster rate. Several different carbonation pathways have been identified.

In experiments started with brucite ($Mg(OH)_2$), the hydration product of periclase (MgO), and carried out at $P_{CO_2} = 10^{-3.5}$ atm and 25°C, hydromagnesite was formed about 1100 hours after initiation of the runs. Chemical speciation modeling based on experimentally determined solution compositions indicates that solutions are supersaturated with respect to hydromagnesite soon after initiation (after about 500 hours). The modeling also indicates that the tendency to precipitate nesquehonite ($MgCO_3 \cdot 3H_2O$) is not favored, especially in high ionic strength solutions. Therefore, the reaction path, periclase → brucite → nesquehonite → hydromagnesite, proposed before based upon the previous experimental results at a relatively high P_{CO_2} of 1 atm, should not be applicable to more realistic levels of P_{CO_2} (i.e., $P_{CO_2} = 10^{-3.5}$ atm or lower). Instead, the reaction path should be periclase → (magnesium chloride hydroxide hydrate) → brucite → hydromagnesite at low P_{CO_2}. This reaction path is well supported by field observations on the carbonation of magnesian lime owing to the exposure to atmospheric CO_2.

---

[1] This work is covered by WBS #1.3.5.4.3.1

The conversion rate from brucite to hydromagnesite in de-ionized (DI) water is tentatively determined to be on the order of 10^{-5} hour^{-1}. Based upon this tentative conversion rate, the time required for the full carbonation of brucite in DI water would be expected to be on the order of a few decades. When more data become available, this conversion rate will be refined, and conversion rates in other solutions will also be obtained. When such conversion rates are available, these in combination with hydration rates of MgO established previously in various solutions (SNL, 2001a; 2001b; 2002) will allow estimation of the time required for the full carbonation of MgO in various solutions.

Introduction and Objectives

In the Compliance Certification Application (CCA), the DOE asserted (US DOE, 1996) that MgO, along with panel closures, shaft seals, and borehole plugs, would help meet the requirement for multiple natural and engineered barriers, one of the assurance requirements in the regulations for the radioactive constituents of transuranic waste (US EPA, 1993). In May 1998, the EPA certified that the WIPP complies with these regulations (US EPA, 1998). In its certification, the EPA ruled that MgO is the only engineered barrier in the WIPP disposal system, and that MgO will prevent or delay the movement of radionuclides toward the accessible environment by consuming the CO_2 generated by possible microbial degradation of organic materials in the waste. Furthermore, hydration of MgO will reduce the amount of brine in the repository. Finally, the reaction products of MgO will maintain the CO_2 fugacity (f_{CO_2}) and pH in the repository within optimal ranges, in which actinide solubilities in brine are at a minimum.

Experimental work carried out previously at Sandia has shown that MgO is effective at absorbing H_2O and CO_2 (Papenguth et al., 1997; 1999). Currently, more MgO will be emplaced in the WIPP than calculations suggest will be necessary to absorb CO_2 generated through microbial degradation of organic materials. At low pressures, the partial pressure of CO_2 equals to the fugacity of CO_2. At high pressures, the partial pressure of CO_2 needs to be corrected by fugacity coefficients to give the fugacity of CO_2, similar to correcting concentrations by activity coefficients to give activities in high ionic strength solutions. In total, about 70,000 metric tons of MgO will be emplaced in the WIPP to absorb CO_2.

Although the work done to date on MgO is sufficient to show that it will be an effective engineered barrier by consuming CO_2, buffering repository conditions, and limiting actinide solubilities, Sandia is currently examining several additional issues, as discussed in SNL (2001a). Experimental programs are evaluating the ability of MgO obtained from a new vendor (Premier Chemicals) to consume H_2O and CO_2, and are determining the hydration and carbonation pathways that Premier MgO will follow under WIPP-relevant conditions. The f_{CO_2} predicted by chemical speciation calculations performed for the CCA results from the assumption of equilibrium with brucite and magnetite ($MgCO_3$). However, during its evaluation of the CCA, the EPA asserted that

metastable hydromagnesite is more likely than magnesite to form and persist throughout the 10,000-year period of performance of the WIPP and will have higher solubilities than magnesite. Furthermore, the EPA assumed that hydromagnesite will buffer f_{CO_2} at values higher than those calculated for the CCA. Previous work with MgO has been criticized for failing to consider the potential effect of metastable hydroxycarbonates such as hydromagnesite on repository chemistry. Sandia is currently working to identify the hydroxycarbonate phase(s) that might form.

To our knowledge, there are no previous experimental studies on the carbonation rates of MgO or its hydration product brucite under conditions relevant to the WIPP. Most of the previous experiments on the carbonation of periclase or brucite were conducted by engineers because hydromagnesite, one of the carbonation products of periclase or brucite, has several useful applications, including its use in pharmaceuticals as an inert vehicle and an adsorbent (Botha and Strydom, 2001). In these previous carbonation experiments, the partial pressures of CO_2 were at least 0.5 atm and as high as 7 atm (Fernandez et al., 1999; Botha and Strydom, 2001; and references therein). In addition, these experiments were conducted in solutions with low ionic strength (DI water, $I \approx 0$ M) (Fernandez et al., 1999; Botha and Strydom, 2001; and references therein). Clearly, such experimental conditions are irrelevant to the WIPP, in which very low partial pressures of CO_2 (at least as low as $10^{-3.5}$ atm) and solutions with high ionic strengths ($I = 7.2$ M for GWB, or 5.2 M for ERDA-6) are expected. Consequently, the results from such experiments conducted under conditions irrelevant to the WIPP cannot be used for the performance assessment of the WIPP. Therefore, carbonation experiments under conditions relevant to the WIPP must be conducted. Although there were preliminary carbonation experiments conducted at Sandia in Albuquerque (Papenguth et al., 1997), these experiments were also conducted at relatively high P_{CO_2} (1 atm).

The objectives of current experiments are multifold: (1) continued characterization of a new batch of Premier Chemicals MgO; (2) determination of hydration rates and pathways; (3) quantification of carbonation rates and identification of the metastable mineral(s) produced; (4) quantification of the effect(s) of possible lithification on hydration and carbonation rates and pathways. These experiments are described by Wang et al. (2001). All of these experiments are being run using MgO from Premier Chemicals, the new vendor supplying the repository, and pure MgO and brucite purchased from Fisher Scientific.

MgO Hydration Experiments

All hydration experiments are continuing. Since January 2002, a large amount of data has been collected. New inundated hydration experiments have been initiated to determine possible phases of magnesium chloride hydroxide hydrate forms at higher temperatures in GWB. However, samples collected to date have not been thoroughly analyzed yet. The results of the hydration experiments have been submitted as an abstract to the Material Research Society for the Fall 2002 conference.

Little space has been dedicated to the status of these experiments since the results to date have not brought forth interpretations fundamentally different than before. Instead it is the goal of this status report to concentrate primarily on what has been occurring with respect to carbonation experiments, for there is a great deal of new data to report.

Carbonation Rate Experiments

Reaction of MgO with CO_2 can produce a series of Mg-carbonate minerals with magnesite as the most stable phase (Königsberger et al., 1999). Different Mg-carbonate and hydroxycarbonate minerals impose different values of the CO_2 fugacity and possibly on brine pH. In the WIPP CCA, it was assumed that metastable Mg-carbonate minerals would ultimately be converted to magnesite. However, the EPA assumed that hydromagnesite would persist throughout the 10,000-year period of performance. The objectives of current experiments are to gain a more mechanistic understanding of MgO carbonation and determine which Mg-carbonate phase will control the f_{CO_2}. These experiments will help determine: (1) how solution chemistry affects Mg-carbonate formation; which in turn will control brine f_{CO_2} and possibly pH; (2) the carbonation rates of Premier Chemicals MgO and brucite under various conditions.

The design of carbonation experiments has been described in detail by Wang et al. (2001). Therefore, only a brief summary of these experimental designs is presented here.

Prior to carbonation, periclase hydrates to brucite or (in the case of inundated experiments with GWB) magnesium chloride hydroxide followed by brucite (SNL, 2002) as follows:

$$MgO\ (s) + H_2O\ (aq.\ or\ gas) = Mg(OH)_2\ (s) \quad (1)$$

Hydration rates can be obtained from hydration experiments described in detail by SNL (2002). The carbonation experiments will provide rates of conversion of brucite to Mg-carbonate in various solutions. Using hydromagnesite as an example, the carbonation of brucite can be expressed as the following reaction,

$$5Mg(OH)_2\ (s) + 4CO_2\ (aq.\ or\ gas) = Mg_5(CO_3)_4(OH)_2{:}4H_2O \quad (2)$$

In order to investigate the overall carbonation rates (MgO conversion to Mg-carbonate), additional experiments are being conducted using periclase as a starting material. The net reaction corresponds to the combination of Reactions 1 and 2.

As suggested by Reaction 2, carbonation can take place in both aqueous (inundated) and gaseous (humid) media. In carbonation experiments using brucite as starting material, experiments are designed to investigate carbonation rates in both aqueous and gaseous media. Most inundated experiments are conducted at $P_{CO_2} = 10^{-3.5}$

atm. Some inundated experiments are conducted at lower P_{CO_2} by utilizing the diffusivity of CO_2 dissolved in aqueous medium into polyethylene bottles containing brucite and solutions of interest. The amounts of dissolved CO_2 diffused into these polyethylene bottles are dictated by the saturation equilibrium of the carbonate phase that is forming. Then, from Henry's Law, the partial pressure of CO_2 can be obtained according to the concentration of the dissolved CO_2. In the carbonation experiments started with MgO, experiments are designed to investigate the carbonation rates in aqueous media only (inundated experiments) at P_{CO_2} of $5x10^{-2}$ and $10^{-3.5}$ atm.

In the following, preliminary results from inundated experiments using both Premier MgO and Fisher brucite as starting materials are reported.

EXPERIMENTS USING MGO AS STARTING MATERIAL

The first set of carbonation rate experiments are run at two different partial pressures of CO_2, under atmospheric conditions ($\sim 10^{-3.5}$ atm) and 5% CO_2 ($5x10^{-2}$). In the future experiments may be run under other partial pressures, such as $1/10^{th}$ atmospheric CO_2.

Experiments At Atmospheric P_{co_2} ($10^{-3.5}$atm)

Experimental Setup

The experiment running under atmospheric P_{CO_2} conditions is using four different solutions: DI water, 4 M NaCl, ERDA-6, and GWB. Each sample bottle includes 5 g Premier Chemicals MgO and 100 ml of electrolyte. Room air is bubbled continuously through the samples using a gas manifold. Each manifold holds 24 samples. To minimize evaporation, the air is humidified by bubbling through water prior to entering the manifold.

Samples were collected at weekly intervals and are now collected on a monthly to bimonthly interval. Samples are measured for pH, filtered, and the solid dried and crushed. Carbonate identification and conversion rates are ascertained by using a UIC carbon coulometer, x-ray diffractometer (XRD), and scanning electron microscope (SEM) to analyze the solid phase, and an inductively coupled plasma optical emission spectrometer (ICP-OES) to analyze the filtrate. The carbon coulometer determines the percent C in the solid, whereas the XRD identifies the carbonate phase present. The SEM qualifies what elements constitute the mineral phases and shows the physical attributes of each mineral. The ICP-OES quantifies concentrations of elements of interest in sampled brines to help in the interpretation of the carbonation pathway(s).

Experimental Results

Carbonate conversion. Carbon coulometer results (corrected for mole percent carbonation) from atmospheric P_{CO_2} conditions are displayed in Figure 1. The data points represent a minimum mole percent carbonation. Calculations used a one to one ratio of moles of C to moles of Mg. If the Mg-carbonate phase were solely hydromagnesite, then the maximum value calculated would be approximately 20% higher than the results reported below. These results show that carbonation is proceeding slowly in both of the WIPP brines (ERDA-6 and GWB). Analysis of samples from ERDA-6 indicates over 7 mol % conversion, whereas samples with GWB have converted approximately 5 mol % Mg. However, these results are not surprising in view of the fact that this experiment is being run at a low P_{CO_2} in order to simulate the very slow rates at which microbial activity will produce CO_2 in the repository. (Experiments carried out at high CO_2 pressures result in faster carbonation rates, but could produce metastable Mg-hydroxycarbonates different from those that will form in the repository. These phases could in turn buffer the P_{CO_2} and pH at a value different from that expected in the repository.) In view of the uncertainties associated with these data (see error bars in Figure 1), it is not believed that the decrease in the C content of the ERDA-6 samples from 264 to 327 days represents de-carbonation, or even a cessation of carbonation, of these samples. Rather, it is likely that the overall upward trend exhibited by the ERDA-6 samples - and the samples from the other three solutions - will continue, albeit slowly.

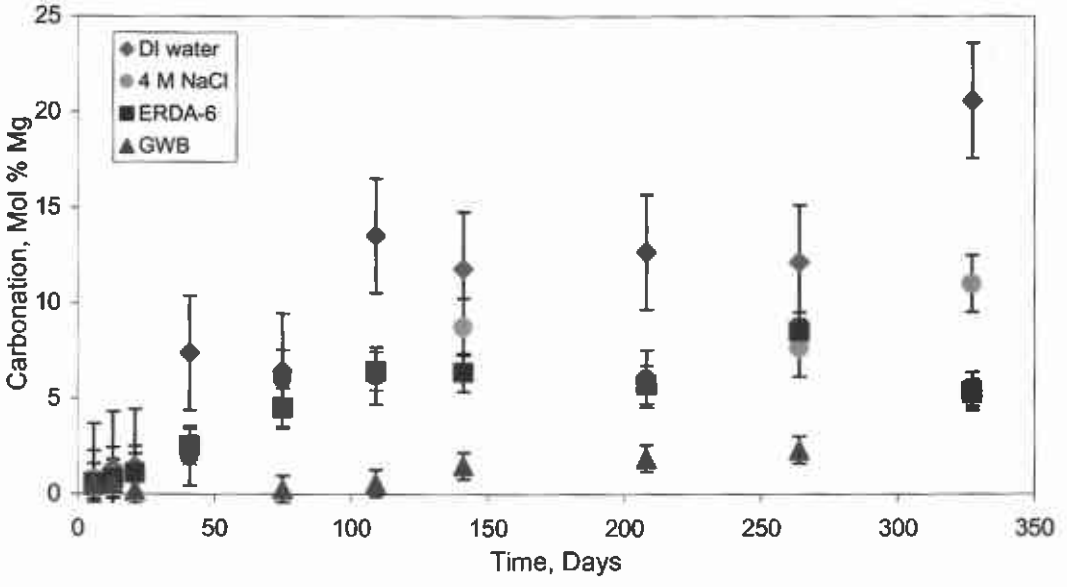

Figure 1. Results from the atmospheric P_{CO_2} experiment.

XRD results. Carbonates were not detected by XRD analysis until 264 days after the experiment had been initiated. The XRD has a detection limit of several percent. If carbonates were present before, they would constitute only a few percent of the total sample. At 264 days, 4 M NaCl was the only sample to display peaks representative of hydromagnesite and calcite ($CaCO_3$). After 327 days all four samples (DI water, 4 M NaCl, ERDA-6, and GWB) exhibited hydromagnesite and calcite peaks (Figure 2).

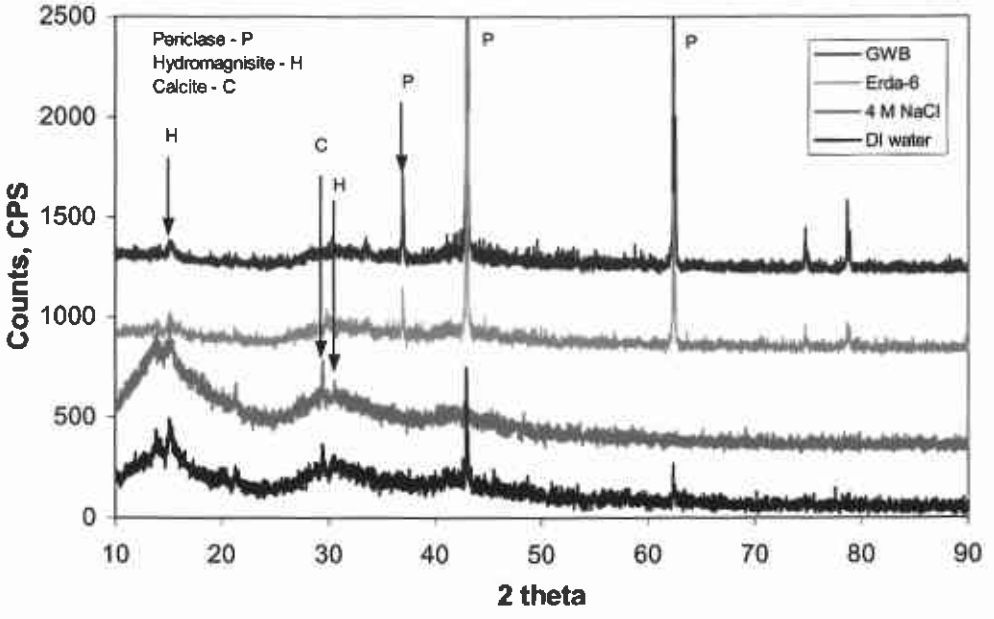

Figure 2. XRD patterns from atmospheric P_{CO2} experiments after 327 days. Note hydromagnesite (5:4:2:4; H) peaks. Hydromagnesite was confirmed using Rietveld refinement.

SEM results. After 141 days, the SEM showed the first evidence of carbonates. Ca-rich carbonates, determined using energy-dispersive x-ray spectrometry (EDS), were seen in both samples that had reacted in DI water and ERDA-6 (Figure 3). An SEM phase identification program was used to identify the carbonate phase(s) present. To identify a mineral, it must have a flat crystal surface that faces towards the detector. A pattern can then be produced as seen in Figure 4. The pattern produced did not have an exact phase ID match. The pattern most closely corresponded to a monoclinic Ca carbonate and, to a lesser degree, a Ca-Mg carbonate.

Although SEM analysis did not provide direct evidence for the conversion of brucite to a Mg carbonate, carbonate conversion calculations provided indirect evidence for carbonation of brucite. Calculations show that 1.7 mol % conversion of the total solid (ERDA-6 at 141 days) is equivalent to the conversion of ~5.7 mol % of Mg or ~7.9 mol % of Ca. However, as stated in SNL (2001), Premier Chemicals MgO contains < 1 wt % CaO. Therefore, there is not enough CaO in this material to have reacted with all of the CO_2 consumed by 141 days in ERDA-6. Assuming that there were 1 wt % CaO in the Premier Chemicals MgO, there would only be enough CaO to react with 12.7 % of

the CO_2 in the ERDA-6 sample after 141 days. This calculation suggests that other carbonate-bearing minerals must be present, most likely Mg-carbonate minerals.

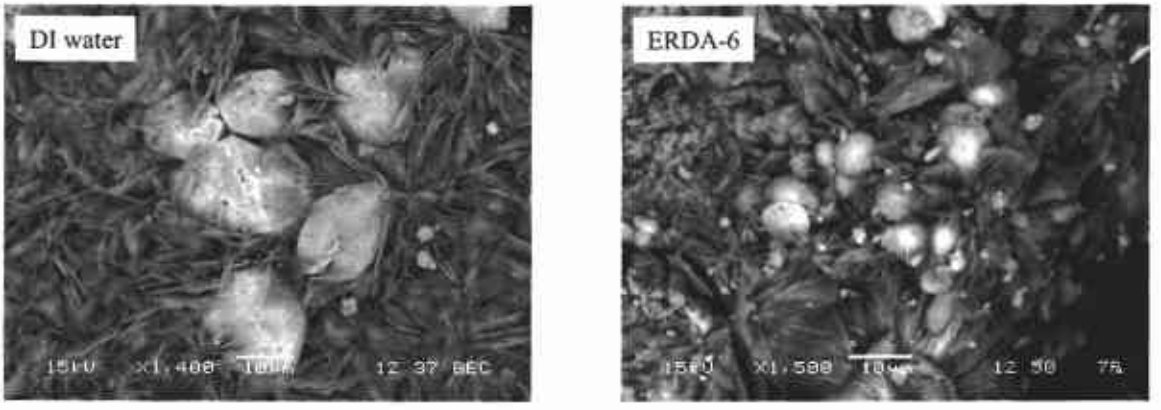

Figure 3. SEM images of Ca-carbonates (white) surrounded by brucite (gray) after 141 days.

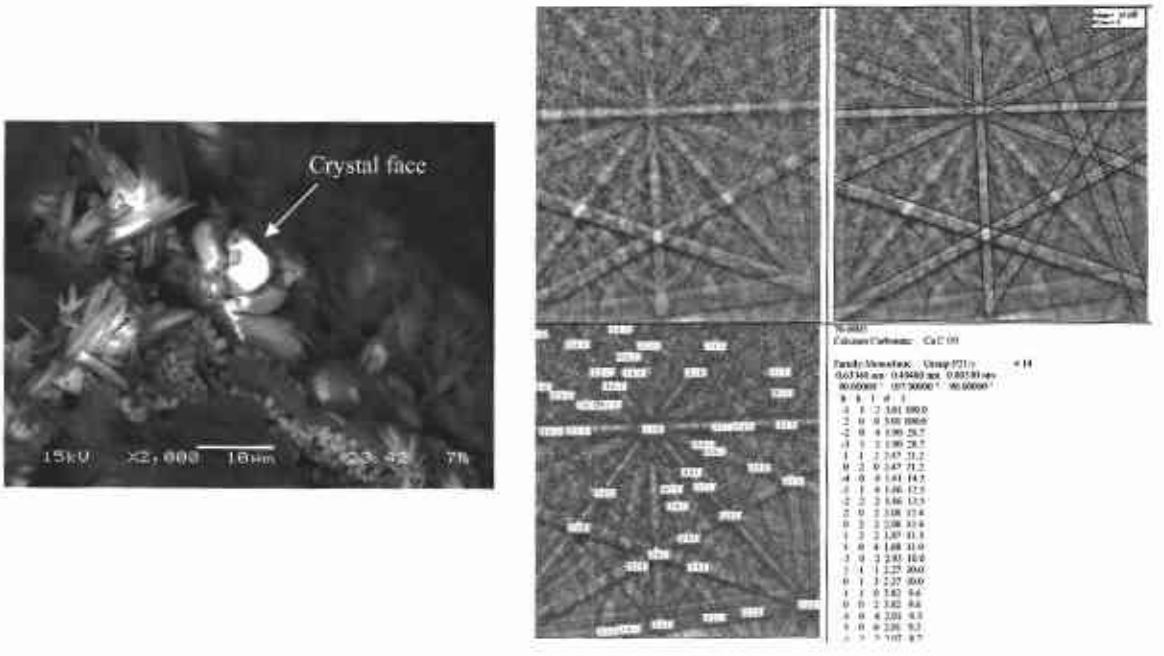

Figure 4. SEM image showing the crystal face (from a DI water sample) that was analyzed to find the accompanying pattern (right) using a SEM Phase ID program. The red lines superimposed on the pattern are a match that the computer found, identifying the mineral as a monoclinic calcium carbonate.

As suspected, after 264 days samples examined under the SEM using EDS confirmed the presence of Mg carbonates in all four solutions (Figure 5). The gray reaction mineral is most likely the Mg-carbonate mineral identified by the XRD as hydromagnesite.

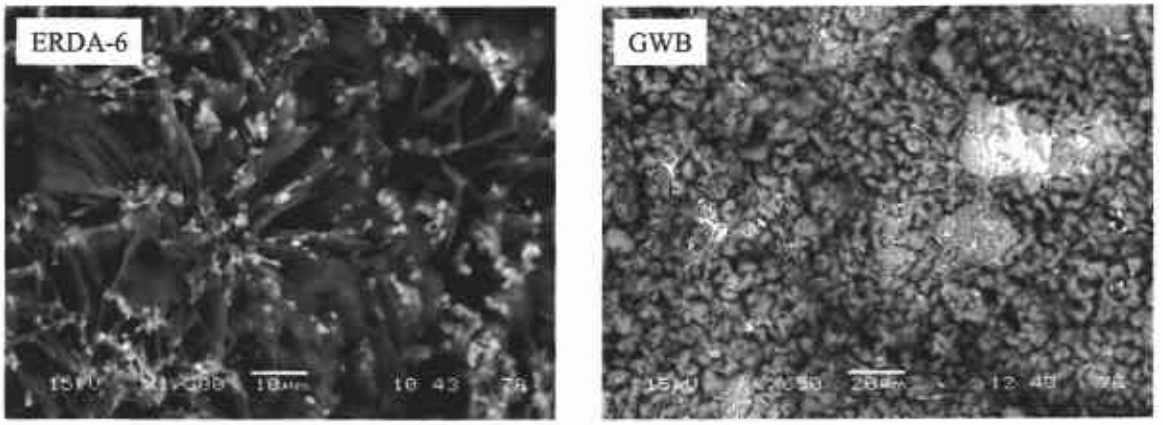

Figure 5. SEM images of Mg-carbonate minerals (gray) covered with halite (white) after 264 days.

ICP-OES results. Brine has been collected at each sampling from the atmospheric CO_2 experiments since the ninth sampling (264 days after experiment was initiated). The ICP-OES will be used to analyze the concentrations of Mg and Ca in each sample. The results will hopefully give additional information into deciphering the carbonate reaction pathway(s). To date only one set of samples has been analyzed. Consequently not enough data have been collected to make an interpretive statement. The other sets will be analyzed in the near future.

Summary

After 264 days, the SEM coupled with the XRD demonstrated that all solutions were forming a Mg-carbonate under atmospheric P_{CO_2} conditions. To date samples are continuing to carbonate, although slowly. MgO carbonates in ERDA-6 at a faster rate than GWB. The carbonates have been identified as calcite and hydromagnesite. Due to the high reactivity of lime (CaO), calcite forms first followed by hydromagnesite, a product from the reaction of periclase with CO_2. There has been no evidence to support the formation of nesquehonite.

Experiments at 5% CO_2 ($5x10^{-2.0}$atm)

Experimental Setup

The 5% CO_2 experiment will quantify carbonation in two brines, GWB and ERDA-6. The matrix of this experiment differs from that used for the atmospheric P_{CO_2} experiment. There are 64 samples (two brines x four solids x eight samples each). Each 125 ml polypropylene bottle contains 5 g of one of the following solids: Premier Chemicals MgO; Fisher Scientific MgO; "pre-hydrated", crushed Premier Chemicals MgO; and "pre-hydrated" Fisher MgO. Hydrated samples are prepared by adding 5 g of either crushed Premier Chemicals MgO, or Fisher MgO to 100 ml of brine. The bottles are placed in a 90°C oven for approximately three to four weeks. Before the "pre-hydrated" samples are added to the manifold, a small portion of the sample was analyzed for brucite. The experiment with 5% CO_2 is sampled at a higher frequency than the experiment with atmospheric P_{CO_2} due to the anticipated accelerated reactions. New sets of samples will be added periodically to extend the life of the experiment. Samples are subject to the same analyses as the atmospheric P_{CO_2} samples.

All 5% CO_2 samples are placed in a glovebox with a controlled atmosphere. The 5% CO_2 is controlled by pumping pre-mixed 5% CO_2 mixed with N_2 into the glovebox at 500 ml/min. To bring the glovebox up to 5% CO_2 in a timely manner after the box is opened for sampling, dilute sulfuric acid is mixed with sodium bicarbonate within the glovebox, which releases a pre-determined amount of CO_2 to the atmosphere. The atmosphere is monitored frequently with a Bacharach CO_2 analyzer.

Experimental Results

Carbonate Conversion. Carbon coulometer results (corrected for conversion of moles of Mg) for all four solids in both ERDA-6 and GWB are shown in Figures 6 and 7. Note that the data points represent a minimum mole percent carbonation. As expected all samples are reacting at a much faster rate than samples subjected to atmospheric partial pressures of CO_2. After only 91 days, ERDA-6 Fisher MgO has converted over 27 mol % of Mg to carbonate, and Fisher "pre-hydrated" MgO, Premier MgO, and Premier "pre-hydrated" MgO have not yet reached over 19% carbonation.

Data collected from GWB samples display more scatter. This may result from the difficulty in keeping all samples bubbling continuously. A cessation in bubbling may cause a CO_2 stratification within the liquid, thus preventing the sample from continuously being in full contact with 5% CO_2. "Pre-hydrated Fisher MgO shows the most scatter. What can be determined is that some hydrated Fisher MgO samples have converted over 18 mol % of Mg to carbonate, Fisher MgO has converted over 14 mol %, and the Premier products have converted between 6 and 11 mol %.

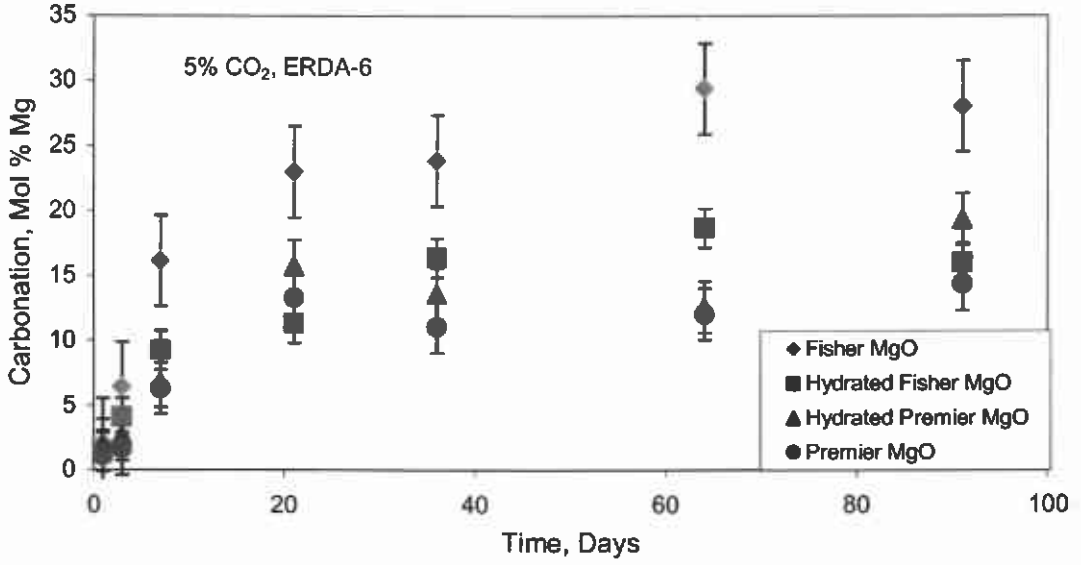

Figure 6. Results from 5% CO_2 samples inundated in ERDA-6 brine.

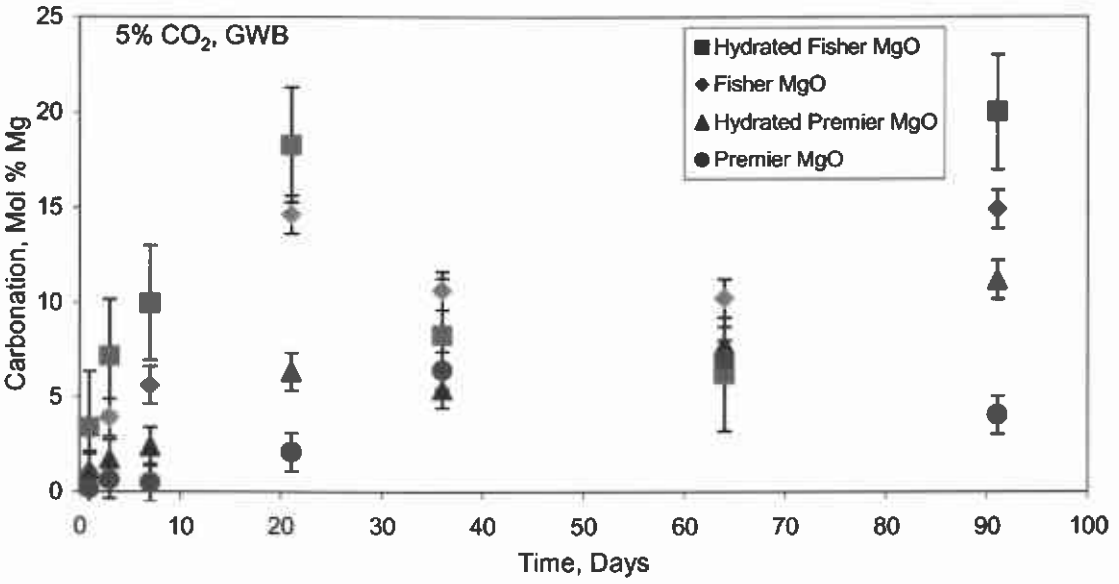

Figure 7. Results from 5% CO_2 samples inundated in GWB.

XRD Results. The XRD results within the 5% CO2 experiment suggest carbonation reaction pathways are dependent on the combination of solids, and/or brine used. ERDA-6 samples with Fisher Scientific products converted to nesquehonite first. Between seven and 21 days, Fisher "pre-hydrated" MgO converted to hydromagnesite (Figure 8). After 91 days Fisher MgO still has strong nesquehonite peaks with a possible,

poorly developed hydromagnesite peak starting to form. ERDA-6 samples with Premier Chemicals MgO behave somewhat differently. Premier "pre-hydrated" MgO forms nesquehonite first. Between 36 and 64 days nesquehonite converts to hydromagnesite. Hydromagnesite is the first Mg-carbonate mineral to show strong peaks in Premier MgO at 21 days (Figure 9). However, there also appears to be a poorly developed nesquehonite peak in the same XRD pattern, but by 36 days this peak disappeared. Samples from the GWB react at a slower rate compared to the ERDA-6 samples.

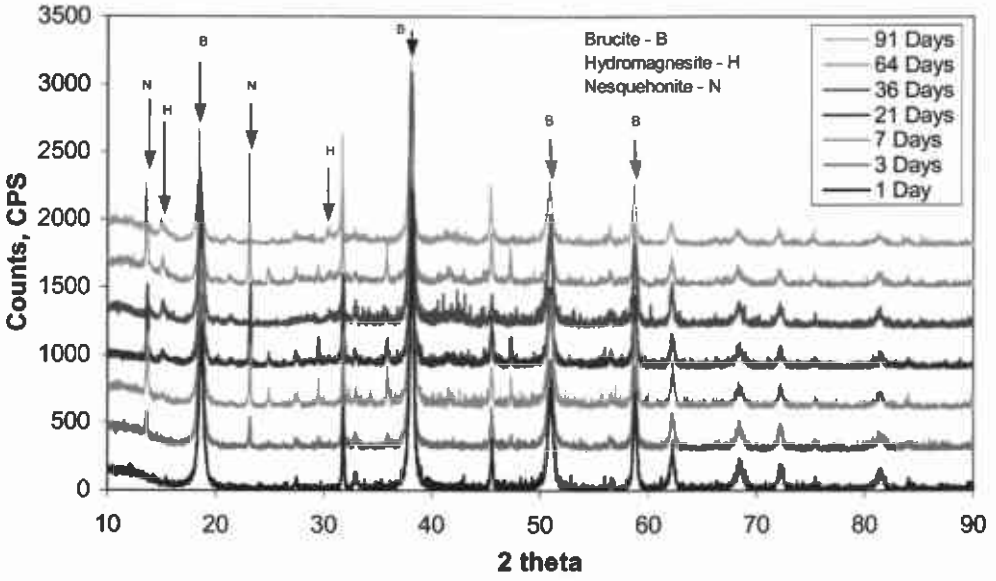

Figure 8. XRD patterns of Fisher pre-hydrated MgO inundated in ERDA-6 brine displayed sequentially through time. Note the nesquehonite (N) and hydromagnesite (5:4:2:4; H) peaks. Hydromagnesite was confirmed using Reitveld refinement. CPS- counts per second.

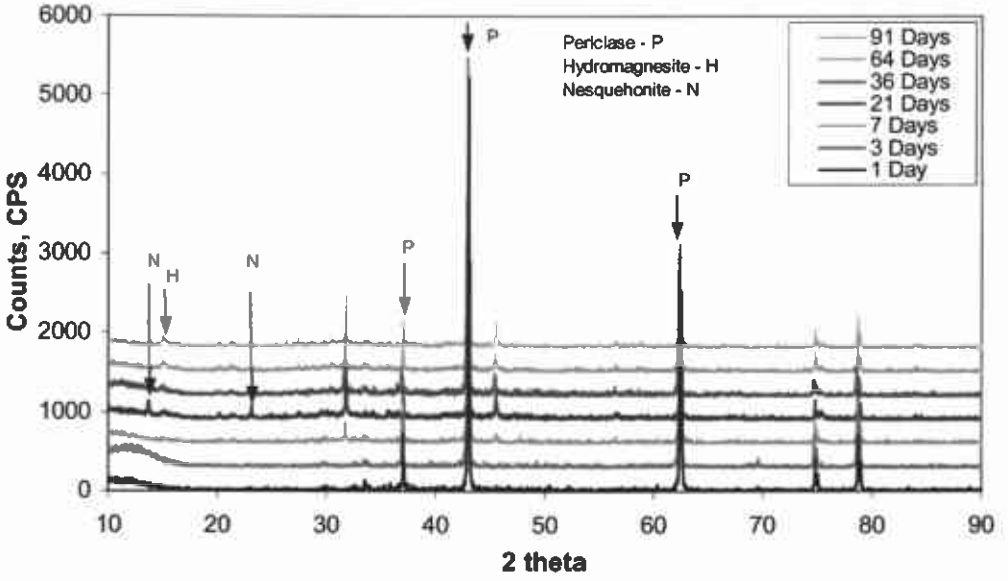

Figure 9. XRD patterns of Premier Chemicals MgO inundated in ERDA-6 displayed sequentially through time. Note hydromagnesite (5:4:2:4; H) peaks. Hydromagnesite was confirmed using Reitveld refinement.

Additionally, the GWB samples appear to skip the step of nesquehonite formation and instead form hydromagnesite. However, the hydromagnesite peak is not well developed, even after 91 days. In the Fisher products the small peak begins to appear after 21 days, whereas the hydromagnesite peak is first noted at 91 days in the samples that contained Premier Chemicals' products (Figure 10).

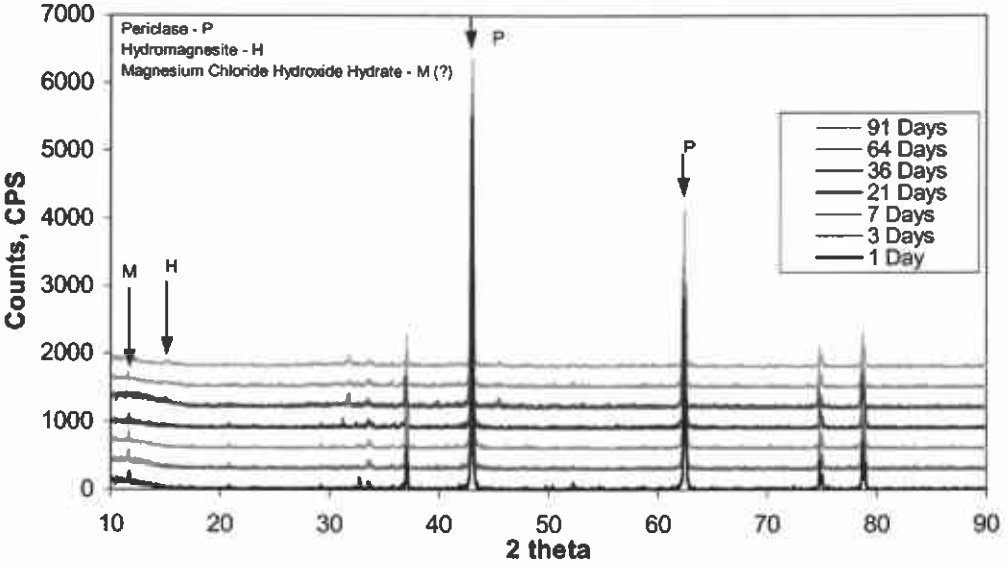

Figure 10. XRD patterns of Premier Chemicals MgO inundated in GWB displayed sequentially through time. Note hydromagnesite (5:4:2:4, H) peaks. Hydromagnesite was confirmed using Reitveld refinement.

SEM Results. The 5 % CO_2 samples taken after 91 days were analyzed on the SEM. With the aid of EDS, all samples show evidence of carbonation. The reaction products are Ca- and Mg-carbonates. All samples, except Fisher MgO in ERDA-6 brine, appear to have formed similar carbonate minerals (Figure 11), the reaction products most likely being Ca-carbonate and hydromagnesite. Fisher MgO in ERDA-6 shows a Mg-carbonate mineral, which exhibits a different crystal structure (Figure 12). Based on the data from XRD, the mineral is nesquehonite.

ICP-OES Results. Brine has been collected from every 5% CO_2 sampling. The ICP-OES will be used to analyze the dissolved concentration of Mg and Ca in each sample. The results will give additional information regarding the carbonate reaction pathway(s). To date the brine has not been analyzed.

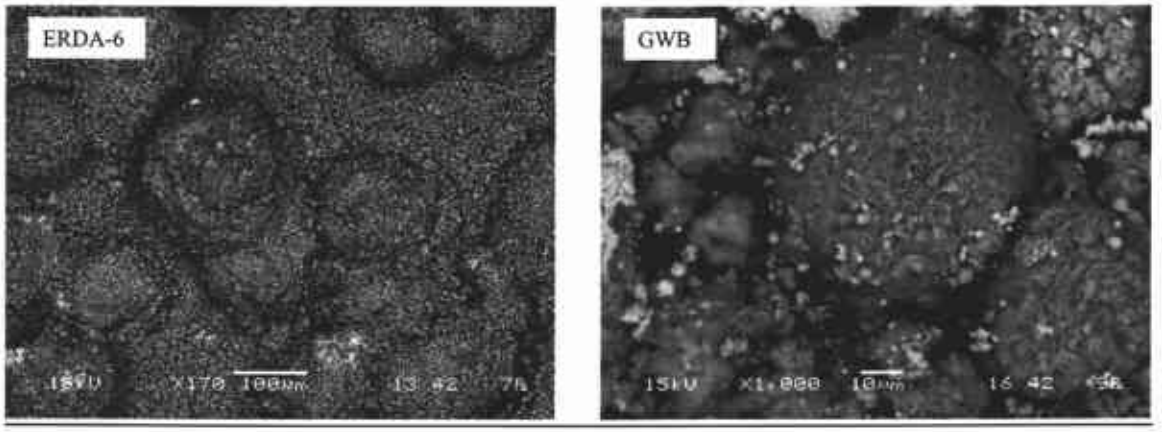

Figure 11. SEM images of Mg-carbonates (gray) found in ERDA-6 and GWB samples containing pre-hydrated Premier Chemicals MgO after 91 days.

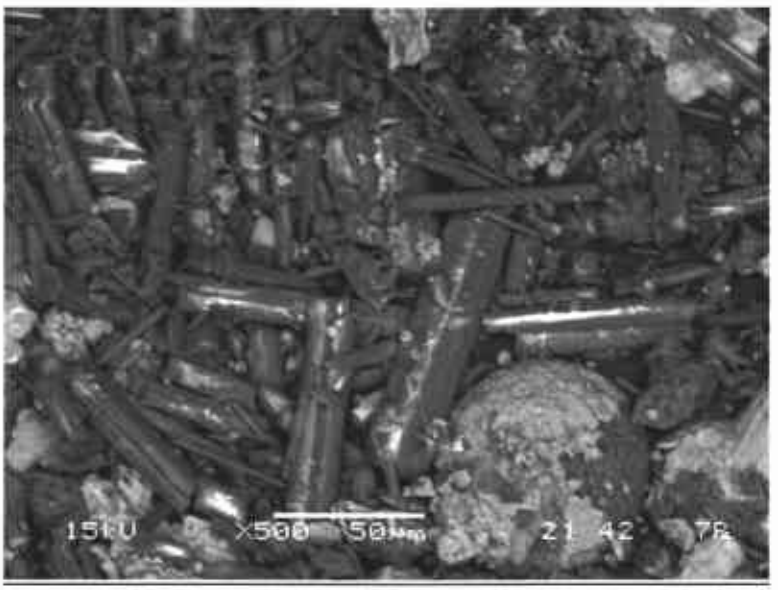

Figure 12. SEM image of nesquehonite (elongate gray crystals) present in the sample that contained Fisher MgO inundated in ERDA-6 brine after 91 days.Summary

Samples from the 5% CO_2 experiment show that carbonation is occurring at a faster rate than in the atmospheric P_{CO_2} experiment. Data exhibit more scatter in GWB, but all solids are continuing to carbonate. Carbonation pathways seem to be dependent on the solution and solid used. All solids in ERDA-6, except Fisher MgO, were converted to nesquehonite before eventually forming hydromagnesite. After 91 days, Fisher MgO has produced only nesquehonite. Solids inundated in GWB appear to have converted directly to hydromagnesite; however, the XRD peaks are not well developed.

EXPERIMENTS USING BRUCITE AS STARTING MATERIAL

In the following, results from inundated carbonation experiments using Fisher brucite in powder form as the starting material are presented in two parts. The first part covers the solution chemistry owing to carbonation processes. The second part describes the amounts of carbon incorporated in solid phases. Analysis of solution chemistry has been conducted on samples from DI H_2O and 4 M NaCl experiments. Analysis of solid phase chemistry has been conducted on samples from DI H_2O, 4 M NaCl, ERDA-6, and GWB experiments. Runs using brucite as starting material are compared to runs using uncrushed Premier MgO directly from the vender and Fisher MgO in powder form as starting material.

Solution Chemistry

In inundated experiments, solutions are sampled periodically and analyzed for Mg, Ca, K, Na, and pH. After the termination of runs, reaction products are filtered, dried and analyzed by a carbon coulometer for the amounts of C that have been incorporated into solid phase(s), and the carbonate phase(s) is determined by XRD and SEM. The advantage in analyzing dissolved chemical elements is that the carbonation processes can also be documented by changes in solution chemistry.

Figure 13 shows the change in pH with time at ionic strength close to zero (DI water) in runs using Premier MgO, Fisher MgO, and brucite. The decrease in pH in all three runs prior to 1500 hours suggests carbonation of starting materials, because it has been well established that carbonation decreases the pH (Butler, 1982). The initial pH in the run with Premier MgO is higher than initial pH in runs with Fisher MgO and brucite. After about 1500 hours, the pH values from these three runs are similar to each other and become stable. The initially higher pH in the run using Premier MgO is related to the buffering capacity of $Ca(OH)_2$, produced by the hydration of CaO:

$$CaO\ (s) + H_2O\ (l) = Ca(OH)_2\ (s) \quad (3)$$

Comparison of the initial pH in the experiment using Fisher MgO with that in the run using brucite also indicates that the initially higher pH in the run using Fisher MgO is initial dissolution of periclase. The pH values in the runs using Fisher MgO and brucite

are very close to each other after about 800 hours, implying the solution in the run using Fisher MgO as starting material reaches saturation with brucite. This will be quantitatively demonstrated in the following saturation calculations.

The negative logarithm of hydrogen ion concentration (pcH) is plotted versus time for 4 M NaCl experiments in Figure 14. It can be seen from Figure 14 that changes in pcH with time in 4 M NaCl solutions have the same trends as in the runs in DI water. Accordingly, explanations for the behavior in DI water should also be true for behavior in 4 M NaCl solution. Notice that pcH instead of pH is used in these runs in 4 M NaCl solution. The relation between the pH electrode reading (pH_{ob}) and pcH can be expressed as (Rai et al., 1995):

$$pcH = pH_{ob} + A \quad (4)$$

In Eq. (4), A is defined as:

$$A = \log \gamma_{H+} + (F/2.303RT)\, \Delta E_j, \quad (5)$$

in which γ_{H+} is the conventional activity coefficient of H^+, and ΔE_j is the difference in liquid junction potential between standards and solution. Both terms on the right-hand side of Equation 5 are not individually measurable, but the combination can be measured. Rai et al. (1995) have already obtained A values for NaCl solutions up to 6.0 m. Therefore, the experimentally measured pH values in this study (pH_{ob}) are corrected with the A value at the corresponding ionic strength to obtain pcH.

In Figures 15 and 16, concentrations of Ca in DI water and 4 M NaCl started with Premier MgO are shown. The steady-state concentrations of Ca are attained after about 1800 hours. The initial concentrations of Ca in these two runs are close. However, the steady state concentrations in 4 M NaCl solution ($\sim 2 \times 10^{-5}$ m) are about four times as high as those in DI water ($\sim 5 \times 10^{-6}$ m).

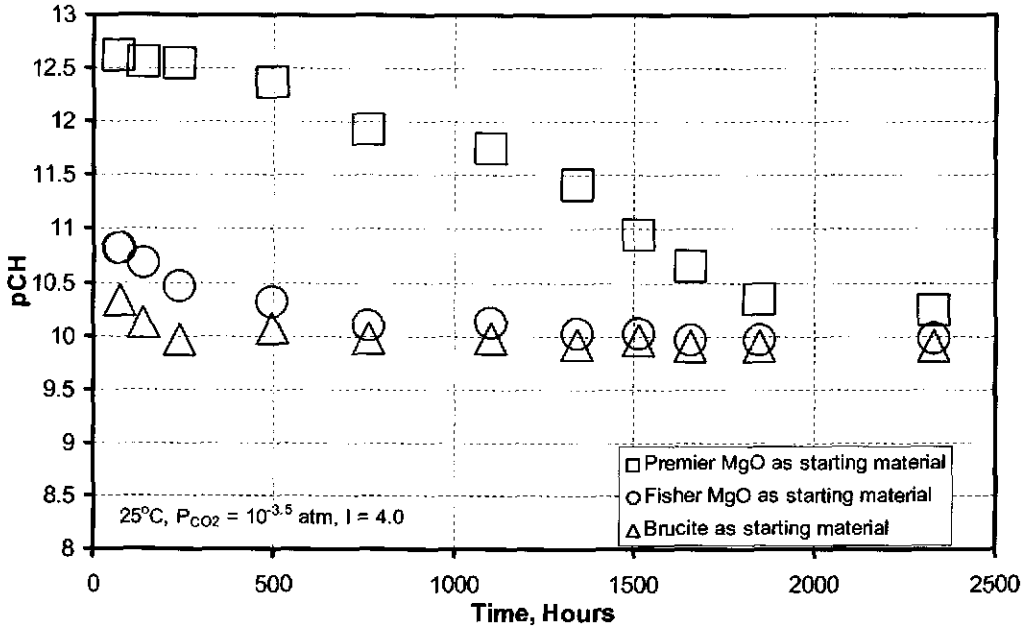

Figure 13. pH as a function of run time in DI water. The uncertainty is less than the size of symbols.

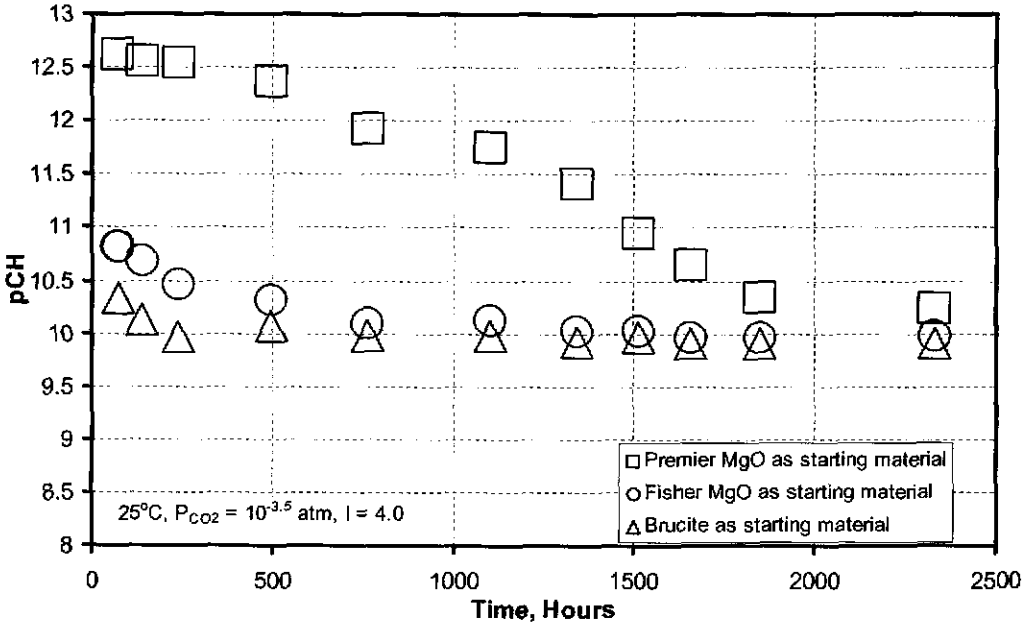

Figure 14. Hydrogen ion concentration (pcH) as a function of run time in 4 M NaCl solution. The uncertainty is less than the size of symbols.

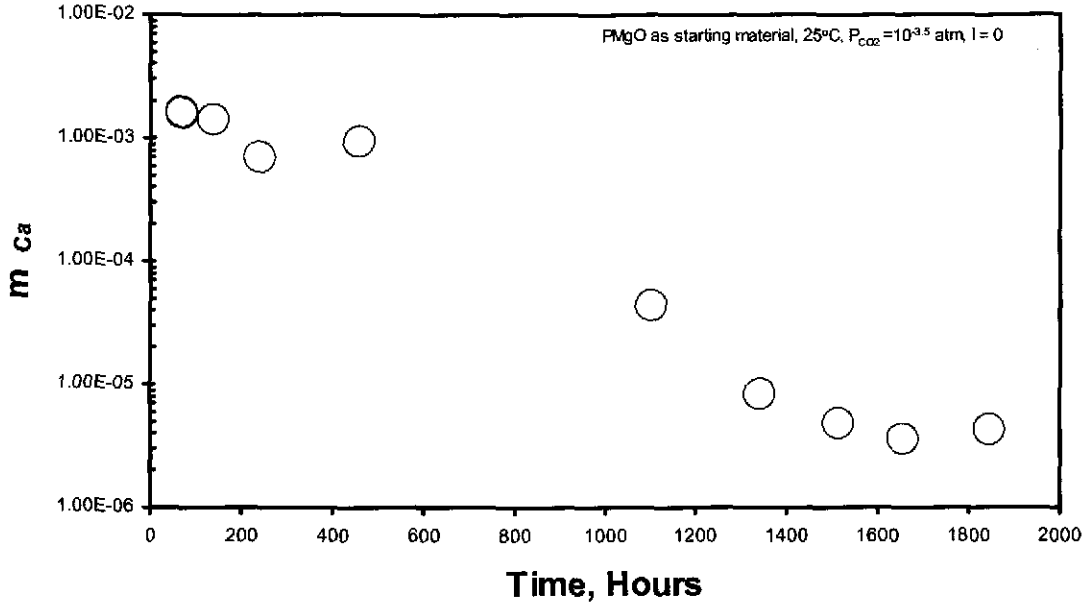

Figure 15. Ca concentration as a function of time in the DI water experiment using Premier MgO as starting material. The uncertainty is less than the size of symbols.

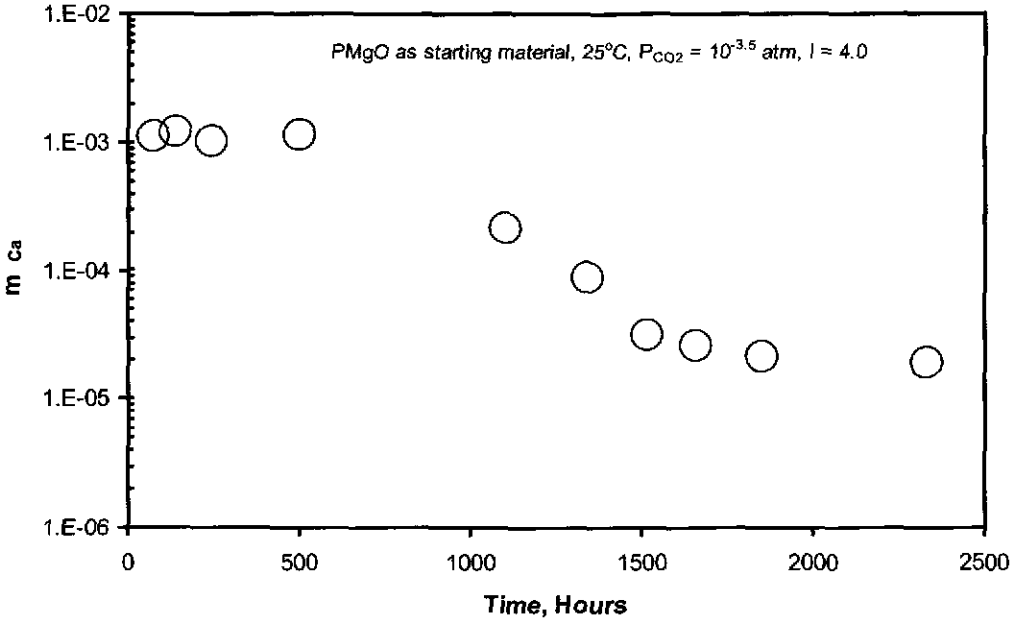

Figure 16. Ca concentration in 4 M NaCl as a function of time in the experiment using Premier MgO. Uncertainty is less than the size of symbols.

In Figure 17, concentrations of Mg in DI water are shown. The concentrations of Mg from the run started with uncrushed Premier MgO are lower than those from the runs using Fisher MgO and brucite in powder form. The lower concentrations in the run using uncrushed Premier MgO may be due to the larger size of MgO or the steady state concentrations have not been reached yet. In the runs using Fisher MgO and brucite as starting materials, the steady-state concentrations were attained after about 1100 hours, and the concentrations of Mg from these two runs using different starting materials are almost the same, implying the formation of the same solid phase(s).

In Figure 18, concentrations of Mg in 4 M NaCl solution are presented. Again, the Mg concentrations from the run using uncrushed Premier MgO are lower than those from the runs using Fisher MgO and brucite in powder form, which is consistent with the results in DI water (Figure 17). The steady-state Mg concentrations are attained after 1500 hours. The Mg concentrations from the runs using Fisher MgO and brucite are very close, implying the formation of the same solid phase(s).

On the basis of these results, the saturation states of various Mg-containing phases were calculated with the computer code EQ3NR, Version 7.2c (Wolery, 1992). Although XRD can determine whether the carbonation product(s) of interest is present when the amount of that phase exceeds a few percent, it cannot provide information regarding the onset of the formation of a particular phase. On the other hand, the saturation states would indicate the onset of the carbonation processes if the kinetics were favorable.

The saturation index (SI) is defined as:

$$SI = \log (Q/K_{sp}), \quad (6)$$

in which Q is ion activity product and K_{sp} is the solubility product for a phase of interest. When the SI of a solid phase of interest is positive in a solution, it means that the solution is supersaturated with that phase, implying that the phase has a tendency to precipitate. When the SI is negative, the solution is undersaturated with that phase, suggesting that the phase has a tendency to dissolve. When the SI is zero, the solution is in saturation equilibrium with that phase. Therefore, the SI for the following Mg-containing phases can be calculated for the following solubility reactions to infer their respective saturation states:

$$MgO\ (s) + H_2O = Mg^{+2} + 2OH^- \quad (7)$$

$$Mg(OH)_2\ (s) = Mg^{+2} + 2OH^- \quad (8)$$

$$Mg_5(CO_3)_4(OH)_2{:}4H_2O\ (s) = 5Mg^{+2} + 4CO_3^{-2} + 2OH^- + 4\ H_2O \quad (9)$$

$$Mg_4(CO_3)_3(OH)_2{:}3H_2O\ (s) = 4Mg^{+2} + 3CO_3^{-2} + 2OH^- + 3H_2O \quad (10)$$

$$MgCO_3{:}3H_2O\ (s) = Mg^{+2} + CO_3^{-2} + 3H_2O \quad (11)$$

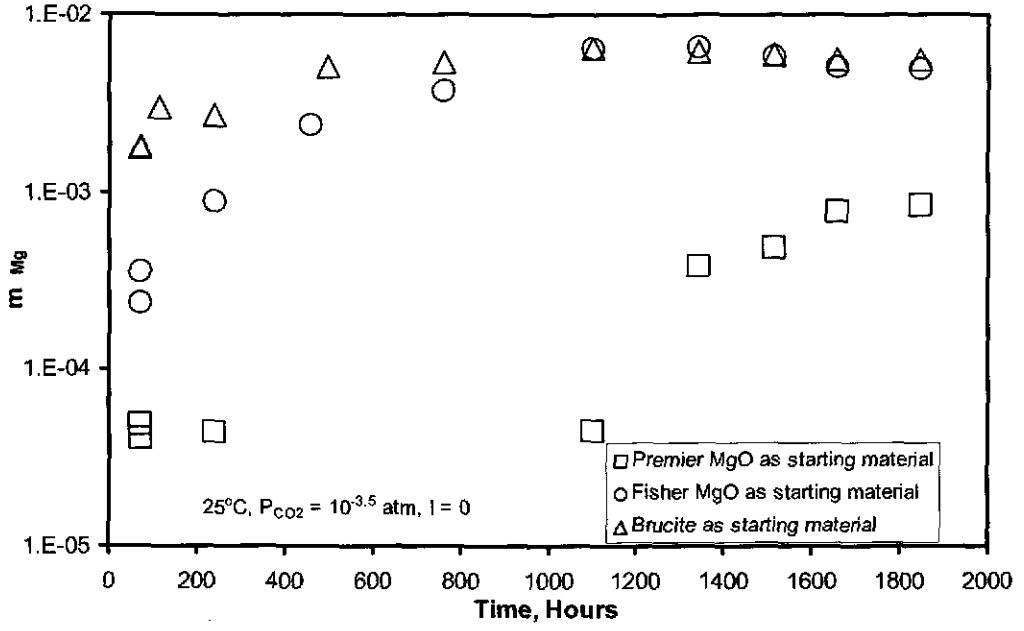

Figure 17. Mg concentration in DI water as a function of time. Uncertainty is less than the size of symbols.

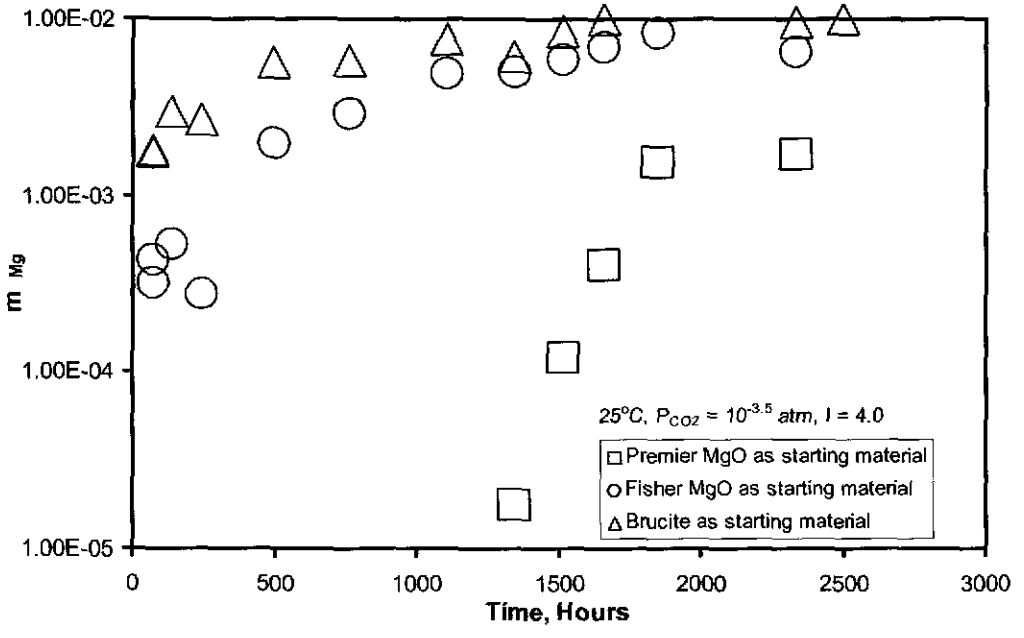

Figure 18. Mg concentration in 4 M NaCl as a function of time. Uncertainty is less than the size of symbols.

Reactions 7, 8, 9, 10, and 11 depict the solubility equilibria for periclase, brucite, hydromagnesite (5:4:2:4), hydromagnesite (4:3:2:3), and nesquehonite, respectively.

In Figure 19, SIs for the above Mg-containing phases are calculated for the results from the run in DI water started with Fisher MgO. It is shown that brucite reaches saturation after about 250 hours. This is in excellent agreement with previous hydration experiments of MgO in which hydration rates of MgO in DI water are found to be very fast (SNL, 2002). After about 500 hours, the solution becomes supersaturated with hydromagnesite (both 5:4:2:4 and 4:3:2:3), implying that hydromagnesite could precipitate because hydromagnesite is supersaturated by a few orders of magnitude. The inference that hydromagnesite is forming from the solution according to the SI of hydromagnesite is further supported by the identification of hydromagnesite in similar experiments described below. It appears from Figure 19 that the precipitation of nesquehonite is not favored. In other words, nesquehonite would not be formed under the experimental condition ($P_{CO_2} = 10^{-3.5}$ atm).

In Figure 20, SIs are shown for a run using brucite as starting material in DI water (Fisher $Mg(OH)_2$-0Cl). In contrast to the SIs described above, hydromagnesite reaches supersaturation very early in the run (after about 100 hours), suggesting that hydromagnesite could form from the solution soon after the start of the run. That hydromagnesite forms is supported by results from an almost identical run ($Mg(OH)_2$-25/AQ-1) in which hydromagnesite was positively identified using XRD (Figure 21). The run $Mg(OH)_2$-25/AQ-1 was terminated after about 1100 hours.

Figures 22 and 23 illustrate SIs for experiments in 4 M NaCl solution starting with Fisher MgO and brucite. In the run using pure MgO, hydromagnesite (5:4:2:4) reaches saturation after about 1100 hours. In contrast, in the run using brucite as starting material, hydromagnesite (both varieties) reaches saturation after about 500 hours. In both runs, nesquehonite is more clearly undersaturated (SI less than or equal to -1) than in the DI water runs. Another difference between the experimental runs in DI water and those in 4 M NaCl is that brucite seems slightly undersaturated in the latter.

An important conclusion from these results and EQ3NR modeling of experiments started with brucite is that the tendency to form nesquehonite is not thermodynamically favored in the DI water runs, and especially in 4 M NaCl runs, at $P_{CO_2} = 10^{-3.5}$ atm. Therefore, we are confident that the reaction path periclase → brucite → nesquehonite → hydromagnesite, inferred from previous experimental results at high P_{CO_2} (1 atm) at SNL in Albuquerque (Papenguth et al., 1997), is not applicable to the WIPP, in which low P_{CO_2} is expected. Instead, the reaction path in the repository and other low P_{CO_2} environments will be periclase → (magnesium chloride hydroxide hydrate) → brucite → hydromagnesite. The reaction path from periclase to brucite and from magnesium chloride hydroxide hydrate to brucite has been well documented in Papenguth et al. (1997) and SNL (2002). The reaction path from brucite to hydromagnesite is clearly demonstrated in the runs using brucite as starting material.

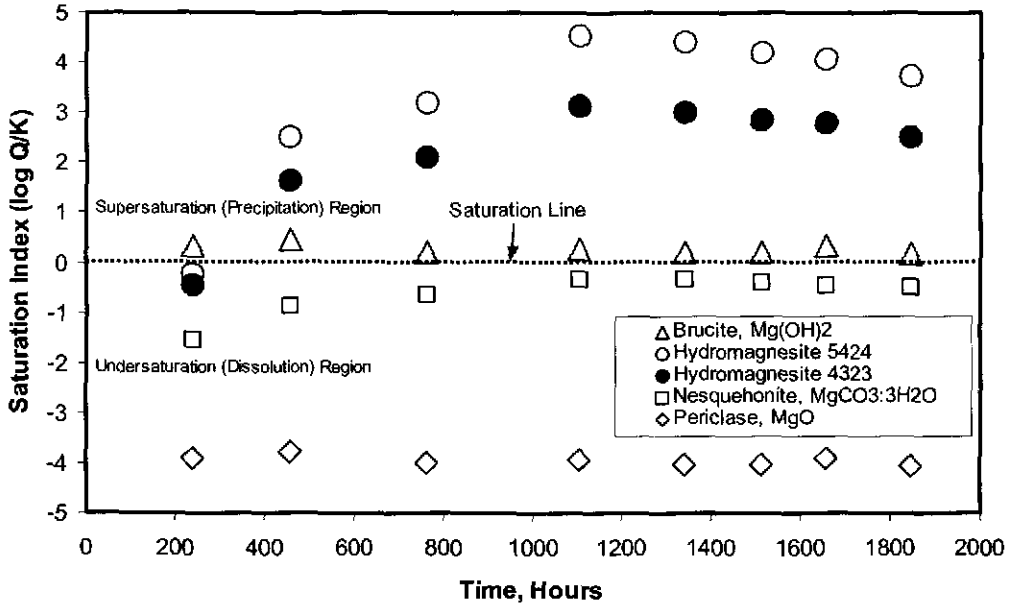

Figure 19. Saturation indexes for Mg-containing phases in the experiment containing Fisher MgO as the starting material in DI water.

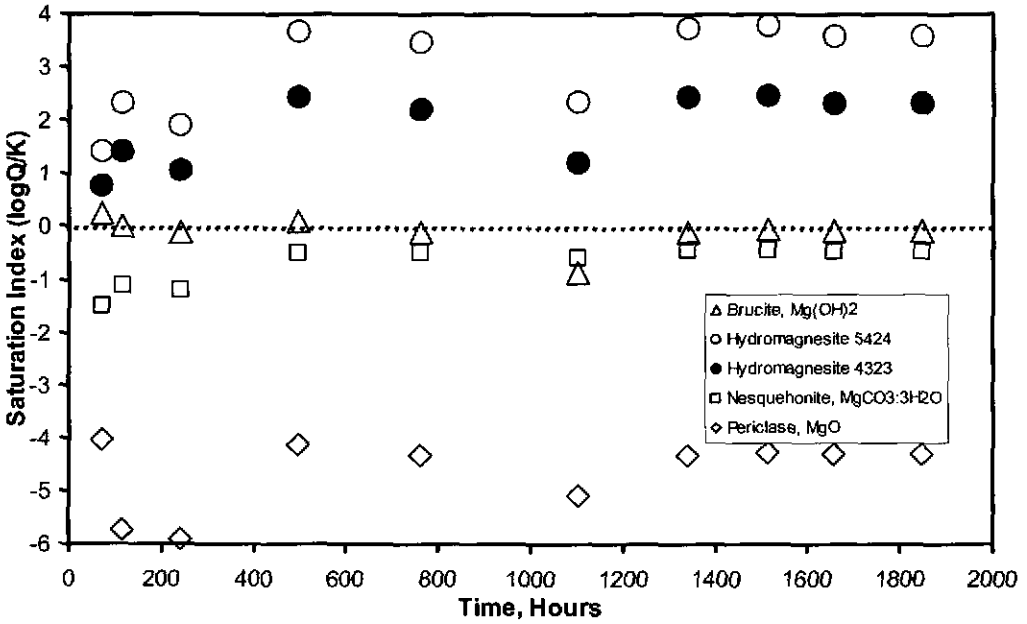

Figure 20. Saturation indexes for Mg-containing phases in the experiment using brucite as the starting material in DI water.

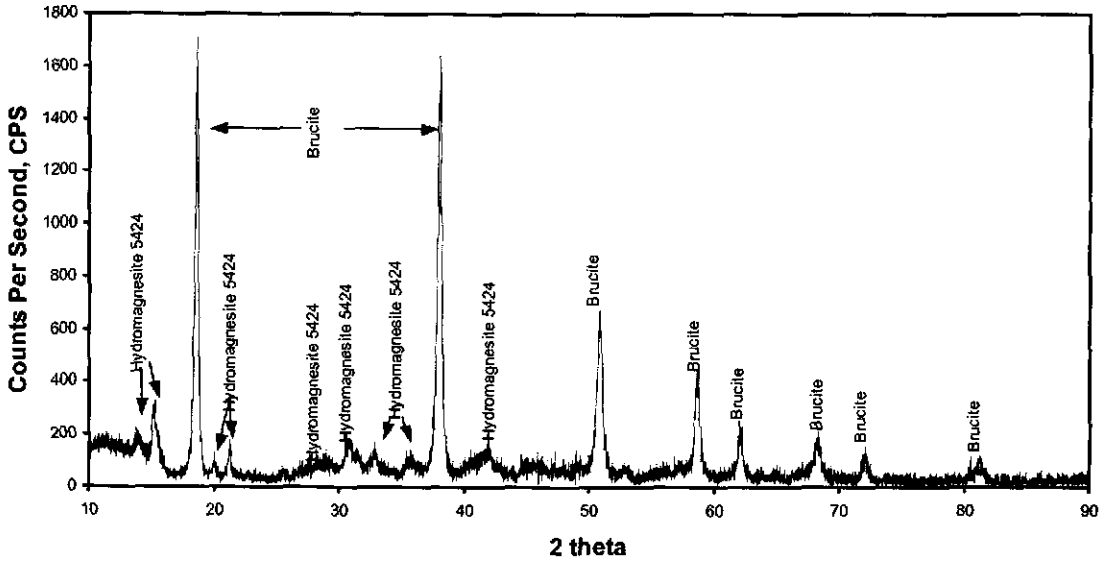

Figure 21. XRD pattern for the reaction product of the experimental run Mg(OH)2-25/AQ-1 using brucite as starting material. The experiment was conducted in DI water at $P_{CO_2} = 10^{-3.5}$ atm and 25°C. The experiment was terminated after about 1100 hours of the initiation of the experiment.

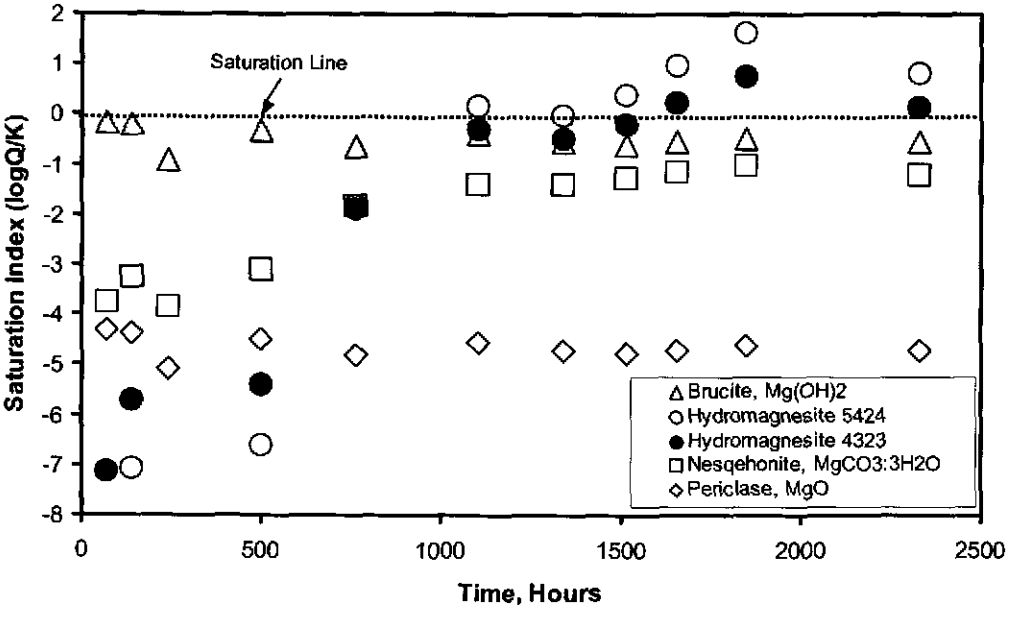

Figure 22. Saturation indexes for Mg-containing phases in the experiment using Fisher MgO as the starting material in 4 M NaCl solution.

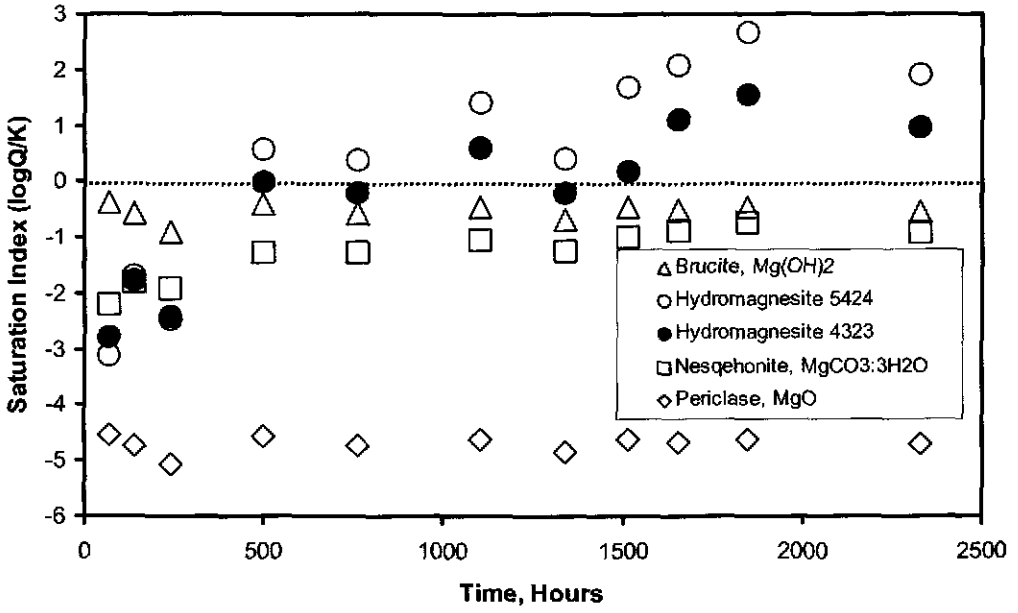

Figure 23. Saturation indexes for Mg-containing phases in the experiment using brucite as the starting material in 4 M NaCl solution.

In fact, Papenguth et al. (1997) were aware that nesquehonite would not be formed in low P_{CO_2} environments and favored the metastable phase hydromagnesite in these environments.

The above reaction path periclase → (magnesium chloride hydroxide hydrate) → brucite → hydromagnesite is well supported by field observations on the carbonation of magnesian lime exposed to atmospheric CO_2 (Bruni et al. 1998; Dheilly et al., 1999). For example, the carbonation products of historical mortars containing magnesian lime in the northern Italy exposed to air have hydromagnesite but no nesquehonite (Bruni et al., 1998).

Solid Phase Chemistry

After filtration and drying, reaction products in inundated experiments are analyzed for C using a carbon coulometer. Then, the quantities of brucite converted to hydromagnesite are calculated. In Figure 24, preliminary data for the conversion of brucite to hydromagnesite are plotted against run time. Based on preliminary data, the carbonation rate in DI water is faster than those in 4 M NaCl and ERDA-6. The carbonation rates in 4 M NaCl and ERDA-6 are similar, which may be due to the ionic strength effect. (The ionic strength of 4 M NaCl is similar to that of ERDA-6.) The C contents in the runs in GWB terminated so far are below the detection limit of the carbon coulometer. In the future, when more data, especially the data in 0.01 M, 0.1 M and

1.0 M NaCl solutions, become available, the effect of the ionic strength on the carbonation rate will be quantitatively addressed.

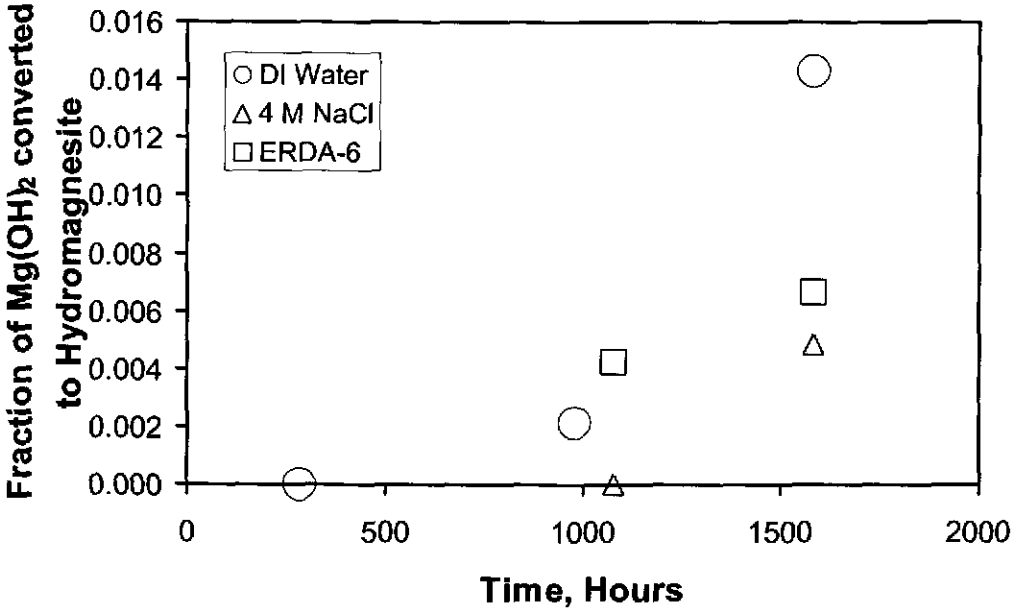

Figure 24. Brucite converted to hydromagnesite as a function of time.

The conversion rate for the experimental data in DI water obtained so far is tentatively determined to be 1.1×10^{-5} hour^{-1}. Using this rate, the time required for the full carbonation of brucite (i.e., 100% conversion) in DI water is on the order of 10^5 hours. Therefore, brucite should carbonate completely in a few decades. When more data become available, this rate constant of carbonation in DI water will be refined, and rate constants of carbonation in other solutions will also be determined. Then, we will be able to quantify the time required for the full carbonation of the engineered barrier.

Summary

In runs using Premier MgO as starting material at $P_{CO_2} = 10^{-3.5}$ atm (atmospheric CO_2), hydromagnesite has been positively identified in the experiment in 4 M NaCl after 264 days. After 327 days of run time, hydromagnesite has been identified in all experiments in DI water, 4 M NaCl, ERDA-6 and GWB. No nesquehonite has been observed in any experiments at $P_{CO_2} = 10^{-3.5}$ atm. However, nesquehonite is observed in the experiments at higher P_{CO_2} (5×10^{-2} atm), about 160 times the partial pressure of CO_2 in the atmosphere. In most experiments, nesquehonite was eventually converted to hydromagnesite, implying that hydromagnesite is more stable than nesquehonite even at $P_{CO_2} = 5 \times 10^{-2}$ atm.

In experiments using brucite (the hydration product of MgO) as starting material at $P_{CO_2} = 10^{-3.5}$ atm and 25°C, hydromagnesite was formed after about 1100 hours of the initiation of the runs. EQ3NR modeling using experimental results indicate that solutions are supersaturated with respect to hydromagnesite soon after the initiation (after about 500 hours). The modeling also indicates that nesquehonite remains undersaturated.

Based upon the above experimental results at $P_{CO_2} = 10^{-3.5}$ atm using Premier MgO and brucite as starting materials and corresponding EQ3NR modeling, it is concluded that the reaction path, periclase → brucite → nesquehonite → hydromagnesite, proposed before based upon the preliminary experimental results at high P_{CO_2} (1 atm) generated at SNL in Albuquerque (Papenguth et al., 1997), is not applicable to low P_{CO_2} environments such as the WIPP (i.e., $P_{CO_2} = 10^{-3.5}$ atm or lower). Instead, the reaction path in the repository and other low-P_{CO_2} environments will be periclase → (magnesium chloride hydroxide hydrate) → brucite → hydromagnesite. This reaction path is well supported by field observations on the carbonation of magnesian lime exposed to atmospheric CO_2.

The conversion rate of brucite to hydromagnesite in DI water was tentatively determined to be in the order of 10^{-5} hour^{-1}. Based on this rate, the time for the full carbonation of brucite in DI water will be in the order of a few decades. When more data become available, this conversion rate will be refined, and conversion rates in other solutions will be obtained. When such conversion rates are available, in conjunction with hydration rates of MgO already determined (SNL, 2001a; 2001b; and 2002), the time required for complete carbonation of MgO in various solutions will be estimated.

References

Botha, A., and C.A. Strydom. 2001. "Preparation of a Magnesium Hydroxy Carbonate from Magnesium Hydroxide," *Hydrometallurgy*. Vol. 62, 175-183.

Bruni, S., F. Cariati, P. Fermo, A. Pozzi, and L. Toniolo. 1998. "Characterization of Ancient Magnesian Mortars Coming from Northern Italy," *Thermochimica Acta*. Vol. 321, 161-165.

Butler, J.N. 1982. *Carbon Dioxide Equilibria and Their Applications*. Reading, MA: Addison-Wesley Publishing Co.

Dheilly, R.M., A. Bouguerra, B. Beaudoin, J. Tudo, and M. Queneudec. 1999. "Hydromagnesite Development in Magnesian Lime Mortars, *Materials Science and Engineering A*. Vol. A268, 127-131.

Fernandez, A.I., J.M. Chimenos, M. Segarra, M.A. Fernandez, and F. Espiell. 1999. "Kinetic Study of Carbonation of MgO Slurries," *Hydrometallurgy*. Vol. 53, 155-167.

Königsberger, E., L.C. Königsberger, and H. Gamsjäger. 1999. "Low-Temperature Thermodynamic Model for the System Na_2CO_3-$MgCO_3$-$CaCO_3$-H_2O," *Geochimica Cosmochimica Acta*. Vol. 63, 3105-3119.

Papenguth, H.W, J.L. Krumhansl, R.V. Bynum, E.J. Nowak, Y. Wang, J.W. Kelly, and N.J. Linarez-Royce. 1997. "Chemical Conditions Model: Results of the MgO Backfill Efficacy Investigation." Draft report to the WIPP Conceptual Models Peer-Review Panel, April 23, 1997. Albuquerque, NM: Sandia National Laboratories.

Papenguth, H.W, J.L. Krumhansl, R.V. Bynum, Y. Wang, J.W. Kelly, H.L. Anderson, and E.J. Nowak. 1999. "Status of Research on Magnesium Oxide Backfill," *International Workshop on the Uses of Backfill in Nuclear Waste Repositories, Carlsbad, New Mexico, USA, May, 1998*. Eds. D.G. Bennett, H.W. Papenguth, M.S.Y. Chu, D.A. Galson, S.L. Duerden, and M.L. Matthews. R&D Technical Report P178. Bristol, United Kingdom: Environment Agency.. 3-43 to 3-63.

Rai, D., A.R. Felmy, S.I. Juracich, and F.F. Rao. 1995. *Estimating the Hydrogen Ion Concentration in Concentrated NaCl and Na_2SO_4 Electrolytes*. SAND94-1949. Albuquerque, NM: Sandia National Laboratories.

Sandia National Laboratories. 2001a. "Sandia National Laboratories Technical Baseline Reports, January 31, 2001." Carlsbad, NM: Sandia National Laboratories.

Sandia National Laboratories. 2001b. "Sandia National Laboratories Technical Baseline Reports, July 31, 2001." Carlsbad, NM: Sandia National Laboratories.

Sandia National Laboratories. 2002. "Sandia National Laboratories Technical Baseline Reports, January 31, 2002." Carlsbad, NM: Sandia National Laboratories.

US DOE. 1996b. *Title 40 CFR Part 191 Compliance Certification Application for the Waste Isolation Pilot Plant, Vol. 1-21*. Carlsbad, NM: US Department of Energy Carlsbad Area Office.

US Environmental Protection Agency. 1993. "40 CFR Part 191 Environmental Radiation Protection Standards for the Management and Disposal of Spent Nuclear Fuel, High-Level and Transuranic Radioactive Wastes; Final Rule," *Federal Register*. Vol. 58, 66398-66416. Washington, DC: EPA Office of Radiation and Indoor Air.

US Environmental Protection Agency. 1998. "40 CFR 194, Criteria for the Certification and Recertification of the Waste Isolation Pilot Plant's Compliance With the Disposal Regulations. Certification Decision: Final Rule," *Federal Register*. Vol. 63, 27354-27406. Washington, DC: EPA Office of Radiation and Indoor Air.

Wang, Y., C. Bryan, and N. Wall. 2001. "Experimental Study of WIPP MgO Backfill at Sandia National Laboratories Carlsbad Facility." TP 00-07, Rev. 1. Carlsbad, NM: Sandia National Laboratories.

Wolery, T.J. 1992. EQ3NR: A Computer Program for Geochemical Aqueous Speciation-Solubility Calculations: Theoretical Manual, User's Guide, and Related Documentation (Version 7.0). UCRL-MA-110662 PT III. Livermore, CA: Lawrence Livermore National Laboratory.

4.2 Experimental Work to Develop a Model for Cement-Brine Interactions[1]

Charles R. Bryan
Sandia National Laboratories, MS 1395
4100 National Parks Highway
Carlsbad, NM USA 88220

Abstract

Sandia National Laboratories/Carlsbad (SNL) is currently performing research to develop a model for cement-brine interactions relevant to performance assessment (PA) calculations for recertification of the Waste Isolation Pilot Plant (WIPP). Several laboratory experiments are currently in progress. In the first, the kinetics of cement-brine reactions are being examined by long-term equilibration of powdered cement-brine systems, with periodic sampling to monitor changes in brine chemistry. In the second, alteration reactions and reaction products are being investigated by long-term equilibration of cement-brine systems with varying solid:solution ratios. Both the brine and the solid are being sampled. Solids are being analyzed by X-ray diffraction (XRD), scanning electron microscopy (SEM), and chemical analysis to determine the phase composition. In the third experiment, cement wafers are being aged in WIPP-relevant brines, and are sampled periodically to monitor the effects of non-equilibrium processes, which through limiting or enhancing transport, may affect the cement degradation rate. These include precipitation of low-porosity mineral coatings or pore-filling phases, selective dissolution of certain cement phases, and fracturing due to the formation of expansive alteration phases. These experiments, together with core-column experiments and solubility experiments to determine Pitzer parameters for Al (aluminum) and Si (silicon), will be used to develop and validate a thermodynamic model for cement-brine interactions, and a degradation rate model for cement borehole plugs.

Introduction and Objectives

An understanding of cement-brine interactions is important in evaluating the future performance of the WIPP repository. In 1996, the National Academy of Sciences Committee on the WIPP stated that the only credible scenarios resulting in release of radionuclides from the repository are those involving human intrusion, such as drilling for potash or oil (NRC, 1996). Calculated releases during and after intrusion are dependent upon the predicted integrity of cement borehole plugs. These directly control brine flow into and out of the repository, determining the Culebra source term and indirectly affecting other important parameters such as gas generation rates and spallings releases. In addition, cementitious waste forms are a significant fraction of the waste inventory, and cement-brine reactions will affect repository chemistry. Dissolution of cement components could result in high-pH microenvironments, while calcium released during cement degradation will serve as an additional sink (with MgO) for carbon dioxide released by microbial degradation of organic components in the waste.

[1] This work is covered by WBS #1.3.5.4.3.2

A primary goal of the cementitious materials work at SNL/Carlsbad is to develop a model for the degradation and failure of cement borehole plugs. Although this is inherently a kinetic model, extrapolating data from laboratory-scale experiments to WIPP relevant spatial and temporal scales will require development of a thermodynamic model for cement-brine interactions, which can also be used to evaluate the potential effects of cement on repository chemistry.

The degradation of borehole plugs is being examined both by laboratory investigations and by opportunistic sampling of downhole cement and casing corrosion products during plugging and abandonment (P&A), recompletion, and general maintenance of water monitoring wells in and around the WIPP site. The test plans for these activities are, respectively, Bryan and Wang (2000) and Bryan and Martell (2000).

Opportunities for meaningful borehole sampling are few, and have not occurred since SNL (2002). However, considerable laboratory work has been carried out in the last six months, and the results to date are summarized here. In the first experiment, the kinetics of cement-brine reactions are being examined by long-term equilibration of powdered cement-brine systems, with periodic sampling monitor changes in brine chemistry. In the second, alteration reactions and reaction products are being investigated by long-term equilibration of cement-brine systems with varying solid:solution ratios. Both the brine and the solid are being sampled. Brine chemistry is being monitored, while solids are being analyzed by XRD, SEM, and chemical analysis to determine the phase composition. In addition to determining the equilibrium mineral assemblages present in cement-WIPP brine (Castile and Salado) systems, the compositional data for the brines and solids in these experiments will also be used to validate the thermodynamic model. In the third experiment, cement wafers are being aged in simulated Castile and Salado brines, and are sampled periodically to evaluate rates of cement degradation (by monitoring development of cement alteration products and/or dissolution of cement phases) and of diffusion of brine components into the cement, and to evaluate the effects of non-equilibrium processes, which through limiting or enhancing transport, may affect the cement degradation rate. These include precipitation of low-porosity mineral coatings or pore-filling phases, selective dissolution of certain cement phases, and fracturing due to the formation of expansive alteration phases.

The data generated from these experiments and other planned experiments, including cement core flow-through experiments for evaluating the kinetics of cement degradation in a system in which the cement is continuously being exposed to fresh brine, will be used to develop and calibrate a thermodynamic model for cement-brine interactions, and a degradation rate model for borehole plugs.

General Experimental Procedures

All data generated in these experiments is recorded in laboratory notebooks and binders. Each notebook will be submitted upon completion to SNL's Nuclear Waste Management Program Records Center, in accordance with Allan (2001).

CEMENT PREPARATION

Three types of cement were prepared for use in these experiments. These are: (1) Type C oil field SO_4^{2-} (sulfate)-resistant) cement, mixed with halite- (NaCl)-saturated H_2O (water); (2) Type C oil field cement, mixed with deionized (DI) water only; (3) ordinary Portland cement (OPC). The first two types are relevant to borehole plug degradation studies, and the third, to repository chemistry. The rationale for using these cements and mixing and preparation procedures are given in SNL (2002). The cements were mixed under atmospheric P_{CO_2} conditions, since cement for borehole plugs or in cementitious waste forms would be mixed under those conditions. After curing, fractions of each were prepared for different experiments. One fraction was crushed to <150 μm, for powdered cement-brine equilibration experiments. A second fraction was cut into 25-mm-square x 3-mm-wide wafers, for brine/wafer experiments. For the oil-field cements, 25-mm-diameter cores were extracted from a third fraction for column transport studies.

ATMOSPHERIC CONDITIONS

The experiments currently in progress are being carried out in sealed polycarbonate or polypropylene tubes or bottles, stored inside Plexiglas glove boxes. To minimize CO_2 (carbon dioxide) inflow, which might affect system pH, N_2 (nitrogen) is being pumped into the glove boxes at a rate of 50 ml/min, and the atmosphere inside is being sparged through a 0.1 M NaOH-(sodium hydroxide)-0.05 M $BaCl_2$ (barium chloride) solution at a rate of 2000 ml/min to remove CO_2.

Cement-Brine Equilibration-Rate Experiment

This experiment has several goals, but primary among them is to determine, by monitoring changes in electrolyte chemistry, the time scale necessary for long-term equilibration experiments to be run in order to see significant formation of reaction products. Different cement:brine ratios are being used (1g/110ml and 5g/110ml). The cement:brine ratio may affect the reaction products formed and reaction rates, by influencing the pH and the brine chemistry as Ca (calcium) and OH (hydroxide) are released by dissolution of cement phases. The initial experiment was sampled several times over 3.5 months; a second, longer term experiment, is being initiated.

In general, the type of cement used in the rate experiment has very little effect on brine chemistry, while the cement:brine ratio has a much greater effect. The variation in measured pH with equilibration time is shown in Figure 1. In Generic Weep Brine (GWB), a Salado-

Formation brine, the systems with 5 g of cement had initial pH values of ~8.5, and drifted downwards to a final pH, after 3.5 months, to about 8.0. Systems with 1 g of cement initially had a pH of about 8.0, and this did not change. Systems containing ERDA-6, a Castile-Fm. brine, had higher pH values; the 5g systems had initial pH values of 11.8 to 12, and these did not change, while the 1 g systems initially had lower pH values, of about 10, which rose with time to approximately 11.5.

The pH buffering capacity of the two systems, and the final pH, is largely a function of the Mg (magnesium) content of the two brines, and of the borate content. Both act to buffer pH to moderate values, by formation of the aqueous species $Mg(OH)^+$ and precipitation of brucite ($Mg(OH)_2$) in the case of Mg, and by deprotonation in the case of borate. Both processes are much more important in the simulated GWB, as it contains over 50 times as much Mg, and 2.5 times as much borate as ERDA-6. The relative importance of the two processes has not been evaluated.

The compositional changes in GWB are shown in Figures 2a and 2b, for the 5 g cement and 1 g cement systems, respectively. In the 5 g systems, there are sharp drops in Mg and SO_4 concentrations with time, while the Ca concentration rises. In the 1 g systems, the Mg and SO_4 concentrations drop slightly with time, while the Ca remains constant, at about 700 µg/ml. It seems probable that, as $Ca(OH)_2$ (calcium hydroxide) is leached from the cement, magnesium hydroxide and gypsum are precipitating, and the Ca concentration is being determined by the solubility of gypsum ($CaSO_4$).

In ERDA-6 (Figure 3), both 5 g and 1 g systems behave very similarly. Mg drops from

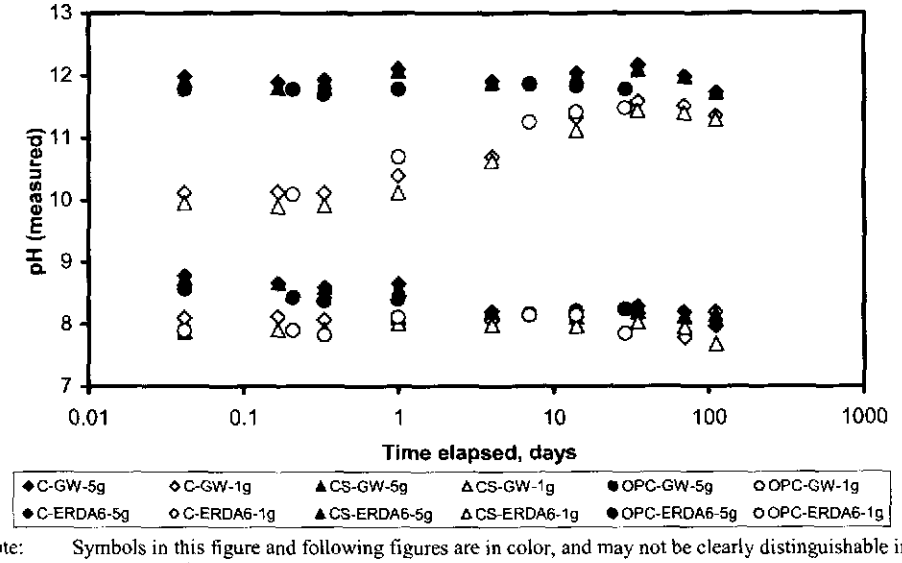

Note: Symbols in this figure and following figures are in color, and may not be clearly distinguishable in a black and white reproduction.

Figure 1. The change in the measured pH values in cement/brine systems with equilibration time. C–Type C cement; CS–Type C cement, salt saturated; OPC–ordinary Portland cement.

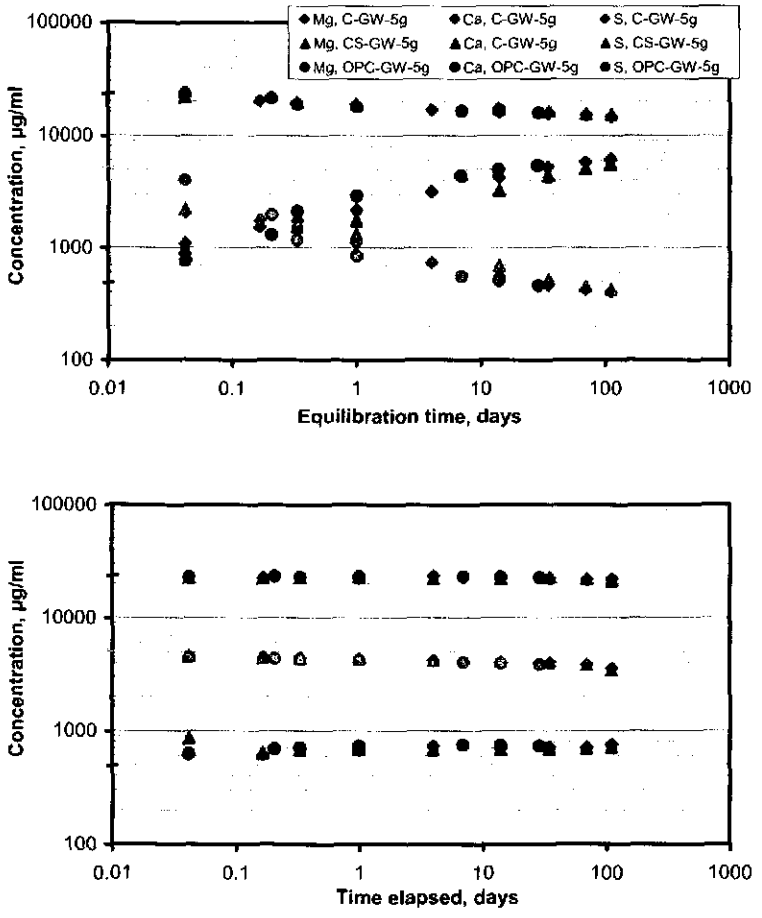

Figure 2. Variation in GW brine chemistry with equilibration time, in systems with a cement/brine ratio of a) 5g/110ml, and b) 1g/100ml.

500 µg/ml to below detection limits very quickly, while Ca rises very rapidly from 500 µg/ml to ~ 875 µg/ml and does not change over time. Similarly, SO_4 drops from 5250 µg/ml to ~ 4400 µg/ml, and then does not change further. In these systems, there is too little magnesium to act as a sink for the hydroxide, so the pH rises, and portlandite ($Ca(OH)_2$) is the solubility-limiting phase for Ca.

Long-Term Cement-Brine Equilibration Experiment

In this experiment, powdered cement was equilibrated with brine at varying cement/brine ratios, and both the solid and liquid were sampled for analysis. All three cement types were used, and both GWB and ERDA-6. Cement/brine ratios covered the range from 0.1g/30ml to 5g/30ml. Samples were collected and analyzed after 3.5 months. Once again, cement type had little or no effect on the results. Measured pH values for the Type C cement samples are shown

in Figure 4; in ERDA-6, the pH rises rapidly with the mass of cement added, and reaches a plateau at a value of ~12. In GWB, the pH rises with the mass of cement added, but at a much slower rate that in the ERDA-6. This is due to the high Mg content of the brine — precipitation of brucite is controlling the pH. However, as more cement is added to the system and the Mg content of the brine drops, a progressively higher pH is possible. In the absence of a higher P_{CO_2}, the Mg in solution and the presence of a brucite solid phase are insufficient to buffer the pH.

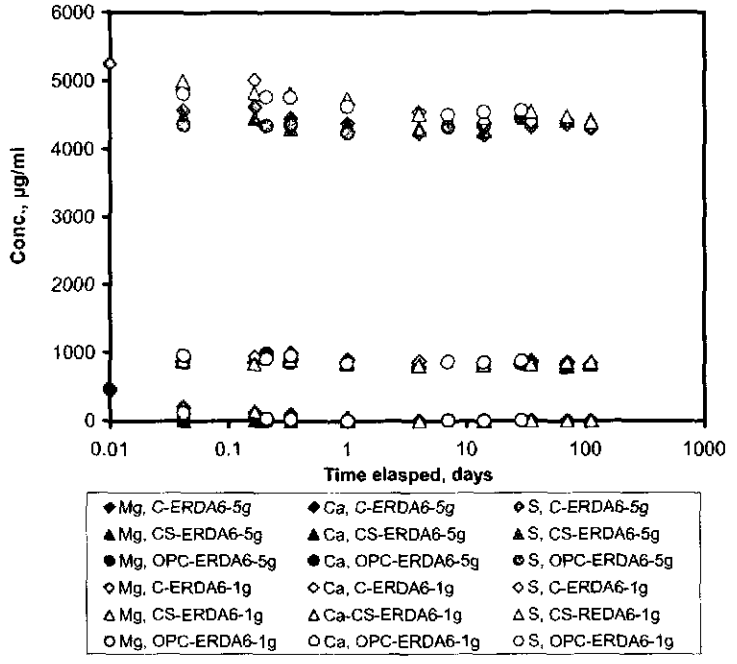

Figure 3. Variation in ERDA-6 brine chemistry with equilibration time, in systems with a cement/brine ratios of 5g/110ml and 1g/100ml.

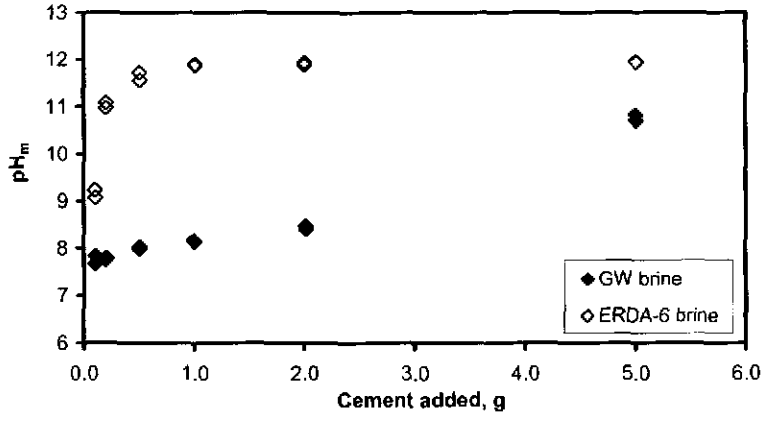

Figure 4. Variation in measured pH value with the amount of cement initially added. Each system contains 30 ml brine.

The variation in the major element composition of GWB with solid:electrolyte ratio, after an equilibration time of 3.5 months, is shown in Figure 5. The dominant effect of the cement is to act as a source of Ca and OH. With increasing cement content, the Mg content of the brine drops as brucite is precipitated, and the SO_4 concentration drops as gypsum is precipitated.

The addition of small amounts of cement has a large effect on the chemistry of ERDA-6, causing large changes in pH, and precipitating out the Mg as brucite. In addition, there are significant drops in SO_4 content and rises in Ca content. However, adding more cement actually results in a reversal of these trends, presumably because the pH rises and portlandite becomes the solubility-limiting phase for Ca.

Analysis of the solids from each system has not been completed. XRD analysis indicates that gypsum is a dominant phase in all samples. Results for one set of samples, those run using Type C cement in GWB, are shown in Figure 6a. All patterns are identical; gypsum is the only identifiable phase. In some of the cement-rich ERDA-6 systems, portlandite was also identified.

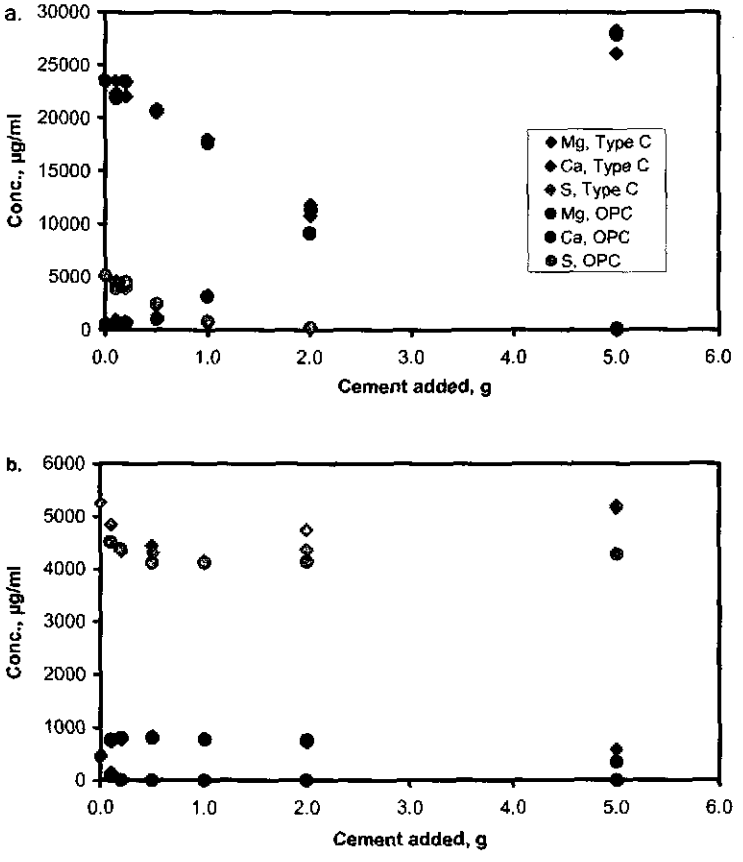

Figure 5. Variation in brine chemistry, after 3 ½ months equilibration time, with cement/brine ratio. Each system contained 30 ml brine. a) GW brine; b) ERDA-6 brine.

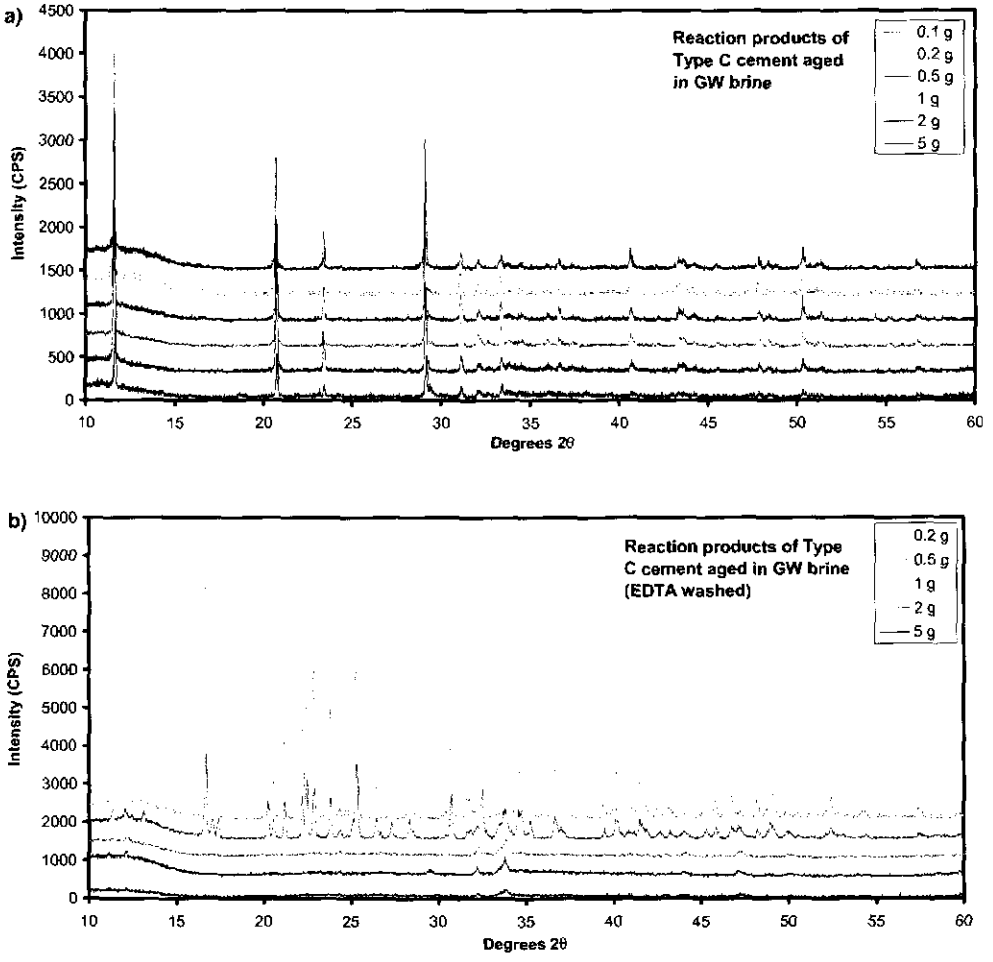

Figure 6. XRD patterns for the solid phases recovered from the cement/ brine equilibration experiment, before (a) and after (b) treatment with 0.1 M EDTA.

In order to examine the silica/alumina phases present, an aliquot of each solid (0.1 to 2.0 g) was mixed with 50 ml 0.1 M Na_2EDTA, and agitated for one hour. This dissolved the gypsum and the portlandite, removing from 25 to >90% of the total material (the less cement in the system, the more of the total solid that was removed by EDTA washing). The remaining material was re-analyzed by XRD. Results are shown in Figure 6b. The gypsum and portlandite have been removed, and the remaining materials show a strong variation in crystallinity with the cement/brine ratio. Samples from the cement-rich systems were largely amorphous or poorly crystalline, with only a few broad diffraction peaks visible, corresponding to atomic d-spacings of 2.65 to 2.74 Å (32° to 34° 2θ). However, in the systems with little cement, several sharp diffraction peaks, representing as-yet unidentified crystalline phases, are present. The XRD spectra do not vary with cement type used, but do vary with the brine type. The solid phases sampled from the ERDA-6 systems are largely amorphous at all cement/brine ratios. The few broad peaks that are present do not correspond to any found in the GWB samples.

Although none of the phases has been identified yet, preliminary analysis by SEM indicates that several different Mg, Ca, and Mg-Ca oxides and hydroxides, silicates, and aluminosilicates are present in the samples. Identification of these phases is currently in progress. It must be noted here that the EDTA treatment may have digested or reacted with some silicate minerals, as well as gypsum and portlandite. Thus, it is not clear that all phases initially present in the samples are being observed in the EDTA-washed aliquot.

Cement Wafer Experiments

In order to examine non-equilibrium processes, especially transport-limiting processes, cement wafers have been immersed in GWB and EDRA-6 and allowed to age for several months. All three types of cement — Type C, salt-saturated Type C, and OPC — were used. The wafers are 3-mm-thick by 25-mm-square, and small sample clips hold them upright (on edge) in the brines. The samples are not being agitated, as surface mineral precipitates may play a significant role in inhibiting cement-brine interactions, and agitation could prevent such layers from forming. Samples of both brine and wafers are being collected on a monthly schedule. The brine samples are analyzed for chemical composition, and the wafers are impregnated with epoxy and polished for SEM analysis.

Initial results suggest that cement type has little or no effect on alteration rate or alteration pathway. This is unexpected, as OPC is not sulfate resistant, and was anticipated to be less stable in the SO_4-rich WIPP brines due to formation of ettringite (Havlica and Sahu, 1992; Xie and Beaudoin, 1992; Poole et al., 1994). However, no significant differences have been observed to date (after five months) between the OPC and Type C cement systems, either in

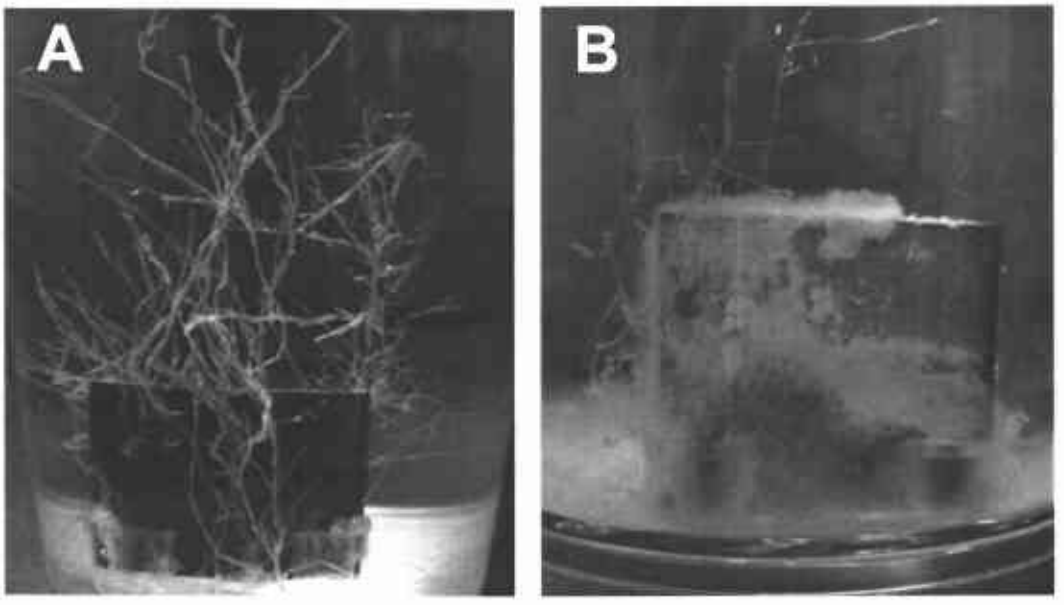

Figure 7. Photographs of Type C cement wafers aged for 5 months in a) GW brine, and b) ERDA-6 brine. Wafers are 25 mm square.

terms of chemistry, mineral phases present, or observed alteration pathways.

The only significant factor affecting the cement-brine systems is brine type. Visually, cements in the two brines showed variations in the development of mineral coatings and alteration within a few days of immersion. After five months, these differences are very apparent (see Figure 7). Cement wafers immersed in GWB have heavy growths of gypsum dendrites on otherwise relatively clean surfaces, while those in ERDA-6 are heavily coated with a gelatinous precipitate of brucite and gypsum, and display little growth of gypsum dendrites. This is counterintuitive, as the SO_4 concentrations of the two brines are very similar, and as it is the GWB that contains much higher concentrations of Mg.

Because the samples were not agitated, significant stratification occurred in the brine in the containers. This resulted in the gypsum dendrites "growing" upwards, into brine that was not depleted in SO_4, and in general was responsible for the development of thicker mineral coatings on the lower parts of each wafer relative to the top. This is most apparent in the ERDA-6 samples, but occurs on the GWB samples as well. This was at least in part due to precipitation of brucite as a gelatinous mass on the surface of the wafer, and subsequent gravity-driven slumping to the bottom of the container.

SEM examination of wafers removed from the brines and impregnated with epoxy reveals that there are both similarities and differences between the GWB and ERDA-6 cement-brine systems. One such wafer, removed from ERDA-6 after two months, is pictured in Figures 8 and 9. Figure 8 is a backscattered electron image of the entire wafer, showing several zones within it. Figure 9 is a close-up of two areas on the wafer, one near the top, where there is only minor precipitated mineral coating, and one near the bottom, where the coating is heavy. X-ray element maps, showing the distribution of Mg, Si, S, and Ca in each image, are also shown.

The schematic drawing in Figure 8 illustrates several features that are common to all of the wafers examined. Going from the edge to the center, these consist of:

1. A coating of precipitated minerals. Only gypsum and brucite have been observed to date. This coating is much thicker on samples immersed in ERDA-6, and is invariably thicker towards the bottom of the wafer. The brucite in the coating is not visible in Figure 8, but is readily discerned in Figure 9 by examination of the Mg element maps.

2. A zone of Mg alteration, in which Mg has infiltrated the cement, and reacted with the Ca-silicate cement phase (CSH), replacing the Ca and forming Mg silicate hydrate (MSH). This zone is commonly very thin, and is invariably most pronounced towards the top of the wafer, where the mineral coatings are thin or absent. This zone is readily observed in Figure 9, in the Mg, Si, and Ca element maps.

3. A zone of Ca depletion, which has been interpreted as a zone from which portlandite has been leached. This zone can readily distinguished in Figure 8, but is difficult to see in the Ca maps in Figure 9. This zone is thinner where minerals thickly coat the surface of the wafer. Though this zone is initially more porous than the original cement, it has commonly been partially or completely infiltrated with gypsum. This can be seen in the

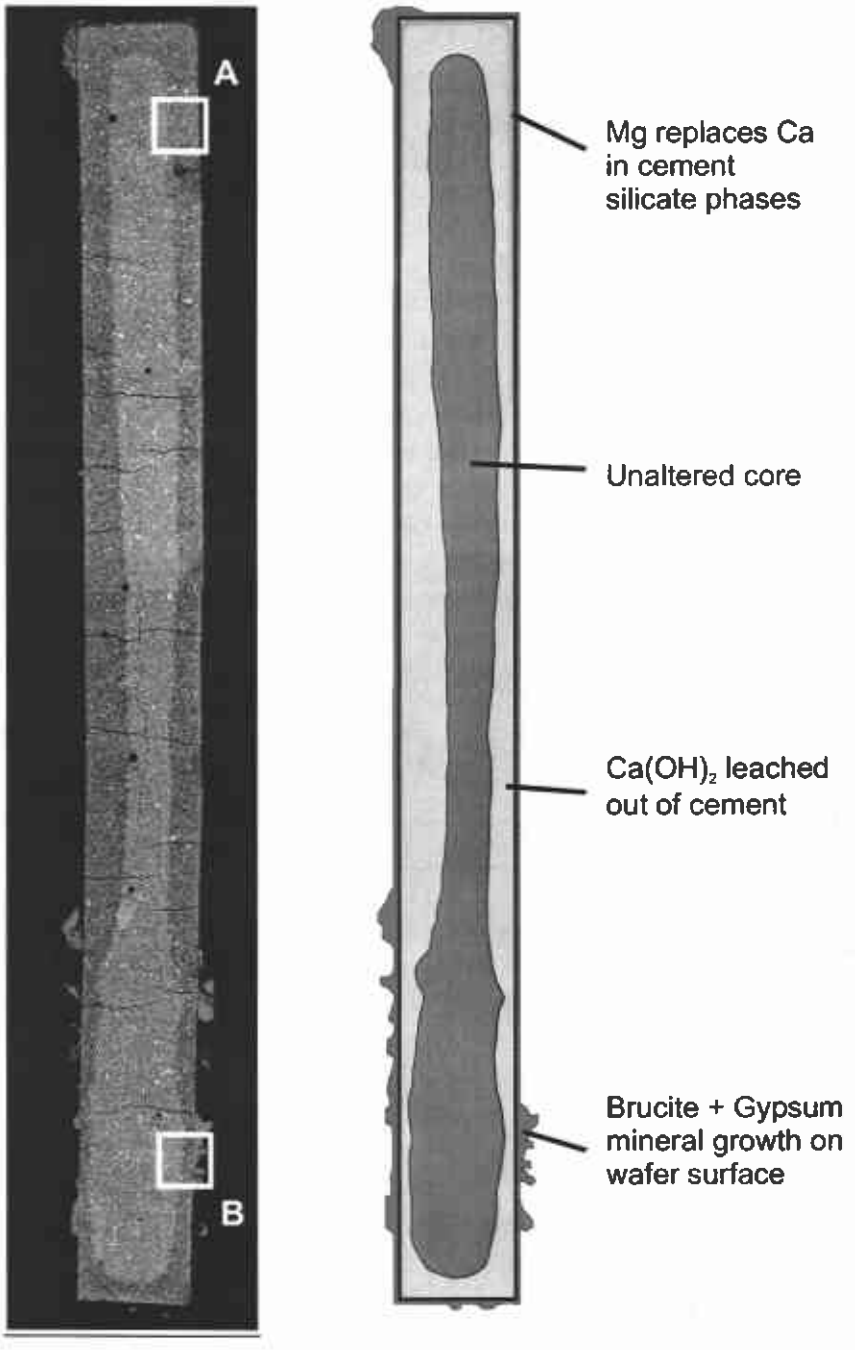

Figure 8. SEM backscattered electron image of the polished cross section of a Type C oilfield cement wafer after immersion in ERDA-6 brine for 2 months (fractures in the wafer are an artifact of epoxy impregnation). The schematic drawing on the right identifies important features, and squares A and B indicate the locations of the close-up images shown in Figure 9. Wafer cross-section is 25 mm long.

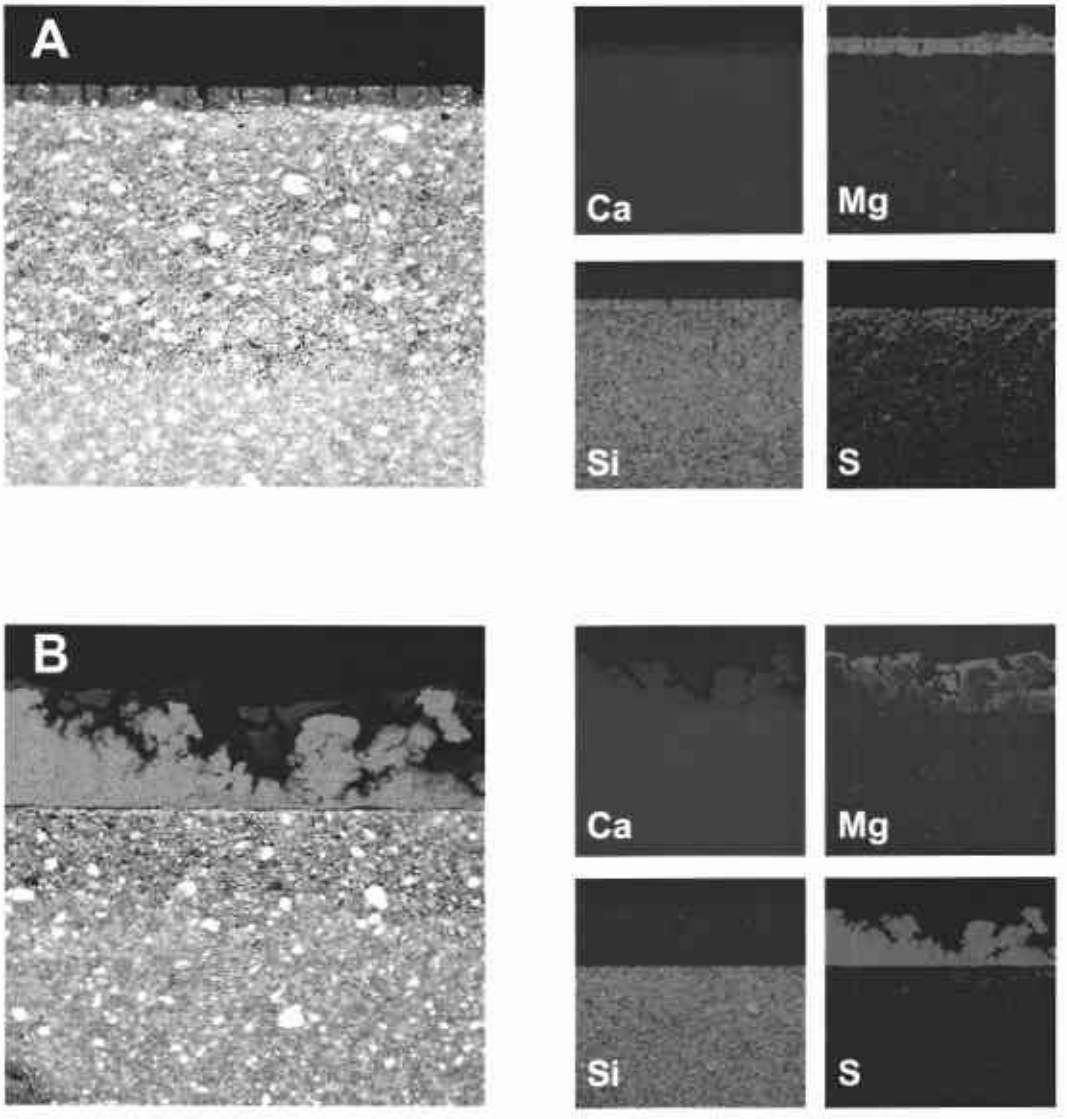

Figure 9. Magnified images and X-ray element maps of areas A and B in Figure 8. Field of view is 1 mm.

S maps for image A, in Figure 9. The depth to which SO_4 has diffused into the leach zone is also affected by the mineral coatings — it is virtually nonexistent in area B, where a thick mineral coating is present.

4. A core of apparently unaltered cement, readily visible in Figure 8. This core is wider towards the bottom of the wafer, and at any location where heavy mineral coatings are present. The core shrinks with immersion time, and is absent in some samples.

All three cements exhibited identical behavior in the two brines; this is illustrated for salt-free Type C cement in Figure 10. In GWB, portlandite is readily leached from the wafer, and after three months, no core remains. Although gypsum dendrites grow abundantly on the surface

of the wafer, little of the surface is actually covered with precipitated minerals. In ERDA-6, the core shrinks, but is still present after five months. The wafers develop a heavy brucite and gypsum coating with time, and after ~ four months sparse gypsum dendrites start to form. In neither brine is there a clear correlation between the thickness of the Mg alteration layer and time, nor is there a correlation between the depth to which SO_4 has precipitated and time. However, in both cases, the presence of a mineral coating appears to significantly inhibit or slow the formation of these features.

Several potentially important processes are occurring in this experiment. The development of the Ca-leached zone results in an increase in the porosity and permeability of the cement. However, this is offset by the diffusion of SO_4 into the cement and precipitation of gypsum in the pore space. Ultimate failure of the cement may perhaps be best defined by the replacement of CSH with MSH, as the cement shrinks and cracks, and crumbles as this well-known (Bonen, 1992; Bonen and Cohen, 1992; Poole et al., 1994) degradation reaction occurs (see Figures 8 and 9A). In addition, the reaction does not seem to be inhibited by the presence of gypsum in the cement pore space; all Ca, including that in the gypsum, is removed from the alteration zone (see Figure 9A). However this alteration zone develops very slowly, and *does* appear to be inhibited by the presence of a coating of precipitated minerals on the cement surface. In fact, mineral precipitates seem to inhibit all reactions between the cement and brine, at least over the time scale of these experiments. It is not clear if the same is true over longer time intervals.

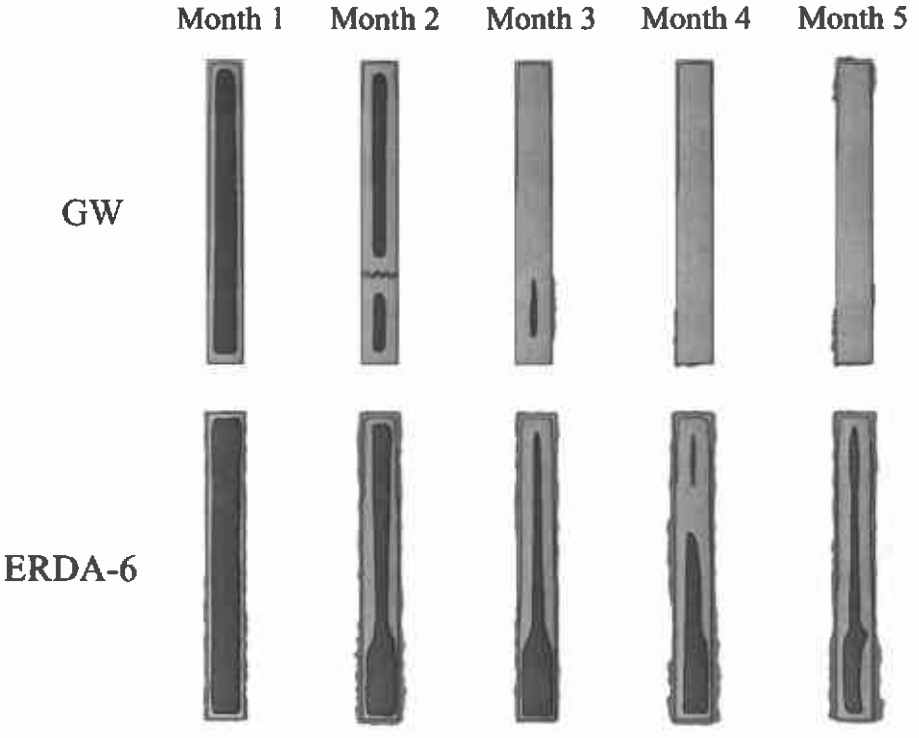

Figure 10. Sketch showing the development of mineral precipitation and alteration zones in Type C oilfield cement wafers immersed in GW and ERDA-6 brines for 1 to 5 months. Zones are delineated as in Figure 8.

As stated earlier, the lack of any significant magnesium hydroxide precipitate in the GWB systems was unexpected. It is evident from the rapid development of the Ca-leach zone, the disappearance of the unreacted cement core, and the relatively low measured pH values (around 9) in these systems that some phase is acting as a sink for OH. Given that there is not enough OH-bearing alteration mineral present to account for the observed effects, that phase is probably an aqueous one. Wang (pers. comm.) states that $Mg(OH)^+$ is an important aqueous species at these pH values; it seems reasonable to assume that this is the OH^- sink in the GWB systems. Thermodynamic modeling will be carried out to test this hypothesis.

Future Work

Several experiments will be continued in the next 6 months, including the wafer experiment, and an extended cement/brine equilibration experiment. The solid phases present in the completed experiment will be identified, and the brine samples collected from all experiments still must be analyzed for Si and Al. Finally, cement core column experiments will be run with Type C oilfield cement and simulated ERDA-6/GW brines. However, it is probable that flow through such an experiment will cease very rapidly due to formation of mineral surface precipitates, and that any long-term predictions of cement borehole plug longevity will be ultimately be based upon the results of the wafer and powdered cement studies, and upon reaction rates based on estimated brine delivery rates and mass balance considerations.

References

Allan, F.C. 2001. "Records." NP 17-1, Rev. 2. Carlsbad, NM: Sandia National Laboratories.

Bonen, D. 1992. "Composition and Appearance of Magnesium Silicate Hydrate and Its Relation to Deterioration of Cement-Based Materials," *Journal of the American Ceramic Society.* Vol. 75, 2904-2906.

Bonen, D., and M.D. Cohen. 1992. "Magnesium Sulfate Attack on Portland Cement Paste II. Chemical and Mineralogical Analysis," *Cement and Concrete Research.* Vol. 22, 707-718.

Bryan, C.R., and M.A. Martell. 2000. "Collection and Analysis of Downhole Cement and Steel Samples During Borehole Plugging and Abandonment." TP 00-02. Carlsbad, NM: Sandia National Laboratories.

Bryan, C.R., and Y. Wang. 2000. "Experimental Work to Develop a Model for Cement Borehole Plug Degradation at the WIPP Site." TP 00-06. Carlsbad, NM: Sandia National Laboratories.

Havlica, J., and S. Sahu. 1992. "Mechanism of Ettringite and Monosulfate Formation," *Cement and Concrete Research.* Vol. 22, no. 4, 671-677.

National Research Council. 1996. *The Waste Isolation Pilot Plant: A Potential Solution for the Disposal of Transuranic Waste.* Washington, DC: National Academy Press.

Poole, T.S., L.D. Wakeley, and C.L. Young. 1994. *Individual and Combined Effects of Chloride, Sulfate, and Magnesium Ions on Hydrated Portland Cement Pastes*, SAND93-7040. Albuquerque, NM: Sandia National Laboratories.

Sandia National Laboratories. 2002 "Sandia National Laboratories Technical Baseline Report, January 31, 2002." Carlsbad, NM: Sandia National Laboratories.

Xie, P., and J.J. Beaudoin. 1992. "Mechanism of Sulphate Expansion. I. Thermodynamic Principle of Crystallization Pressure," *Cement and Concrete Research.* Vol. 22, no. 4, 631-640.

5 ROCK MECHANICS

5.1 Fracture Analyses[1]

D. M. Chapin, Jr. and F. D. Hansen
Sandia National Laboratories, MS 1395
4100 National Parks Highway
Carlsbad, NM USA 88220

Abstract

The disturbed rock zone (DRZ) surrounding underground openings in salt provides a path of increased permeability, which could bypass seals or closure systems installed in geologic radioactive waste repositories such as the Waste Isolation Pilot Plant (WIPP). Compliance application performance assessment calculations for salt repositories include characteristics and parameters of the DRZ that model brine influx into the disposal room and influence important evolutionary processes. Quantification of spatial and temporal characteristics of the DRZ plays a vital role in verification and validation of calculational and predictive methodologies. This paper presents petrophysical evidence of DRZ development derived from the analysis of US and German repository salt cores drilled from the DRZ/EDZ (excavation disturbed zone).

Introduction

This work is a continuation of ongoing studies of the DRZ/EDZ in halite at the Waste Isolation Pilot Plant and in German salt repositories, and supports the DRZ observational study published in the January 30, 2000, Sandia National Laboratories DOE Milestone (Bryan et al., 2000). Planning documents and the scientific notebook supporting the petrographic structural analysis performed in this paper are:

1. TP99-04; WBS No. 1.2.01.09.03 (08/05/99): "Disturbed rock zone characterization program."
2. TP00-04; WBS No. 1.2.01.09.03.02 (04/20/00): "Laboratory analysis of samples collected from the disturbed rock zone."
3. Laboratory notebook WIPP-DRZ-Lab3.

In addition to WIPP repository salt core, this current work investigates two salt cores procured from the German TSDE Test Field. The TSDE (Thermal and Structural Demonstration Experiment) was conducted at the Asse Mine, near Braunschweig, Germany, by GRS (Gesellshaften Rohstoffe und Sicherheit). BAMBUS II is the post-facto evaluation of the TSDE. BAMBUS II addresses the behavior of the EDZ, as well as backfill material within a geologic repository for heat generating radioactive waste in rock salt. Its objective is to increase the knowledge of important processes occurring in salt repository drifts and to strengthen the scientific knowledge required for repository design and performance assessment. A comprehensive introduction to laboratory approaches undertaken to characterize damage in repository rock salt is provided in the above-mentioned milestone (Bryan et al., 2000). This stage

[1] This work is covered by WBS #1.3.5.4.4.1

of the DRZ/EDZ observational study focuses on microstructural analyses (petrographic fracture mapping) of three cores: (1) WIPP core QGU39 (2.25 m),(2) TSDE core A (0.72 m), and (3) TSDE core D1 (0.77 m). The dimensions in parentheses indicate the length of the cores referenced from the opening or drift face in which the cores were recovered. Fracture mapping entails the creation of thin sections of repository salt core to investigate fracture densities, apertures, angles and spatial distributions to help add to our knowledge of the geometry of the DRZ/EDZ and to delineate damage within this zone. Information gathered from these three cores will be plotted with data previously obtained on salt from WIPP and salt from a different site at the Asse Mine (Wieczorek and Zimmer, 1999).

CORE SAMPLES

WIPP core QGU39 was recovered from a horizontal borehole drilled into the rib of the Q-Room access drift as shown in Figure 1. The recovered core, with an approximate coring axis angle of 45-50° to the inside rib face (see Powers et al., 2001), extended through the DRZ and into the intact Salado Formation. Observations from the Q-Room alcove have necessitated the drilling of orthogonal paths through the DRZ to describe the anisotropy of fracturing within the zone (Holcomb and Hardy, 2001). Holcomb and Hardy have used ultrasonic wave velocities to delineate the DRZ as a function of depth from the drift wall and as a function of the varying stress-state that surrounds the approximately rectangular drift cross-section.

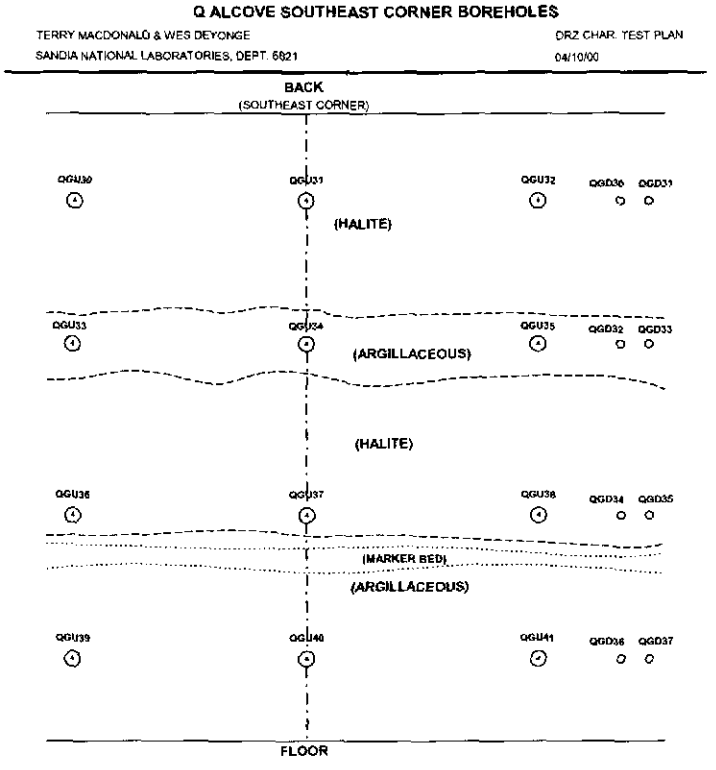

Figure 1. Layout of holes found in the Q-Room alcove; WIPP core QGU39 was recovered from the area shown in the lower left region of the figure. The 12 large holes, including hole QGU39, are used for ultrasound analyses. The 8 small holes were drilled for hydrologic analyses (from test plan TP99-04; WBS No. 1.2.01.09.03; "Disturbed rock zone characterization program.")

Understanding the time-dependent changes in damage, a proxy for permeability, as the DRZ develops is important because these changes can strongly affect the sealing of underground openings at WIPP (Holcomb and Hardy, 2001). GRS provided the two TSDE cores, for the purpose of performing the same petrographic microstructural analyses. Both TSDE cores were obtained from the Asse Mine's Northern Drift B, at the 800 m level (Figures 2 and 3).

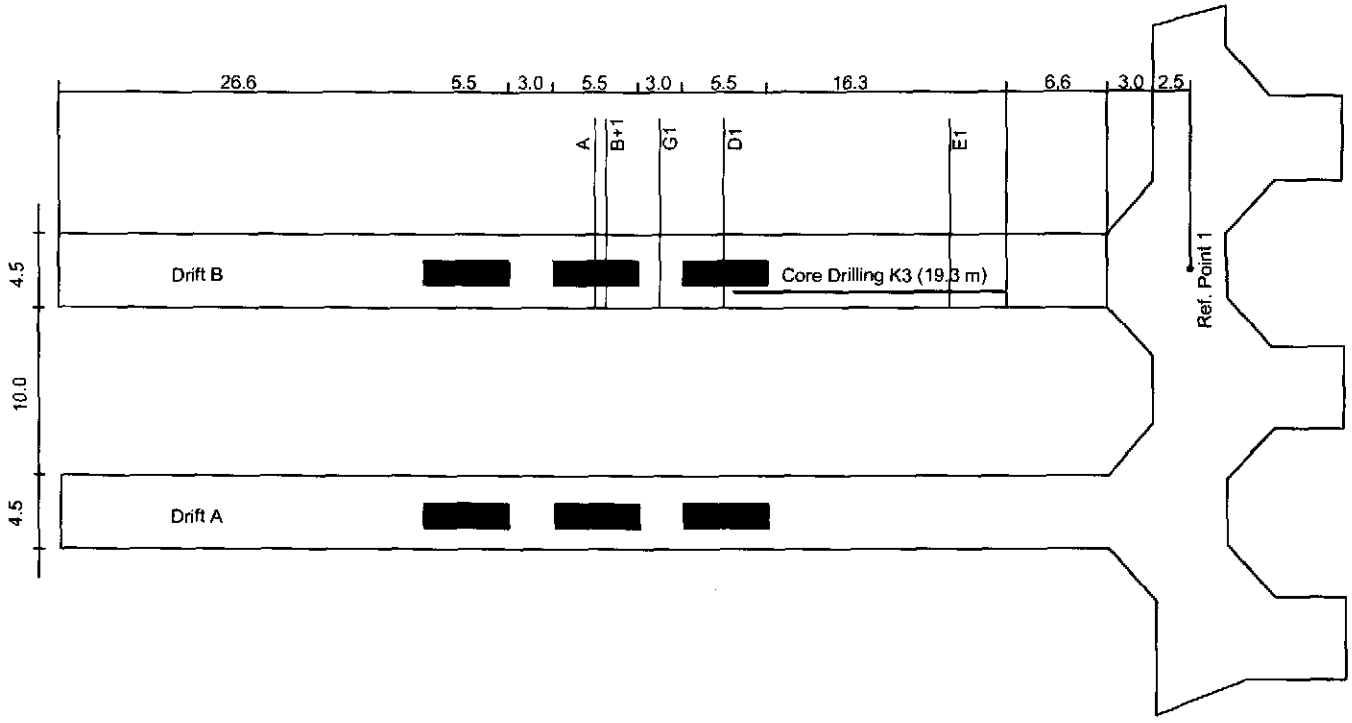

Figure 2. Plan view showing the drilling positions of EDZ sampling holes and surrounding host rock in the Northern Drift B of the TSDE Test Field. This investigation focuses, in part, on cores A and D1 drilled from the Northern Drift at a depth of 800 m.

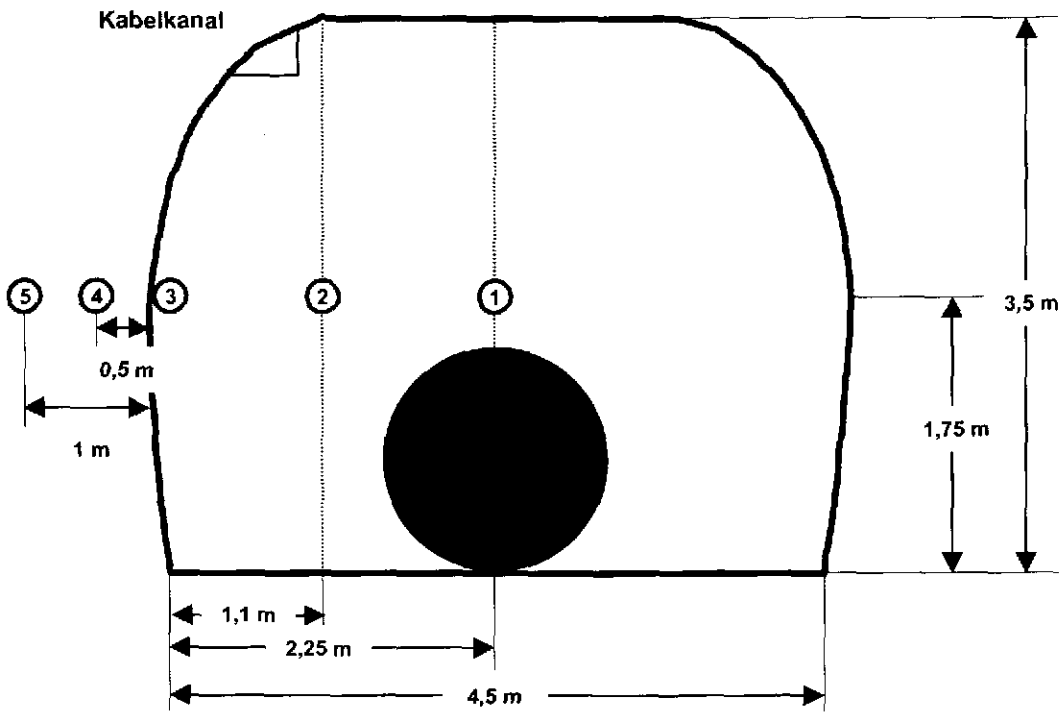

Figure 3. North drift cross-section showing the core A and core D1 recovery locations. Core A and core D1 were recovered from positions between locations 4 and 5 at horizontal distances of 0.72 m and 0.77 m, respectively.

METHODS

All core samples were sawed lengthwise into halves. Subsequently, one half was cut in half again to produce a one-quarter core billet from which thick sections (approximately 1 mm in thickness) could be fabricated. A diamond-impregnated wire-line saw was employed to cut these billets to the appropriate thickness. Quartered billets were subsequently impregnated with fluorescent dyed Epo-thin epoxy, ground flat, mounted on 2x6-inch glass plates, then cut and polished as thick sections. Measurements of the fracture distributions, fracture apertures, and fracture spacing (distance from the inside rib face or wall) were taken across the centerline of each thick section (parallel to the core axis), which would intersect fractures oriented parallel to the drift axis and cross-cutting the core hole. In addition, fracture angles (the angle each fracture makes with respect to the core axis) were measured for the WIPP QGU39 core.

RESULTS

Results of the fracture analyses of the WIPP and TSDE repository salt cores are presented in Figures 4-8. In WIPP QGU39, 454 fractures were observed filled with yellow-dyed epoxy, each indicating the presence of a permeable pathway, in the first 2.25 m of the core (2.0 fractures/cm; Figure 4). The thinnest fracture aperture measured is 2.5 μm, the widest measured is 545 μm, and the mean fracture aperture is 46.6 μm. Mean fracture apertures are wider proximal to the rib face (at approximately 0.1 m and 1.25 m) as compared to apertures measured

farther from the rib face. Measured fracture angles range between 12°-146° from the core axis (as shown in Figure 5), which itself is oriented approximately 45-50° to the rib face. Fracture angles closest to the rib face lie at approximately 50° to the core axis, or sub-parallel to the rib face. At approximately 2 m, the fracture angles have rotated normal to the core axis.

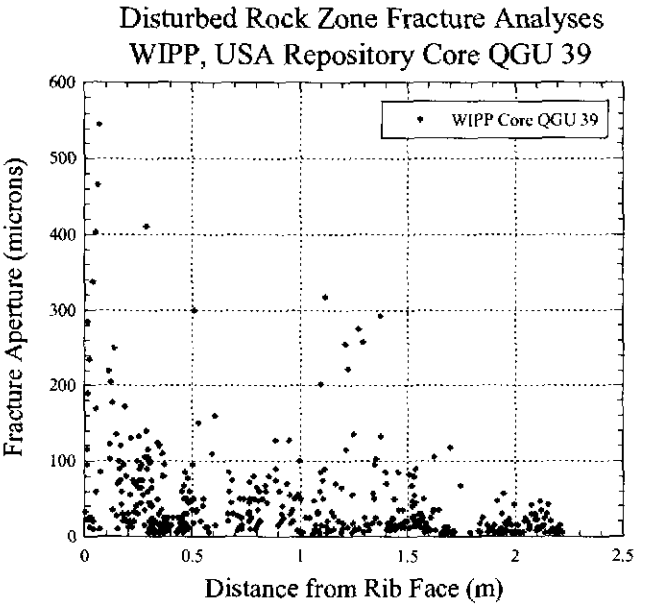

Figure 4. Plot showing the distribution of fractures and fracture apertures in WIPP core QGU39.

In the 0.72 m of TSDE core A, 103 fractures were measured (1.4 fractures/cm; minimum aperture = 2.5 μm; maximum aperture = 105 μm; mean aperture = 15 μm; Figure 6). In the 0.77 m of TSDE core D1, 122 fractures were measured (1.6 fractures/cm; minimum aperture = 2.5 μm; maximum aperture = 147.5 μm; mean aperture = 20 μm; Figure 6). The highest density of fractures in both cores occurs in the first 0.5 m of the core. A comparison of the fracture distribution and fracture apertures for all core investigated is presented in Figure 7. The highest density of fractures is observed closest to the rib walls and the predominant fracture apertures are $\leq$ 100 μm wide.

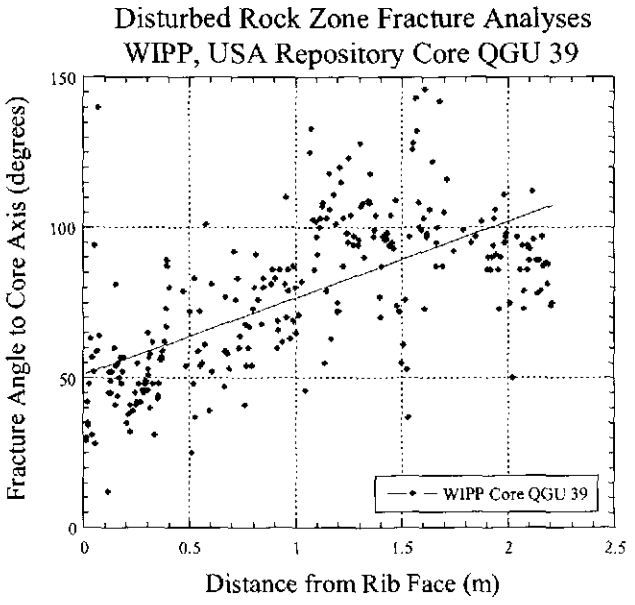

Figure 5. Plot showing the distribution of fracture angles in the first 2.25 m of WIPP core QGU39.

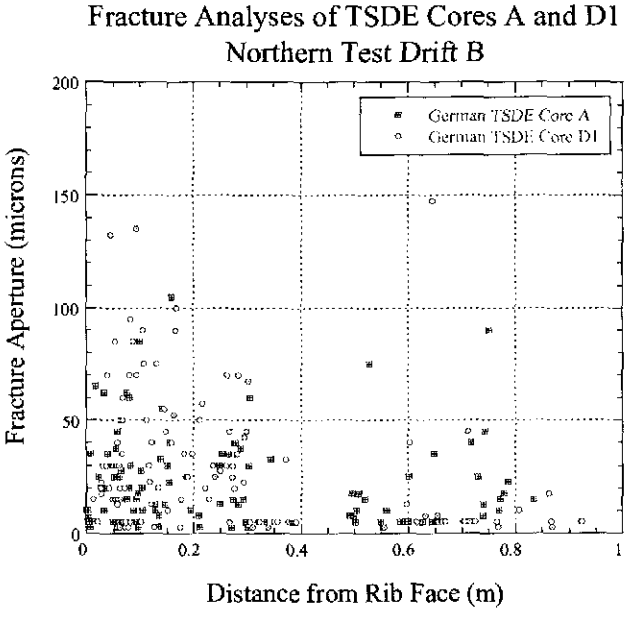

Figure 6. Plot showing the distribution of fractures and fracture apertures observed in the first meter of cores A and D1, TSDE Test Field, Germany.

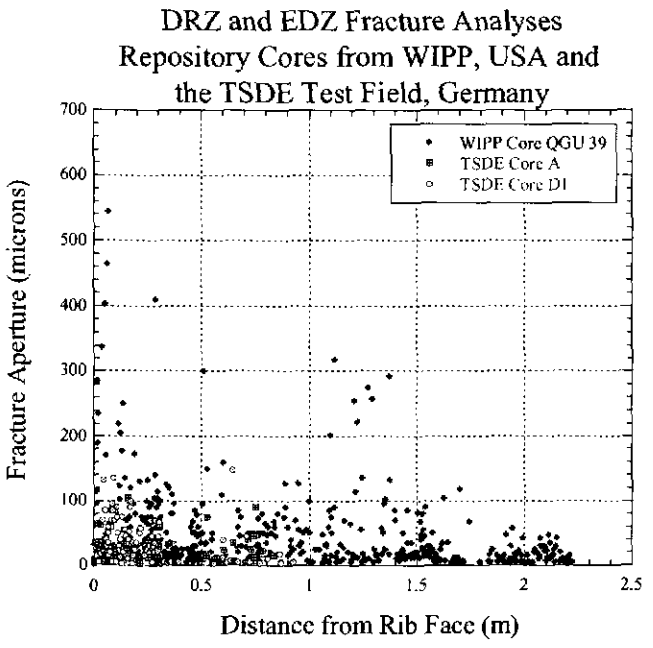

Figure 7. Plot comparing the distribution of fractures and fracture apertures found in the first meter of the TSDE cores and the first 2.25 meters of WIPP core QGU39.

Results of the fracture analyses of WIPP core QGU39, TSDE core A, and TSDE core D1, are presented in Figure 8 together with results obtained from previous studies of other WIPP and Asse salt cores (Bryan et al., 2000; Powers et al., 2001). Altogether, three WIPP cores and four German cores (all from the Asse Mine) have been investigated to date. Of particular interest are the WIPP fractures. Of the 744 fractures measured in the WIPP core (QGU14 = 164 fractures; QGU36 = 126 fractures; QGU39 = 454 fractures), only two fractures found at a distance of greater than 2 m have apertures wider than 125 μm (~0.3% of all fractures measured). Four fractures have apertures wider than 100 μm (~0.5% of all fractures measured) and 10 fractures observed have apertures wider than 50 μm (~1.0% of all fractures measured) at a distance greater than 2 m from the inside rib face (Figure 8).

DISCUSSION

The microstructural analyses performed on WIPP core QGU39, TSDE core A and TSDE core D1 reveal that the distribution of fractures is higher and that the fracture apertures are wider closer to the repository rib face. This has been observed in other WIPP cores and in the Asse Mine cores. Investigation of fracture angles in WIPP core QGU39 reveals that the fractures closest to the rib wall trend parallel to the excavated inside face. As the fractures are mapped further out into the DRZ and into the host rock, these angles tend to increase and trend perpendicular or normal to the core axis.

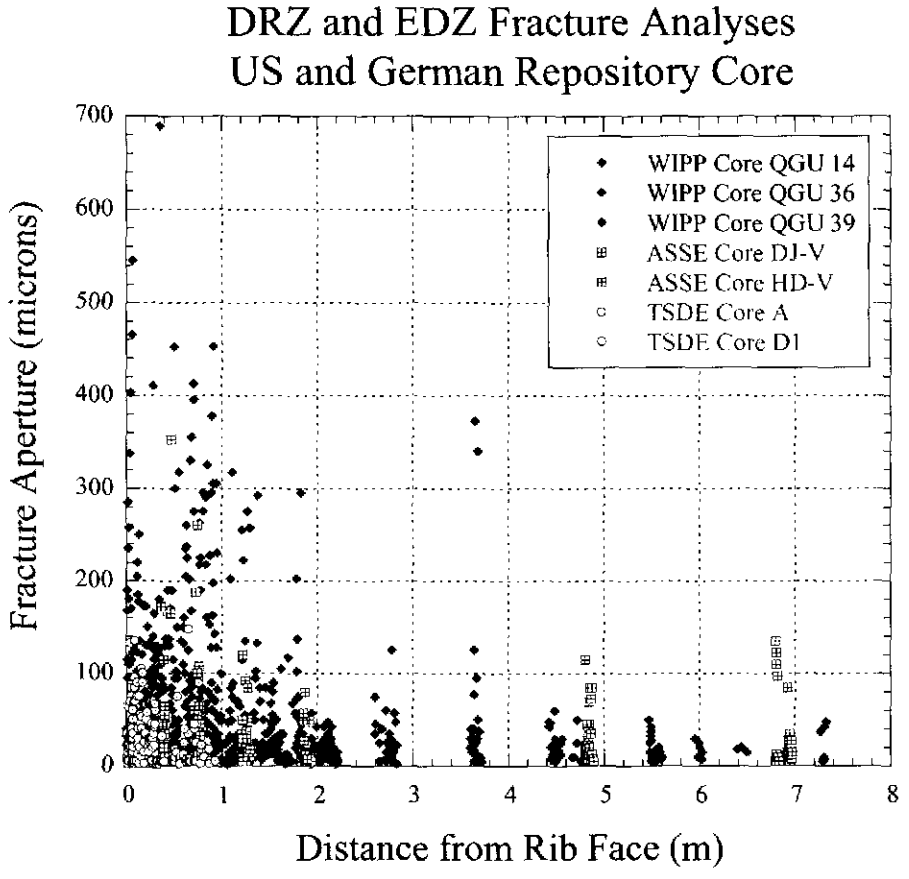

Figure 8. Plot showing the distribution of fractures and fracture apertures in core drilled from the WIPP, USA, the Asse Mine, Germany and the TSDE Test Field, Germany. Fracture distributions and apertures are plotted as a function of distance from the inside of the repository rib wall (face). Original plots of fracture distributions and fracture apertures as a function of distance from the rib face for cores WIPP QGU14, Asse DJ-V, and HD-V are found in Bryan et al. (2000); the original plot of this fracture analyses for WIPP core QGU36 can be found in Powers, et al. (2001).

FUTURE WORK

In addition to the fracture analyses discussed in this paper, subsamples of WIPP core QGU36 and QGU39 and German TSDE cores A and D1 will be disaggregated and individual halite crystals cleaved, then etched using a $PbCl_2$-saturated methanol solution and butanol to investigate substructural features within the salt. Qualitative and quantitative analyses will compare subgrain sizes and dislocation density distributions between both repository salts. The methods employed for this investigation will include use of the SEM, petrographic microscope, and image analysis software. Free dislocations and structural features can be used as a correlative tool, where a higher defect density correlates with strain magnitudes and structural features provide evidence of deformation processes.

Ultimately, all data will be assembled, analyzed and reported in reference documents (either proceedings or SAND reports). In addition, the fracture studies will be made available to our German partners (GRS) and to the BAMBUS II consortium for their EU reports.

References

Bryan, C.R., D.M. Chapin, and A.C. Snider. 2000. "DRZ Observational Studies: Characteristics of the Disturbed Rock Zone in salt at the Waste Isolation Pilot Plant." In Sandia National Laboratories, "Sandia National Laboratories Technical Baseline Reports, January 31, 2001." Carlsbad, NM: Sandia National Laboratories.

Holcomb, D.J., and R. Hardy. 2001. "Assessing the disturbed rock zone (DRZ) at the Waste Isolation Pilot Plant in salt using ultrasonic waves: *Proceedings of the 38th U.S. Rock Mechanics Symposium; Rock Mechanics in the National Interest, Vol. 1*, Elsworth, D., Tinucci, J.P. and Heasley, K.A., eds. July, 2001, Washington, D.C., p. 489-496.

Powers, D., C. R. Bryan, and D. M. Chapin. 2001. "DRZ Observational Studies: Laboratory Studies of Salt Cores from the WIPP Disturbed Rock Zone." In Sandia National Laboratories, "Sandia National Laboratories Technical Baseline Reports, July 31, 2001." Carlsbad, NM: Sandia National Laboratories.

Wieczorek, K. and U. Zimmer. 1999. "Hydraulic Behavior of the Excavation Disturbed Zone around Openings in Rock Salt," *Radioactive Waste Management and Environmental Remediation.* ASME. 6

5.2 Crushed Salt Studies[1]

D. M. Chapin, Jr. and F. D. Hansen
Sandia National Laboratories, MS 1395
4100 National Parks Highway
Carlsbad, NM USA 88220

Abstract

Crushed salt studies are fundamental to WIPP applications in sealing systems and rock mechanics and crushed salt properties are of great interest to international collaborators. An understanding of the compaction behavior of crushed salt is necessary to perform engineering calculations, to model convergence effects, to quantify backfill consolidation, and, currently, to assess a panel closure system redesign for WIPP. These investigations examine crushed salt cores and similar materials using scanning electron microscopy to characterize porosity, mineralogy and structural features. The permeability of each salt sample was measured in the laboratory prior to impregnation. Compositional, structural, textural, diagenetic (compactional) and hydrologic features are documented. Characteristics of crushed salt and similar materials from the USA, Germany and Canada are compared.

Introduction

Sandia National Laboratories is the science advisor for the Waste Isolation Pilot Plant (WIPP), a nuclear waste repository situated in the bedded salt of the Permian Salado Formation. The US Department of Energy, represented by the Carlsbad Field Office (CBFO), is the government agency responsible for WIPP. The CBFO has signed a contract with the European Union research centers to investigate several issues specific to salt repositories. The consortium of ten research centers is called BAMBUS II (Backfill and Material Behavior in Underground Salt). Between the years 1985-93, the TSDE (Thermal and Structural Demonstration Experiment) was conducted at the Asse Mine, near Braunschweig, Germany, by GRS (Gesellschaft für Anlagen und Reacktorsicherhiet). BAMBUS II is the post-facto evaluation of the TSDE. Partners in the BAMBUS II consortium are evaluating ten research topics, whereas the CBFO is concentrating on three specific topics: 1. re-consolidation of crushed salt, 2. the excavation damage zone (EDZ or DRZ) and modeling. This status report summarizes progress on our crushed salt work which includes samples from Germany, Canada and the USA.

The US-WIPP-CBFO, through its scientific advisor, Sandia, is performing ongoing research emphasizing crushed salt backfill, as well as the disturbed rock zone (DRZ; EDZ in Europe) and modeling. Consolidation characteristics of crushed salt are needed for the design and analysis of seal systems, an increased knowledge of the structural integrity of salt repositories, as well as the performance assessment of WIPP. To add to the fundamental understanding of these consolidation characteristics, this study provides permeability, porosity, mineralogical and structural analysis of several representative reconsolidated and dynamically compacted, US, German and Canadian salt samples. Data obtained from this study will be used to calibrate and refine constitutive equations developed to predict the mechanical and hydraulic

[1] This work is covered by WBS #1.2.2.2.2

behavior of both backfill material and host rock in the vicinity of emplacement drifts (Bechthold, 01). All crushed salt samples analyzed in this study were examined as either recovered core, sawn or extracted block specimens or as plugs, employing scanning electron microscopy and other petrographic methods to qualitatively and quantitatively characterize all representative thick sections and freshly broken sample surfaces. Planning documents and the scientific notebooks supporting the petrographic structural analysis performed in this paper are:

1.) TP00-04; WBS No. 1.2.01.09.03.02 (04/20/00): "Laboratory analysis of samples collected from the disturbed rock zone."
2.) Laboratory notebook ALOHA II: Bulkhead Drift.
3.) German, US and Canadian Reconsolidated and Dynamically Compacted Salt Investigation: A Correlative Analysis with BAMBUS II; Sandia National Laboratories in house progress presentation, July, 2001.

Materials

The reconsolidated backfill analysis includes the characterization of several uniquely compacted salt samples, two of which were obtained from the BAMBUS II:

A. German BAMBUS II Block: extracted from the TSDE drift during a site visit.
B. German BAMBUS II Core: provided by the German collaborator Bundesanstalt für Geowissenschaften und Rohstoffe (BGR).

The BAMBUS II salt consolidation characteristics were then compared and contrasted with other similar materials. Materials studied are identified as follows:

C. US Dynamically-Compacted: from WIPP's dynamic compaction demonstration – specified compacted energy was approximately 168,600 ft-lbs/ft^3.
D. US Reconsolidated: WIPP's dynamically-compacted sample after hydrostatic consolidation.
E. Canadian K2: natural backfill recovered from the Canadian K2 Mine.
F. Canadian Reconsolidated: naturally reconsolidated backfill material.
G. German Kali und Salz: from reconsolidated backfill within the K&S operations.
H. German SVV Self-Sealing Plug: provided by Wernt Brewitz.

Methods

MODAL ANALYSIS

Modal analysis was performed on thick sections ($\leq$ 1 mm) fabricated from the US, German and Canadian reconsolidated salt samples. Each thick section was impregnated with yellow-fluorescent dyed resin epoxy to differentiate true porosity from relic pore spaces created during section preparation. Thick sections were coated with gold to perform two-dimensional, qualitative, back-scattered electron (BSE) mineralogic analysis and to determine total macroporosity. Analysis was performed on a JEOL scanning electron microscope and a petrographic microscope, both operated by the Sandia National Laboratory's Carlsbad Operations Group, Carlsbad, New Mexico. Macroporosity features quantified in the analysis include intergranular and intragranular primary, secondary and fracture porosity.

A multisupport gas permeameter (MSP) was recently developed at Sandia National Laboratories, Albuquerque, New Mexico, for the purpose of: 1) rapidly and inexpensively collecting extensive permeability data sets from the flat surfaces of different lithologic samples (sandstones, tuffs, carbonates, evaporites) in a nondestructive matter, and 2) investigating permeability upscaling in a laboratory setting (Tidwell and Wilson, 1997). Although the MSP was employed to perform this analysis, the permeameter was not implicitly developed with DOE funds for this investigation. The MSP (Figure 1) comprises five main components: 1) an electronic permeameter, 2) an x-y positioning system, 3) a computer control system, 4) a tip seal, and 5) a pneumatic piston capable of compressing the tip seal. Automation of this apparatus is achieved by integrating the electronic permeameter with the x-y positioning system through specially adapted, PC-based software. Automation also allows for the unattended operation of the MSP (the system has the capability of collecting over 400 permeability measurements from a sample rock face in an eight hour period). The x-y positioner has a bi-directional repeatability of $\pm$ 0.1 mm over a 1.5 by 1.5 m sampling area; its carriage is coupled with a pneumatic piston, which has also been automated for positioning and compressing the permeameter tip seals against the rock surface.

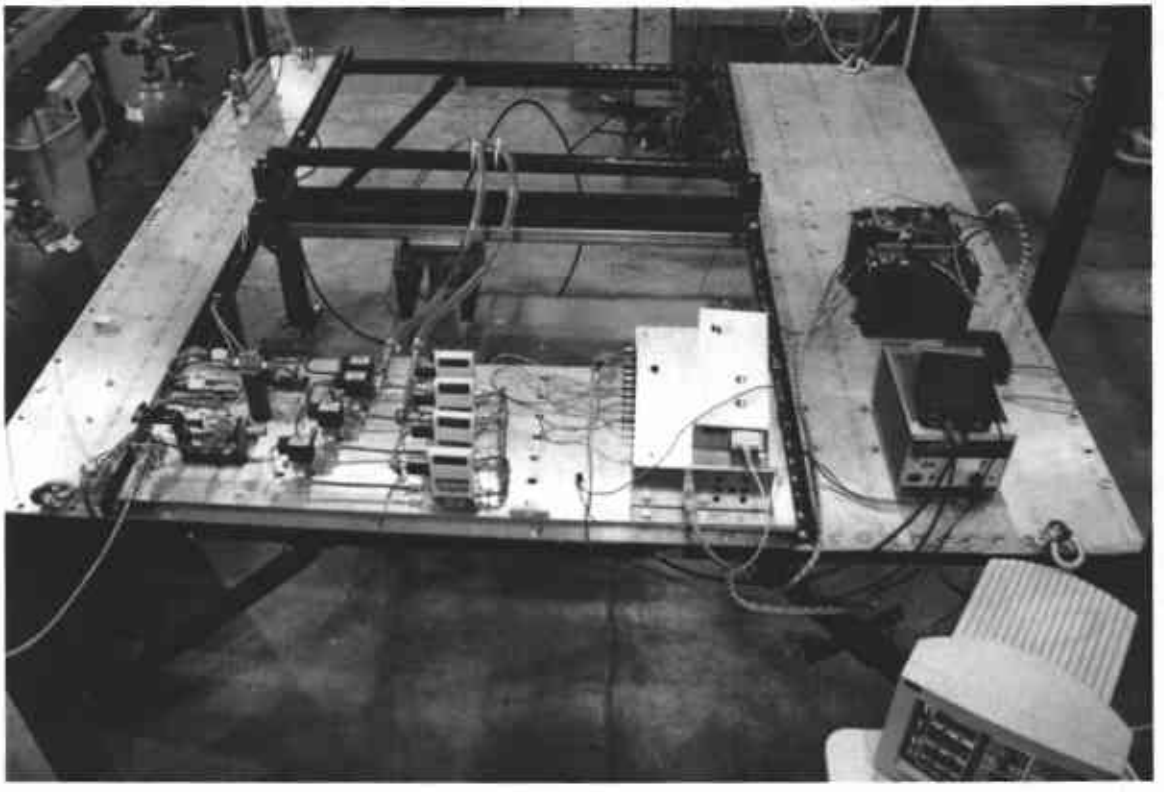

Figure 1. Photograph of the multisupport permeameter (MSP), the x-y positioner and computer control system. Permeability measurements are acquired by compressing a selected tip seal squarely against the flat, lithologic sample surface while injecting laboratory grade nitrogen into the rock at a constant pressure. Measurements are made following a user-designed sampling grid programmed into the x-y positioner. Automation of the MSP is achieved by the integration of two stepper motors and three belt drives on the

positioner. The positioning system is affixed to a rigid table supported by a unistrut frame, the height of which may be adjusted over a 1.5 m distance to accommodate differences in sample sizes. Sample blocks are placed under the positioning system where they remain stationary during sampling by virtue of their own weight (after Tidwell and Wilson, 1997).

Gas permeant penetrates the sample surface with a predetermined injection pressure. Instrumentation on the permeameter measures the injection pressure, the resultant steady state gas flow rate and gas temperature within each lithologic sample. Four mass-flow meters (0-50, 0-500, 0-2000 and 0-20,000 sccm), two pressure transducers (0-100 and 0-350 KPa gauge), a barometer and a temperature sensor are connected to a regulated source of compressed nitrogen on the MSP. Subsequently, the gas flow rate is measured as laboratory grade nitrogen is directed into the sample via a series of distinctly sized, spring loaded tip seals (Figure 2). The diameter of each tip seal defines the scale of measurement and is used to establish a known boundary condition on the lithologic surface. By changing the size of the tip seal, the permeameter interrogates volumes of rock ranging in scale from tenths to thousandths of cubic centimeters. The employment and exchange of these tip seals with the computer controlled, electronic gas permeameter allows for the exhaustive collection of permeability data from the rock sample on multiple scales.

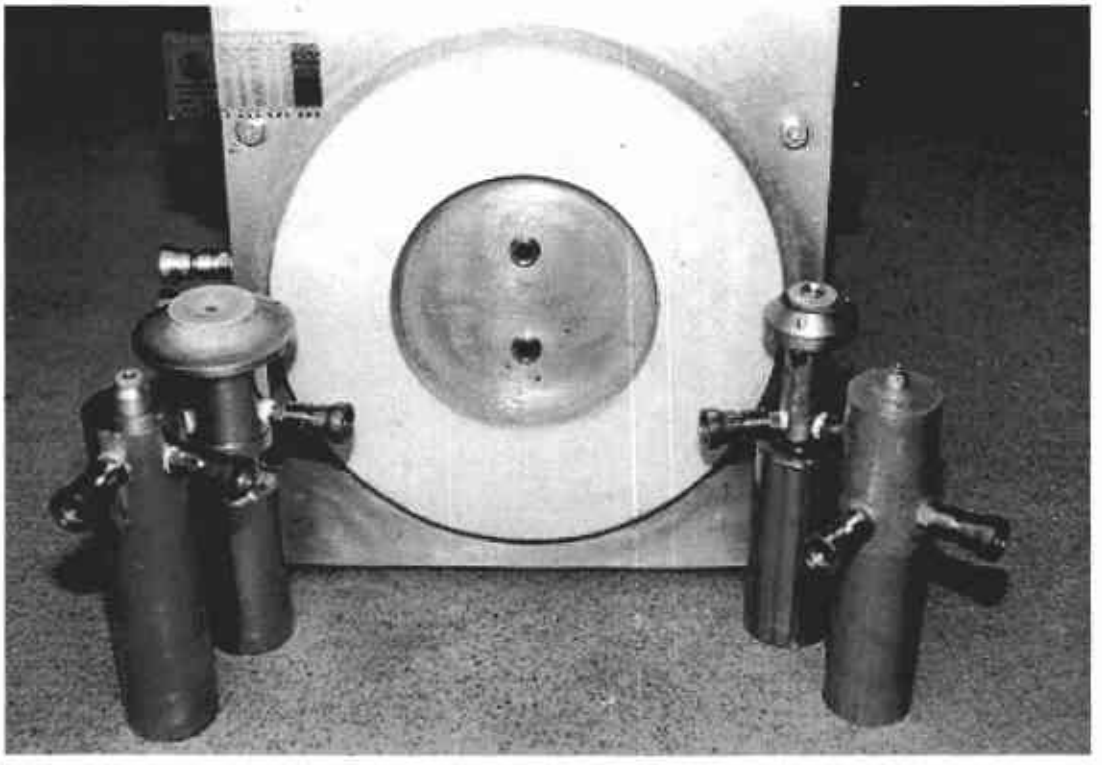

Figure 2. Photograph of five of the six tip seals currently employed by the MSP. Tip seals shown have inner radii of 0.15, 0.31, 1.27, 2.54 and 7.62 cm and outer radii measuring twice that of the inner radii. These specifically designed tip seals investigate a known boundary condition on a specific rock surface. A thin seal (0.5 cm thick) constructed of hard silicone rubber is used to create the 0.15 and 0.31 cm inner radii tip seals used in this investigation (after Tidwell and Wilson, 1997).

Permeability is calculated directly from information on the specific tip seal geometry, the measured nitrogen flow rate, the injection pressure, the barometric pressure and the gas temperature (Tidwell and Wilson, 1997). Permeability is a measure of the capacity of a porous medium to transmit fluids and is a function of pore aperture and tortuosity. Permeability measurements made with the MSP relate the cross-sectional area, pressure gradient, viscosity and total recharge of a rock fluid system to a property intrinsic to the porous medium. For this investigation, permeability estimates were derived using a modified form of Darcy's Law developed by Goggin et al. (1988):

$$k\,(Q_1, P_1, P_0, r_i, r_0) = Q_1 P_1 \mu(T) / (0.5)\, r_i G_0 (r_0 / r_i)[P_1^2 - P_0^2]$$

where $k\,(Q_1, P_1, P_0, r_i, r_0)$ is permeability, Q_1 is gas flow rate, P_0 is atmospheric pressure, P_1 is the gas injection pressure, $\mu(T)$ is gas viscosity (a function of temperature) and $G_0 (r_0 / r_i)$ is a geometric factor that varies according to the ratio of the outer tip seal radius, r_0, to the inner tip seal radius, r_i (Tidwell and Wilson, 1977).

SUBSTRUCTURE

Photomicrographs were shot on fresh faces from each salt sample. Samples were broken to an appropriate size and then the exposed fresh faces were gold coated to perform structural analysis. Analysis was performed using a JEOL scanning electron microscope to examine: 1) compaction, 2) grain-to-grain contacts, 3) fractures and 4) the possible existence of pressure solution. Images were collected and analyzed for structural integrity and heterogeneity.

BULK SAMPLE MINERALOGY

Polished and coated thick sections were examined using the scanning electron microscope for: 1) mineralogy; 2) any evidence of secondary mineral precipitation; and 3) characterization of overgrowth textures along fractures.

Results

Photomicrographs presenting grain-to-grain contacts and porosities (typical void space) for the US, German and Canadian backfill material samples were captured for qualitative and quantitative comparison (Figures 3-17). Compaction terms are qualified in Figure 18. Permeability, porosity, mineralogy and structural characteristics and measurements are subsequently summarized in Table 1. Mean permeability was plotted against mean porosity for all reconsolidated and dynamically compacted salt samples analyzed (Figure 19).

The BAMBUS II Block (Figures 3 and 4), Canadian K2 (Figures 5 and 6) and BAMBUS II Core (Figures 7 and 8) samples exhibit the highest mean permeabilities (2.54e-11 m^2, 1.38e-12 m^2, and 4.17e-13 m^2, respectively; Table 1) and the highest mean porosities (28.9%, 24.2%, and 20.7%, respectively, Table 1). Visual inspection of grain-to-grain contacts in the BAMBUS II samples reveals that these reconsolidated salts have undergone the lowest degree of compaction when compared to all samples. The salt grains predominately exhibit tangential and long contacts, floating grains are prevalent and the degree of grain sorting is poor (Figure 18). Pores

or voids are large and well connected. The Canadian K2 samples reveal an increasing compaction state compared to that of the BAMBUS II samples. Although long and tangential contacts are still prevalent, concavo-convex contacts are present. Large, connected pores separate the salt grains, supporting the relatively high permeability and porosity measurements.

Porosity standard deviation percentages for these three samples are rather large, and are most likely explained by addressing the textural issue. These samples are poor to very poorly sorted with large voids juxtaposing large halite and anhydrite grains. Measured porosities for the BAMBUS II Block range between 7.8% and 42.1%. Canadian K2 porosities range between 17.7% and 38.7%. As for the BAMBUS II Core samples, measured porosities fall between 17.1% and 25.1%.

The US Dynamically Compacted (WIPP Mine Run; Figures 9 and 10) samples reveal a marked increase in the compaction state as compared to the BAMBUS II and Canadian K2 samples. The measured mean permeability of these samples is 3.85e-14 m^2 and the mean porosity was determined to be 11.5% (Table 1). Although sutured contacts do not appear to be prevalent, concavo-convex and long grain contacts are ubiquitous. Pores are much smaller and more isolated than those found in the higher permeability and porosity samples.
The Kali und Salz (Figures 11 and 12), Canadian Reconsolidated (Figures 13 and 14), SVV Self-Sealing Plug (Figures 15 and 16) and the US Reconsolidated (Figure 17) samples exhibit the lowest measured mean permeabilities (7.60e-15 m^2, 1.08e-15 m^2, 2.69e-16 m^2, 1.00e-20 m^2, respectively; Table 1) and the lowest mean porosities (1.4%, 1.7%, 5.1%, and 0.78%, respectively; Table1). All grain contacts (if grains can be discerned) are sutured; otherwise the samples are amalgamated. Porosity is isolated in the form of singular vugs and fractures.

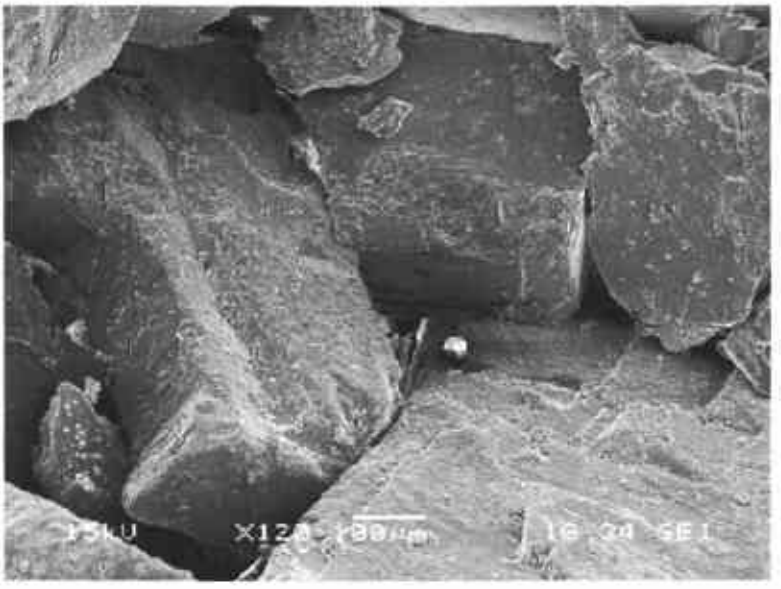

Figure 3. Scanning electron image of BAMBUS II Block grain-to-grain contacts. The mean permeability measured by the MSP is 2.54e-11 m^2 and the mean porosity derived from image analysis is 28.9%. The predominant mineralogic phases exhibited within the BAMBUS II Block include halite and anhydrite.

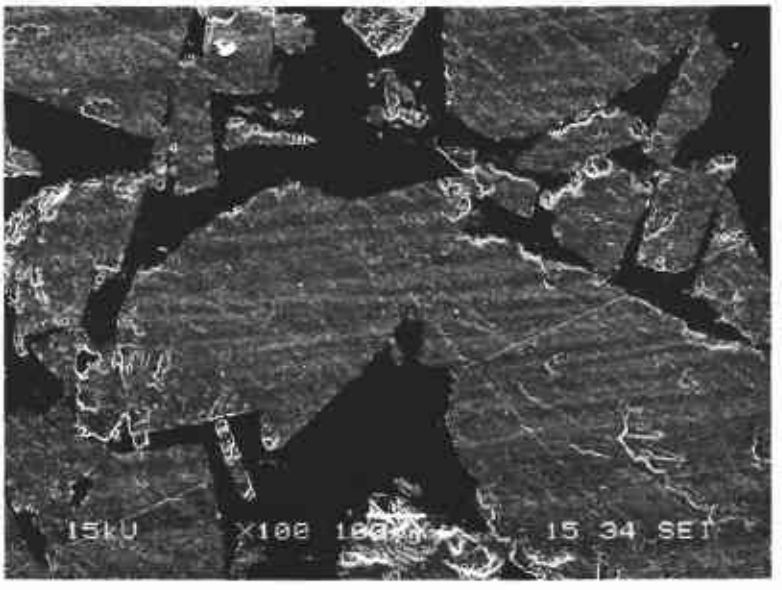

Figure 4. Scanning electron image of a portion of a BAMBUS II Block thick section. Porosity was derived using the image analysis software package 'Image Pro Plus 4.0' (mean porosity = 28.9%).

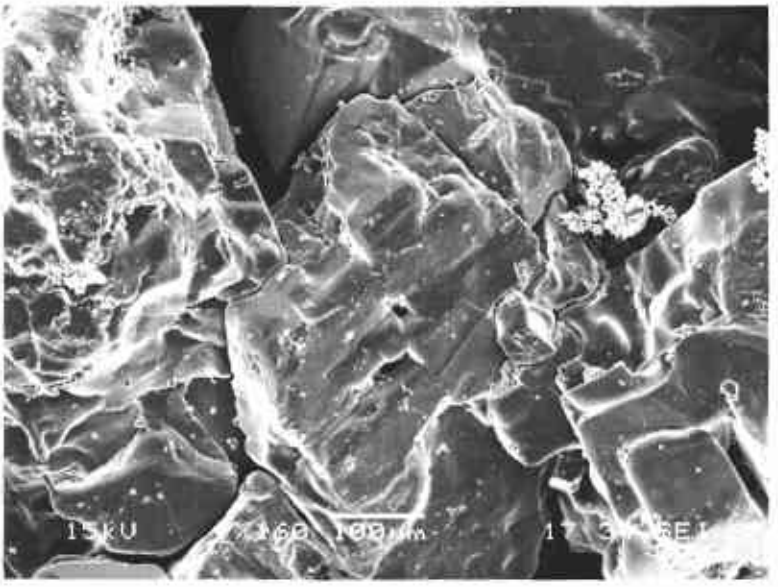

Figure 5. Scanning electron image of Canadian K2 grain-to-grain contacts. The mean permeability measured by the MSP is 1.38e-12 m^2 and the mean porosity derived from image analysis is 24.2%. The predominant mineralogic phases exhibited within the Canadian K2 salt include halite and magnesium and calcium rich aluminosilicates or clay minerals.

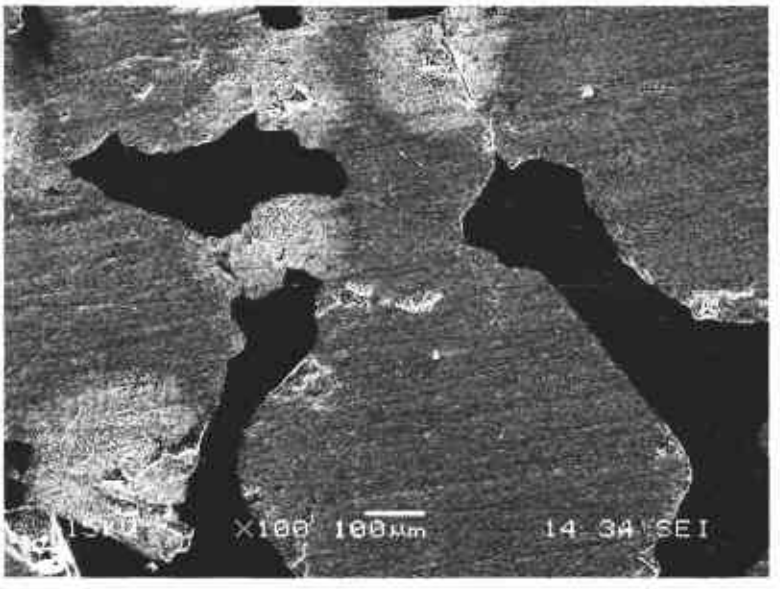

Figure 6. Scanning electron image of a portion of a Canadian K2 sample thick section. Porosity was derived using the image analysis software package 'Image Pro Plus 4.0' (mean porosity = 24.2%).

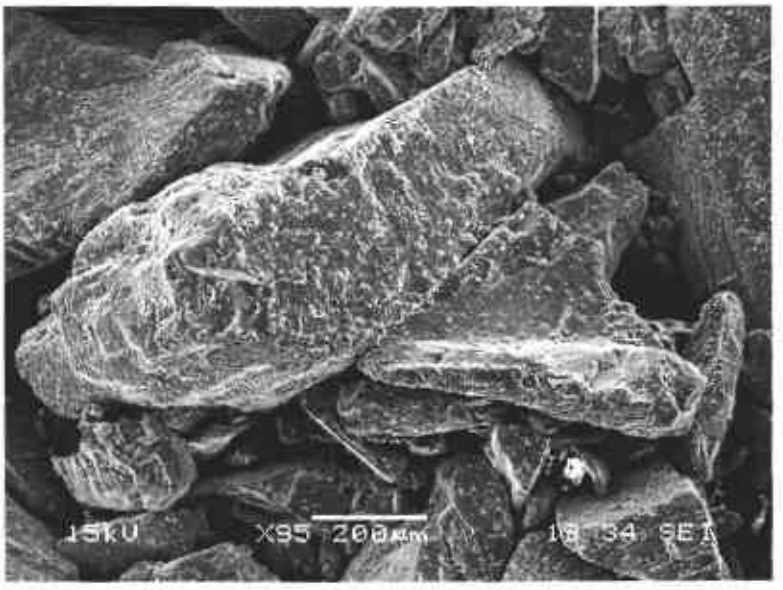

Figure 7. Scanning electron image of BAMBUS II Core grain-to-grain contacts. The mean permeability measured by the MSP is 4.17e-13 m^2 and the mean porosity derived from image analysis is 20.7%. The predominant mineralogic phases exhibited within the BAMBUS II Core include halite and anhydrite.

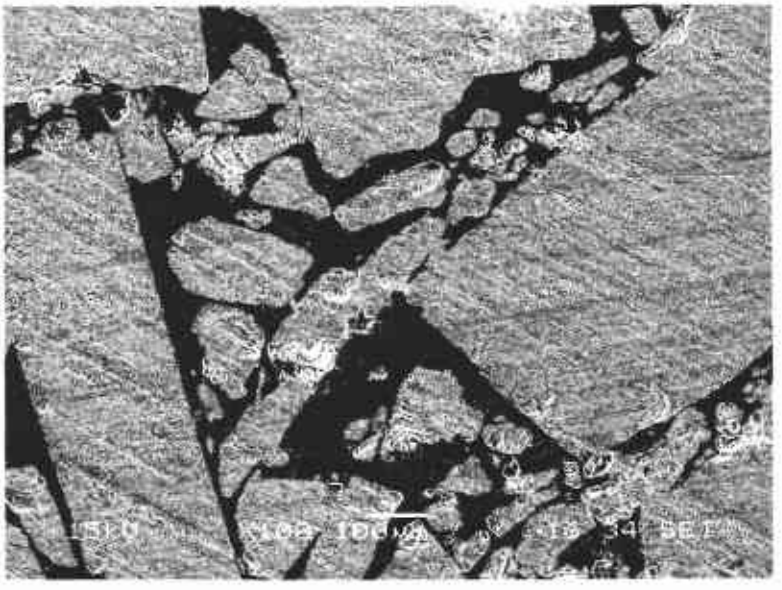

Figure 8. Scanning electron image of a portion of a BAMBUS II Core thick section. Porosity was derived using the image analysis software package 'Image Pro Plus 4.0' (mean porosity = 20.7%).

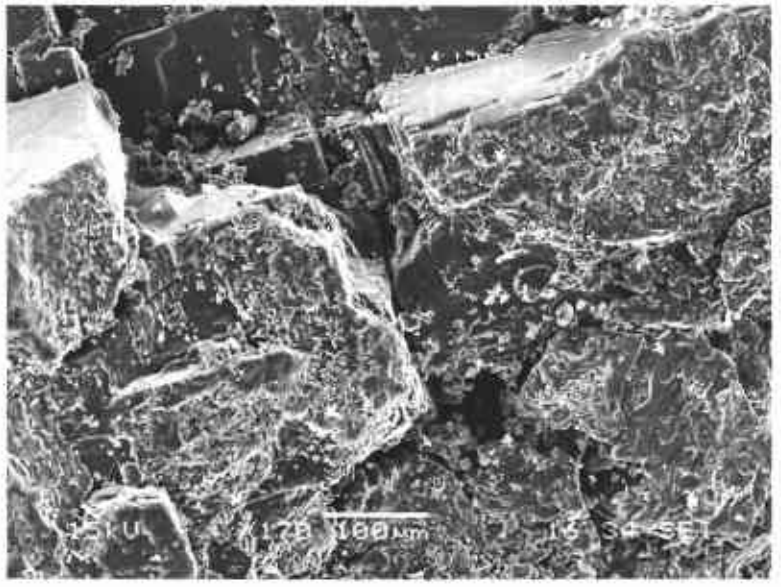

Figure 9. Scanning electron image of the dynamically compacted WIPP mine run salt, USA. The mean permeability measured by the MSP is 3.85e-14 m^2 and the mean porosity derived from image analysis is 11.5%. The predominant mineralogic phases exhibited within the WIPP salt include halite and quartz.

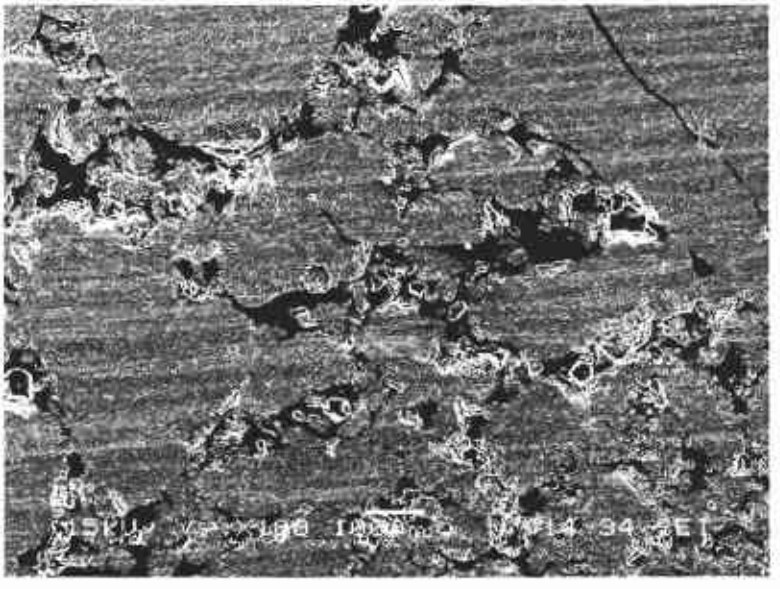

Figure 10. Scanning electron image of a portion of a dynamically compacted WIPP mine run salt sample thick section. Porosity was derived using the image analysis software package 'Image Pro Plus 4.0' (mean porosity = 11.5%).

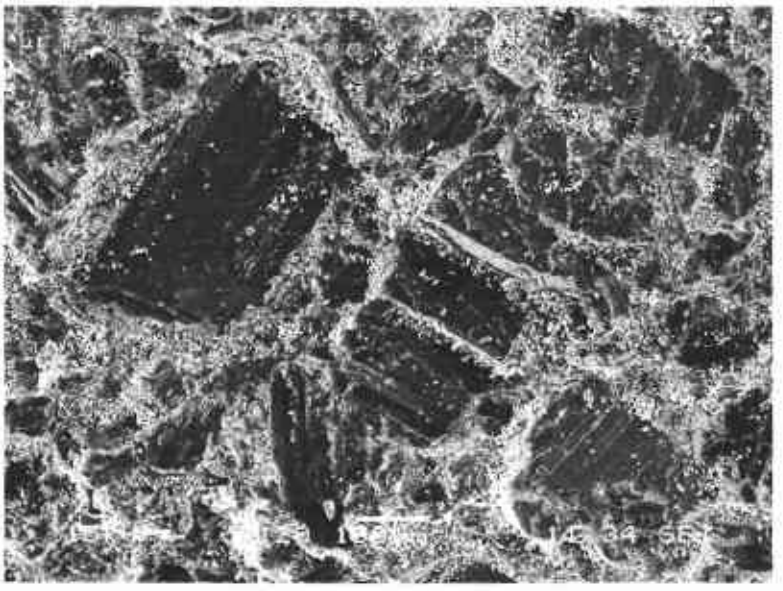

Figure 11. Scanning electron image Kali und Salz sample grain-to-grain contacts. The mean permeability measured by the MSP is 7.60e-15 m^2 and the mean porosity derived from image analysis is 1.4%. The predominant mineralogic phases exhibited within the Kali und Salz include halite, sylvite, anhydrite and quartz.

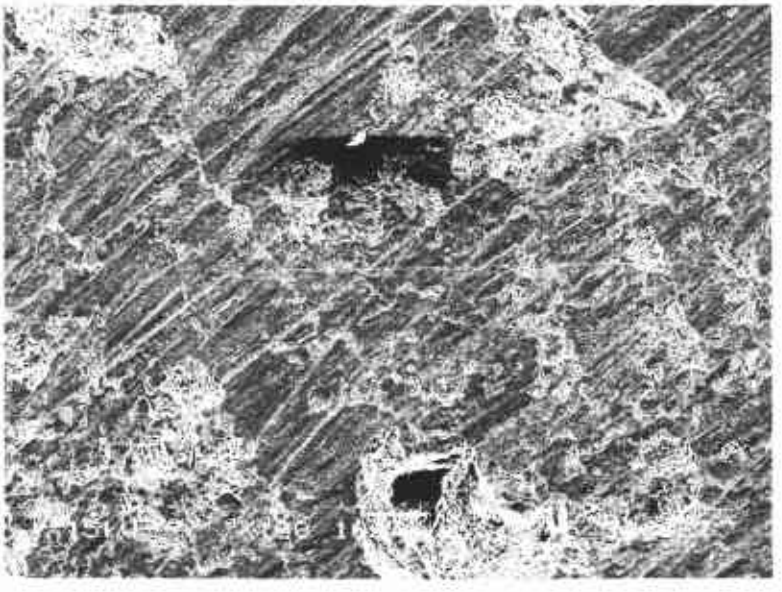

Figure 12. Scanning electron image of a portion of a Kali und Salz sample thick section. Porosity was derived using the image analysis software package 'Image Pro Plus 4.0' (mean porosity = 1.4%).

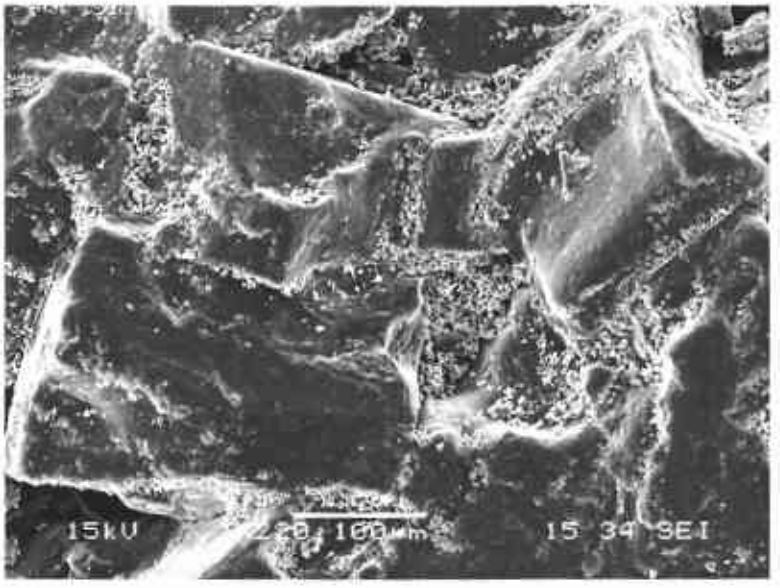

Figure 13. Scanning electron image of the Canadian Reconsolidated grain-to-grain contacts. The mean permeability measured by the MSP is 1.08e-15 m^2 and the mean porosity derived from image analysis is 1.7%. The predominant mineralogic phase exhibited within the Canadian Reconsolidated sample is halite.

Figure 14. Scanning electron image of a portion of a Canadian Reconsolidated sample thick section. Porosity was derived using the image analysis software package 'Image Pro Plus 4.0' (mean porosity = 1.7%).

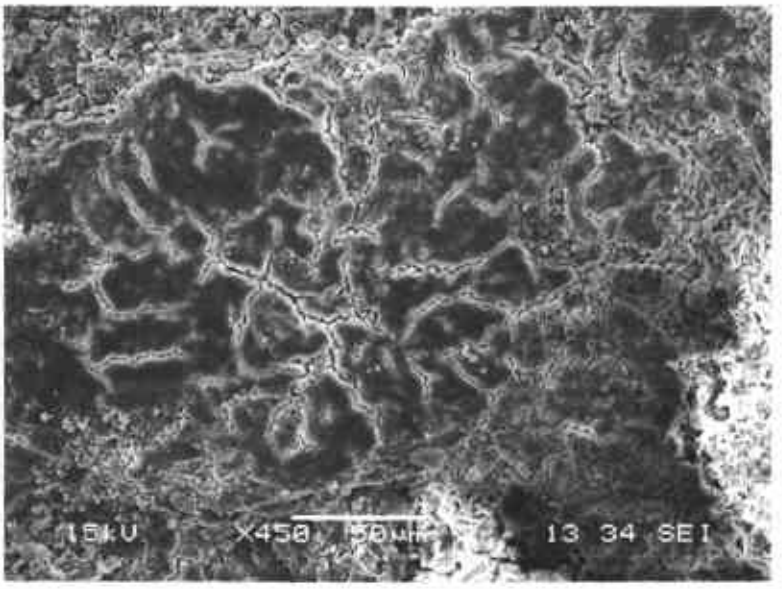

Figure 15. Scanning electron image of the SVV Self-sealing plug. The mean permeability measured by the MSP is 2.69e-16 m^2 and the mean porosity derived from image analysis is 5.1%. The predominant mineralogic phases exhibited within the SVV Self-sealing plug include magnesium sulfate, halite, anhydrite and sylvite.

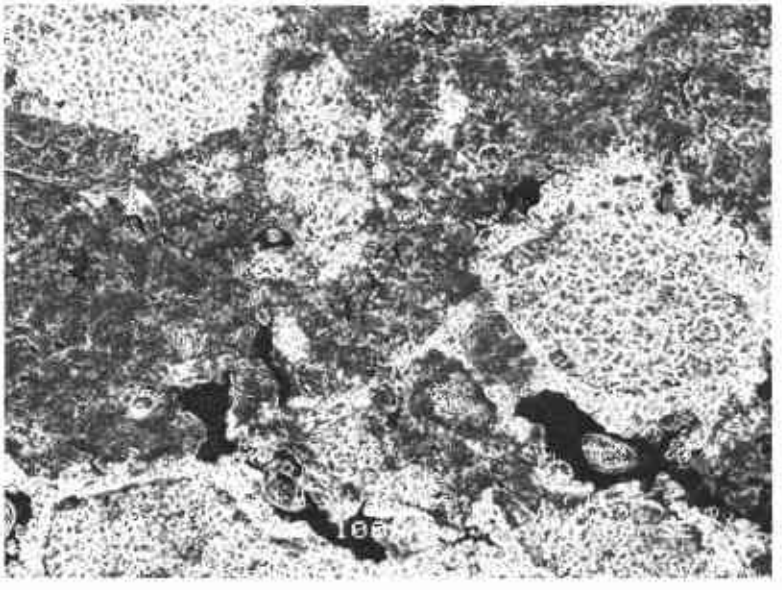

Figure 16. Scanning electron image of a portion of an SVV Self-sealing salt plug sample thick section. Porosity was derived using the image analysis software package 'Image Pro Plus 4.0' (mean porosity = 5.1%).

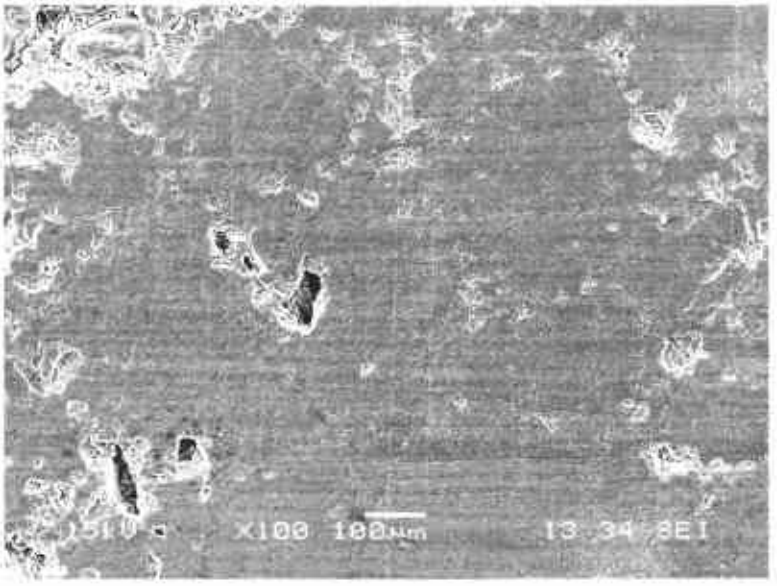

Figure 17. Scanning electron image of a portion of a US Reconsolidated sample thick section. Porosity was derived using the image analysis software package 'Image Pro Plus 4.0' (mean porosity = 0.8%).

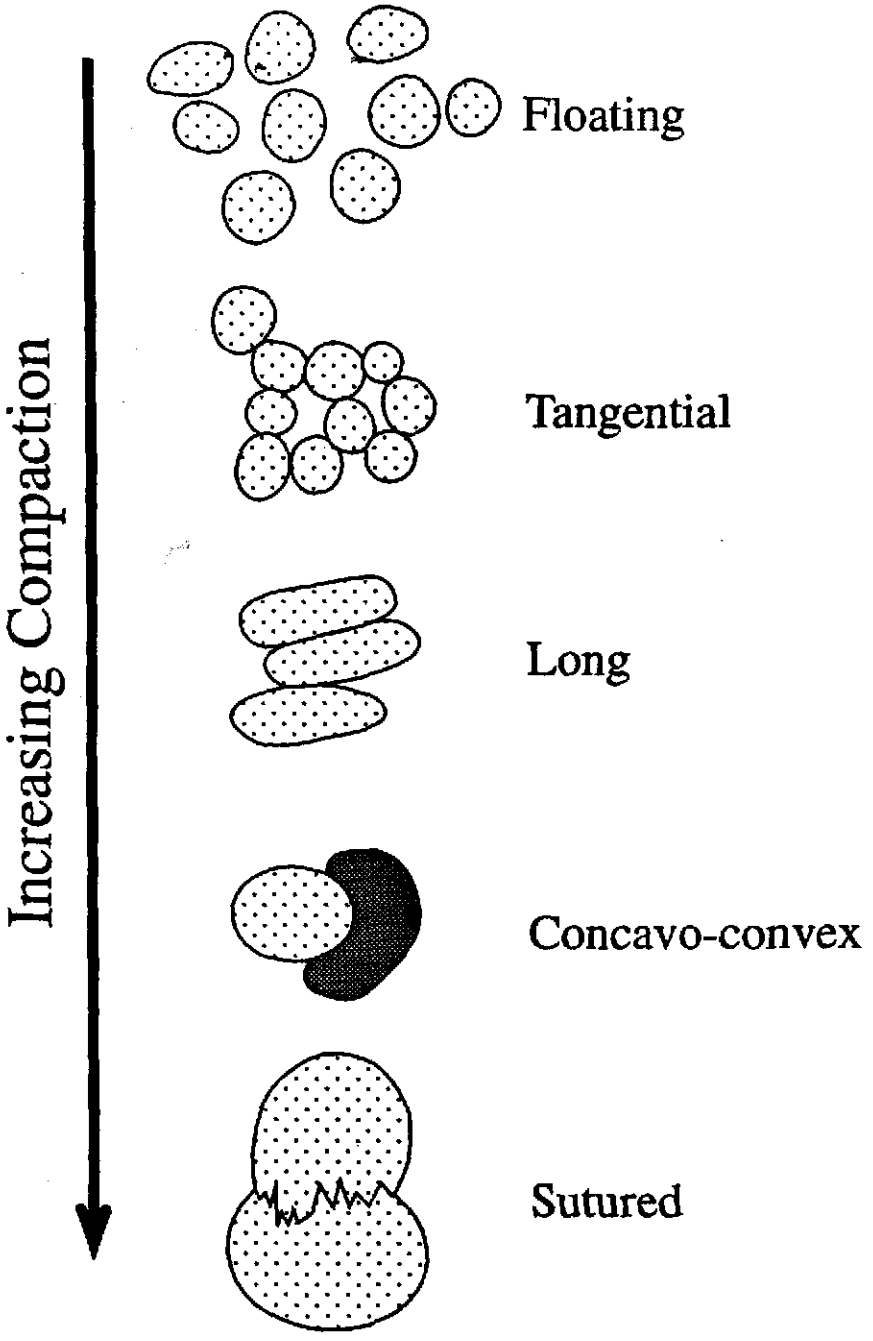

Figure 18. Cartoon presenting relative grain-to-grain contact states as a function of increasing compaction (from Mozley, 1997).

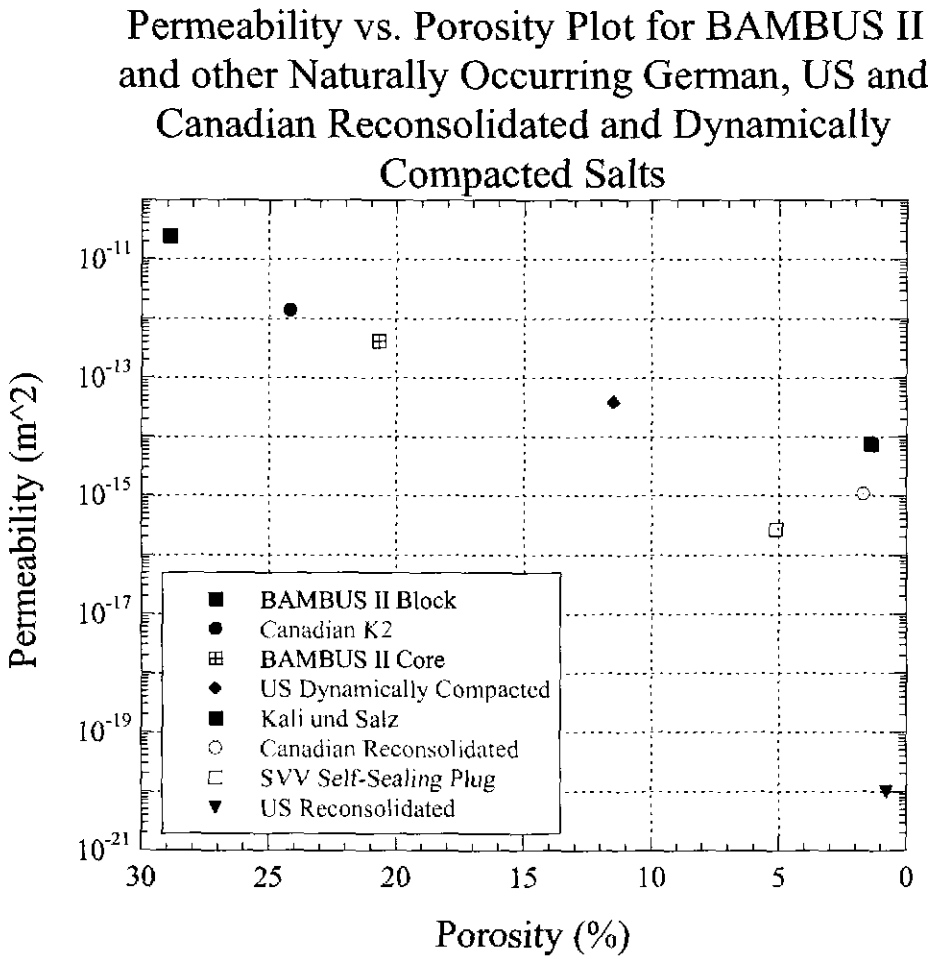

Figure 19. Plot showing the relationship between mean, laboratory measured permeability and porosity values observed in US, German and Canadian reconsolidated and dynamically compacted salt samples. Analysis was performed at Sandia National Laboratory, Albuquerque and Carlsbad, NM, USA.

Porosity standard deviation percentages for these three samples are rather large, and are most likely explained by addressing the textural issue. These samples are poor to very poorly sorted with large voids juxtaposing large halite and anhydrite grains. Measured porosities for the BAMBUS II Block range between 7.8% and 42.1%. Canadian K2 porosities range between 17.7% and 38.7%. As for the BAMBUS II Core samples, measured porosities fall between 17.1% and 25.1%.

The US Dynamically Compacted (WIPP Mine Run; Figures 9 and 10) samples reveal a marked increase in the compaction state as compared to the BAMBUS II and Canadian K2 samples. The measured mean permeability of these samples is 3.85e-14 m^2 and the mean porosity was determined to be 11.5% (Table 1). Although sutured contacts do not appear to be prevalent, concavo-convex and long grain contacts are ubiquitous. Pores are much smaller and more isolated than those found in the higher permeability and porosity samples.

Future Work

Gathering basic data for various crushed salt samples is nearing completion. A more in depth analysis will be compiled for the BAMBUS II consortium and its final report. The BAMBUS II group has two more meetings before the project is completed (approximately June 2003). The consortium will meet in Peine, Germany in September 2002 and plans to meet in Carlsbad NM in February 2003, for the last meeting before the final report is due.

References

Bechthold, W. 2001. Backfilling and sealing of underground repositories for radioactive waste in salt, Phase II (BAMBUS Project): First Annual Scientific Technical Report, EC-5th EURATOM Framework Program, contract no. FIKW-CT-2000.

Goggin, D.J., R.L. Thrasher, and L.W. Lake. 1988 A theoretical and experimental analysis of minipermeameter response including gas slippage and high velocity flow effects: In Situ, v. 12, n. 1-2, p. 79-116.

Mozley, P.S. 1997 The elements of sedimentary petrography: Chapter 4 – Diagenetic minerals and textures; graduate studies class notes, Department of Earth and Environmental Science, NMIMT, Socorro, NM.

Tidwell, V.C. and J.L Wilson. 1997 Laboratory method for investigating permeability upscaling: Water Resources Research, v. 33, n. 7, p. 1607-1616.

Table 1: Permeability and porosity measurements of US, German and Canadian reconsolidated and dynamically compacted salts.

Salt Sample	Mean Permeability (m^2)	Number of Measurements	St. Dev. (m^2)	Mean Porosity (%)	Number of Measurements	St. Dev. (%)	Mineralogy
BAMBUS II Block	2.54E-11	7	1.39E-11	28.9	5	13.5	Halite, Anhydrite, Fe, Zn
Canadian K2	1.38E-12	7	1.08E-12	24.2	5	8.4	Halite, Mg and Ca rich Aluminosilicates (clays)
BAMBUS II Core	4.17E-13	2	5.59E-14	20.7	5	3.3	Halite, Anhydrite, B, Zn
US Dynamically Compacted*	3.85E-14	4	1.11E-14	11.5	5	0.8	Halite, Quartz, Mg
Kali und Salz	7.60E-15	2	5.37E-15	1.4	5	1.3	Halite, Sylvite, Silica, Anhydrite
Canadian Reconsolidated	1.08E-15	2	9.19E-16	1.7	4	2.5	Halite
SVV Self-Sealing Plug	2.69E-16	1	N/A	5.1	5	1.7	Magnesium Sulfate, Halite, Anhydrite, Sylvite
US Reconsolidated*	1.00E-20	1	N/A	0.8	5	1.1	Halite, Quartz, Mg

* WIPP Mine Run Salt

Data presented in this table is recorded in the following sources:

1.) Laboratory notebook ALOHA II: Bulkhead Drift.
2.) German, US and Canadian Reconsolidated and Dynamically Compacted Salt Investigation: A Correlative Analysis with BAMBUS II; Sandia National Laboratories in house progress presentation, July, 2001.

5.3 Observational Studies of Halite Salt Cores Extracted from A Disturbed Rock Zone/Excavation Damage Zone At the Waste Isolation Pilot Plant[1]

Charles R. Bryan, Dennis W. Powers, D. Michael Chapin, and Francis D. Hansen
Sandia National Laboratories, MS 1395
4100 National Parks Highway
Carlsbad, NM 88220 USA

This paper summarizes and updates observations of features of WIPP cores associated with the disturbed rock zone. A special workshop was conducted at the North American Rock Mechanics Symposium, which was held in Toronto, Ontario Canada. Unfortunately, nobody from Sandia was authorized to attend the workshop.

[1] This work is covered by WBS #1.3.5.4.4.1

Observational Studies of Halite Salt Cores Extracted From a Disturbed Rock Zone/Excavation Damage Zone at the Waste Isolation Pilot Plant

Charles R. Bryan*, Dennis W. Powers†, D. Michael Chapin*, and Francis D. Hansen*

*Sandia National Laboratories, Carlsbad, NM

†140 Hemley Road, Anthony, TX 79821

ABSTRACT: The disturbed rock zone (DRZ) surrounding underground openings in salt provides a path of increased permeability, which could permit fluids to bypass seals or closure systems. Waste Isolation Pilot Plant performance assessment calculations include characteristics and parameters of the DRZ that influence brine flux into and gas flow out of the disposal room and other important repository processes. Quantification of spatial and temporal characteristics plays a vital role in verification and validation of calculational and predictive methodologies. This paper presents petrophysical evidence obtained from laboratory observations of core retrieved from the underground. Fracture widths and orientations determine DRZ porosity and permeability, and were measured on oriented petrographic thin sections. DRZ properties determined by fracture analysis are consistent with measured borehole sonic velocity results. Atomic defect densities and distributions in salt grains provide signatures of deformational processes, and were evaluated by scanning electron microscopy (SEM) and digital image analysis of etched cleavage fragments. Dislocation densities do not vary significantly with depth into the DRZ. SEM evaluation of sample mineralogy indicates that brine evaporation and mineral precipitation are not important processes for sealing fractures in the DRZ. This work and related studies, when completed, will provide a damage profile for model validation.

1. INTRODUCTION

Several laboratory approaches have been used to evaluate damage in rock salt. In this paper, we discuss the use of observational studies of core samples to characterize the damage zone, or disturbed rock zone (DRZ), surrounding excavations at the Waste Isolation Pilot Plant (WIPP). Properties of the damage zone have significant consequences in terms of performance assessment and operation of the WIPP, and are relevant to cavern storage research programs and to several German waste isolation programs, which engage in complementary research to characterize and model salt damage evolution. During the waste disposal (operational) period, rock mechanics research continues in the WIPP underground, in the laboratory, and in model development. Rock mechanics research played a fundamental role in regulatory compliance certification by the EPA and opening of WIPP, a milestone of national and international interest.

Disposal room excavation creates stress states that induce fracture. The disturbance is manifested by dilation of formerly competent rock, altering its intact properties. The DRZ enhances permeability in proximal rock and evolves spatially and temporally. Creation, evolution and engineering properties of the DRZ influence nuclear waste repository performance during operations and after closure. Characteristics of the DRZ are particularly important to the WIPP performance assessment conceptual model. The WIPP project supports research of the disturbed zone through mechanical laboratory experiments, *in situ* permeability testing, petrofabric observations, and modeling. The research goal is to provide a predictive model capable of delineating DRZ evolution and ascribing permeability parameters.

Here, we present the results of microstructural and mineralogical analysis of core samples retrieved from damage zones at the WIPP and at the Asse Mine, in Germany. Sample mineralogy was examined to evaluate the effect of evaporation-driven mineral precipitation on fracture permeability in the proximal DRZ. Fracture analysis was performed to evaluate porosity and permeability, and atomic dislocation analysis, to evaluate deformational processes in the salt.

2. PREVIOUS RESULTS

Over the life of the WIPP project, laboratory, field, and modeling studies have examined the mechanics

and characteristics of DRZ development. Gas and brine tests have quantified permeability around many horizontal openings at WIPP [1, 2]. Other techniques, such as visual observations [3,4], ground-penetrating radar [5], and sonic velocity methods [6,7,8], have also been applied to characterize the conditions of rock around the WIPP openings. Recently, Beauheim & Roberts [9] compiled hydrologic profiles surrounding circular and rectangular WIPP underground openings based on age and position. Similar testing of damaged salt around openings is pursued in German research programs [e.g., 10]. In addition, field permeability testing was conducted in the waste-handling shaft [11] and the air-intake shaft [12] and around small-scale seals [13]. Laboratory testing of salt cores has provided significant insight into DRZ development [14, 15]. Van Sambeek et al. [16] characterized dilatancy as a function of stress invariants for a large number of rock salt laboratory tests on WIPP salt, as well as salt from the Avery Island salt dome. Their analyses were consistent with other international work at that time [17, 18] which clearly demonstrated dilatancy under conditions of low confining stress and modest-to-high deviatoric stress. Development of a constitutive model for the compressibility/dilatancy boundary has been advanced by a number of workers, most notably Cristescu & Hunsche [19]. Recent concepts and applications of dilatancy criteria for salt have been put forward by RESPEC personnel [20], following several years of development work by Chan and co-workers [e.g., 21].

3. METHODS

Against the backdrop of extensive field measurements, laboratory tests and model developments, little observational evidence has been forthcoming to provide a tactile understanding of the damaged salt itself. To address this vacancy in the holistic picture of the salt DRZ, a plan was implemented to study basic characteristics of salt cores. Execution of the plan included microstructural analysis to characterize fractures and dislocation densities in the core, and mineralogical analysis to evaluate the effect of evaporation-driven mineral precipitation on fracture permeability in the proximal DRZ.

3.1. Field Coring

WIPP salt cores used in this study were 100 mm in diameter and were recovered from two borehole arrays, each comprising nine or twelve parallel horizontal boreholes spaced on 1 m grid patterns. The boreholes also provided access for *in situ* sonic velocity measurements [7,8]. Cores from only two of the 21 boreholes were examined - one from each borehole array (Figure 1). The first, QGU-14, was taken from the wall of a 13-year-old, 4-m-high by 7-m-wide corridor. The borehole was located at the vertical midpoint of the wall, in a relatively pure halite layer approximately 1 m thick. More clay-rich layers occur above and below the sampled unit. The second core, QGU-36, was from a borehole near the corner of a nearby 4-m-high by 10-m-wide alcove of the same age. The borehole was drilled at an angle of ~50° relative to the face, in the same halite layer as QGU-14. Both cores were discontinuous across open fractures near the face. Beyond the first 50 cm, intact core was obtained, though it was thereafter purposely broken to fit storage boxes. Core fragments were wrapped in cellophane and placed in heat-sealed plastic bags immediately upon retrieval to prevent moisture loss.

In addition to the WIPP salt cores, two 50-mm diameter cores from an 80-year-old salt drift in the Asse research mine in Germany were examined. Both were taken vertically from the floor of a drift at the 700-m level. One core (designated DJ) was taken from a segment of the drift that had been lined with steel tubing 60 years ago and the other (HD) is from the adjacent, unlined segment of the drift. Six samples from each Asse borehole were provided by Klaus Wieczorek [e.g., 10]. The Asse core samples were more pure halite than the WIPP cores, and contained less moisture. Most of the Asse core samples exhibited significant flow foliation.

3.2. Petrographic and laboratory methods

Core specimens were sliced lengthwise into quarters using an extremely precise diamond wire saw (0.3 mm blade) to prevent introduction of damage. Quartered pieces were impregnated with fluorescent dye, ground flat, mounted on oversize glass plates, and then cut and polished as oversized thick (2-3 mm) sections. Oriented sections were prepared for the

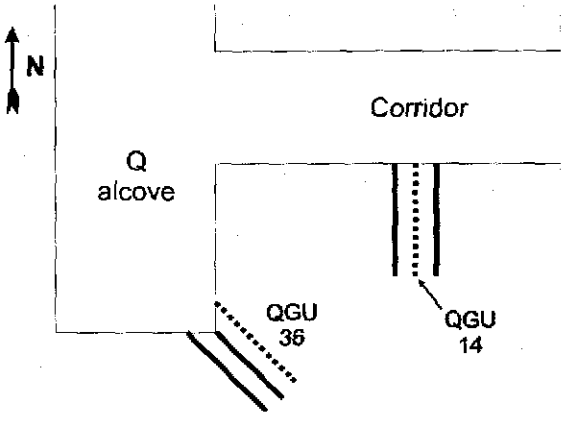

Figure 1. Locations of WIPP boreholes sampled for this study.

first one meter of core and at one meter intervals along the length of the relatively "clean," 7-m long, horizontal salt cores. Measurements of fracture aperture and spacing were taken along the centerline of each section (parallel to the core axis), which would intersect fractures oriented parallel to the opening axis and perpendicular to the core hole. Measurements were taken at 200X using an optical microscope with a micrometer eyepiece. Fracture apertures and the intersection of the fracture with the centerline, used to calculate fracture porosity, were measured with an accuracy and precision of 2.5 μm.

Dislocation density was determined by etch-pit techniques. One quarter core was disaggregated, and individual grains were isolated and cleaved. The cleavage chips were etched with a saturated solution of $PbCl_2$ in methanol and rinsed in butanol. Free dislocation emergent sites preferentially etch owing to strain energy in the distorted lattice. The cleavage chips were sputter coated using an Au-Pd target, and etch pits were imaged on a scanning electron microscope (SEM). The defects were counted using Image-Pro, a digital image processing and analysis package.

Since Salado formation brines are compositionally distinct from the salt (being relatively enriched in Mg, K, and S), sample mineralogy might provide evidence for brine evaporation and salt precipitation, potentially coating or sealing fractures within the damaged zone and modifying the porosity and permeability. Bulk sample mineralogy was determined by dissolution and chemical analysis of the third quarter of each core sample at each borehole depth location. Polished and coated sections were examined by SEM for evidence of mineral precipitation or overgrowth textures along fractures.

The final quarter of each sample was used to determine the moisture content by weight loss at 110 °C. Samples were not disaggregated prior to analysis, as the desire was to measure the accessible brine within the fractured salt, not the total water content, which would include fluid inclusions and hydrous minerals.

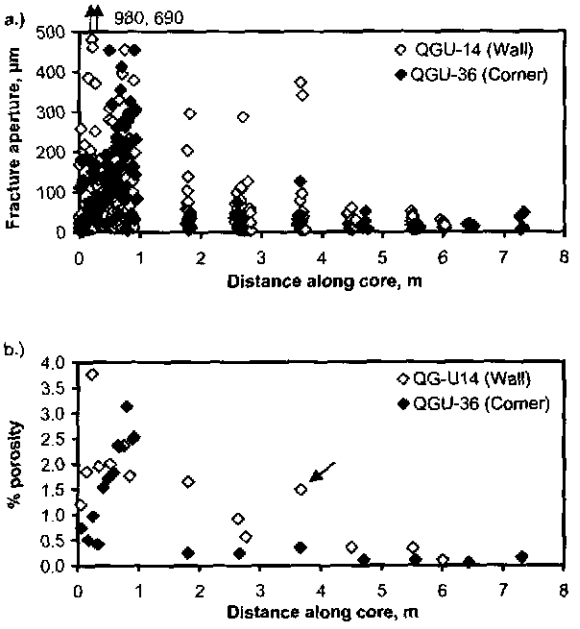

Figure 2. Measured fracture apertures (a) and fracture porosity (b) in salt cores extracted from the WIPP DRZ adjacent to a 13-year-old excavation. Coring-induced damage was evident in the sample from 3.7 m in QGU-14 (arrow).

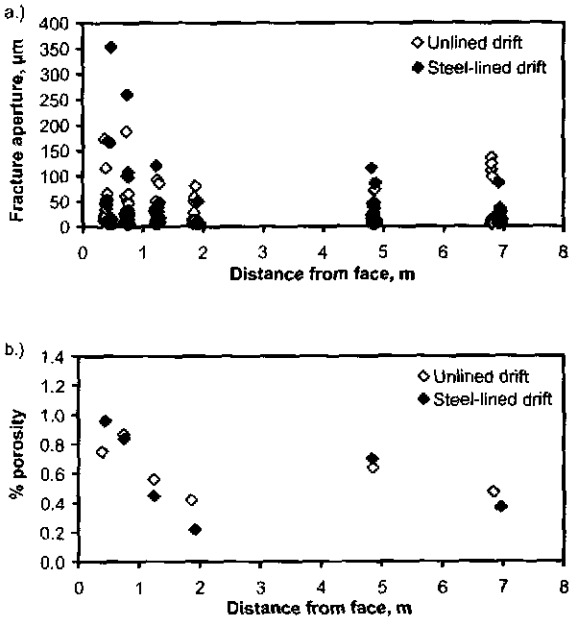

Figure 3. Measured fracture apertures (a) and fracture porosity (b) in salt cores extracted from the DRZ adjacent to an 80-year-old excavation at Asse.

4. RESULTS

4.1. Fractures

Results of the fracture analysis of the WIPP and Asse salt cores are presented in Figures 2 and 3. Several trends are evident in the WIPP DRZ cores. Fracture density does not change significantly or consistently throughout either core; measured core specimens contained 1.7±0.5 fractures/cm in QGU-14, and 0.7±0.2 fractures/cm in QGU-36. However, the maximum fracture aperture and the aperture variability decrease markedly from the open face to the end of the core. It should be remembered that, near the face, centimeter-sized fractures sometimes separated the core specimens, and these fractures are not included in the figure. The strong trends in frac-

ture aperture with depth suggest that most of the fractures were not induced during the coring process, but a few samples (most notably the fragment at 3.7 m in core QGU-14) did show evidence of local coring damage.

The German salt cores have nearly similar fracture densities, of 2.0±0.5 and 1.6±0.5 fractures/cm, for the core from the lined and unlined drift, respectively. Average and maximum aperture widths are slightly larger near the excavation face, and overall, there is a modest decrease with depth. Fractures from the lined and unlined segments of the drift are not appreciably different. The deepest samples exhibit a bimodality in fracture aperture, which might suggest coring-induced damage.

In WIPP core QGU-36 and to a lesser degree in QGU-14, the fracture porosity increased to a depth of 1 m and then decreased consistently with the increasing depth. In QGU-14, the porosity drops to <0.4% in about 3 meters, but significant fracture porosity is present to the end of the core. In QGU-36, fracture porosity drops rapidly to a value of <0.25 % in less than 2 meters (considerably less than 2 meters from the face, due to the fact that the hole was drilled at a 50° angle), and to about 0.1% by the end of the core. In both Asse cores, the porosity is greatest near the face, but is relatively constant (0.5%) beyond 1 m depth.

The apparent increase in fracture porosity from the face to a depth of about 1 m in the WIPP cores may be an artifact of the sampling method. Core samples close to the face tended to be short and fragmented, and the apertures of the fractures bounding them could not be quantified, and are not included in the porosity calculation.

In the first general description of cores from the Q Room Alcove, Powers [22] noted an apparent foliation or elongation of halite crystals in a plane parallel to the rib face. The strain features in this plane [23] are observable macroscopically to depths between about 0.85–1.05 meters (perpendicular to the rib face). Open fractures are generally very close to the rib face. Grains are elongated because fractures (or stepped cleavages) subdivide coarse, subequant halite grains; there is no observable flow, and the feature is not true foliation. In the QGU-36 core, core breaks near the rib face tend to parallel the rib face, and the angle to the core axis increases with depth (Figure 4). Beyond the 0.70–1.05 meters depth, core breaks are generally perpendicular to the core axis, as is observed with cores taken perpendicular to the rib face (e.g., QGU-14). Crystal cleavage patterns along the shallow core breaks tend to reflect crystal size and orientation. Larger cleavage faces occur on coarser crystals whereas small stepped cleavages across smaller grains mimic the angle of the rib face to the core axis. Cores taken from the actual corner show shallow breaks with fitted convex and concave surfaces that likely reflect the stress regime around the corner. The change is fracture orientation observed in core QGU 36 is consistent with the sonic velocity data [8]. This is the first observational evidence at the WIPP of fracture orientations changing to maintain a fixed orientation with respect to the local stress field. These data strongly support the conclusion [4] that the fractures observed in the laboratory core studies are not induced by coring or sample preparation, because induced fractures would be expected to lie perpendicular to the core axis.

4.2. Dislocation density

Dislocation densities were measured on cleavage chips from three separate salt grains extracted from disaggregated salt core at 10 locations along WIPP core QGU-14, and at the 6 locations represented by each of the Asse cores. Typical dislocation etch-pit densities are shown in Figure 5a and 5b. Figures 5c and 5d are SEM micrographs of the substructures, which display both free dislocations and subgrain boundaries.

Free dislocation density as a function of depth is plotted in Figure 6. In terms of dislocation measurements of this type, these results are uniform. These initial results for the WIPP salt are unexpected, based on previous results that clearly quantified decreased dislocation density with depth away from Room D at WIPP. In addition, dislocation densities in the current study average $8.7 \cdot 10^7$ dislocations/cm^2, about twice the values measured previously by Hansen.

Results for the German boreholes were similar be-

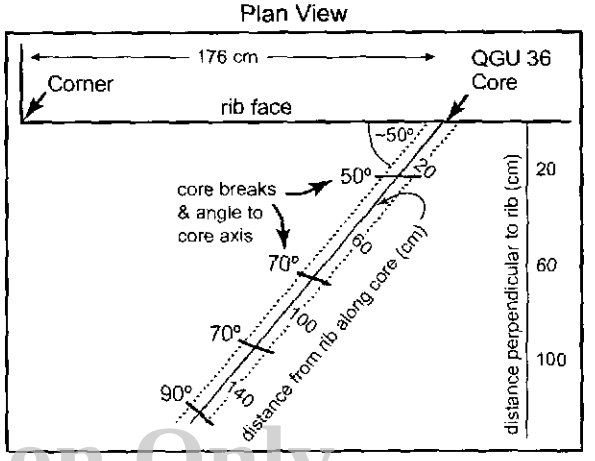

Figure 4. Fracture orientations in core QGU-36 change with depth, reflecting the change in the local stress field.

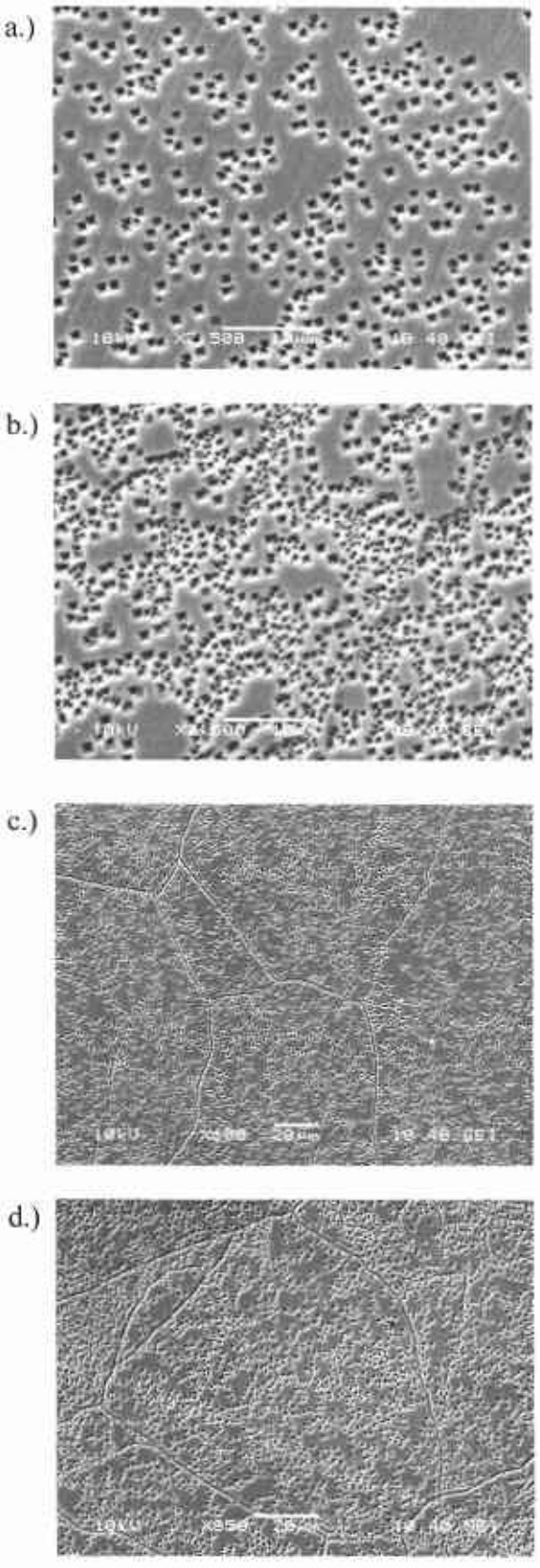

Figure 5. Dislocations in WIPP and German salt. a) relatively low dislocation density at a distance of 6 meters from the face, WIPP hole QGU14. b) a sample showing a higher density of dislocations, at a distance of 3.7 meters from the face, same borehole. c) subgrain boundaries, 6 meters from the face, WIPP hole QGU14. d) subgrain boundaries, 1.25 meters from the face, German borehole DJ, from the lined portion of the drift.

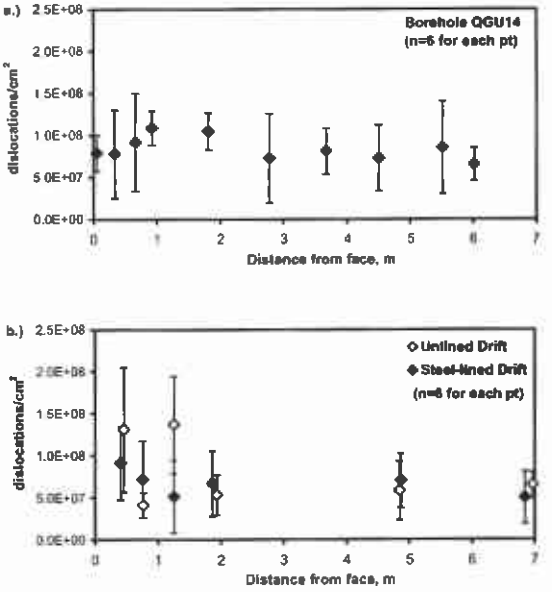

Figure 6. Dislocation densities in a) WIPP and b) German DRZ salt cores. No systematic variations in dislocation density (a measure of strain) with depth are apparent.

tween the two sets of samples. As displayed in Figure 6, there is no significant difference between the two holes. Dislocation densities decrease slightly with depth, and overall densities are slightly lower than for the WIPP QGU-14 core, and agree more closely with the Room D results determined previously by Hansen (unpublished data).

4.3. Mineralogy

As the Salado brines are enriched in Mg, Ca, K, and S relative to the Salado salt, if brine evaporation and precipitation of brine minerals (including langbeinite, bischofite, and polyhalite) occurs in the DRZ, it will change the composition of the salt matrix. Bulk samples 5–10 cm in length were analyzed at 15 locations along the WIPP core. Although the salt along the borehole is relatively pure, containing less than 5% impurities of Mg, Ca, K, and S evaporate minerals, the compositional variations in the bulk salt are sufficient to obscure any effect of brine precipitation, and no consistent chemical trends were observed with depth in the borehole. Core thick sections were also examined by scanning electron microscope for evidence of brine mineral precipitation sealing fractures, and none was observed. Brine mineral efflorescences occur on freshly excavated surfaces in the WIPP, but apparently evaporation is confined to the open surface, and is not an important process in the DRZ.

Although WIPP salt contains 1-3% brine as fluid inclusions, the accessible moisture content of the WIPP core samples examined, from borehole QGU-

14, was extremely low (maximum of 0.03%) and did not vary systematically with depth. Borehole QGU-14 is in a relatively pure halite layer, in the center of the excavated face. Other cores, not yet examined, are from "argillaceous" zones below and above the sampled unit, and field observations of borehole moisture suggest that they contain more brine. Accessible moisture contents of the German salt core samples were even lower (maximum value of 0.01%) and constant with depth.

5. DISCUSSION

For the two WIPP cores examined, the DRZ as determined by core fracture data is broadly consistent with the results determined by borehole acoustic wave velocity measurements [7,8], and is wider at the center-wall location (QGU-14) than at the room-corner location (QGU-36). Sonic velocity values along borehole QGU-14 increase to a constant value at 2 m depth, but sonic velocity techniques are not sensitive to fracture apertures below ~50 μm. Fracture results plotted in Figure 2 show larger fractures occupy the region near the face and decrease to apertures below 50 μm beyond about 3-m depth. When aperture void space is calculated as porosity (Figure 2), it can be seen that the damage zone drops below 1% porosity beyond 2 m depth, not withstanding the value at 3.7 m depth, which we believe has additional coring damage.

Fracture data for QGU-36 defines a narrower damage zone. Core samples from depths of greater than 1 m have less than 0.3% fracture porosity. These results are consistent with the borehole acoustic wave velocity results [8], which indicate a narrower DRZ in this core relative to the QGU-14 core.

Both WIPP cores exhibit significant fracture porosity (0.10–0.35%) even at the distal end of the core. While it is clear that many of the observed fractures cannot be core damage (for example, the strongly oriented fractures at the near-face end of core QGU-36), it is possible that these deeper fractures are artifacts of sample collection, thus explaining why the sonic velocity data does not show a DRZ extending deeper than a few meters into the wall. However, there is widespread evidence of halite re-precipitation on fracture walls over the entire length of the cores (Figure 7). We interpret this to be the product of pressure solution along undilated grain boundaries and precipitation on free surfaces via brine movement into the intersecting fractures (Figure 8). Apparently, the modest amount of grain-boundary brine film is sufficient for epitaxial growth. Widespread evidence of halite precipitation along fractures indicates that at least the majority of

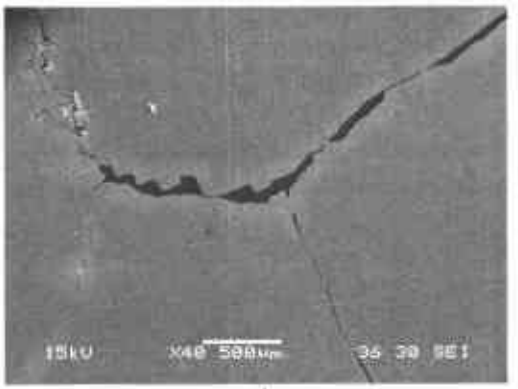

a.)

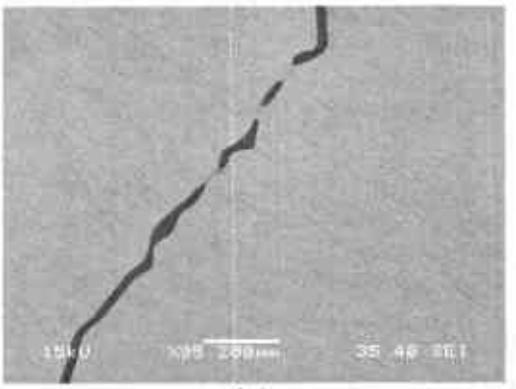

b.)

Figure 7. Evidence of halite overgrowth by evaporation and epitaxial growth along fractures in the WIPP salt cores. a) euhedral salt crystals lining; b) salt "bridges" spanning a fracture, at a depth of 6 m into the DRZ.

the fractures observed are *not* the result of core damage, as pressure solution and re-precipitation could only have occurred before the core was extracted from the borehole.

Salt re-precipitation on fracture walls serves to reduce the fracture aperture, often completely bridging the fracture, as shown in Figure 7. When considered in the two dimensions of the fracture plane, these bridges are of limited extent, and do not prevent flow completely—during vacuum impregnation, the epoxy penetrates the entire length of the fracture. However, they do serve to reduce the effective length of the fractures, and thus may make them harder to detect by sonic velocity measurements.

The Asse cores have a measured porosity below 1% throughout. The German researchers through personal communications (Wieczorek) have provided permeability measurements made in the lined and unlined sections of the Asse drift. They measured low permeability below the lined drift (10^{-19} m^2) and permeability ranging from 10^{-15} to 10^{-18} m^2 as a function of depth below the unlined drift. However, the damage profiles for the Asse salt, as determined from these core studies, are identical. To further

complicate interpretation of the damage/permeability function, laboratory tests exhibit several orders of magnitude increase in permeability for volumetric strains less than 1%. Reconciliation of these various measurements is essential in development of a damage/permeability function for the constitutive model.

The fracture data are consistent with the acoustic wave velocity measurement data presented previously [7], and in the companion paper [8]. The acoustic velocity data delimit a well-defined DRZ extending 2-3 meters from the face. The core studies presented here show that this corresponds to a drop in the measured porosity and to a drop in the average fracture aperture to below 50 μm.

Cores extracted from the corner of the Q Room Alcove exhibit fracture orientations that follow the stress field. Fractures in core taken adjacent to the corner (1.4 m from the corner) parallel the face near the opening and become progressively more tangential to the corner with depth. Core from the corner exhibits cuplike fracture near the face, paralleling the stress field as it bends around the corner. This is the first field-scale observational evidence of fracture orientations changing to maintain a fixed orientation with respect the local stress field.

The defect analysis results for the WIPP and German cores are somewhat conflicting with earlier results, but are consistent with each other. Both WIPP and Asse dislocation densities suggest that there is no significant variation in plastic strain with depth into the DRZ; possibly, strain near the face is accommodated by brittle deformation.

6. CONCLUDING REMARKS

These studies illustrate the usefulness of observational studies with respect to field and laboratory test data interpretation. SEM mineralogical analysis of salt cores indicates that evaporation of formation brines and the resulting precipitation of brine minerals in fractures is not a significant process in the DRZ, even directly adjacent to the face. Acoustic wave velocity measurements correlate well with the fracture porosity profile determined from the cores. However, permeability determined in field tests is markedly lower than permeability calculated on laboratory samples, for similar architecture of fractures. Difficulties in scaling fracture connectivity may make application of salt damage/permeability functions derived in laboratory core experiments problematic.

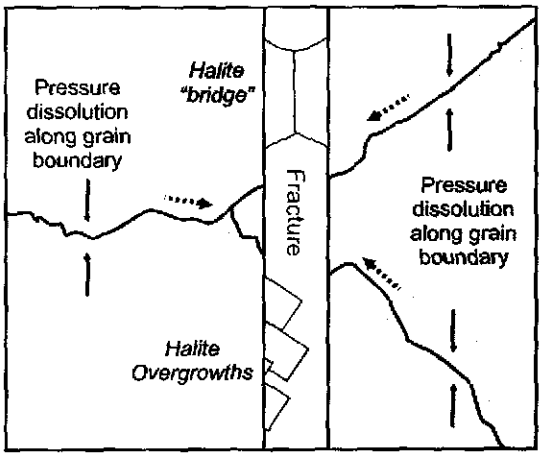

Figure 8. Pressure solution-reprecipitation model for growth of halite bridges and overgrowths on fracture surfaces.

Sandia is a multiprogram laboratory operated by Sandia Corporation, a Lockheed Martin Company, for the United States Department of Energy under Contract DE-AC04-94AL85000.

7. REFERENCES

1 Stormont, J.C., E.W. Peterson, and P.L. Lagus. 1987. Summary of and observations about WIPP facility horizon flow measurements through 1986. SAND87-0176. Albuquerque, NM: Sandia National Laboratories.

2 Stormont, J.C. 1990. Summary of 1988 WIPP facility horizon gas flow measurements. SAND89-2497. Albuquerque, NM: Sandia National Laboratories.

3 Borns, D.J. and J.C. Stormont. 1988. An interim report on excavation effect studies at the Waste Isolation Pilot Plant: The delineation of the disturbed rock zone, SAND87-1375. Albuquerque, NM: Sandia National Laboratories.

4 Bryan, C.R., F.D. Hansen, D.M. Chapin, and A.C. Snider. 2001. Characteristics of the disturbed rock zone in salt at the Waste Isolation Pilot Plant. In Proceedings of the 38th US Symposium on Rock Mechanics, Vol. 1, Washington, DC. 7-10 July 2001, eds. D. Elsworth et al, 511-516. Lisse: Balkema.

5 Kannenberg, M.K. and W.M. Roggenthen. 1997. Ground-penetrating radar studies of the Waste Isolation Pilot Plant (WIPP) near Carlsbad, New Mexico, Environ. Eng. Geosci. 3: 349-358.

6 Holcomb, D.J. 1988. Cross-hole measurements of velocity and attenuation to detect a disturbed zone in salt at the Waste Isolation Pilot Plant. In Proceedings of the 29th US Symposium on Rock Mechanics, Minneapolis, MN, 633-640. Brookfield, VT: Balkema.

7 Holcomb, D.J. and R. D. Hardy. 2001. Assessing the disturbed rock zone (DRZ) at the Waste Isolation Pilot Plant (WIPP) in salt using ultrasonic waves. In Proceedings of the 38th US Symposium on Rock Mechanics, Washington, DC. 7-10 July 2001, Vol. 1, eds D. Elsworth et al, 489-496. Lisse: Balkema.

8 Holcomb, D.J., T. MacDonald, and R.D. Hardy. In press. Using ultrasonic waves to assess the disturbed rock zone (DRZ) in an alcove corner excavated in salt at the WIPP (Waste Isolation Pilot Plant). North American Rock Mechanics Society Meeting, NARMS-TAC 2002, Toronto, Canada, 7-10 July 2002.

9 Beauheim, R.L. and R.M. Roberts. 2002. Hydrology and hydraulic properties of a bedded evaporite formation. J. Hydrol. 259; 66-88.

10 Wieczorek, K. and U. Zimmer. 1999. Hydraulic behavior of the excavation disturbed zone around openings in rock salt. In Proceedings of the Seventh International Conference on Radioactive Waste Management and Environmental Remediation, ICEM '99, 26-30 September, Nagoya, Japan. New York: American Society of Mechanical Engineers (CD-ROM).

11 Saulnier, G.J. and J.D. Avis. 1988. Interpretation of hydraulic tests conducted in the waste-handling shaft at the Waste Islolation Pilot Plant (WIPP) site. SAND88-7001. Albuquerque, NM: Sandia National Laboratories.

12 Dale, T. and L.D. Hurtado. 1998. WIPP air-intake shaft disturbed-zone study. In 4th International Conference on the Mechanical Behavior of Salt, Montreal, Canada, June 17-18, 1996, eds. M. Aubertin and H.R. Hardy, Jr., 525-535. Clausthal-Zellerfeld, Germany: Trans Tech Publications.

13 Knowles, M.K. and. C.J. Howard. 1996. Field and laboratory testing of seal materials proposed for the Waste Isolation Pilot Plant. In Waste Management '96 Proceedings, Tucson, AZ. Tucson: Laser Optics (CD-ROM).

14 Rath, J.S., T.W. Pfeifle, and U. Hunsche. 2000. RATDAMPER—a numerical model for coupling mechanical and hydrological properties within the disturbed rock zone at the Waste Isolation Pilot Plant. In Fourth North American Rock Mechanics Symposium, NARMS 2000, Seattle, Washington, 31 July-3 August, eds. J Girard et al. Rotterdam: Balkema.

15 Hunsche, U. and O. Schulze. 2000. Measurement and calculation of the evolution of dilatancy and permeability in rock salt. In Proc. 3. Workshop, Kluft-Aquifere: Gekoppelte Prozesse in Geosystemen, Hannover, Nov., 2000, eds. O. Kolditz et al., Bericht Nr. 60/2000, 107-113. Inst. f. Strömungsmechanik u. Elektr. Rechnen im Bauwesen der Universität Hannover.

16 Van Sambeek, L.L., J.L. Ratigan, and F.D. Hansen. 1993. Dilatancy of rock salt in laboratory tests. Int. J. Rock Mech. Min. Sci. Geomech. Abstr. 30: 735-738.

17 Hunsche, U.E. 1993. Failure behaviour of rock salt around underground cavities. In 7th Symposium on Salt, Kyoto, Japan, 6-9 April, 1992, eds H. Kakihana et al., 59-65. New York: Elsevier.

18 Spiers, C.J., C.J. Peach, R.H. Brezesowsky, P.M.T.M. Schutjens, J.L. Leizenberg, and H.J. Zwart. 1988. Long-term rheological and transport properties of dry and wet salt rocks, EUR 11848, prepared for Commission of the European Communities by the University of Utrecht, Utrecht, The Netherlands. Luxembourg: Publications of the European Communities.

19 Cristescu, N.D. and U.E. Hunsche. 1998. Time effects in rock mechanics. New York: John Wiley & Sons.

20 National Energy Technology Laboratory (NETL). 2000. Advanced gas storage concepts: technology for the future. US Department of Energy. www.netl.doe.gov (CD-ROM order source).

21 Chan, K.S., S.R. Bodner, A.F. Fossum, and. D.E. Munson. 1997. A damage mechanics treatment of creep failure in rock salt. Int. J. Damage Mech., 6: 121-152.

22 Powers, D.W. 2001a. Geology of cores from Q room alcove for the DRZ Test Program (available as ERMS# 516559). Carlsbad, NM: Sandia WIPP Records Center.

23 Powers, D.W., 2001b, Macroscopic strain features in selected cores from the disturbed rock zone (available as ERMS#518592). Carlsbad, NM: Sandia WIPP Records Center.

[1] This work is covered by WBS #1.3.5.4.4.1

Using Ultrasonic Waves to Assess the Disturbed Rock Zone (DRZ) in an Alcove Corner Excavated in Salt at the WIPP (Waste Isolation Pilot Plant)

David J. Holcomb, Terry MacDonald, Robert D. Hardy
Sandia National Laboratories, Albuquerque, NM, USA

Abstract: Cross-hole and same-hole measurements of compressional wave velocities were used to delineate the Disturbed Rock Zone that had developed around an interior room corner during the 12 years since the room was mined. A complex pattern of damage was observed, corresponding to the complex stress state present around a corner in a material that exhibits both brittle and creep-related damage. The DRZ was observed to extend to shallower depths than previously observed in two-dimensional (2-D) stress states, with almost no damage observed along the axis of the room corner.

1. INTRODUCTION

There is a need to understand the spatial and temporal development of the disturbed rock zone (DRZ) around openings at the Waste Isolation Pilot Plant (WIPP). Possible leakage paths around seals, effects on closure rates and safety issues related to deterioration of the salt mechanical properties are issues affected by the DRZ. An alcove constructed about 12 years ago provided an opportunity to conduct geophysical investigations of the damage developed in the salt for a three-dimensional (3-D) configuration. Specifically, an interior room corner was used to study the damage caused by the complex stress fields existing near the corners of rectangular openings in salt formations. The mature DRZ found in such a location is the macroscopic manifestation of grain-scale and larger cracks that form as a result of the instantaneous shear stress induced around a newly created opening, and as a result of creep-related damage over a period of years. Elastic wave velocity in the salt is a function of the density of cracks, as is the permeability.

As part of a suite of measurements designed to study the hydrological and mechanical properties of the salt in the alcove corner, twelve, 10-cm diameter ultrasonic transducer emplacement holes were drilled in the alcove corner rib to a depth of about 6 meters. The design of the borehole array and the transducer assemblies allows the measurement of elastic wave velocities along vertical and horizontal paths parallel to the walls intersecting at the alcove corner and, within the same hole, at a 45^{O} angle to the rib. Orthogonal paths are necessary to detect the anisotropy of the cracking in the DRZ.

Previous work at the WIPP [1, 2, 3, and 4], delineated the DRZ as a function of depth from the drift wall and as a function of the varying stress-state around the approximately rectangular drift cross section. Using results published by Brodsky [5], changes in velocity can be related to the damage due to microcracking required to produce the observed changes. Holcomb and Hardy discussed the results of measurements conducted in a near-by drift [4], which is geometrically simpler than the current study area because the drift's length results in a plane strain-state around the drift. Cross-hole and same-hole velocity measurements gave a consistent picture of the DRZ around the Q Room Access Drift. The DRZ was well developed at mid-height on the rib, extending in 2 m and possibly as much as 4 meters. Near the back and floor, the DRZ was shallower (1 meter or less) or not detectable. Compressional mode (P) waves in

All work has been performed under the Nuclear Waste Management Program Quality Assurance Test Plan 99-04, *Disturbed Rock Zone Characterization Test Plan.*

Sandia is a multi-program laboratory operated by Sandia Corporation, a Lockheed Martin Company, for the United States Department of Energy under contract DE-AC04-94AL85000.

same-hole measurements are most sensitive to the DRZ because of favorable orientation of particle motion perpendicular to the cracking. Changes in compressional velocity, V_P, as large as 22% were observed for P waves propagating perpendicular to the drift axis at room mid-height. Using results from Brodsky [5, Fig. 4-2], these changes would correspond to the velocity changes observed in salt loaded close to failure in triaxial compression.

Results reported here delineate the DRZ as a function of depth from the alcove corner and as a function of the varying stress-state around a rectangular alcove corner cross-section. The significance of the results lies in the length of time the DRZ has had to develop (approximately 12 years), the geometrical complexity of the alcove corner, which will allow a more rigorous test of models than is possible in simpler geometries, and the hydrological measurements made in conjunction with the velocity and attenuation measurements. Understanding time-dependent changes in damage, and thus permeability, as the DRZ develops is important because these changes strongly affect the sealing of underground openings at the WIPP.

1.1. Approach

Open cracks and loosened grain boundaries decrease elastic moduli and therefore, elastic wave velocities. Elastic wave velocities are most affected by cracks oriented perpendicular to the particle motion induced by the wave. Thus, the physical extent of the disturbed zone can be determined by propagating elastic waves through successive portions of the formation until an undisturbed zone is reached, as indicated by a constant velocity with increasing depth from the rib. In this case, the cracking responsible for the disturbed zone is expected to vary as a function of distance from the walls of the Q Room Alcove and to depend on the position of the measurement path relative to the back, floor and corner.

Measurements were made in holes cored parallel to a line bisecting the corner angle, along horizontal and vertical paths lying in vertical planes parallel to the corner walls. Transducer positions were surveyed to an accuracy of $\pm$ 1 mm, allowing absolute velocity measurements. One set of measurements was completed at approximately 30-cm intervals to a depth of about 6 m, along cross-hole vertical and horizontal paths parallel to the walls of the alcove and same-hole paths, necessarily at 45^{O} angles to the walls. A second set of measurements was repeated in five of the boreholes at approximately 15-cm intervals for the first shallowest 2 m, and at 30-cm intervals for an additional 4 meters.

The cross-hole measurement paths were nominally one-meter long, while the same-hole measurements all had the same fixed path length of 33 centimeters. Figure 1 shows the arrangement and naming scheme for the measurement holes, QGU30, QGU31, ... QGU41. Travel time measurements were made using the technique commonly used for laboratory determinations of sound speed in rock; a sound pulse was applied to the rock at a known time and place and, after traveling through the rock, was received by a transducer at a known distance. The travel time and distance combine to give the average velocity over that path.

1.2. Lithology and Hole Layout

Twelve holes were cored (see Figure 1) to sample the lithologies exposed in the alcove corner and the stress state as it varied near the corner. Two rows of holes, 1 and 3 counting from the top, were in halite, while rows 2 and 4 were in argillaceous salt. Each hole was 10.16 cm (4 inches) in diameter, 6+ m deep and as close to horizontal as possible. Great effort and care was taken by the surveying and drilling crews to align the holes parallel and horizontal, resulting in hole-to-hole separations that varied by less than 10 cm over the 6 m depth, indicating very good control on the starting angle and carefully controlled drilling. Hole locations were chosen that sampled the map units present (labeled halite and argillaceous in Fig. 1), and also the expected variation in damage around the corner.

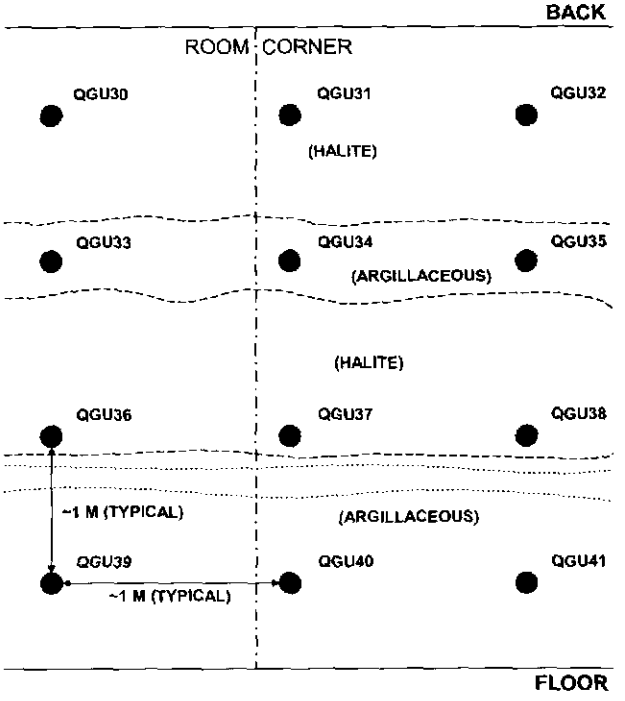

Fig. 1: Layout of holes (filled circles) used for ultrasound measurements.

1.3. Measurement System

Piezoelectric transducers were used as both the transmitter and receivers of the ultrasonic elastic waves. In the current work, only compressional mode transducers were used, although in certain configurations, a shear mode can be generated. A 300 kHz, PZT-5A piezoelectric disk was the basic element; four of these were used, two as transmitters and two as receivers. Each disk was mounted inside of a housing that could be pressed against the side of the 4-inch boreholes using air pressure. Suitably curved faces on the aluminum housing increased the area of contact when the housing was extended by pressurization to, typically, 60 psi. To further, and very substantially, increase the energy transmission across the housing-rock interface, a couplant was extruded between the housing face and the rock. Corn syrup was used for this work; it is inexpensive, cleans up easily and provides good coupling for both compressional and shear elastic waves.

Two transducer housings were coupled together (Figure 2) to form the tool inserted into the borehole. By placing two transducers in one hole; one transducer can be driven as a transmitter while the other acts as a receiver, similar to a technique discussed by Maxwell et al. [6]. In this way, same-hole measurements can be made along paths at a 45° angle to the rib face and orthogonal to the cross-hole measurements. As the orientation of the damage is expected to be anisotropic, it adds information to be able to measure the effects of damage along orthogonal paths. In particular, it is expected that the cracking planes will be preferentially parallel or sub-parallel to the rib, resulting in the largest changes in velocity along paths normal to the rib.

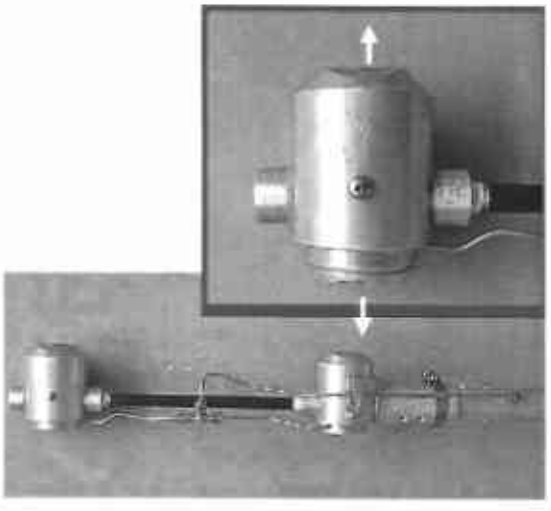

Fig. 2: Transducer assembly showing two air-actuated clamping heads. Enlarged photograph is a close-up of one of the heads with the direction of motion during clamping indicated by arrows.

Once positioned and pressurized, a 100-volt square pulse, with a rise time of about 200 ns, excited the chosen transducer. The resulting wave was detected by the chosen receiver, amplified by 60 dB and recorded on a digital oscilloscope to 16-bit precision, at a sampling rate of 10 or 20 MHz. Each data set, consisting of the recorded driving pulse and received pulse, was transferred to computer storage for later analysis. To enhance signal quality, 100 signals were averaged at each position.

2. DATA ANALYSIS

Calculating the velocity was a several step process involving coordinate determination, corrections for various offsets and choosing the arrival time for the P wave at the receiver. Coordinates were determined by parameterizing the North, East and vertical coordinates (N, E, Z) of the surveyed centerline of each hole as a function of depth into the hole. Three, second order-fits for N, E, and Z, as functions of depth, were determined and found to reproduce the surveyed coordinates within the required precision of $\pm$ 1 mm. For each measurement set, the measured depth of emplacement for the transducer was used in the second-order fits to calculate the coordinates of the transducer in space. Offsets were applied to account for the actual position of the transducer against the wall, instead of the centerline of the hole and for platen delay, the time required for the wave to travel through the transducer body. Knowing the coordinates of the transmitter and receiver, the path length could be calculated. Non-systematic errors are estimated to make the uncertainty in cross-hole path length less than 3 millimeters. Same-hole measurements used the fixed 0.33-m separation of the transducer heads (see Figure 2), eliminating path length as a systematic error.

Determining travel time requires a determination of the difference between the time of the initiating electrical pulse applied to the transmitter and the time of arrival of the P or S wave at the receiver. Pulse time, which is easily determined from the recorded rapidly rising square wave to an accuracy limited only by the typical sample interval of 50 or 100 ns, contributed a negligible amount to uncertainty in velocity. It is much more difficult to fix the arrival time of the wave at the receiver. The waveform is an emergent sinusoid, not a square wave pulse, whose unsharp beginning is additionally obscured by electrical noise in the highly amplified signal. S waves, which travel slower and arrive later than P waves, are

additionally confounded by the coda of the P wave that extends into the S-wave signal.

Although signal quality was improved by signal averaging, the determination of arrival times could still be difficult especially for measurement paths that passed close to the surface where damage was greatest, resulting in high attenuation of the signal. Typically, the first arrival is small in amplitude, making it easy to miss the first cycle or more in a highly attenuated signal. This would result in unacceptable errors in the travel time and velocity. Visual comparison of the signals in a given data set can be used to minimize the risk of missing first arrivals. Low pass filtering was also used on some data sets to equalize the frequency content of the signals, easing comparison of the filtered traces.

An interactive Matlab™ program was used that allows the signals from a given data set to be plotted, and offset so that the arrival times are aligned. When arrival times are correctly chosen, the similarity of the signals is usually obvious. The program allows the arrival times to be adjusted interactively until the signal-to-signal correlation is good. For the measurement paths at some distance from the free surface, the actual arrival time is easily determined, allowing these signals to be used as a guide for choosing the arrival time for the less distinct signals from paths near the free surface. Typically, one clear arrival is used as a reference and all the other signals are adjusted to correlate well with that reference. This builds in a systematic error corresponding to the error in picking the reference signal, but reduces the scatter between measurements, making it much easier to see trends in the velocity with depth. The systematic error is determined by the error in picking the arrival time of the reference, which for the cross-hole P waves is less than 200 ns, a negligible amount. Same-hole P waves are much lower amplitude because of the unfavorable geometry of the transmitter and receiver. As a result, the errors are larger, and the effect more significant due to the shorter path lengths. The systematic error is close to 1% for these paths, but of course, that is a constant error for all measurements. Trends are not obscured as a result.

3. RESULTS AND DISCUSSION

Measurements were made for all cross-hole possibilities, resulting in nine sets of measurements for vertical paths and eight horizontal paths in planes parallel to the corner walls. Twelve same-hole measurement sets were completed. All data plots follow the same format, consisting of a title giving the location data and the wave type, P, and the data plotted as the measured velocity plotted at the depth of the transmitter. A typical title would be QGU31 → QGU30, P for a compressional wave measurement set, with the wave propagating between holes QGU30 and QGU31 (see Figure 3). To ease comparison of various paths, data are plotted in sets corresponding to logical subsets, such as all horizontal paths on the left-hand wall. An icon in each data plot shows the subset being plotted, using filled circles to indicate the source of the data.

3.1. Horizontal Paths

The P wave velocity, V_P, was measured at 30-cm intervals for the eight possible horizontal paths. Figure 3 summarizes measurements made in the left-hand wall with four plots arranged in the same way as the physical arrangement of the holes in the rib. The icon at the right of the plots shows, using filled circles, the eight holes between which the four plotted data sets were measured. Beginning at the top of Figure 3, V_P is plotted as a function of depth for the horizontal path between the top left and top center holes nearest the back (Figure 1), and similarly for the next three hole pairs in descending order down the page and rib wall. Results for the horizontal paths in the right hand wall are shown in an identical arrangement in Figure 4. Overall, the compressional velocity was observed to be 4.5 km/sec $\pm$ 0.1 km/sec for all four levels at depths greater than about 1 m from the rib. A variation of less than $\pm$ 2% indicates several things. First, the surveying and corrections for non-parallelism of the holes has been correctly handled. Even with excellent control on drilling the holes, the runout between any given pair of holes frequently exceeded 10% of hole spacing. If not corrected for, the cross-hole velocities would show a significant trend with depth, and indeed, several errors in the analysis were revealed by such trends. Second, only small velocity differences were observed between the two halite layers and the two argillaceous layers, indicating little difference in the elastic moduli, despite the visual differences. There is a difference between halite, where $V_P = 4.5$ km/sec and the argillaceous units where V_P at depth is closer to 4.4 km/second.

Results for QGU31 → QGU30 (Figure 3, first plot) show how constant the velocity can be at depth. At depths greater than about 1 m, variations from the mean are less than 0.5%, which is getting close to the attainable accuracy. Similarly, constant velocities were observed in the other paths through halite (QGU37 → QGU36, Figure 3, QGU31 →

QGU32 and QGU37 → QGU38, Figure 4). In contrast, V_P along paths in the argillaceous layers varied by several percent even at depths beyond the DRZ. (QGU34 → QGU33 and QGU40 → QGU39, Figure 3, QGU34 → QGU35 and QGU40 → QGU41, Figure 4). This variation was particularly noticeable for the measurements made in the thin argillaceous layer (Holes QGU33, QGU34 and QGU35). Given the constancy observed in the halite layers, it is reasonable to argue that the variations of V_P with depth observed in the argillaceous layers are real. In the access drift, Powers describes significant variations in lithofacies for the core in the argillaceous layers and speculates that the differences may be of such magnitude as to influence the elastic wave velocity [7, p. 6]. This observation is believed to be the case in this study. Further work will be required to correlate the velocity results with the core logging.

All four data sets for the horizontal cross-hole V_P measurements made in halite layers indicate a constant velocity as the measurement depth approaches 6 meters. Two of these data sets show clear evidence of a disturbed zone extending in about one meter – QGU31 → QGU30 (Figure 3) and QGU37 → QGU38 (Figure 4). At the surface, V_P is about 10% below the value observed at depth. A smooth increase in velocity was observed over the first meter. Two sets of measurements were made between QGU31 and QGU30, along slightly different paths, resulting in the offset and overlap of data points between 1 and 2 meters depth. Little or no evidence for a DRZ was found in the other two measurements in halite -- QGU37 → QGU36 (Figure 3) and QGU31 → QGU32 (Figure 4). Only at the shallowest depth, where signal quality is lowest, was there any evidence for velocity reduction.

Because of the symmetrical arrangement of the hole pairs around the corner, we expected that a similar pattern of DRZ development would be observed in the left and right walls if the assumption is made that the stress distribution near the corner is unaffected by the layout of the room and the nearby access drift. Conversely, if stresses on either side of the corner are significantly different, then a distinct asymmetry should be observed that 3-D modeling could relate to the geometry of the room and its surrounding. Symmetry was not observed for the paths in halite. There was a well-developed DRZ in the upper left corner (QGU31 → QGU30) but not in the upper right corner (QGU31 → QGU32). Lower down, the second set of hole pairs in halite did exhibit a more symmetric DRZ, with a slightly clearer development seen in QGU37 → QGU38 than in the matching pair on the left side of the corner, QGU37 → QGU36.

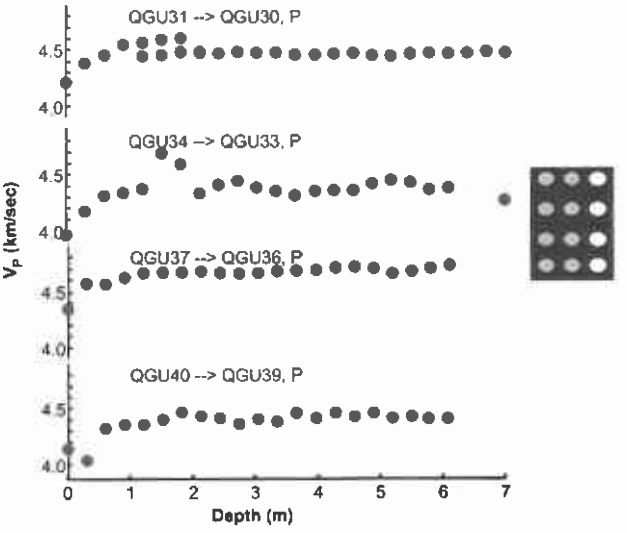

Fig. 3: Vp for the four sets of horizontal cross-hole paths running parallel to the left-hand wall of the alcove corner. The center column holes were drilled into the intersection of the corner walls.

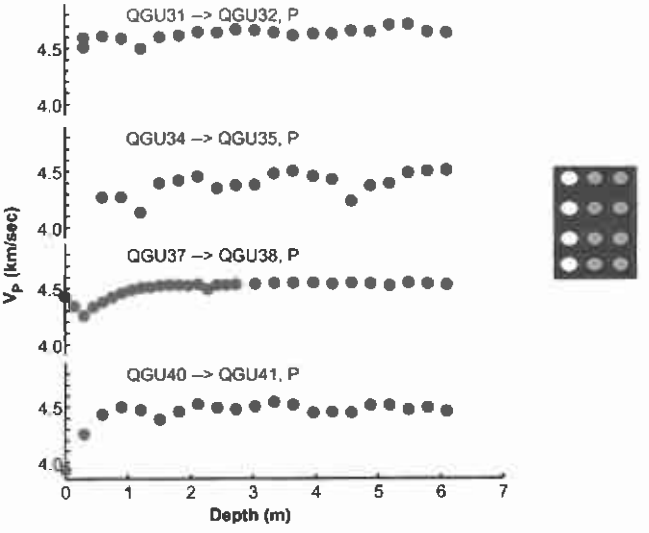

Fig. 4: Vp for the four sets of horizontal cross-hole paths running parallel to the right-hand wall of the alcove corner. The center column holes were drilled into the intersection of the corner walls.

An unexpected feature is the increase in velocity observed between 0.5 and 0 m in QGU37 → QGU38 (Fig. 4). A closely spaced series of measurements was made to clearly delineate the increase. The implication is that the shallowest halite is largely undamaged; contrary to the expectation that the greatest damage would occur where the confining stress was lowest.

Large, abrupt, variations in velocity occurred for paths in the upper argillaceous layer (QGU34 → QGU33 and QGU34 → QGU35), making it more difficult to discern a DRZ. Smaller variations were

observed in the lower argillaceous layer. With the exception of QGU34 → QGU35 there appears to be a shallow low velocity zone near the surface (0 to 1 m) in the argillaceous layers that could be interpreted as evidence for a DRZ. Measurements on both paths in the lower argillaceous layer QGU40 → QGU39 (Figure 3) and QGU40 → QGU41 (Figure 4) do show a DRZ, with a very low value of V_P near the surface, extending in about one meter. The DRZ appears to be symmetrically developed about the corner axis in the lower argillaceous layer.

Previous work by Holcomb and Hardy in the access drift leading into the Q Room Alcove [4], showed a much simpler pattern of DRZ development and a more extensive damaged zone. In the access drift, where the geometry is essentially 2-D, the DRZ was observed to be best developed at mid-height of the drift and to extend in as much as two meters. The complexity observed in the current work reflects the influence of the 3-D geometry on the stress-state and subsequent development of the DRZ.

3.2. Vertical Paths

Nine sets of vertical cross-hole paths were used to measure V_P, one set of three paths each in the left and right walls and one set of three in the walls' intersection. Results for the paths in the walls will be discussed together and contrasted with the observed velocities in the intersection.

Figure 5 contains the results of measurements made along vertical paths in the left wall, showing V_P to a depth of seven meters. All three sets of data indicate a shallow DRZ, extending to a depth of no more than 1 m and more reliably to about 0.5 meters. Velocity decreased the most and to the greatest depth in the center hole pair (QGU33 → QGU36) where V_P was lowered by about 8% from the far field value of 4.4 km/sec to 4.1 km/sec at the surface. Only the outermost meter shows a clear DRZ. In the upper and lower hole pair, QGU33 → QGU30 and QGU36 → QGU39, the evidence for a DRZ is slight; a small decrease in V_P appears to exist in the outermost 0.3 m, particularly near the top of the room between QGU33 and QGU30.

As discussed earlier, the symmetry of the vertical paths about the corner can be used to examine the symmetry of the stress state and the influence of nearby openings such as the Q Access Drift. A symmetric stress state would be expected if the local geometry dominates, leading to the expectation that the pattern of velocities should be identical for the paths in the left and right walls. Greater symmetry was observed for the vertical paths (Fig. 5 and 6), than for the horizontal paths discussed earlier. Partly this is true because there is less evidence of damage for measurements made along the vertical paths, as compared to the horizontal paths.

Between QGU35 and QGU32, (top plot, Figure 6), considerable variation in V_P was observed, at three distinct points near 0, 1.5 and 6.3 m depth. These appear to be real, as indicated by the duplication of the values at adjacent points, but are rather large to be due to lithology fluctuations. Localized macro-cracking may explain the results at shallow depths but seems unlikely at 6.3 meters. Examination and filtering showed that the anomalous velocity values were associated with signals that, when compared to the signals observed at adjacent points, appeared to have had the high frequency components removed during their passage through the salt. Distributed damage typically acts as a high frequency filter, providing credibility to the possibility that real damage is being observed, especially given the duplication at adjacent measurement points. At this time, there is no better explanation for the anomalous results, particularly the low values of V_P observed near 6.3 meters. More closely spaced data give clear evidence of a DRZ in the region between QGU38 and QGU41 (bottom plot, Figure 6) where the decrease in V_P extends in almost a meter.

Compared to the horizontal paths discussed earlier, damage measured along vertical paths is less extensive, reaching shallower depths and producing smaller changes in V_P. The general pattern of damage is similar and slightly asymmetric, with greatest damage observed in the upper portion of the left wall and the lower portion of the right wall.

A very different picture of damage was observed in the third set of vertical paths that lay in the plane bisecting the room corner (Figure 7). To the limits of measurement accuracy, no DRZ was observed, even at the shallowest depths. This is a novel observation and unlike anything observed at other locations in the WIPP. This is also the only measurement of V_P made into a room corner at WIPP, although the geometry is related to the arrangement in the Air Intake Shaft (AIS) [2,3], where measurements are being made in the wall of a 24-foot diameter shaft. Only a shallow DRZ has been observed in the AIS. Given the length of time the Q Room Alcove has been open, to find no DRZ is a surprising result.

Damage along the entire measurement path contributes to the decrease in velocity that is a signature of the DRZ. Thus, the constant V_P

observed in the alcove corner along vertical paths indicates that no point from ceiling to floor has experienced significant damage in the form of cracks that could decrease the speed of a compressional wave propagating vertically. Cracks oriented perpendicular to the direction of propagation are most effective in decreasing V_P; in this case, horizontal cracks would be most effective. Thus, it appears that little or no horizontal cracking has occurred near the bisecting plane of the corner, at any depth, even 12 years after excavation. A meter away (Figs. 5 and 6), the stress-state is sufficiently different that V_P in the vertical direction is decreased, indicating some horizontal, or at least non-vertical, cracking did occur.

3.3. Same-hole Paths

Same-hole paths, where the transmitter and receiver are in the same hole offer a number of advantages: maximum sensitivity of V_P to the expected orientation of cracks, fixed path length to eliminate surveying as a source of error, and the ability to measure both P and S waves with one set of transducers. To offset these advantages there is the poor quality of the P wave signal due to the geometry of the transducer arrangement and the lower sensitivity of V_S. In this arrangement, the shear wave is propagating perpendicular to the expected crack orientation, but the particle motion is parallel to the plane of the cracking, thus reducing the effect of the DRZ on the velocity of the shear wave.

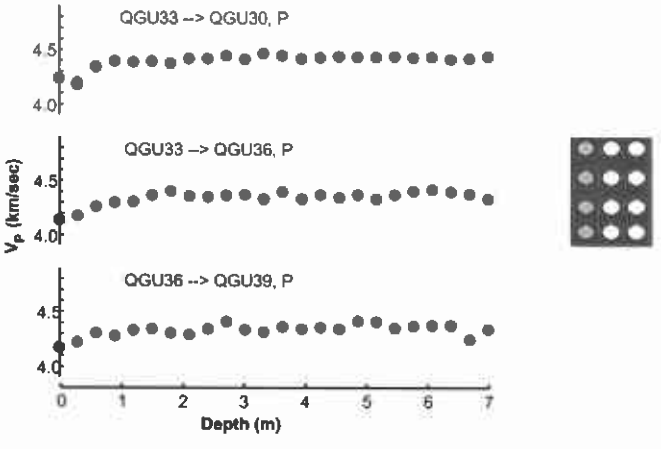

Fig. 5: V_P for the three sets of vertical cross-hole paths in the left-hand wall of the alcove corner.

Because of the shallowness of the DRZ and to confirm the absence of a DRZ in the room corner, a more extensive series of measurements was carried out in some of the holes. Measurements were made every 0.15 m for the first 2 meters. The general pattern of damage seen in the cross-hole measurements was also observed in these same-hole measurements. Two sets of data are particularly effective in showing the strong variation in damage near the corner; V_P

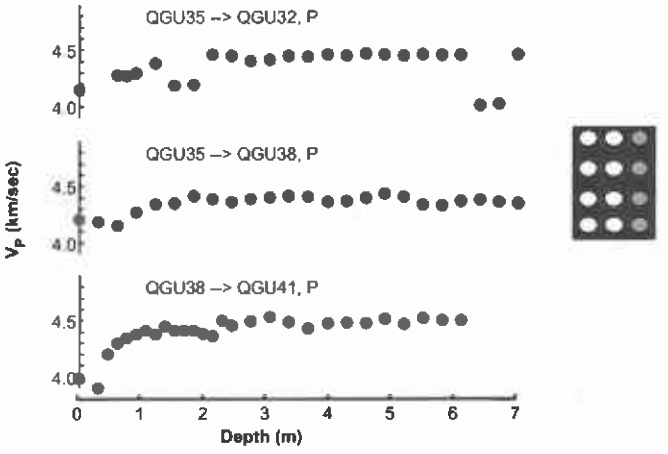

Fig. 6: V_P for the three vertical sets of cross-hole paths in the right-hand wall of the alcove corner.

measured along the axes of holes QGU36 and QGU37 are plotted in Figure 8. A DRZ was clearly present in QGU36, located about a meter to the left of the corner, but no hint of a DRZ is observed in QGU37, drilled directly into the corner. V_P decreased from 4.4 to 3.9 km/s, with the decrease beginning at about 1.2 m, indicating that there was substantial damage at this location. Just a meter to the right, in QGU37, there is little or no evidence of damage. The DRZ is clearly much less well developed here, as compared to the same horizon only a meter away. A short distance from the corner, the DRZ is similar to that observed in the access drift by Holcomb and Hardy [4]. Clearly the difference is due to the dependence of the stress-state on proximity to the corner.

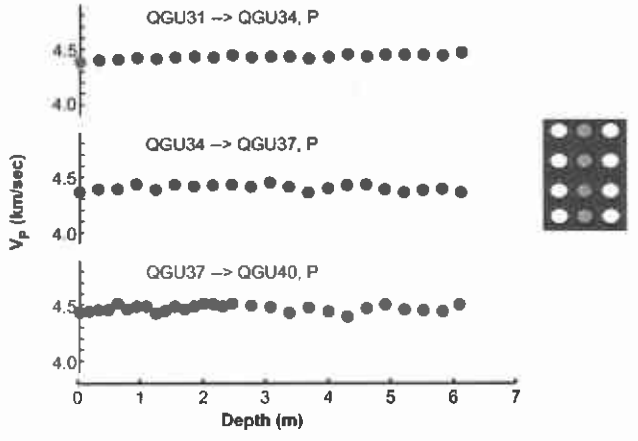

Fig. 7: Vp for the three sets of vertical cross-hole paths in the alcove corner. The center column holes were drilled into the intersection of the corner walls.

3.4. Comparison of Laboratory and In situ Results

Previous laboratory work by Brodsky determined the changes in V_P under axisymmetric stress conditions [5]. However, the *in situ* stress-state is fundamentally non-axisymmetric with the minimum compressive stress approaching zero along the normal to the surfaces of openings. Parallel to the surfaces, stress concentrations vary, depending on the shape of the opening and its orientation. For a long drift, stress parallel to the drift is essentially the same as the far field lithostatic stress, which is about 15 MPa. The vertical stress concentration factor is approximately two, leading to a vertical stress of 30 MPa, although higher values can be attained initially near corners. Damage due to cracking is driven by both instantaneous processes and time-dependent creep, both of which produce more damage at higher stress differences. An experiment was carried out to help separate the instantaneous and time-dependent contributions to damage.

Using a true-triaxial test frame, WIPP salt was subjected to a stress path designed to simulate the instantaneous (short-term) stress path experienced by salt near a drift as it was mined. In the following discussion, a numbered coordinate system will be used to refer to the axes along which stresses and strains were measured, using subscripts to denote the proper axis. Thus, the stress or strain measured along the one (1) axis would be σ_1 or ε_1. By the usual convention for geomechanics, the maximum compressive stress is applied along the one (1) axis, intermediate stress is parallel to the two (2) axis and the minimum compressive stress is parallel to the three (3) axis. During this test, the maximum compressive stress, σ_1, was increased from 15 to 30 MPa, the intermediate stress, σ_2, was held constant at 15 MPa, and the minimum compressive stress, σ_3, decreased from 15 to 0 MPa. This condition approximated the *in situ* stress near the free surface during mine-by and allowed the effect of the instantaneous damage on V_P to be determined. Figure 9 summarizes the experiment, showing the sample and the stress-strain data from the test. Samples were approximately 5 cm by 5 cm in cross section and 12 cm long. After jacketing with copper foil, strain gages and LVDT gages were mounted to measure the three principal strains. Piezoelectric transducers mounted on the sample or in the platens were used to measure V_P at intervals during the test. Stresses were servo-controlled so that σ_1 and σ_3 changed in equal but opposite increments, while σ_2 was held constant. The intermediate stress was slightly above the goal of 15 MPa for experimental reasons. Strain in the one direction, corresponding to maximum compressive stress, was the control variable, increasing at a fixed rate during the test.

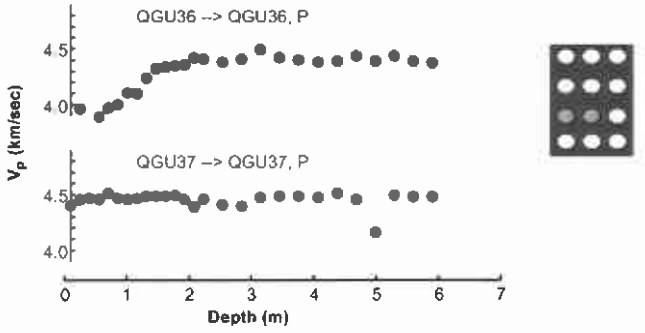

Fig. 8: Same-hole measurements for adjacent holes, one in the left-hand wall (top plot) and in the corner (bottom plot).

Figure 9 includes a plot of strains versus σ_1, with compression to the right; strain parallel to the maximum compressive stress is plotted as a solid line, strain parallel to the intermediate stress is plotted as a dashed line, and in the minimum compressive stress direction, strain is indicated by the dotted line. Yielding occurred after σ_1 surpassed 22 MPa, followed by more-slowly increasing stress, until the test was halted after σ_3 reached 0 MPa. At that point, all stresses were returned to the initial values. Dilatational strain, assumed to be due to opening of cracks as the salt was damaged, can be seen in ε_{33}, which began increasing rapidly when σ_1 exceeded the yield stress. In contrast to both ε_{11} and ε_{33}, ε_{22} remained unchanged.

Velocities, measured along the stress axes, are plotted in Figure 10 superimposed on the stress history. Lines show the stress history as a function of time, beginning near a hydrostatic stress-state and evolving to the final stress of (30, 17, 0) MPa, before the stress was returned to the starting values. Shaded dots are used to plot the normalized values of V_P during the course of the test (right-hand scale). Parallel to σ_1 and σ_2, the maximum and intermediate compressive stresses, V_P was essentially constant as shown by the white and gray dots, respectively. Although initially constant, V_{P3} began to decrease when the yield stress was exceeded and decreased throughout the test, reaching a final value about 3.5% below the starting value (black dots). An electronics problem caused loss of signal between 72,000 and 82,000 seconds. Increasing pressure always increases V_P so the final value of V_P, measured after pressure was increased

to 15 MPa, is a conservative estimate of V_P at the end of the depressurization phase.

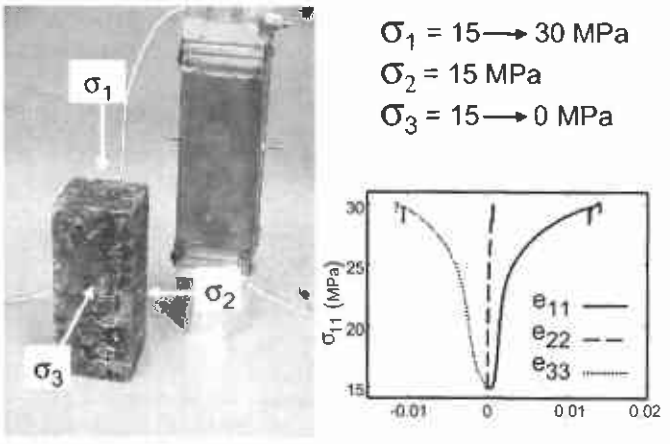

Fig. 9: Photograph of sample, unjacketed and ready for testing, with stress-strain data for a test simulating results of a mine-by.

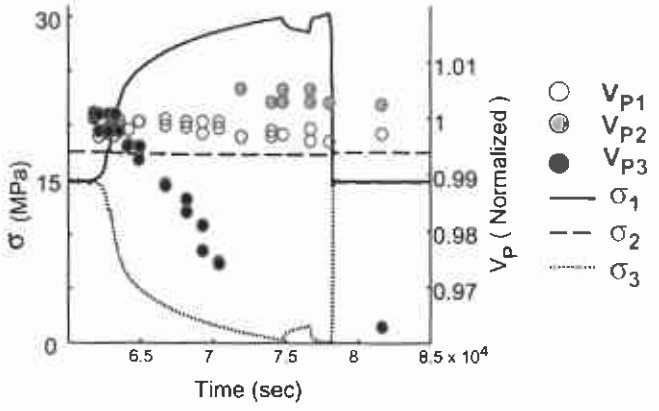

Fig. 10: Stress history (lines, left axis) and normalized V_P (dots, right axis) as a function of time for the mine-by simulation experiment.

Strains and velocities are telling a consistent story of anisotropic damage under stresses similar to those expected instantaneously during a mine-by. Compressive strain along the one (1) axis (maximum compressive stress) would close, not open cracks, leading to little change in V_P along the axis parallel to σ_1. Along the two (2) axis, parallel to σ_2, little strain was observed at any time during the test. Again, this is consistent with no cracks opening and no change in V_{P2}. Dilatational strain was only observed in the three (3) direction, parallel to the minimum compressive stress, and this is the direction where a decrease in V_{P3} was measured. The primary strain contribution of cracks opening in the three (3) direction would be to cause the magnitude of ε_{33} to increase more rapidly than would be observed for the Poisson contribution in the more-or-less elastic, low-stress, portion of the test. Increased dilatational strain is assumed to be the result of cracks opening under the shear stress being applied and newly opened cracks cause V_P to decrease for waves propagating in the direction of the opening cracks. The primary strain contribution of cracks opening in the three (3) direction would be to cause the magnitude of ε_{33} to increase more rapidly than would be observed for the Poisson contribution in the elastic, low-stress, portion of the test.

Instantaneous damage under stresses similar to what would be encountered near a drift, or other opening being mined, only changed V_P in the direction of the minimum compressive stress and then by only 3.5 percent. As the previous discussion and earlier work in a nearby drift showed [4], much larger changes were observed *in situ*. Figure 11 compares the *in situ* results with the laboratory experiment discussed above. *In situ*, V_P was found to be change by up to 7% in the vertical and horizontal directions, parallel to the drift, and 20% perpendicular to the drift. Equivalent results for the instantaneous effects of applying appropriate stresses in the laboratory were 0% change in the horizontal and vertical directions and 3.5% in the minimum stress direction, which is equivalent to perpendicular to the drift. The prominent difference is a measure of the impact of time-dependent deformation on the production of damage *in situ*.

4. SUMMARY:

Previous work had examined the DRZ in simple geometries, typically a room wall or a long drift. The current work is an extensive look at what happens in the corner of a room, an area intentionally chosen for its complexity. As expected, the pattern of damage was found to be more complex than in the simpler geometries previously studied. Two features were unexpected: damage did not extend in as far as in the previous studies, and along the bisecting axis of the corner, no DRZ was observed, even along the direction most favorable for detecting damage.

First, the similarities will be summarized. Near the floor and ceiling the DRZ was less pronounced than in similar zones closer to the mid-height of the room. Damage was clearly anisotropic, with the maximum decrease in V_P being observed in directions closer to perpendicular to the walls. This fits with the assumption that the DRZ is the result of cracks opening in the direction of minimum compressive stress. The decreases in V_P were similar to those observed before, but the spatial variation of DRZ development was very different.

In previous work, velocity measurements typically indicate a DRZ extending in about 2 meters. An exception to that rule was found in the AIS [3], where the DRZ only extends 0.5 to 1 meters. In the current work the DRZ, when found at all, only extended in about 1 meter and there were many areas that did not appear to be damaged. Of greatest interest are the results from the cross-hole, vertical path and the same-hole measurements made in holes drilled into the bisecting axis of the corner. No DRZ was observed here, even for the same-hole measurements, which are most sensitive to damage in the expected orientation. Same-hole measurements made in a hole only a meter away from that hole where no DRZ was observed found a well-developed DRZ. The complete absence of discernable damage, even after 12 years, indicates the effectiveness of a rounded interior corner in suppressing damage.

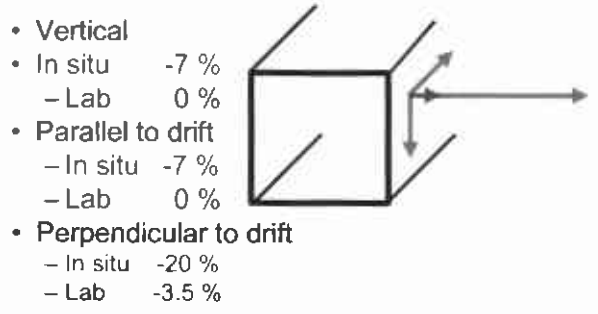

Fig. 11: Summary of velocity changes observed in the simulated mine-by experiment compared to the results observed *in situ*. Sketch indicates orientation and magnitude, relative to a drift. Overlapping arrows perpendicular to drift show relative magnitude of laboratory and *in situ* velocity changes.

This observation suggests a possibility for constructing seals that would avoid the effects of the DRZ on permeability. If a slot with a rounded end were mined into the wall of an existing drift to a depth of about 3 meters, then the slot would extend past the DRZ induced by the drift, reaching relatively undisturbed, low-permeability salt. The results of the current work suggest that there would be a zone, approximately along the axis of the slot, where no or limited damage would occur, either immediately or for years. Thus, leaks past the seal through a DRZ could potentially be eliminated since the DRZ may not form to begin with. Given the complexity of the geometry studied in the current work, it is clear that a more systematic investigation would be required to substantiate this possibility. In particular, the details of the influence of curvature and width of the slot on extent of the DRZ would need to be studied to see if the absence of a DRZ is reproducible and predictable.

A comparison of laboratory and *in situ* results show that plastic creep is producing more crack damage than was produced by the instantaneous effect of applying shear stresses equivalent to the 3-D stress expected *in situ* (Figure 11).

REFERENCES

1. Munson, D.E., D.J. Holcomb, K.L. DeVries, N.S. Brodsky, and K.S. Chan, Correlation of theoretical calculations and experimental measurements of damage around a shaft in salt, pp. 491-496, *Proc. 35th U.S. Symposium. On Rock Mechanics*, Eds. J.J.K. Daemen and R.A. Schultz, A.A. Balkema, 1995
2. Holcomb, D.J., Assessing the disturbed rock zone (DRZ) around a 655 meter vertical shaft in salt using ultrasonic waves, pp. 965-972, *Proc. 37th U.S. Rock Mechanics Symposium*, Eds. B. Amadei R.L. Kranz, G.A. Scott, and P.H. Smeallie, A.A. Balkema, 1999
3. Hardy, R.D. and D.J. Holcomb, Assessing the disturbed rock zone (DRZ) around a 655 meter vertical shaft in salt using ultrasonic waves, An Update, pp. 1353-1360, *Proc. 4th North American Rock Mechanics Symposium*, Eds. J. Girard, M. Liebman, C. Breeds and T. Doe, 2000
4. Holcomb, D.J. and R.D. Hardy, Assessing the disturbed rock zone (DRZ) at the WIPP (Waste Isolation Pilot Plant) in salt using ultrasonic waves, *Proc. 38th U.S. Rock Mechanics Symposium, DC Rocks 2001*, pp. 489-496, Ed. D. Elsworth, J.P. Tinucci and K.A. Heasley, A.A. Balkema, 2001
5. Brodsky, N.S., *Thermomechanical damage recovery parameters for rock salt from the Waste Isolation Pilot Plant*, SAND93-7111, Sandia National Laboratories, Albuquerque, NM, 1995
6. Maxwell, S.C., R.P. Young and R.S. Read, A micro-velocity tool to assess the excavation damaged zone, *Int. J. Rock. Mech. Min. Sci.*, 35(2), 235-247, 1998
7. Powers, D.W., *Core descriptions from Location 1, S90 Drift, for DRZ Test Program, April 2000, contractor's report*, Sandia WIPP Records Center ERMS #510137, Sandia National Laboratories, Carlsbad, NM, 2000.